Dynamics of ion-driven fishbones in tokamaks : theory and nonlinear full scale simulations

Guillaume Brochard

INSTITUT POLYTECHNIQUE DE PARIS

NNT : 2019IPPAX002

Thèse de doctorat

Dynamique du fishbone ionique dans les tokamaks : théorie et simulations non-linéaires multi-échelles

Thèse de doctorat de l'Institut Polytechnique de Paris
préparée à l'École Polytechnique

École doctorale n°626 Institut Polytechnique de Paris (IP Paris)
Spécialité de doctorat : Optique, laser et plasma

Thèse présentée et soutenue à Cadarache, le 11 Octobre 2019, par

GUILLAUME BROCHARD

Composition du Jury :

Jonathan Graves Professeur, Swiss Plasma Center EPFL	Rapporteur
Gregorio Vlad Directeur de recherche, ENEA Frascati	Rapporteur
Jean-Marcel Rax Professeur, École Polytechnique	Président du jury
Steven Cowley Professeur, Princeton University	Examinateur
Magali Muraglia Chargée de recherche, PIIM CNRS	Examinateur
Xavier Garbet Directeur de recherche, IRFM CEA Cadarache	Examinateur
Hinrich Lütjens Directeur de recherche, CPHT CNRS	Directeur de thèse
Rémi Dumont Directeur de recherche, IRFM CEA Cadarache	Encadrant CEA

Remerciements

I would like first of all to address my warmest acknowledgment to my referees, Dr. Jonathan Graves and Dr. Gregorio Vlad, who carefully went through my entire manuscript this summer, despite the marvelous weather we all had in August. I would like also to thank my entire Ph.D committee, Pr. Jean-Marcel Rax, Pr. Steven Cowley, Dr. Magali Muraglia and my referees, to have accepted to be part of my jury. I feel deeply honored to have received my Ph.D degree from such respected experts in our field. All the talks we had around my Ph.D defense were extremely intrusctive, and will help me develop my work further in the near future.

I will now continue this section in a language that is quite shockingly rarely used in this thesis. Je voudrais exprimer mes remerciements les plus profonds à mes encadrants, Rémi Dumont, Hinrich Lütjens et Xavier Garbet, qui m'ont remarquablement soutenu tout au long de cette thèse. Rémi, je tiens à te remercier pour ta grande rigueur et ta patience, dont tu m'as fait bénéficier, autant dans l'analyse de mon travail que dans mon acquisition progressive (et peut être encore imcomplète) de ces mêmes qualités à ton contact. Hinrich, je souhaite te remercier pour m'avoir autant appris sur le langage parfois obscur que peut être celui de la programmation informatique, ainsi que son utilisation à une échelle qui était encore toute nouvelle pour moi. Je tiens aussi saluer la grande patience avec laquelle tu m'as toujours encadrée, malgré les quelques sueurs froides que j'ai du provoquées avec ma gestion parfois ... personnelle des deadlines, en particulier celle liée à ce manuscrit ! Xavier, je m'ajoute à la longue liste de ceux qui comme moi doivent une grande partie de leur thèse à ton expertise infaillible. Que ce soit pour la fulgurance incroyable avec laquelle tu peux trouver une solution aux problèmes les plus techniques et obscurs, pour ton savoir encyclopédique couvrant une majeure partie de la physique des tokamaks et des plasmas en général, ou pour ton optimisme et ton humour lui aussi si personnel, travailler avec toi a vraiment été une expérience fabuleuse. Je tiens surtout à te remercier pour les encouragements et les conseils que tu m'as donnés au début de ma troisième année, lorsque je sentais la plupart de mes résultats m'échapper quelques mois avant de partir en conférence.

Ma thèse n'aurait pas non plus été la même sans tous les thésards qui ont vécu à mes côtés et moi au leur cette expérience si particulière et toujours inattendue qu'est le doctorat ! Merci à Elisabetta, Anastasia, Adrien, Peter, Alberto, Camille, Axel, Damien, Raffaele, Serafina, Giacomo, Mathieu et tant d'autres, autant pour ce qu'on a pu partager à l'IRFM, ou dans les profondeurs de la rue de la Verrerie ! Merci aussi aux chercheurs de l'étage théorie et du CPHT pour toutes ces discussions sur la fusion et bien d'autres sujets, Timothée, François, Fabien, Patrick, Guilhem, Philippe, Guido, Yves et Yanick !

Pour ce qui est des non-fusionnistes, je tiens tout d'abord à remercier Louisa, qui a su me supporter quotidiennement au moment le plus stressant et épuisant de ma thèse : la rédaction de ce manuscrit ! Sans ton soutien et ton amour, le résultat aurait été bien différent ma chérie ! Merci à toi. Je tiens aussi à rendre justice à Valentin, Jimmy, Jean, JB, Louis, Alejandro, Simon, Thomas et Francesca, pour l'amitié sans failles que vous m'avez apportée durant ma thèse et encore aujourd'hui. Nous avons passé de merveilleux moments ensemble durant ces trois ans. Votre amitié m'a également grandement aidé à surmonter les lourds moments de blues qui sont également les compagnons d'infortune d'une thèse. Merci pour tout !

Pour finir, je tiens aussi et surtout à remercier ma famille, Papa, Solène et Silvie, dont la présence à mes côtés ne m'a jamais fait défaut, hier comme aujourd'hui. Mille fois merci !

Avant-propos en français

Cette thèse vise à discuter un problème technique émergeant du contrôle en régime continu d'un réacteur de fusion par confinement magnétique : le tokamak. Avant de donner un bref résumé du dit problème et des moyens qui ont été mis en place durant cette thèse pour comprendre son origine, son déclenchement, ses conséquences et son potentiel contrôle, une brève discussion doit être tenue quant à la raison d'être de ce type de réacteur.

La recherche liée à ce type de machine s'inscrit dans l'effort international qui a été entrepris depuis plusieurs décennies pour décarboner dans un futur proche les moyens de production énergétiques de nos sociétés. L'utilisation actuelle des énergies fossiles n'est pas pérenne vis-à-vis de la stabilité de notre éco-système et de son climat. Cette utilisation doit être à moyen terme abandonnée au profit de nouvelles sources d'énergie non productrices de carbone, et s'appuyant sur des réserves en matières premières abondantes. Les énergies renouvelables peuvent alors être vues dans ce contexte comme des sources d'énergies idéales. Cependant, le caractère transitoire de leur génération d'énergie pose problème pour nos sociétés ayant un besoin énergétique important, dans la mesure où des moyens de stockage performants de leur énergie ne sont pas encore opérationnels. La fusion thermonucléaire, dont les réactifs sont les isotopes d'hydrogènes, abondants sur Terre, est alors une alternative intéressante. Une telle réaction est plus énergétique que les réactions de fission nucléaire, et s'éxonére des problèmes d'instabilité intrinsèque de telles réactions, liés à leur déclenchement en chaîne, de par la nature initialement répulsive des réactifs de la fusion.

La recherche liée à cette nouvelle forme de réaction nucléaire existe depuis la seconde moitié du XXème siècle, et doit encore répondre à un large prisme de problématiques fondamentales et techniques afin de rendre possible la création d'un réacteur économiquement viable. Parmi ces nombreuses problématiques, l'instabilité dite de "fisbhone" est celle discutée dans ce manuscrit.

Au sein des tokamaks, les particules rapides générées par les réactions de fusion et par les méthodes de chauffage non-inductives peuvent interagir avec les instabilités Magnéto-Hydro-Dynamiques, conduisant potentiellement à leur transport en dehors du plasma de coeur. Cette problématique est importante dans le contexte des plasmas en combustion, où la relaxation collisionnelle des particules alpha est nécessaire pour compenser la perte d'énergie lors la décharge. Le temps de transport résonant des particules rapides étant bien plus petit que leur temps de thermalisation sur le plasma thermique, ces instabilités MHD-cinétiques peuvent engendrer une dégradation de l'efficacité énergétique de la réaction, qui est d'importance cruciale pour les futurs réacteurs commerciaux. Dans cette thèse, nous étudions l'interaction des ions énergétiques avec le mode de kink interne, qui conduit à l'émergence de l'instabilité fishbone. À cette fin, nous utilisons le code non-linéaire hybride XTOR-K, pour simuler les phases non-linéaires du fishbone ionique, durant lesquelles les particules rapides sont tranportées. Dans un premier temps, la théorie linéaire de l'instabilité fishbone est reproduite, retrouvant une relation de dispersion similaire à celle du modèle de Porcelli. Un écart est constaté pour les particules très passantes. Un code linéaire a été implémenté pour résoudre de façon non perturbative la relation de dispersion du fishbone obtenue. Les résultats obtenus avec ce code sont cohérents avec ceux d'XTOR-K dans la phase linéaire des simulations, avec des taux de croissance, des fréquences de rotation et des surfaces de résonance similaires. Ces résultats fournisent une vérification linéaire de XTOR-K, permettant son utilisation sur des équilibres plus complexes, et durant des phases non-linéaires. Dans un second temps, une étude paramétrique est fournise par XTOR-K sur la stabilité linéaire du fishbone alpha, avec

des équilibres pertinents pour le cas ITER 15 MA. Nos simulations montrent que ce scénario sera probablement instable à l'égard du fishbone alpha, pour des densités de particules alpha réalistes dans ITER. Les résultats non-linéaires obtenus avec XTOR-K sur un équilibre circulaire peu énergétique et sur le cas ITER 15 MA sont ensuite présentés. Ces résultats documentent la dynamique auto-cohérente des particules rapides et des modes MHD lors de plusieurs oscillations fishbone. Le transport résonant de particules rapides est une caractéristique commune dans ces simulations, accompagnée d'une décroissance charactéristique de la fréquence du mode MHD-cinétique. Les différences dans ces simulations sont discutées, ainsi que le régime non-linéaire charactérisant le mode observé sur la base des théories existantes. Durant quelques oscillations fishbone, dans nos différentes simulations, le transport total de particules alpha au coeur du plasma est de l'ordre de 5 % de la population initiale, ce qui montre que la réduction des performances de fusion due à l'instabilité fishbone-alpha est limitée. À partir de ces simulations, un mécanisme expliquant le couplage non-linéaire entre le transport résonant de particules et la décroissance en fréquence du mode MHD-cinétique est présenté.

De par le caractère international de la recherche en fusion par confinement magnétique, ce manuscrit est écrit en langue anglaise, afin que les travaux entrepris lorss cette thèse puissent à leur échelle contribuer autant que possible à l'effort global entrepris vers l'obtention de sources d'énergies abondantes, pérennes, et sûres.

Contents

Chapter 1

Introduction

1.1 Stakes of controlled nuclear fusion

1.1.1 The nuclear fusion reaction

The concept of nuclear fusion takes its origin in a conjecture made by A. Eddington in 1920 [Eddington, 1920]. At the time, very little was known about the physical processes that allow stars to shine over several billions of years. The only certitude was that the stars' energy could not take its source from chemical combustion reactions, or from a conversion of their gravitational energy into thermal energy. The size and composition of stars did not allow them to radiate energy over so long periods of time.
At the beginning of the XX^{th} century, it was discovered by Aston [ASTON, 1920] that the mass of atoms' nuclei is inferior to the sum of its individual nucleons mass. This is now known as the mass defect, which is associated to the strong force interaction. This force enables nuclei to remain stable against their electrostatic repulsion. This mass defect can be linked to the nuclei binding energy ΔE through the mass-energy equivalence. For a nucleus with Z protons and N neutrons [Rax, 2011]

$$\Delta E(Z,N) = Zm_pc^2 + Nm_Nc^2 - Mc^2 \tag{1.1}$$

where m_p is the proton's mass, m_n the neutron's mass, M the nucleus's mass, and c the speed of light. The measurement of binding energies using mass spectroscopy was performed by Aston for most elements of the periodic table, and can be found on Figure (1.1). According to this figure, iron is the most stable element of the periodic table, having the highest binding energy. This figure implies that nuclear energy can be released from two processes. Either nuclear fission of nuclei heavier than iron, with for example the fission of uranium 235 into lighter nuclei. Or the fusion of nuclei lighter than iron, such as the fusion of hydrogen into helium. In both cases, the combined masses of the products is lower than the reactant masses. The nuclear energy released from the fusion reaction is generally one order of magnitude higher than for the fission reaction, according to (Figure 1.1)

It was this discovery, together with the composition of stars, that led Eddington to believe that nuclear fusion was the stars' energy source. The nuclear reactions among stars are now known to be more complex than the simple fusion of four hydrogen nuclei into helium. They in fact involve complex fusion chain reactions that are beyond the scope of this thesis. In order to be able to fuse together, nuclei, that are positively charged, must have enough kinetic energy so that they can overcome their Coulomb barrier. When they do, the nuclear strong force attracts nuclei together and fuse them. The rate τ_{fus} at which fusion reactions

arise between two species X and Y for a given volume V can be formally expressed as

$$\tau_{fus} = n_X n_Y \langle \sigma v \rangle V \tag{1.2}$$

where n stands for the density, and $\langle \sigma v \rangle$ the reaction's cross section. This last term is weighted by the relative velocity between the two species, averaged over velocity. The dependence of

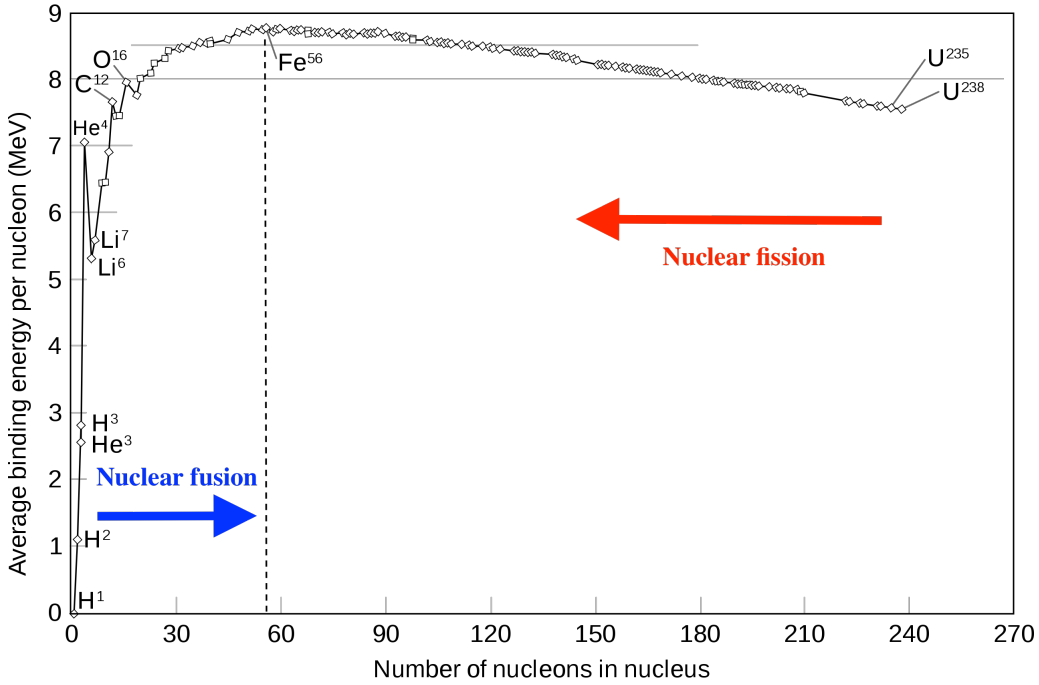

Figure 1.1: Aston's curve. The binding energy per nucleon is expressed as a function of the number of nucleons.

this quantity over the species X and Y kinetic temperature is displayed on Figure 1.2 for different fusions reactions. From this figure, it can be noted that the fusion reaction with the largest cross section at low temperature involves deuterium ${}^2_1D$ and tritium ${}^3_1T$. These elements are heavy isotopes of hydrogen. The fusion reaction associated to these elements is

$${}^2_1D + {}^3_1T \rightarrow {}^4_2He\ [3.56MeV] + n\ [14.03MeV] \tag{1.3}$$

where ${}^4_2He$ is the helium nucleus, also referred to as an alpha particle, and n a neutron. The energies in brackets are the kinetic energies of each particle. The total energy released per reaction is then $E_{DT} = 17.6MeV$. The amount of energy per mass that can be extracted from nuclear fusion is far superior to any other physical processes. Controlling this reaction on Earth would generate vast quantities of energy. The DT reaction is particularly interesting in this regard since it enables to get the most energy at the lower cost, cost being the temperature at which it is needed to heat up the reactants.

On Earth, for the reaction to exhaust a sufficient amount of energy, it is needed to heat a deuterium/tritium gas at a temperature of order $20keV$ ($\sim 2.10^8 K$). This temperature is 20 times as hot as the Sun's core temperature. Higher temperatures are required on Earth since the Sun compresses its gas through its gravitational force, easing its nuclear fusion chain reactions. A gas at these temperatures is not really a gas anymore. The hydrogen atoms are fully ionized by the high temperatures. It means that the electrons are not longer bounded to their nucleus. This medium is called a plasma. An evaluation of the deuterium and tritium stocks on Earth is now presented, in order to assess the opportunity that represents fusion energy for the global energy consumption.

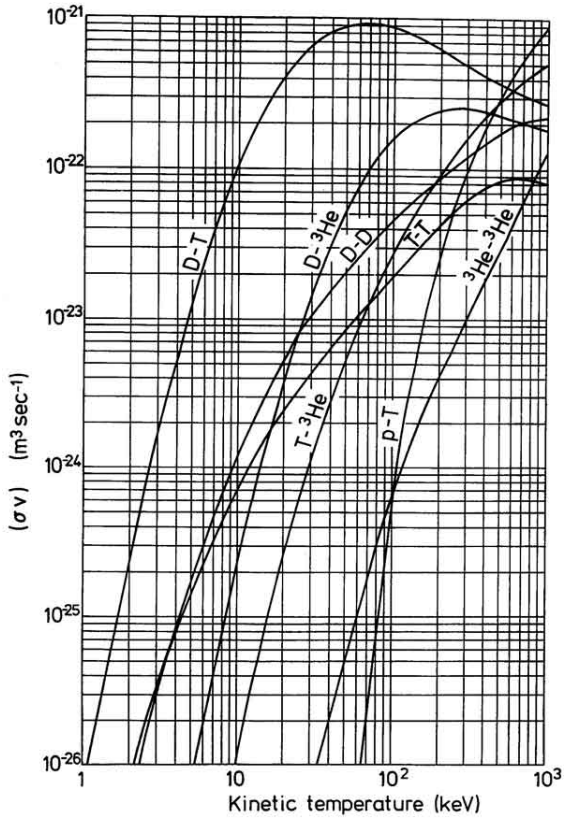

Figure 1.2: Average cross sections of several fusion reactions as a function of kinetic temperature

1.1.2 Opportunities and principles of controlled nuclear fusion

Assessment of the world resources for fusion energy

The current world energy consumption over a year is 1 weu $= 7.5 \times 10^{19} J$, which represents 2.4 terawatt per year [Cowley, 2016]. In order to facilitate this discussion, the world energy unit (weu) has been introduced. Assuming that it possible to create a fusion power station, the production of one gigawatt of electricity would consume 120 kg of deuterium and tritium per year. Deuterium is vastly present in sea water, with 0.02 g per liter. Its extraction can be performed at minimal cost. The total volume of sea water on Earth being of order $10^{18}\mathrm{m}^3$, the world ressources in deuterium could then lead to the total energy production of 5×10^{10} weu.

However, the amount of energy that could be created through nuclear fusion is limited by tritium. Tritium is almost inexistent on Earth since it has a half life of 12.32 years. In order to produce fusion reactions, tritium needs to be obtained from lithium, through the nuclear reactions

$$n +^6 Li \rightarrow^4_2 He\ [2.1MeV] +^3 H\ [2.7MeV] \tag{1.4}$$

$$n +^7 Li \rightarrow^3 H + n - 2.46MeV \tag{1.5}$$

with the last nuclear reaction being endothermic. Creating 120kg of tritium through these reactions would require four tonnes of litium. Currently, it is only feasible to obtain lithium from the Earth's crust. World resources in the Earth's crust are about 13.5 millions tonnes, which could provide about 10^3 weu of fusion energy. Tritium is also present in sea water, with the low concentration of 0.2 $\mathrm{mg.L}^{-1}$. If its extraction from sea water can be achieved efficiently, the world reserves would then rise to 230 billions tonnes, ensuring a total fusion

energy of $\sim 25 \times 10^6$ weu. Compared to the energy that can be extracted from others Earth's resources, displayed on Figure (1.3), the advantages of fusion energy are clear. Fossil energies such as oil, gas or coal, could only sustain the world energy consumption for ~ 100 years, and could not been used without leading to a catastrophic climatic situation. Fission energy in its existing form can only produce 10 weu from uranium stocks. Advanced breeder technology could increase this energy to about 10^3 weu, for the same uranium resources.

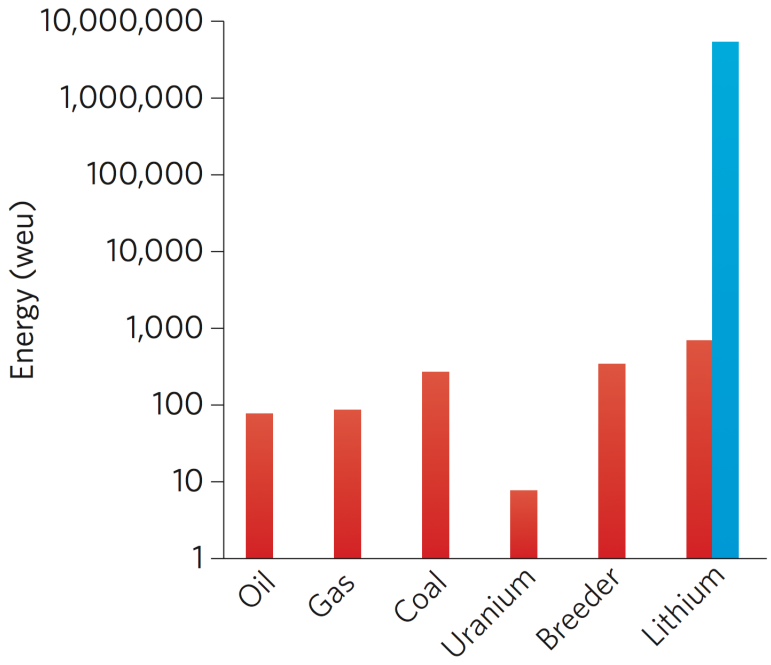

Figure 1.3: Comparaison of the total energy in world energy unit (weu) that could be extracted from the world stocks, for different physical processes. Chemical processes such as combustion of oil, gas and coal could only sustain the current world energy consumption for about 100 years each. Uranium world resources can only provide the world with energy for 10 years with the current technology, and up to 500 years with advanced breeder technology. The resources of lithium in the Earth's crust could sustain the world consumption for $\sim 10^3$ through fusion reactions, and up to ~ 10 millions years if lithium can be extracted efficiently from sea water. (Source : [Cowley, 2016])

Requirements and basic principles of fusion reactors

Nuclear fusion has then the potential of becoming a major component of the future world energy production, being more abundant and more energetic than any other energy sources. However, controlling nuclear fusion on Earth requires the formidable task of confining a DT plasma long enough so that fusion reactions can occur. For a reliable industrial reactor, it is required that the power outcast by fusion exceeds largely both the power needed to heat up initially the plasma, P_{aux}, and the power lost from the plasma P_{loss}. Power losses arise mainly through collisional and turbulent transport. The first requirement can be characterized by the amplification factor Q

$$Q \equiv \frac{P_{fus}}{P_{aux}} \tag{1.6}$$

Breakeven (Q=1) is reached when the total power outcast by fusion equals the power used to bring the plasma at 20 keV. Ignition ($Q \to \infty$) is achieved when the plasma heats up itself through fusion reactions, and that the auxiliary heating system can be turned off.

For the plasma to heat up itself, the second requirement needs to be met. When fusion reactions arise in a confined plasma, the energetic neutrons outcast can not contribute to its heating, since they are not charged. These particles exit the plasma to heat up lithium blankets. It creates tritium nucleus through the nuclear reactions in 1.4 and 1.5, and produces electrical energy by heating pressurized water. Only the charged alpha particles, which carry a fifth of the fusion reaction's energy, can maintain the plasma at fusion temperatures. Therefore, the following power balance needs to be respected

$$P_\alpha + P_{aux} \equiv P_\alpha \left(1 + \frac{5}{Q}\right) = P_{loss} \tag{1.7}$$

The power outcast by alpha particles is evaluated through the fusion reaction rate, $P_\alpha = P_{fus}/5 = n^2 \langle \sigma v \rangle E_{fus} V/20$. The power losses during the plasma's confinement are characterized by $P_{loss} = W/\tau_E$, where $W = 3nk_BT$ is the plasma internal energy, and τ_E the confinement time. It has been assumed in computing these quantities, that the ion and electron densities are equal, as well as their temperature. Balancing these powers leads to the Lawson criterion [Rax, 2011]

$$n\tau_E = \frac{60 k_B T}{\langle \sigma v \rangle E_{fus}(1 + 5/Q)} \tag{1.8}$$

A future fusion reactor would require to operate with an enhancement factor $Q \in [40, +\infty]$. For a confined plasma of 20 keV, it is then required that $n\tau_E$ exceeds $2.10^{20}\mathrm{m}^{-3}\mathrm{s}$. Two main approaches have been considered to control nuclear fusion. The first one is called inertial confinement fusion. High density plasmas $n \sim 10^{31}\ m^{-3}$ are confined on very short times $\tau_E \sim 10^{-11}$s by compressing a target of a few millimeters, using megajoule lasers. This approach is beyond the scope of this thesis. The second approach is to confine a low density plasma $n = 10^{20}\ \mathrm{m}^{-3}$ on longer times, $\tau_E \sim 1$ s. This can be achieved by confining the plasma in a closed magnetic configuration. Charged particles follow the magnetic field lines by gyrating along them, with a finite excursion called the Larmor radius. This radius is inversely proportional to the local magnetic field, therefore a good confinement is provided by a strong magnetic field. In present day magnetic confinement devices, the magnetic field is around $1 - 5$T, which is four orders of magnitude above the Earth's magnetic field. The β parameter gives a measure of the ratio between the thermal pressure of the plasma and of the magnetic pressure exerted onto the plasma. Its formal expression is

$$\beta = \frac{n k_B T}{B^2/2\mu_0} \tag{1.9}$$

Confinement is characterized by $\beta << 1$. It implies that the magnetic force confining the plasma largely exceeds the pressure force that would lead the plasma to expand outward. It enables to obtain a high pressure gradient, confining the thermonuclear plasma far from the edges of the magnetic device.

The magnetic devices that have revealed to provide a better confinement are those with a closed magnetic configuration. It means that the magnetic field lines circle around the magnetic device, and are not connected to the device's edges. The most successful configurations so far are the stellarator and the tokamak reactors. Both of them are shaped like a torus (Figure 1.4), in which lies an helicoidal magnetic field, with toroidal (B_φ) and poloidal (B_θ) components. The toroidal field is dominant in both these configurations. It implies that at first order, the particles inside the plasma circulate along the torus. However, a toroidal

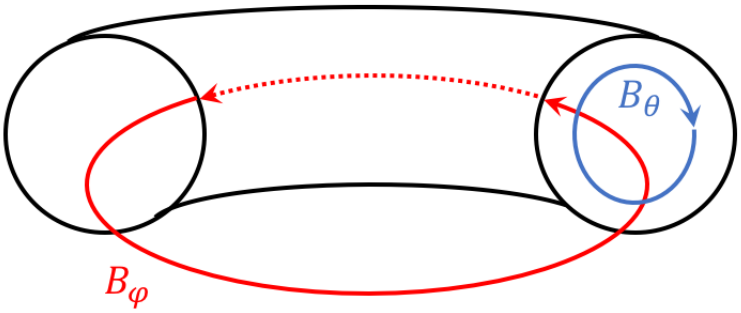

Figure 1.4: Example of closed configuration : An helicoidal magnetic field inside a torus

field could not alone confine particles, since they experience drifts when following the field lines (see Chapter 2). The poloidal field ensures that particles do not drift away from the torus' core by averaging out these drifts along their trajectory.

The stellarator configuration creates this helicoidal magnetic field directly through a set of specifically shaped magnets. Recent results obtained from the Wendelstein 7-X stellarator are very promising [Pedersen et al., 2018], but are still at an early stage regarding tokamaks' performances. It is currently the only magnetic device to be close to reach break-even. It constitutes the configuration studied in this thesis.

1.1.3 The tokamak configuration

Primary heating and current generation

In tokamaks, the toroidal magnetic field is created by a set of coils encircling the torus, displayed in blue on Figure (1.5). The poloidal field is created by a strong current of several MA that flows in the toroidal direction, along the torus. The plasma is initially heated up by the central solenoid at the middle of the torus, or inner poloidal coils as displayed on Figure (1.5) A strong current is varied in the solenoid, which induces a toroidal electric field inside the tokamak. Due to the finite resistivity η of the plasma, a toroidal current is created. This current generates the poloidal magnetic field, and heats up the plasma by Joule effect. However, the plasma resistivity scales like $\eta \propto T^{-3/2}$. Therefore, as the plasma is heated up, the efficiency of inductive heating decreases. Additional heating and current generation techniques are needed to reach temperatures of ~ 20 keV and toroidal currents of $\sim 10^7$ A.

Non-Inductive heating and current generation

Two main non-inductive heating techniques have been developed for tokamaks. The first one is the Neutral Beam Injection (NBI) : the idea is to heat up the core plasma with a beam of energetic particles, with kinetic energy of ~ 1 MeV. Since charged particles cannot penetrate the plasma core from the outside due to the magnetic field, deuterium ions are accelerated to the required energy and get neutralized by electrons. The deuterium atoms created are launched inside the plasma and are only ionized at the plasma core, where they give away their kinetic energy through successive collisions.

The other heating technique uses electromagnetic waves to heat up the plasma. Electrons and ions are gyrating around the magnetic field lines with the frequency $\omega_{c_{i,e}} = e_{i,e}B/m_{i,e}$,

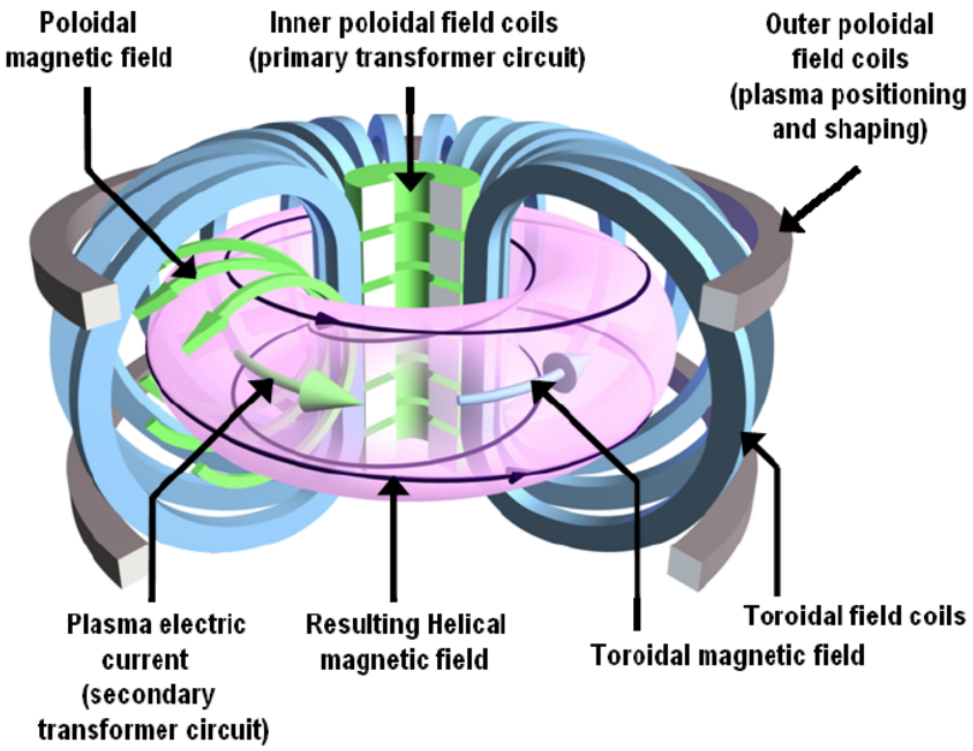

Figure 1.5: Sketch of the tokamak configuration

where e and m are the particles charge and mass. Subscript i is used for ion and e for electrons. When the electromagnetic waves are launched at these frequencies, ~ 50 MHz for ions and ~ 150 GHz for the electrons, they interact resonantly with the particles, resulting in a net energy transfer from the waves to the plasma. These techniques are called Ion Cyclotron Resonance Heating (ICRH) and Electron Cyclotron Resonance Heating (ECRH).

Non-inductive current generation is needed for two reasons in tokamaks. First, as said above, the current created by induction is not strong enough for fusion operations. Second, the amount of current that can be varied in the center solenoid is finite. In order to pass from a pulse regime to a steady-state regime, other current generation techniques need to be employed. A first one relies on the same principle as the resonance heating techniques. The Electron Cyclotron Current-Drive (ECCD) and the Lower-Hybrid Current Drive (LHCD) use respectively the electron cyclotron resonance and the lower-hybrid resonance to create a current along the torus.

A non-inductive current can also be generated naturally by the plasma. This is called the bootstrap current. It takes its source from the presence of "trapped" particles inside the torus. The tokamak configuration induces a magnetic field gradient towards the center solenoid. Particles with low velocity parallel to the magnetic field can be trapped in low field region of the device. This is discussed in greater length in Chapter 2. When the collision frequency of these particles is lower than their bounce frequency along their trapped trajectory, combined with a strong pressure gradient, a toroidal current known as the bootstrap current occurs. In large tokamaks, this current is expected to represent 30% of the total toroidal current.

The Joint European Torus (JET) tokamak is today the largest magnetic device built. Some of its characteristic can be found in Table 1.1. It holds the record [Keilhacker et al., 2001] of

	JET	ITER
Major radius (m)	3	6.2
Minor radius (m)	1	2
Plasma volume (m^3)	125	830
Plasma current (MA)	6	15
Magnetic field amplitude (T)	3.4	5.3
Pulse duration (s)	10	400
Fusion power (MW)	16	500
Amplification factor Q	0.62	~ 10

Table 1.1: Main parameters for the JET and ITER tokamaks

highest fusion power created $P_{fus} = 16MW$ with a record enhancement factor of $Q = 0.62$ in transient regime. It also holds a record in steady-state regime, with a fusion power of 4MW produced over 4 s.

Unfortunatly, due to physical and technical difficulties that are briefly discussed in the next section, the JET tokamak will not be able to exceed its records. Larger magnetic devices are required to overcome these issues. To this end, a tokamak known as the International Thermonuclear Experimental Reactor (ITER) is currently being built in southern France. It will be approximatively seven times larger in volume than the JET tokamak. ITER is expected to be able to reach an amplification factor of $Q = 10$ in a steady state regime of 400 to 600 s, producing 500 MW of fusion power. It will also be the first device to confine burning plasmas. A burning plasma is a plasma where the fusion reactions are self sustained by the alpha particles over long period of time.

1.1.4 Physical and technical issues to be solved

A brief summary of the physical and technical issues faced by nuclear fusion today is presented here. It is by no mean exhaustive. The goal of this discussion is merely to provide a brief explanation of what prevents nuclear fusion from reaching an industrial phase in the present decades.

Turbulence

In a tokamak, heat and particle transport are mainly due to turbulence. The confinement time τ_E is therefore dominantly conditioned by turbulent transport. Given the intrinsic nonlinear nature of turbulence, transport coefficients can hardly be predicted by analytical theory. 5D gyrokinetic simulations and tokamak experiments are needed to obtain the confinement time for a given set of plasma parameters. Increasing the number of equilibria on which gyrokinetic simulations are performed, and of devices on which experiments are conducted, enables to obtain τ_E dependencies over plasma parameters. Compiling these results leads to the creation of scaling laws, that help to design future tokamaks with higher confinement times.

On Figure (1.6), the scaling law used to design the ITER tokamak [Doyle et al., 2007] has been displayed. This scaling law is built on experimental data from 16 different tokamaks. Scaling laws generally show that the confinement time is an increasing function of the torus major radius, R_0. Larger tokamaks can therefore obtain larger enhancement factor Q.

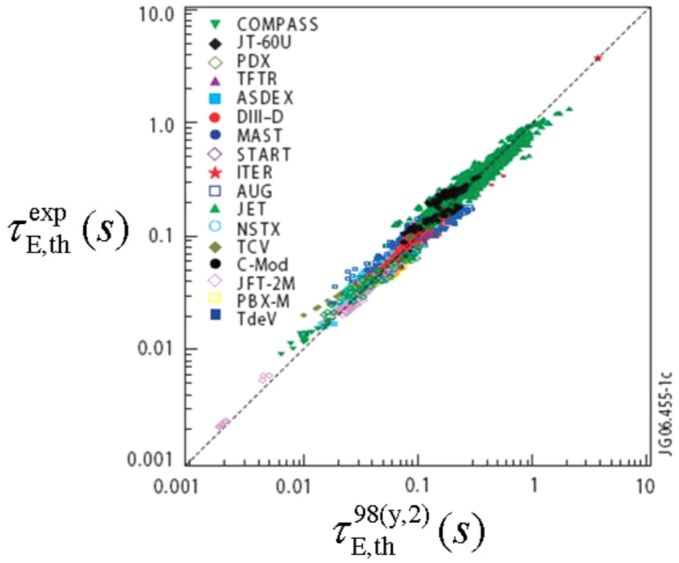

Figure 1.6: Comparison between the theoretical confinement time predicted by the scaling law from [Doyle et al., 2007] (X-axis) and between the experimental confinement time obtained from different devices.

Plasma-Wall interaction

All magnetic field lines are not closed inside of a tokamak. At the edge of the device lies a magnetic separatrix, beyond which the field lines are directed toward a target named a divertor. This zone of the plasma is called the Scrape Off Layer (SOL). Particles transported by turbulence and other physical processes are eventually transported to this region, which enables them to exit the plasma without damaging the walls. The divertor is made out of tungsten, a material that can withstand heat fluxes up to 10 $MW.m^{-2}$. Most present day tokamaks cannot create heat fluxes this large on their divertor over long durations, which would enable to test the resistance of this material on ITER relevant scenario.

An other open question on ITER and future tokamaks is the long term evolution of the plasma facing components and the tokamak's structure exposed to heavy 14 MeV neutron fluxes. Neutrons created by fission reactions are at least one order of magnitude below in energy. Their study do not permit to extrapolate how the ITER structure will withstand the atomic displacement caused by these highly energetic neutrons. To investigate this issue, the International Fusion Materials Irradiation Facility (IFMIF) is currently under development in Rokkasho, Japan. The goal of this facility is to produce 14 MeV neutrons from deuterons beams interacting with a lithium target. The ITER plasma facing components will then be tested for ITER relevant neutron fluxes.

MHD and Kinetic-MHD instabilities

Being able to sustain a plasma core at 20 keV, and at a few eV at its edge requires the presence of very large pressure and current gradients. In addition to these steep profiles, burning plasmas contain a lot of species that are supra-thermal. These particles are either alphas created by the fusion reactions, or fast ions due to the non-inductive heating techniques. Their velocity distribution is far from being of Maxwellian type. Tokamak plasmas are out of thermodynamic equilibrium. These plasmas represent therefore huge free energy tanks, that can be tapped to develop different kinds of macroscopic instabilities. Some of

these instabilities are of fluid type and called MagnetoHydroDynamics (MHD) instabilities. They can occur at various locations inside the plasma. ELMs instabilities arise at the plasma edge, where they add an additional heat load on the divertor. This heat load can be up to 20 MW.m^{-2}, which could be critical for ITER's divertor. Instabilities can also occur in the core plasma. The internal kink instability can lead to a phenomenon named sawtheeh. This instability periodically eject out of the tokamak core a fraction of the plasma, which decreases the plasma's temperature, and therefore the fusion power. If controlled, this instability could reveal to be positive if it is used to transport impurities and ashes from the plasma, since they strongly decrease the fusion power too.

Another type of macro-instabilities are of Kinetic-MHD type. Macroscopic instabilities can interact resonantly with particles eigenfrequencies, which leads to the development of Energetic Particle Modes (EPM). One of the main instability of interest for ITER is the fishbone instability. It takes its source from the interaction between the internal kink rotation frequency, and the precessional, bounce/transit frequencies of energetic particles. This resonant interaction has been observed experimentally to lead to energetic particle transport out of the plasma core. In the context of alpha particles, this is problematic because they could be transported before they have time to heat up to the background plasma, which would diminish the fusion performances. Understanding and predicting the amount of particle transported by the fishbone instability is then crucial for future ITER operations. This issue constitutes the subject of this thesis.

1.2 Content of the thesis

1.2.1 Introduction to the fishbone instability

Experimental evidences of fishbone instability

The fishbone instability was observed for the first time in the PDX tokamak in the early 80's [McGuire and al., 1983]. When the NBI was oriented nearly perpendicular to the magnetic field, successive bursts of $m = 1$ MHD activity were observed on the soft X-ray signal and on the Mirnov coils measurements (Figure 1.7). The name fishbone comes from the particular shape of the signal obtained with the Mirnov coils. This MHD activitity was linked to a decrease of the neutron emissivity, which indicates a transport of the particles injected with the NBI. It was found that the particles ejected lied in the energy range $[E_{inj}/2, E_{inj}]$, where $E_{inj} = 50$ keV is the injection energy of the beam. It was observed that the frequency of the mode, $f \sim 10$ kHz, was comparable to the precessional frequency of deeply trapped particles in this energy range. The authors conjectured that a resonance between the $m = 1$ mode and the beams ions existed, and associated the particles losses to this resonance.

The fishbone instability was later observed in other tokamaks, using various non-inductive techniques (ICRH, NBI) [Campbell et al., 1988][Heidbrink and Sager, 1990] [Nave et al., 1991][Mantsinen et al., 2000]. In particular in the JET tokamak, a stabilization of the sawteeth instability was observed when activating the ICRH power [Campbell et al., 1988]. This stabilization led to monster sawteeth, characterized by violent crashes and important redistribution of the core plasma outside the $q = 1$ surface. Fishbones were observed on JET with and without sawteeth activity. Fast-time scale diagnostics were able to highlight a fall of 9-19% of the total neutron rate, associated to the loss of fast particles during a fishbone oscillation. This was accompanied by a down chirping of the mode frequency [Nave et al., 1991] (Figure 1.8).

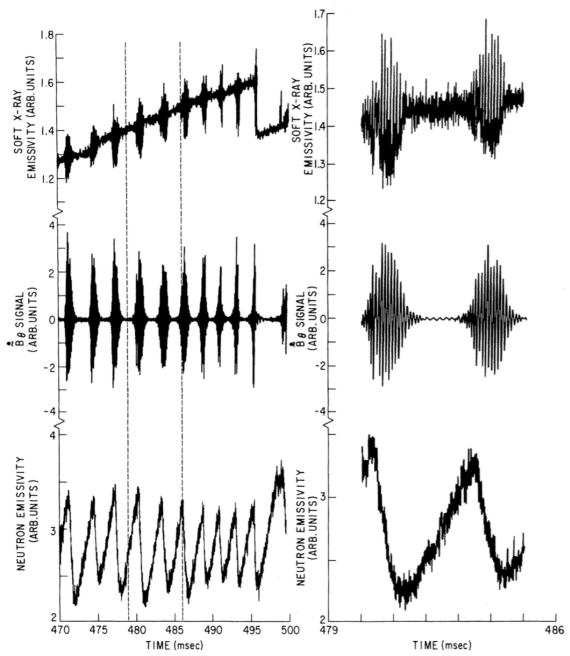

Figure 1.7: Fishbone oscillations observed on the PDX tokamak. Traces of soft X-ray emissivity (top) Mirnov coils measurements (middle) and neutron emissivity (bottom) are displayed. Source : [McGuire and al., 1983]

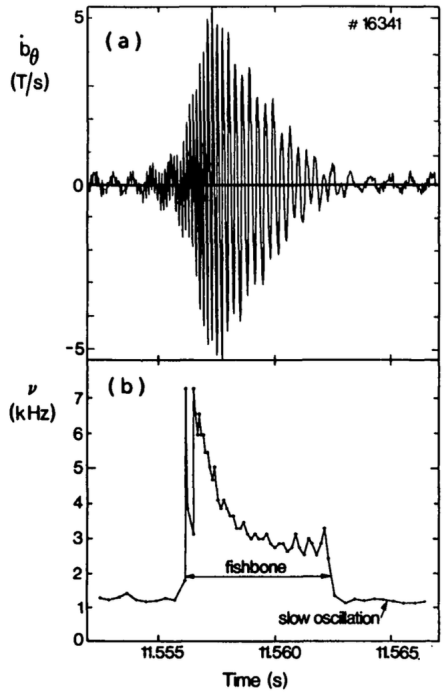

Figure 1.8: Fishbone oscillation on the JET tokamak.(a) Traces of Mirnov coils (b) Time evolution of the fishbone frequency. Source : [Nave et al., 1991]

Linear models and codes

Theoretical linear models where developed to explain the interaction between fast particles and MHD modes. The first models were formulated by [Chen et al., 1984] and [Coppi and Porcelli, 1986]. Both of them highlighted the resonance between the MHD frequency and the

precessional frequency of trapped particles as the drive of the fishbone instability, together with a fast particle negative density gradient.

These models differed however regarding the nature of the mode described. Chen et al. [Chen et al., 1984] argued that the fishbone frequency was fixed by the fast particles precessional frequency, the fishbone being a continuum resonant mode. This type of fishbone are called precessional fishbones. Coppi et al. [Coppi and Porcelli, 1986] however argued that the fishbone frequency is related to the ion diamagnetic frequency, which means that it can be identified as a discrete gap mode. This type of fishbone are called diamagnetic ion fishbones. It was later understood [Coppi et al., 1990][White et al., 1990][Porcelli, 1991][Wu et al., 1994] that these two regimes are in fact limiting cases of a more general dispersion relation. The ion diamagnetic limit corresponds to the partial stabilization of the internal kink at low beta of fast particles, which explains the sawteeth stabilization observed in JET. The precessional limit corresponds to the emergence of a new Energetic Particle Mode, at high beta of fast particles. A window of stability between this two modes was first predicted by White et al. [White et al., 1990], and illustrated by [Wu et al., 1994] (Figure 1.9). A more complete linear model was eventually proposed by [Porcelli et al., 1994], to take into account resonances with passing particles and finite orbit width effects. On the basis of these

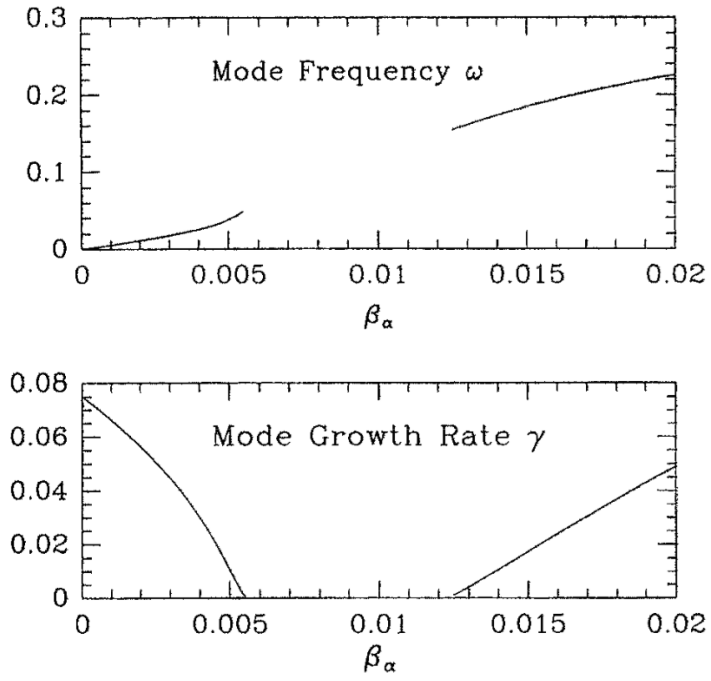

Figure 1.9: Mode frequency and growth rate as a function of the alpha particle beta. A stable window is visible for $\beta_\alpha \in [0.005, 0.012]$. Source : [Wu et al., 1994]

models, hybrid Kinetic-MHD linear codes [Cheng, 1992][Borba and Kerner, 1999][Lauber, 2013][Nabais et al., 2015] were developed to predict and control Kinetic-MHD instabilities in present and future experiments such as JET and ITER[Cheng, 1990][Cheng, 1991][Nabais et al., 2005]. Direct analytical Kinetic-MHD calculations were also performed to efficiently control the sawteeth instability in JET using ICRH power [Graves, 2004][Graves et al., 2009]. These results highlighted the importance of considering passing resonances in linear models.

Non-linear models and simulations of the fishbone instability

The first numerical nonlinear study of the fishbone instability was performed by [Candy et al., 1999]. This work used a linear MHD model and a nonlinear model to describe fast particles, and retrieved the characteristic down chirping of the fishbone frequency. Such results were also reproduced by [Odblom et al., 2002], using a nonlinear MHD model and linear fast particle model. The fishbone instability was studied in the limit of marginal stability, where it was shown that the MHD nonlinearities dominate the dynamics. In addition to the frequency chirping, an explosive growth rate of the fishbone instability, as well as a double step structure, were observed in the nonlinear phase.

These results were later generalized by simulations using nonlinear hybrid kinetic-MHD codes, such as M3D-K [Park et al., 1999], XHMGC [Briguglio et al., 1995][Briguglio et al., 1998][Wang et al., 2011] and MEGA [Todo et al., 1995][Todo and Sato, 1998][Todo, 2006]. These codes are able to treat self-consistently the MHD and kinetic nonlinearities, which is a crucial feature to simulate the fishbone instability in its nonlinear phase. A first self-

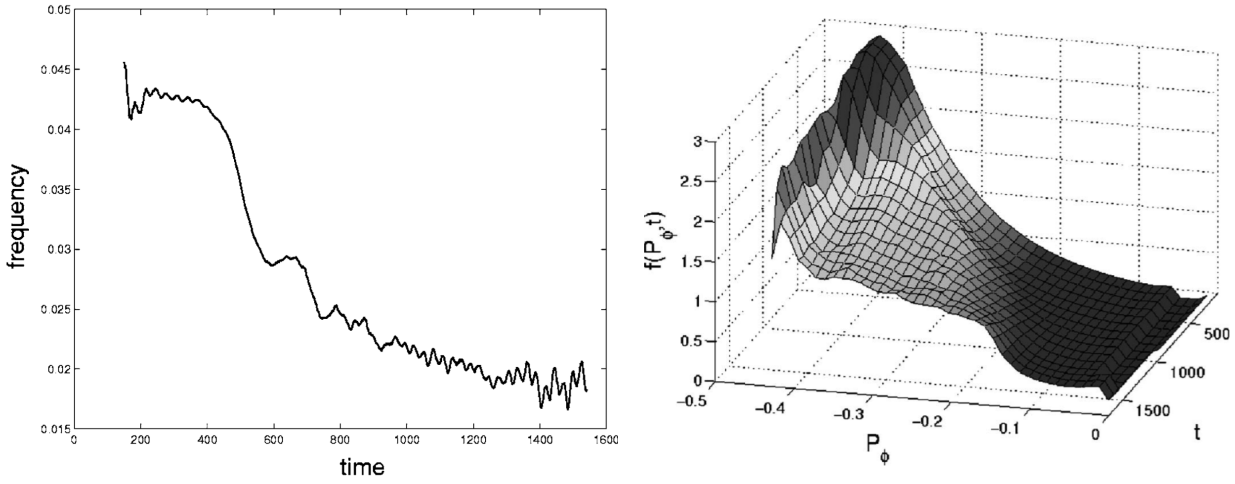

(a) (b)

Figure 1.10: (a) Time evolution of the fishbone frequency. (b) Time evolution of the trapped alpha distribution along the toroidal canonical momentum P_φ. P_φ can be considered as a radial coordinate for trapped particles.

consistent hybrid simulation was performed by [Fu et al., 2006] on the alpha fishbone for ITER and ITER-like equilibria. A down chirping of the fishbone frequency was seen to be associated with a transport of alpha particles (Figure 4.12), coherently with experimental observations. These effects were later retrieved with other types of energetic particles. [Wang et al., 2013] [Pei et al., 2017][Ren et al., 2018] studied the NBI driven fishbone for respectively spherical tokamaks, the EAST tokamak and the DIII-D tokamak. The simulations performed compare well with the experimental observations made on these devices. Simulations of the fishbone instability driven by supra-thermal electrons were performed in [Vlad et al., 2013]. Advanced phase space diagnostics were used to understand the nonlinear interplay existing between mode chirping and resonant particle transport. For the electron fishbone, mode chirping is due to phase-locking of resonant particles inside phase space islands.

Open questions

A number of questions remain untackled regarding the ion fishbone instability. Most of the recent nonlinear studies focus on ion fishbones driven by NBI and ICRH. It is still unclear whether or not the fishbone instability driven by alpha particles will be unstable on ITER. Contradictory results for the ITER 15 MA scenario [iTER physics basics, 2000] have been obtained. Alpha particles have been found to be stabilizing in [Fu et al., 2006], and destabilizing in [Hu et al., 2006] for this scenario. New linear self-consistent simulations are needed to assess the linear stability of the ITER configuration regarding the alpha fishbone.

In case that the alpha fishbone is indeed unstable on ITER, nonlinear hybrid simulations are required to assess the amount of alpha particles transported during several fishbone oscillations. The losses in fusion performances can be deducted from this transport.

Moreover, the physical mechanism coupling mode chirping and resonant particle transport is still not well understood for the ion fishbone instability. Two limits exist for this nonlinear coupling. A first one is the low kinetic drive limit [Berk et al., 1999][Breizman and Sharapov, 2011], where the fishbone instability is marginally unstable. In this limit, particle are expected to be locked inside phase space island. Some results obtained from hybrid reduced models [Idouakass, 2016] showed that resonant particle are giving on average energy to the fields through a phase slippage of the resonant island. The particle transport is induced by this energy transfer. The other limit is the strong kinetic drive [Zonca and Chen, 2014][Zonca et al., 2015], in which it is expected that resonant particles detune rapidly with the phase space island. Self-consistent hybrid simulations in 3D toroidal realistic geometry are required to understand the nonlinear dynamics of the fishbone instability in both regimes. Understanding this dynamics would help for the control of the alpha fishbone instability on ITER and future industrial devices.

1.2.2 Outline of the thesis

The alpha fishbone instability is the main focus of this thesis. The instability is simulated with a newly implemented nonlinear code, XTOR-K. This code originates from the nonlinear code XTOR-2F [Lütjens and Luciani, 2010], that solves the extended resistive MHD equations with two fluid effects in 3D toroidal geometry. A PIC module has been implemented in the code to evolve kinetic populations self-consistently with the MHD fields.

Chapter 2 details the trajectories of particles in a tokamak configuration. The particles characteristic frequencies are derived using an Hamiltonian angle-action formalism. This formalism is convenient for the study of wave-particle resonance.

In chapter 3, a brief introduction to MHD is given. The two fluid Kinetic-MHD equations solved by XTOR-K are then derived. A brief explanation on the numerical integration of XTOR-K equations and on noise control is provided. The linear theory of the internal kink instability is then detailed, using the Energy Principle.

In chapter 4, the Kinetic Energy Principle is presented, in order to derive a dispersion relation for the fishbone instability. Some differences are found with existing linear models. Afterwards, the implementation of a new particle distribution function and phase space diagnostics in XTOR-K is discussed. These implementations are essential to study numerically the fishbone instability.

In chapter 5, the linear verification of XTOR-K by the fishbone dispersion relation developed in chapter 4 is performed. Results obtained from the linear theory and XTOR-K are in good agreement. XTOR-K is then used to study the linear stability of the ITER 15 MA scenario against the fishbone instability. Results show that, for the Kinetic-MHD equilibria studied, the alpha fishbone is likely to be unstable.

In chapter 6, nonlinear simulations of the alpha fishbone are performed on ITER-like and ITER 15 MA equilibria. The strong drive limit is studied on both of them. Resonant particle transport and mode frequency chirping are retrieved in both these simulations. Phase space diagnostics highlight in which zone of phase space the transport arises, and what is the total amount of alpha particles transported over several fishbone oscillations. Based on these results, a mechanism for the nonlinear coupling of resonant transport and mode chirping is proposed. Preliminary results from a low kinetic drive simulation on the ITER 15 MA scenario are also presented. These results are shown to be coherent with some features present in [Odblom et al., 2002][Idouakass, 2016].

Chapter 2

Particle trajectories in a tokamak

Understanding the resonant mechanisms by which energetic particles can trigger instabilities in tokamak plasmas requires to explain the particles trajectories inside the torus. These trajectories are entirely determined by the magnetic configuration. In this chapter, the tokamak's magnetic configuration is presented. The different types of orbits in this configuration are detailed, as well as the drifts experienced by particles. From the motion of particles inside the torus, three invariants of the dynamics are identified, as well as three rotation frequencies. These frequencies divide the dynamics of charged particles on different time scales. Taking advantage of the presence of three invariants of motion, an Hamiltonian formalism can be used to describe the particles' dynamics, with a set of angle-action variables. This formalism is particularly well adapted for the study of motions with several time scales, and it enables to reduce the particles' dynamics to a 3D invariants space. General expressions of these variables are derived for the tokamak configuration, and explicit formulations are given for a simplified magnetic equilibrium with circular flux surfaces. This formalism enables to threat in a simplified and direct manner wave-particle resonance, providing a framework for the study of wave-particle energy exchange in linear theory and nonlinear hybrid simulations.

2.1 Configuration of the magnetic field in a tokamak

As described in Chapter 1, the magnetic field is composed of a toroidal component, that ensures that particles follow confined orbits inside the torus, and of a poloidal component, that prevents particles from drifting away from the field line they are following. Its structure at the tokamak's core is composed of a set of nested magnetic poloidal flux surfaces on which the magnetic field lines lie. A convenient way of expressing the magnetic field is to use the toroidal and poloidal magnetic fluxes. Their expression for a given radial position using the toroidal coordinates (r, θ, φ) reads

$$\psi_P(r) = \iint_{S_P(r)} \mathbf{B} \cdot d\mathbf{S} = \oint_{C_p} \mathbf{A} \cdot d\mathbf{l} \tag{2.1}$$

$$\phi_T(r) = \iint_{S_T(r)} \mathbf{B} \cdot d\mathbf{S} = -\oint_{C_t} \mathbf{A} \cdot d\mathbf{l} \tag{2.2}$$

the subscript P standing for poloidal, and T toroidal. The poloidal and toroidal contours of integration and surfaces are displayed on Figure 2.1, in blue for the poloidal flux, and red for the toroidal ones. For the poloidal flux, the surface of integration lies in between the blue dash lines, and is directed by $\hat{\theta}$. It has been defined without loss of generality at $\theta = 0$, for a given radial position r. The toroidal surface lies inside the toroidal contour, and is directed by $\hat{\varphi}$. The nested structure of the magnetic flux surfaces are materialized on Figure 2.1 by the

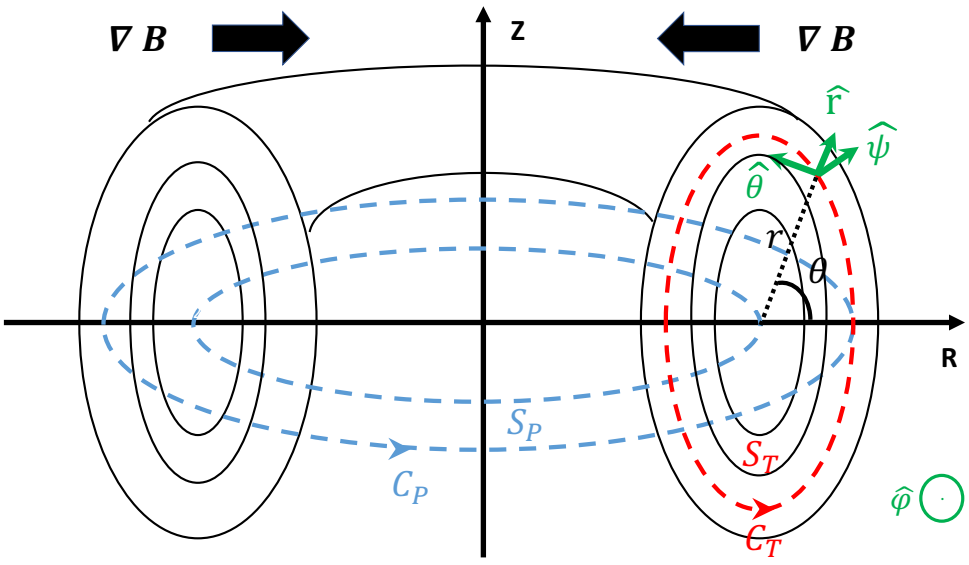

Figure 2.1: Topology of the magnetic field in a tokamak. The nested magnetic flux surfaces appear as black ellipses, and the contour and surfaces of integration of the poloidal and toroidal fluxes are respectively represented in blue and red dash lines. The unitary vectors $\hat{r}, \hat{\psi}, \hat{\theta}, \hat{\varphi}$ are defined at a given point with toroidal coordinates $(r, \theta, \varphi = 0)$. The flux direction is normal to the local magnetic surface, and the poloidal direction is normal to the radial one.

black ellipses. The natural set of coordinates used to describe this configuration is $(\psi_p, \theta, \varphi)$, where ψ_p plays the role of a radial coordinate. In the rest of this thesis, the poloidal magnetic flux will be noted $\psi = -\psi_p/2\pi$ for simplicity. The angle θ stands for poloidal angle of the flux coordinates, so that the magnetic field lines appear as straight lines in the (θ, φ) plane. The direct covariant basis used is $(\nabla\psi, \nabla\theta, \nabla\varphi)$, with $\nabla\psi \propto \hat{\psi}$, $\nabla\theta \propto \hat{\theta}$ and $\nabla\varphi \propto \hat{\varphi}$.

Using the toroidal and poloidal fluxes, the potential vector $\mathbf{A}$ can be defined as

$$\mathbf{A} = \phi_T \nabla\theta - \psi\nabla\varphi \tag{2.3}$$

The potential vector being related to the magnetic field by $\mathbf{B} = \nabla \times \mathbf{A}$, in the direct basis $(\nabla\psi, \nabla\varphi \times \nabla\psi, \nabla\varphi)$, the magnetic field can be expressed as

$$\mathbf{B} = I(\psi)\nabla\varphi + \nabla\varphi \times \nabla\psi \tag{2.4}$$

This formulation enables to describe directly the magnetic field poloidal component as a function of the poloidal flux, and the toroidal component as function of the total current crossing the poloidal surface S_1 at a given ψ. Due to the nested structure of the magnetic field, its expression verifies $\mathbf{B} \cdot \nabla\psi = 0$. In the same set of coordinates, the Jacobian of the system is given by

$$\mathcal{J}^{-1} = (\nabla\varphi \times \nabla\psi) \cdot \nabla\theta = \mathbf{B} \cdot \nabla\theta \tag{2.5}$$

The helicity of the magnetic field is defined by the safety factor q. It represents the number of toroidal turns done by a magnetic field line over a poloidal turn at a given radial position inside the torus. Its expression as a function of the magnetic flux is given by

$$q(\psi) = \frac{\mathbf{B} \cdot \nabla\varphi}{\mathbf{B} \cdot \nabla\theta} \tag{2.6}$$

The Jacobian of the system (ψ, θ, φ) can therefore be recast as $\mathcal{J} = I(\psi)/qR^2$. Also, it is useful for the derivation of the angle-action coordinates to adopt the Clebsch formulation for

the magnetic field, in order to express it solely as a function of the magnetic flux and the safety factor. Using this formulation, the magnetic field is defined as

$$\mathbf{B} = \nabla(\varphi - q(\psi)\theta) \times \nabla\psi \tag{2.7}$$

2.2 Particles trajectory in real space

2.2.1 Invariants of motion

As stated above, at equilibrium, charged particles possess three invariants. A first one is the particle energy $E = \frac{1}{2}mv^2 + Ze\phi$, where ϕ is the electric potential. In the absence of collisions and wave-particle interaction, the particle energy can be considered invariant when the electric field evolves on time scales that are slower than the cyclotron rotation. This is the case in general in MHD.

A second invariant in a tokamak configuration comes from the slow temporal evolution of the magnetic field with respect to the particle gyro-frequency $\omega_c = ZeB(t)/m$, such as $d[\ln \omega_c]/dt \ll \omega_c$. It is therefore possible to construct an adiabatic invariant, that appears to be the particle magnetic moment $\mu = mv_\perp^2/2B$. This quantity is equivalent to the magnetic dipole moment of a magnet, the cyclotron motion of a charged particle generating a dipolar magnetic field.

A last invariant comes from the axisymmetry of the configuration, which implies that the particle Lagrangian $\mathcal{L}$, defined in presence of an electromagnetic field as

$$\mathcal{L}(\mathbf{x}, \dot{\mathbf{x}}, t) = \frac{1}{2}m\dot{\mathbf{x}} \cdot \dot{\mathbf{x}} - Ze[\phi(\mathbf{x}, t) - \dot{\mathbf{x}} \cdot \mathbf{A}(\mathbf{x}, t)] \tag{2.8}$$

does not depend on the toroidal angle. Using Euler-Lagrange equation, it can be shown that the toroidal canonical momentum P_φ is an invariant of motion

$$\frac{d}{dt}\left(\frac{\partial \mathcal{L}}{\partial \dot{\varphi}}\right) = 0 \Leftrightarrow P_\varphi = mRv_\varphi - Ze\psi = cst \tag{2.9}$$

where the contravariant toroidal component $\dot{x}_\varphi = R\dot{\varphi}$ has been used. R is the particle major radius. For thermal particles at $T = 20$ keV, the ordering $|mRv_\varphi| \ll |Ze\psi|$ is respected, which implies that particles stay attached to their reference magnetic flux surface ψ, with a thin excursion along the trajectory of order $\delta_b \sim mRv_\varphi/Ze\psi$. This invariant is usually used as a radial coordinate for this type of particles. However, for supra-thermal particles, for example the alphas generated by fusion reactions, the previous ordering is not respected. Energetic particles exhibit large excursion across their reference magnetic surface, that can lead to non-standard trajectories near the magnetic axis, describing so-called "potato orbits". P_φ cannot be used as a radial coordinate for these particles.

2.2.2 Orbits in the poloidal plane

Given that the particle's energy and magnetic moment are invariants, the particle parallel velocity along the magnetic field $v_\parallel = \mathbf{v} \cdot \mathbf{B}/B$ and the local magnetic field $B(\psi, \theta)$ of a particle cannot evolve independently, being linked as

$$v_\parallel = \sqrt{\frac{2}{m}\Big[E - \mu B(\psi, \theta)\Big]} \tag{2.10}$$

In a tokamak configuration, a gradient of magnetic field is present, directed toward the center solenoid that lies at $R = 0$ (see Figure 2.1). It implies that for a given magnetic surface ψ, the magnetic field is maximal at $\theta = \pi$ and minimal at $\theta = 0$, which is usually referred to as the high field and low field sides. When a particle follows the magnetic field line, it is advanced in the toroidal direction and in the poloidal one. However, when it evolves in the poloidal direction from the low field side to the high field one, it experiences a mirror force $\mathbf{F} = -\mu\nabla_{\parallel}B$ that opposes to the particle parallel poloidal motion. The physical origin of this phenomenon is the Lorentz force that arises from the conjunction of the particle cyclotron motion and the magnetic field perpendicular to the considered field line, due to the inhomogeneous magnetic field.

Therefore, depending on their parallel velocity on the low field side at $\theta = 0$, some particles, described as trapped, can have their parallel motion fully suppressed by the mirror force. In this case, they bounce back on the magnetic field line, inverting the sign of their parallel velocity. It implies that for a given set of invariants (E, μ), according to equation (2.10), the equation $E = \mu B(\psi, \theta)$ has a solution $\theta = \theta_b$, such that orbits with $\theta > \theta_b$ cannot be described. The trajectory is bounded. It is equivalent to consider that the particle is trapped in a magnetic well, as described on Figure 2.2. Particles with energy higher than

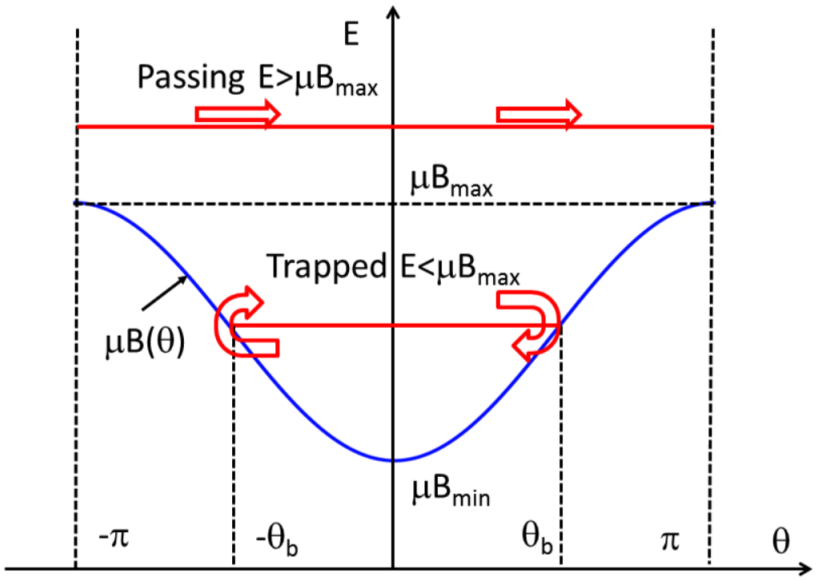

Figure 2.2: Magnetic well in the (E, θ) diagram, due to the inhomogeneity of the magnetic field. The blue curve describing μB is a function of (E, θ) at a fixed magnetic flux ψ. Particles with energy higher than μB_{max} with $B_{max} = B(\theta = \pi)$ follow passing orbits, whereas particles observing $E = \mu B(\theta_b)$ follow bounded trajectories with $\theta \in [-\theta_b, \theta_b]$, called trapped orbits.

$\mu B(\theta = 0)$ do not have a poloidal angle solution of $v_{\parallel} = 0$ along their trajectory, therefore their orbit spans the entire field line. Those particles are called co-passing when they follow the field line in the same direction as the local poloidal magnetic field ($v_{\parallel} > 0$), and counter-passing when they are going in the opposite direction ($v_{\parallel} < 0$).

It can be convenient to rewrite equation (2.10) using the pitch angle $\lambda = \mu B_0/E$. Assuming that the electric potential in negligible regarding the kinetic energy of particles

$$v_{\parallel} = v\left(1 - \lambda\frac{B(\psi, \theta)}{B_0}\right)^{1/2} \tag{2.11}$$

with $\lambda \in [0, B_0/B_{min}]$. The lower bound of this interval corresponds to a passing particle with almost no parallel velocity (deeply passing particle), and the upper bound to a trapped particle with $\theta_b = 0$ (deeply trapped particle).

The boundary between the trapped and passing domain for a given flux coordinate ψ is given by particles with a bouncing angle on the high field side $\theta_b = \pi$, which yields $\lambda = B_0/B_{\psi,\theta=\pi}$, with $B_{\psi,\theta=\pi} = B_{max,\psi}$. The set of invariants (E, λ) is therefore preferred to (E, μ) for analysis carried out in phase space, since it provides a simple criterion for a separation between trapped and passing orbits. An example of trapped orbit is given in Figure 2.3

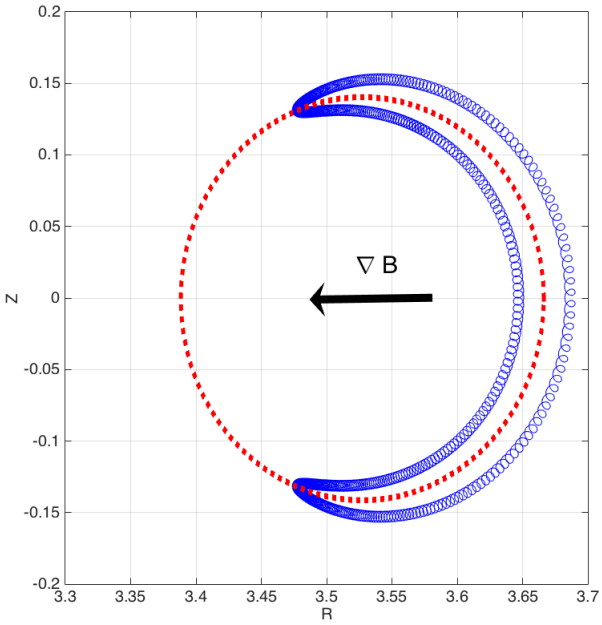

Figure 2.3: Typical trapped trajectory of a particle with energy $E = 100$ keV in the poloidal (R, Z) plane. The dashed red line stands for the particle's reference magnetic flux surface.

2.2.3 Particle drifts

Due to the presence of forces exerted on the plasma, particles experience drifts from their reference magnetic flux surface, such as

$$\mathbf{v}_D = \sum_i \frac{\mathbf{F}_i \times \mathbf{B}}{ZeB^2} \tag{2.12}$$

with $\sum_i \mathbf{F}_i$ the sum of these forces. At equilibrium, three forces are present. Due to the presence of a finite electric field, particles undergo the electric force $\mathbf{F}_E = Ze\mathbf{E}$, which leads to the cross field drift

$$\mathbf{v}_{E\times B} = \frac{\mathbf{E} \times \mathbf{B}}{B^2} \tag{2.13}$$

The two others forces are due to the magnetic field's inhomogeneity in a tokamak. The magnetic field lines are curved, and there is a gradient of magnetic field towards the central solenoid. This induces two forces on the particles, the centrifugal and gradient forces

$$\mathbf{F}_{cent} = m\frac{v_\parallel^2}{R}\boldsymbol{\kappa}, \quad \mathbf{F}_{grad} = -\mu\nabla B \tag{2.14}$$

$\boldsymbol{\kappa} = (\mathbf{b}\cdot\nabla)\mathbf{b}$ being the local curvature of the magnetic field, and $\mathbf{b} = \mathbf{B}/B$ its local direction. This generates a magnetic drift which can be expressed as a function of the pitch angle as

$$\mathbf{v}_d = \frac{2E}{m\omega_c B}\mathbf{B} \times \left[\left(1 - \lambda\frac{B}{B_0}\right)\boldsymbol{\kappa} + \frac{\lambda}{2B_0}\nabla B\right] \tag{2.15}$$

In a tokamak, it can be shown that the magnetic drift velocity is directed along the Z axis when $\beta = 2\mu_0 p/B^2 \ll 1$.

It can be noted that these drifts arise whether or not the magnetic field possesses a poloidal component. The poloidal magnetic field has been historically introduced to partially average them out along particles trajectories, in order to obtain confined orbits.

2.2.4 Characteristic frequencies

Three frequencies characterize the particles' trajectory inside the torus, splitting the dynamics on three distinct time scales. The smallest time scale correspond to the frequency of the particle gyration around the field line $\omega_c = ZeB/m$, illustrated as (1) on Figure 2.4. In a tokamak such as ITER, for alpha particles, it is of order 10^7 Hz.

The second time scale corresponds to the bounce or transit frequency of respectively trapped and passing particles in the poloidal plane, whose expression for an arbitrary geometry is

$$\omega_b(E,\lambda,\psi) \equiv 2\pi\alpha_b\left(\int_{-\theta_{lim}}^{\theta_{lim}} \frac{dl}{v_\parallel}\right)^{-1} = 2\pi\alpha_b\left(\int_{-\theta_{lim}}^{\theta_{lim}} \frac{B(\psi,\theta)d\theta}{v_\parallel(E,\lambda,\theta)\mathcal{J}(\psi,\theta)}\right)^{-1} \tag{2.16}$$

where $\theta_{lim} = \pi$, $\alpha_b = 1$ for passing particles, and $\theta_{lim} = \theta_b$, $\alpha_b = 2$ for trapped particles. The discontinuity of a factor 2 between the passing and trapped domains is due to the fact that the particle needs to bounce twice to come back to its initial position. This frequency can be expressed as a tri-dimensional function of the invariants. For fusion born alpha particles in ITER, the bounce/transit pulsation is of order 10^5Hz. This motion is depicted as (3) on Figure (2.4).

The slowest time scale corresponds to the toroidal precession of particles along the tokamak toroidal direction. This motion is due to the conjugate effect of the magnetic drift that shifts particles from their reference surface, and of the invariance of the toroidal canonical momentum P_φ. The case of trapped and passing particles are discussed separately here.

For trapped particles, their parallel velocity changes sign along the bounce trajectory. Due to the magnetic drift and the flux surfaces configuration, particles are shifted on outer magnetic surfaces when they are located at the tip of the banana trajectory with $\theta = \theta_b$, and inner ones at $\theta = -\theta_b$. Since P_φ is an invariant, the absolute value of the parallel velocity is higher when particles are on outer flux surfaces, and lower when they lie on inner ones. Therefore, over one complete particle bounce, the banana orbit has been slighted shifted in the toroidal direction. Such a drift appears on Figure 2.4 as (2). It should be noted that for most trapped particles, this precessional drift goes along the magnetic direction. However, it can be shown that for trapped particles near the passing-trapped boundary, this drift exhibits a reversal in the opposite direction, due to the fact that particles spend more time on inner magnetic surfaces than outer ones, even if their parallel velocity is lower there.

For passing particles, the parallel velocity does not change sign, the motion along the toroidal direction is therefore quasi-uniform. However, due to the variation of the magnetic drift along

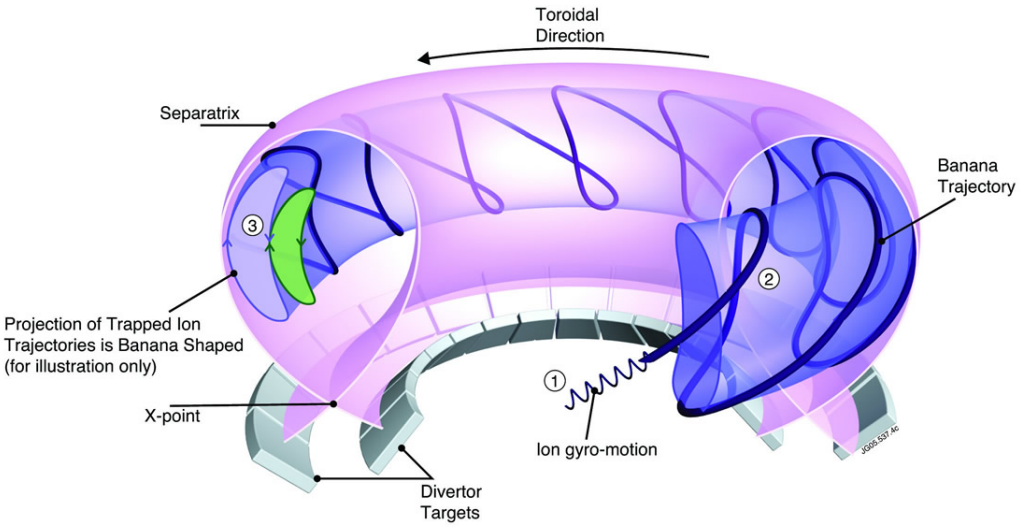

Figure 2.4: Trajectory of a trapped particles along the tokamak's magnetic field. Its dynamics is divided into three different motions evolving on distinct time scales. The gyro-motion of the particle around the magnetic field field, characterized by the pulsation ω_c. The bounce motion between the tipping points of the banana trajectory in the poloidal plane, characterized by the pulsation ω_b . And the precession of the banana trajectory along the tokamak toroidal direction, characterized by the precessional pulsation ω_d. These pulsations usually respect the ordering $\omega_c \gg \omega_b \gg \omega_d$

the trajectory, the parallel velocity increases or decreases slightly over a transit frequency. This small modification constitutes the precessional motion of passing particles. An expression often found in the literature [Coppi and Porcelli, 1986],[Coppi et al., 1990],[Porcelli, 1991] for the precessional pulsation is

$$\omega_d(E,\lambda,\psi) = \alpha_b \omega_b(E,\lambda,\psi) \int_{-\theta_{lim}}^{\theta_{lim}} \mathbf{v}_d(E,\lambda,\psi)\cdot\nabla(\varphi - q(\psi)\theta)/v_{\parallel}\, dl \tag{2.17}$$

It will be shown in the next section that this definition is problematic since the precessional pulsation needs to be defined at a specific magnetic flux surface, for example $\psi_* = -P_\varphi/Ze$, that is an invariant of motion along the particle trajectory. For alpha particles in tokamaks, the precessional frequency is of order $10^4 Hz$.

2.3 Hamiltonian formalism with angle-action coordinates for the tokamak configuration

In this section, a hamiltonian formalism well suited for the description of wave-particle resonance is developed. The properties and existence of such an Hamiltonian system are discussed. Its specific coordinates in the 6D phase space are then derived for the tokamak configuration in the limit of thin orbit width, when particles do not exhibit large excursions across their reference magnetic flux surface. Explicit expressions are then developed for the bounce/transit and the precessional pulsations, for an equilibrium with circular magnetic flux surfaces, and the application to the resonant wave-particle phenomenon is detailed.

Most of the definitions in this section can be found in [Rax, 2011], chapter 5.

2.3.1 Integrability and construction of angle-actions variables

The Hamiltonian formalism is useful when the dynamics of a system can be separated into different motions that evolve on distinct time scales. This formalism is therefore well suited to simplify the underlying equations of the particles' trajectory inside a tokamak. First, the general properties of the Hamiltonian formalism for an arbitrary set of 6D phase space variables $(\mathbf{x}, \mathbf{p})$, with $\mathbf{x}$ positions variables and $\mathbf{p}$ momenta ones, are reminded here. The Hamiltonian for charged particles in an electromagnetic field is defined as

$$H(\mathbf{x}, \mathbf{p}, t) = \frac{1}{2m}[\mathbf{p} - e\mathbf{A}(\mathbf{x}, t)]^2 + Ze\phi(\mathbf{x}, t) \tag{2.18}$$

where the canonical momentum in presence of a magnetic field is given by $\mathbf{p} = m\mathbf{v} + Ze\mathbf{A}(\mathbf{x}, t)$, with $\mathbf{v} = \dot{\mathbf{x}}$. In this case the Hamiltonian is simply $H = mv^2/2 + Ze\phi$, the charged particle energy. In this formalism, the equations of motion are given by the Hamilton-Jacobi equation

$$\frac{dx^i}{dt} = \frac{\partial H}{\partial p_i}, \qquad \frac{dp_i}{dt} = -\frac{\partial H}{\partial x^i} \tag{2.19}$$

Since three invariants of motion are present for this system, and that particles' trajectories are confined (bounded) inside the torus, two theorems proved in [Arnold, 1978] apply to the tokamak configuration. The first theorem states that the motion of particles along the magnetic field lines is integrable. It means that the particle trajectories can be described by simple mathematical formula. The second theorem states that particles evolves on a compact manifold in the 6D phase $(\mathbf{x}, \mathbf{p})$ labelled by the invariants of motion $E(\mathbf{x}, \mathbf{p}), \mu(\mathbf{x}, \mathbf{p}), P_\varphi(\mathbf{x}, \mathbf{p}) = \mathbf{cst}$. It implies that the presence of these invariants simplify the system dynamics to a three dimensional problem, this compact manifold labelled by the invariants being a set of nested 3D tori in the 6D phase space, each tori corresponding to a given set of invariants.

In addition to these properties, it will be shown in this section that the particles trajectories in a tokamak are Poincaré integrable. It implies that it is possible to construct a canonical set of phase space coordinates called angle-action variables. The actions $\mathbf{J}$, standing for the momenta coordinates, are invariants of motions. They are conjugated to the angles, positions coordinates, that evolves linearly in time such as $\boldsymbol{\alpha} = \boldsymbol{\Omega} t + \boldsymbol{\alpha}_0$. $\boldsymbol{\Omega}$ are the eigenfrequencies of the system. These angles can be built so that they relate to the characteristic frequencies of the system described above. These definitions imply that the equilibrium Hamiltonian only depends on the invariants, thus indeed making this problem three dimensional, such as the equations of motion read

$$\frac{d\boldsymbol{\alpha}}{dt} = \frac{\partial H(\mathbf{J})}{\partial \mathbf{J}}, \quad \frac{d\mathbf{J}}{dt} = -\frac{\partial H(\mathbf{J})}{\partial \boldsymbol{\alpha}} = 0 \tag{2.20}$$

In order to create such variables, it is needed to perform a canonical transform of the phase space coordinates $(\mathbf{x}, \mathbf{p})$. Such an transform imposes that is it possible to construct an Hamiltonian so that the new variables are solution of the Hamilton-Jacobi equation. Moreover, doing the change of variable $(\mathbf{x}, \mathbf{p}) \rightarrow (\boldsymbol{\alpha}, \mathbf{J})$, it must verify that for any given closed contour in phase space

$$\oint_{\mathcal{C}} \mathbf{p} \cdot d\mathbf{x} = \oint_{\mathcal{C}} \mathbf{J} \cdot d\boldsymbol{\alpha} \tag{2.21}$$

This property is particularly precious for the derivation of actions variables. For a given angle α_i that has been defined, the conjugated action J_i can be derived by using the closed contour $\mathcal{C}_i$ associated to the angle α_i, so that

$$2\pi J_i = \oint_{\mathcal{C}_i} \mathbf{p} \cdot d\mathbf{x} \tag{2.22}$$

When a system is Poincaré integrable, the 3D tori on which lie the particle trajectories in the 6D phase space are a set of nested tori called the Kolmogorov-Arnold-Moser (KAM) tori. The closed contour $\mathcal{C}_i$ lies on a surface of constant J_i, as depicted on Figure 2.5. Since the mental projection of a 3D torus in a 6D phase space is quite beyond the intuition of the human brain, Figure 2.5 displays a 2D torus defined by the couples (α_1, J_1), (α_2, J_2) in a 3D phase space, in order to give some intuition of the closed contour used.

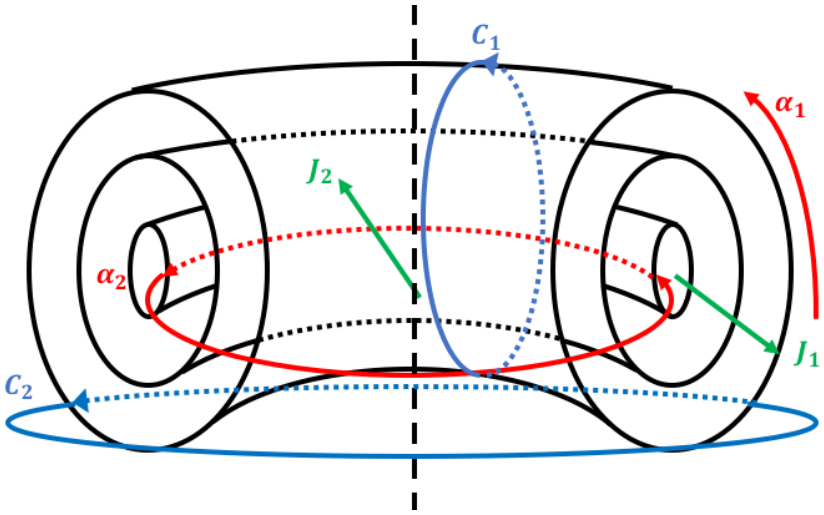

Figure 2.5: 2D KAM tori in a 3D phase space. The direction of increasing actions J_1, J_2 are illustrated by the green arrows. The directions of the angles α_1, α_2 are defined by the red curves. The closed contour used for the derivation of the actions are the blue curves, that only lie in the direction of the considered angle.

In the rest of this section, the angles $\boldsymbol{\alpha}$ are built to relate to the characteristic frequencies of the system $\omega_c, \omega_b, \omega_d$. Then, the action variables are derived by choosing the appropriate closed contour. This derivation is performed in the limit of thin orbit width using the guiding center of particles, which lie at the middle of their cyclotron motion.

2.3.2 Derivation of the angle-action variables

Angle-action couple (α_1, J_1) associated to the cyclotron motion

The first angle is chosen to describe the fast motion of the dynamics, the cyclotron motion. A particle trajectory can be described by its guiding centre $\mathbf{x}_G$ and a periodic function $\mathbf{x}_c$ of the cyclotron angle Φ such as $\mathbf{x}(t) = \mathbf{x}_G(t) + \mathbf{x}_c(t)$ and

$$\mathbf{x}_c(t) = \rho_c(\cos\Phi\ \mathbf{e}_1 + \sin\Phi\ \mathbf{e}_2) \tag{2.23}$$

$$\mathbf{v}_c(t) = v_\perp(-\sin\Phi\mathbf{e}_1 + \cos\Phi\ \mathbf{e}_2) \tag{2.24}$$

where $\rho_c = mv_\perp/ZeB(\mathbf{x})$ is the particle's gyroradius, and $(\mathbf{e}_1, \mathbf{e}_2)$ a set of unitary orthogonal vector perpendicular to the local magnetic field. The gyroangle Φ is then by definition $d\Phi/dt = v_\perp/\rho_c = \omega_c$, and the first angle $\alpha_1 = \Phi$ is defined as

$$\alpha_1 = \int^t dt'\omega_c[\mathbf{x}_G(t')]\ dt' + \alpha_{1,0} \tag{2.25}$$

where $\alpha_{1,0}$ is the initial gyroangle, and the eigenfrequency of this motion is $\Omega_1 = \omega_c$.

Taking the closed contour $\mathcal{C}_1$ to be the cyclotron motion for a fixed guiding center position, the first action reads

$$2\pi J_1 = \oint_{\mathcal{C}_1} m\mathbf{v}_c(t) \cdot d\mathbf{x}_c + Ze \oint_{\mathcal{C}_1} \mathbf{A} \cdot d\mathbf{x}_c \tag{2.26}$$

The first integral yields $2\pi m^2 v_\perp^2/ZeB$, and the second, using Stokes theorem and a constant magnetic field inside $\mathcal{C}_1$, $-\pi m^2 v_\perp^2/ZeB$. The minus sign of the second integral comes from the fact that the surface associated to the closed contour $\mathcal{C}_1$ is directed in the opposite direction to the magnetic field. Therefore, the first action is

$$J_1 = \frac{m}{Ze}\mu \tag{2.27}$$

This result also demonstrates that the magnetic momentum μ is indeed an adiabatic invariant of motion, since it has been assumed that ω_c has no temporal dependency.

Angle-action couple(α_2, J_2) associated to the poloidal motion

Out of simplicity, the electric potential is ignored in the rest of this derivation. This assumption holds well for energetic particles, since their potential energy is negligible regarding their kinetic energy. The equations of motion of the particles' guiding center are needed to derive the angles associated to the motion along the magnetic field lines, α_2, and the slow toroidal motion due to the magnetic drift, α_3. Neglecting the electric field

$$\frac{d\mathbf{x}_G}{dt} = v_{G\parallel}\mathbf{e}_\parallel + \mathbf{v}_d \tag{2.28}$$

with $\mathbf{v}_d$ the magnetic drift described in the previous section. Each toroidal coordinates $(\psi_G, \theta_G, \varphi_G)$ can be obtained using the contravariant basis

$$\frac{dx_G^i}{dt} = \mathbf{v}_G \cdot \nabla x_G^i \tag{2.29}$$

As stated before, the thin orbit width assumption is used in this derivation. It implies that particles along their trajectory exhibit small excursion $\hat{\psi}$ around their reference magnetic surface ψ_*, such as $\psi = \psi_* + \hat{\psi}$ and $\hat{\psi} << \psi_*$. Trapped particles possess an intrinsic reference flux surface since their parallel velocity vanishes at the banana tips. For trapped particles, $\psi_* = -P_\varphi/Ze$, which is indeed an invariant. Passing particles do not possess an intrinsic reference flux surface, therefore, it is arbitrarily chosen to be built on the invariance of P_φ, with $\psi_* = -P_\varphi/Ze = \psi_G - mI(\psi)v_{G\parallel}/ZeB$. The derivation will be conducted with this choice. An alternative definition using the time average $\langle\psi\rangle$ as an invariant will be discussed in the next section. Defining $\bar{\psi} = \langle\psi\rangle$ is preferred for a comparison with particle trajectories obtained from numerical integration of their orbit, as in XTOR-K. Given these conventions, the equations of motion read

$$\frac{d\theta_G}{dt} = \Omega_\theta(\psi_*, \theta_G) + \frac{d\Omega_\theta}{d\psi}(\psi_*) + \mathbf{v}_d \cdot \nabla\theta \tag{2.30}$$

$$\frac{d\varphi_G}{dt} = q(\psi_*)\Omega_\theta(\psi_*, \theta_G) + \frac{d[q\Omega_\theta]}{d\psi}(\psi_*) + \mathbf{v}_d \cdot \nabla\varphi \tag{2.31}$$

$$\frac{d\hat{\psi}}{dt} = \mathbf{v}_d \cdot \nabla\psi \tag{2.32}$$

where Ω_θ is the instantaneous particle transit/bounce frequency, defined as

$$\Omega_\theta(E,\lambda,\psi_*,\theta_G) \equiv \frac{v_{G\parallel}}{dl} = \alpha_b\sqrt{\frac{2E}{m}}\left(1-\lambda\frac{B(\psi_*,\theta_G)}{B_0}\right)^{1/2}\frac{\mathcal{J}(\psi_*,\theta_G)}{B(\psi_*,\theta_G)} \tag{2.33}$$

where the parallel velocity $v_{G\parallel}$ has been developed as a function of the particle pitch angle (2.11). dl is the length element along the guiding center poloidal trajectory.

Regarding the poloidal motion of particles along the field lines, the magnetic drift $\mathbf{v}_d$ can be discarded considering the existing temporal ordering. It simplifies the time evolution of the poloidal angle to

$$\frac{d\theta_G}{dt} = \Omega_\theta(\mathbf{J},\theta_G) \tag{2.34}$$

where the dependency of Ω_θ over the invariants of motion has simply be marked by $\mathbf{J}$. Besides simplifying the poloidal motion, discarding the magnetic drift totally suppresses the precession of particles in the toroidal direction, which implies that the quantity $\varphi_G - q(\psi_*)\theta_G$ does not evolve in time. The particles are following strictly the magnetic field lines. Such an equation describes an autonomous system in θ_G for a given $\mathbf{J}$. It implies that averaging over time can be linked to averaging over θ_G as

$$\int^t F(\mathbf{J},t')\ dt' = \int^{\theta_G}\frac{F(\mathbf{J},\theta'_G)}{\Omega_\theta(\mathbf{J},\theta'_G)}d\theta_G \tag{2.35}$$

This angle does not constitute a good candidate for α_2, since it does not evolve uniformly for trapped particles that bounce back and forth along θ_G. However, regardless of the particle class, the quantity $\theta_G(t)$ is periodic in time, with a pulsation ω_b, computed over the entire periodic poloidal motion as

$$\frac{2\pi}{\omega_b(\mathbf{J})} = \int_{-\pi}^{\pi}\frac{d\theta_G}{\Omega_\theta(\mathbf{J},\theta_G)} \tag{2.36}$$

for passing particles, where its sign depend on the co or counter-passing nature of the particle, and by

$$\frac{\pi}{\omega_b(\mathbf{J})} = \int_{-\theta_b}^{\theta_b}\frac{d\theta_G}{|\Omega_\theta(\mathbf{J},\theta_G)|} \tag{2.37}$$

for trapped particles. ω_b is always defined positive for trapped particles. The angle α_2 is then naturally defined by $\alpha_2 = \Omega_2 t + \alpha_{2,0}$, and the eigenfrequency is $\Omega_2 = \omega_b$. The explicit expression for α_2 is, given the dependency between t and α_2

$$\alpha_2 = \omega_b(\mathbf{J})\int_0^t dt' = \omega_b(\mathbf{J})\int_0^{\theta_G}\frac{d\theta_G}{\Omega_\theta(\mathbf{J},\theta_G)} \tag{2.38}$$

For passing particles, due their uniform motion when averaged over a transit period T_b, $\alpha_2 = \theta_G + \hat{\theta}(\mathbf{J},\theta_G)$, where $\hat{\theta}$ is a periodic function of both α_2 and θ_b, null averaged over a transit period. It can be explicitly computed considering the modulation of the instantaneous poloidal frequency $\tilde{\Omega}_\theta = \Omega_\theta - \langle\Omega_\theta\rangle$, $\langle.\rangle$ standing for a time average over the transit motion of passing particles, that simply reads

$$\langle F\rangle = \frac{1}{T_b}\int_{-\pi}^{\pi}\frac{F(\mathbf{J},\theta_G)}{\Omega_\theta(\mathbf{J},\theta_G)}d\theta_G \tag{2.39}$$

The time evolution of θ_G can then be expressed as $\dot{\theta}_G = \langle\Omega_\theta\rangle + \tilde{\Omega}_\theta$, and the modulation explicitly reads

$$\hat{\theta}_G(\mathbf{J},\theta_G) = \int_0^{\theta_G}\left[1-\frac{\langle\Omega_\theta\rangle(\mathbf{J})}{\Omega_\theta(\mathbf{J},\theta')}\right]d\theta' \tag{2.40}$$

For trapped particles, due to the reversal of the parallel velocity, the time averaged of $\langle \Omega_\theta \rangle$ is null, therefore $\theta_G(\mathbf{J}) = \hat{\theta}(\mathbf{J}, \theta_G)$. The obtention of an explicit expression for α_2 is still possible, but special care needs to be brought to the sign of the parallel velocity when computing α_2 at a given poloidal position θ_G along the bounce motion. The general expression of α_2 for trapped particles is

$$\alpha_2(\theta_G) = \sigma_c \omega_b(\mathbf{J}) \int_{-\theta_b}^{\theta_G} \frac{d\theta'_G}{|\Omega_\theta(\mathbf{J}, \theta'_G)|} + cst \tag{2.41}$$

the constant depending on the modulo used for α_2, and σ_c depending of the sign of the parallel velocity. This ensures that α_2 evolves uniformly along the bounce orbit. α_2 is chosen here to evolve similarly as for passing particles. The corresponding values between θ_G and α_2 along the passing and trapped orbits are presented in Figure 2.6. For $\alpha_2 \in [-\pi, -\pi/2] \cap [\pi/2, \pi]$, the trapped particle lies on the inner magnetic surfaces with negative parallel velocity, then $\sigma_c = -1$. For the first interval, the constant is $-\pi/2$ and $3\pi/2$ for the other one. For $\alpha_2 \in [-\pi/2, \pi/2]$, the trapped particles lie on the outer magnetic flux surfaces with positive parallel velocity, $\sigma_c = 1$ and the constant is $-\pi/2$.

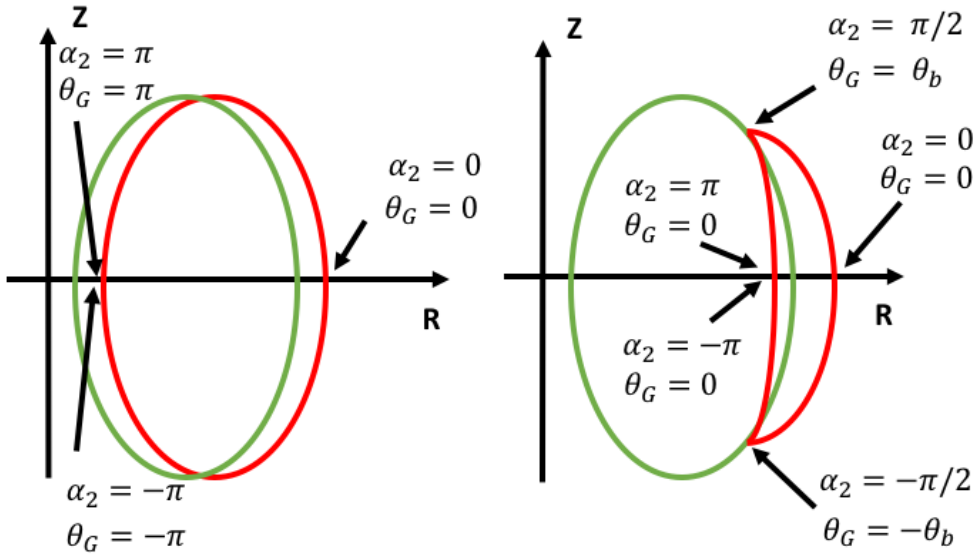

Figure 2.6: Corresponding values between the angle α_2 and the guiding center poloidal angle θ_G. The case of passing particles is presented on the left figure, trapped particles on the right. The green curves represent the reference magnetic surface ψ^*, and the red ones the trajectory of the guidind center in the poloidal plane

The derivation of the conjugated action J_2 is now discussed. Given the definition of α_2, the closed contour $\mathcal{C}_2$ is defined in the θ direction at fixed $\psi = \psi_*$ and toroidal angle φ_G. J_2 can be decomposed in two pieces $J_2 = J_2^{(0)} + J_2^{(1)}$ with

$$J_2^{(0)} = \oint_{\mathcal{C}_2} Ze\mathbf{A} \cdot \frac{d\mathbf{x}}{2\pi} \tag{2.42}$$

$$J_2^{(1)} = m \oint_{\mathcal{C}_2} \mathbf{v} \cdot \frac{d\mathbf{x}}{2\pi} \tag{2.43}$$

The poloidal component of the potentiel vector is the toroidal flux ϕ_T. Therefore, doing a first order Taylor development around $\psi_G = \psi_* + mIv_{G\|}/ZeB$

$$J_2^{(0)} = \epsilon_b Ze\phi(\psi_*) + \oint \frac{d\theta}{2\pi}\frac{qI}{B}mv_{G\|} \tag{2.44}$$

The term ϵ_b is null for trapped particles and unity for passing particles. This is due to the fact that trapped particles bounce back and forth along $\mathcal{C}_2$, and that $\phi_t(\psi_*)$ is solely defined on the reference flux surface. $d\phi(\psi)/d\psi = q(\psi)$ has been used here. Noting that $\mathcal{J} = I/qBR^2$, the toroidal component of the magnetic field is $\mathbf{B}_T = I\nabla\phi$ and that the length element along a field line is $dl = d\theta B/\mathcal{J}$, $J_2^{(0)}$ can be recast as

$$J_2^{(0)} = \epsilon_b Ze\phi(\psi_*) + \oint \frac{dl}{2\pi}\frac{|\mathbf{B}_T|^2}{B^2}mv_{G\|} \tag{2.45}$$

Regarding $J_2^{(1)}$, the velocity is taken at leading order as $\mathbf{v} = v_{G\|}\mathbf{e}_\|$, and the length element can expressed as $d\mathbf{x} = dl\mathbf{B}_p/B$, which leads to

$$J_2^{(1)} = \oint \frac{d\theta}{2\pi}\frac{|\mathbf{B}_p|^2}{B^2}mv_{G\|} \tag{2.46}$$

The second action J_2 is then

$$J_2 = \epsilon_b Ze\phi_T(\psi_*) + \oint \frac{dl}{2\pi}mv_{G\|} \tag{2.47}$$

Angle-action couple(α_3, J_3) associated to the toroidal motion

The last angle-action couple needs to describe the slowest motion of the particles, their toroidal precession. To this effect, the magnetic drift needs to be reintroduced in equations (2.30),(2.31),(2.32). Particles are now precessing in the toroidal direction, but the inclusion of the magnetic drift has two additional effects. Particles exhibit finite magnetic flux excursion $\hat{\psi}$ along their poloidal motion, and the time evolution of the poloidal angle is modified by a factor $d\tilde{\theta}_G/dt = (d\Omega_\theta/d\psi)\hat{\psi} + \mathbf{v}_d \cdot \nabla\theta$. In this approach, the finite excursion $\hat{\psi}$ is kept, and is totally defined by the invariance of the toroidal canonical momentum, and the arbitrary reference flux surface chosen ψ_*. The modifications brought to the poloidal angle motion are first kept in order to dissociate the drift motion from the rest of the dynamics. They will be later discarded when evaluating the time evolution of the toroidal angle, being negligible regarding the pure poloidal evolution along the magnetic field lines.

The drift motion can be characterized using a modified version of the Clebsch angle, $\alpha_* = \varphi_G - q(\psi_*)\theta_G$, defined on the reference magnetic flux surface. Indeed, according to equations (2.31) and (2.32), its time evolution yields

$$\dot{\alpha}_* = \Omega_{\alpha*}(\mathbf{J}, \theta_G) = \mathbf{v}_d \cdot \nabla\varphi - q(\psi_*)\mathbf{v}_d \cdot \nabla\theta + \frac{dq}{d\psi}\Omega_\theta\hat{\psi} \tag{2.48}$$

The frequency $\Omega_{\alpha*}$ entirely defines the precessional motion. As well as for Ω_θ it can be divided into a time average and modulations. At this step, the modifications on the poloidal angle evolution due to the magnetic drift are discarded. Therefore, integrating in time is still equivalent to integrating along the poloidal angle, weighting the poloidal integral by Ω_θ. The time average is then equivalent to integrating over the angle α_2 through the poloidal angle θ_G. Therefore, $\Omega_{\alpha*}(\mathbf{J}, \theta_G) = \langle\Omega_{\alpha*}\rangle_{\alpha_2}(\mathbf{J}) + \tilde{\Omega}_{\alpha*}(\mathbf{J}, \alpha_2)$. This directly implies that the

modulations are a periodic function of α_2. The averaged term can be identified as the precessional frequency ω_d, and its formal expression is

$$\omega_d(\mathbf{J}) = \frac{\omega_b(\mathbf{J})}{2\pi} \int_{-\theta_{lim}}^{\theta_{lim}} \frac{\Omega_{\alpha*}(\mathbf{J}, \theta_G)}{\Omega_\theta(\mathbf{J}, \theta_G)} d\theta_G \tag{2.49}$$

where $\theta_{lim} = \pi$ for passing particles, and θ_b for trapped particles. The fact that this integral only describes a half period is taken into account in the pulsation ω_b given in (2.16), making this expression consistent.

The angle α_* is then defined as $\alpha_* = \omega_d(\mathbf{J})t + \hat{\alpha}_*(\mathbf{J}, \alpha_2)$. Given that $\varphi_G = \alpha_* + q(\psi_*)\theta_G$, and that $\theta_G = \hat{\theta}_G(\mathbf{J}, \alpha_2) + \epsilon_b \alpha_2$, the toroidal angle φ_G can be rexpressed as

$$\varphi_G = \Big(\omega_d(\mathbf{J}) + \epsilon_b q(\psi_*)\omega_b(\mathbf{J})\Big)t + \epsilon_b q(\psi_*)\hat{\theta}_G(\mathbf{J}, \alpha_2) + \hat{\alpha}_G(\mathbf{J}, \alpha_2) \tag{2.50}$$

The last angle of the formalism is then simply $\alpha_3 = \Omega_3 t + \alpha_{3,0}$, and its eigenfrequency is $\Omega_3 = \omega_d + \epsilon_b q(\psi_*)\omega_b$. It can seem at first sight that the eigenfrequency Ω_3 depends on the choice made for the reference flux surface $\psi*$, through the safety factor. This would be problematic since the physics is invariant through a change of coordinates. In fact, if ψ_* is changed, it can be shown that it induces a modification of ω_d that exactly cancels out the change induced on the safety factor. The precessional frequency depends then as expected on the choice of reference magnetic surface. Different expressions has been derived in circular geometry in annex B when considering the present choice (B.2.2) and when considering the reference flux surface as the time average of the flux coordinate over a poloidal orbit $\bar{\psi} = \langle\psi\rangle$ (B.14).

The associated conjugated action J_3 is then derived from the closed contour $\mathcal{C}_3$ that is directed in the toroidal direction at fixed poloidal angle and magnetic flux position. The length element in this case is then $d\mathbf{x} = R^2\nabla\varphi d\varphi$, and the toroidal potential vector is $A_\varphi = -\psi$. Therefore, the final action is the toroidal canonical momentum P_φ

$$J_3 = \frac{1}{2\pi}\int_{\mathcal{C}_3} \mathbf{p}\cdot d\mathbf{x} = mRv_\varphi - Ze\psi = P_\varphi \tag{2.51}$$

The motion of charged particles in a tokamak is therefore Poincaré integrable, since angle-action variables $(\boldsymbol{\alpha}, \mathbf{J})$ have been derived.

2.3.3 Explicit expressions for the characteristic frequencies in circular geometry

It is possible to obtain explicit expressions for the frequencies ω_b and ω_d when working in simplified geometry. Analytical derivations of these expressions are presented in Annex A and B (A.7), (A.18), (B.14), (B.11), considering circular magnetic flux surfaces. As stated above, the precessional frequency for passing particles depends on the arbitrary choice of reference flux surface. In annex B, an explicit derivation of ω_d for an arbitrary reference surface is given with circular geometry, and then applied to the choices $\psi_* = -P_\varphi/Ze$, and $\bar{\psi} =< \psi >_t$.

Figure (2.7) displays the dependencies of ω_b and ω_d for an ITER-like configuration with circular poloidal shape. They are plotted against the considered pitch angle, for alpha particles with fixed birth energy $E_\alpha = 3.5$ Mev at a fixed radial position $r = 0.2a$, with $a = 2$ m

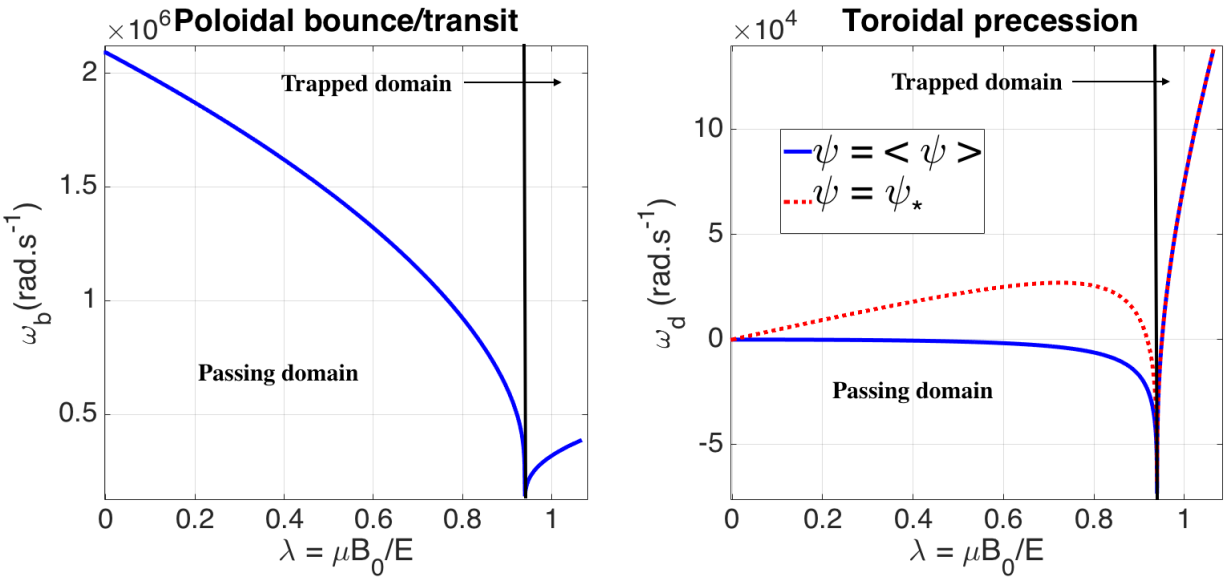

(a) (b)

Figure 2.7: Poloidal bounce/transit pulsation (a) and toroidal precessional pulsation (b) plotted against pitch-angle $\lambda = \mu B_0/E$ at fixed particle energy E and reference magnetic flux surface. The precessional pulsation is plotted for two different definitions of the reference flux surface

the minor radius of the ITER-like configuration. The frequencies of the poloidal and toroidal motions are respectively of order $10^5 Hz$ and $10^4 Hz$. The precessional pulsation is indeed invariant over a change of reference flux surface as displayed on Figure (2.7) (b), with the trapped domain lying beyond $\lambda = B_0/B_{max} = 0.95$ for the considered radial position. Then, its value differs from one definition to an other in the passing domain, as displayed on Figure (2.7). The precessional drift reversal is also present here for trapped particles, when their pitch angle is approaching the trapped-passing boundary.

For direct comparison with results obtained from XTOR-K hybrid simulations, the choice $\psi = \langle\psi\rangle$ is found to be more convenient from the numerical point of view. It is then assumed in the rest of this thesis that particles' reference magnetic flux surface corresponds to its time average along the poloidal trajectory.

2.3.4 Application to the resonant wave-particle interaction

The Hamiltonian angle-action formalism derived in this chapter is used for different purposes in this thesis.

The fishbone linear model

A first purpose is the derivation of a linear model whose goal is to verify hybrid simulations of the fishbone instability with XTOR-K. In order to construct a fishbone dispersion relation predicting the complex frequency of the fishbone mode $\omega = \omega_r + i\gamma$, it is needed to solve linearly Vlasov equation for the alpha particles distribution function F_α such as

$$\partial_t F_\alpha = \{H, F_\alpha\} \tag{2.52}$$

when H the total Hamiltonian of the system and $\{\cdot,\cdot\}$ the Poisson's brackets. The angle-action formalism is ideal to solve this type of equation by expressing in Fourier space the

perturbed distribution function $\tilde{f}_\alpha$ as

$$\tilde{f}_\alpha(\mathbf{x},\mathbf{p}) = \sum \tilde{f}_{\alpha,\mathbf{n}\omega}(\mathbf{J}) e^{i(\mathbf{n}\cdot\boldsymbol{\alpha}-\omega t)} \tag{2.53}$$

with the triplet $\mathbf{n}$ characterizing the harmonics of the trajectories. It is shown in Chapter 4 that the solution of the Vlasov equation as the following dependency

$$\tilde{f}_{\alpha,\mathbf{n}\omega} \propto \frac{1}{\omega - \mathbf{n}\cdot\boldsymbol{\Omega}(\mathbf{J})} \tag{2.54}$$

Therefore, the angle-action formalism provides a framework that naturally highlights the resonant nature of the wave-particle interaction, the perturbed distribution function exhibiting maxima near the wave-resonance condition that is simply defined by $\omega - \mathbf{n}\cdot\boldsymbol{\Omega}(\mathbf{J}) = 0$. Besides providing a proper formulation for the wave-particle resonant interaction, this formalism also gives explicit expressions in the invariant space $\mathbf{J}$ for the eigenfrequencies of the system, that are used in Chapter 4 to build the fishbone dispersion relation for a simple equilibrium with circular poloidal shaping. The actions derived in this chapter are not all used in the developed linear theory. Given the complex expression of J_2, it is replaced by the particle energy E. The others actions are kept, up to a multiplying factor. The set of invariants used to label the KAM tori in the fishbone dispersion relation are then $\mathbf{J} = (\lambda, E, \langle\psi\rangle)$.

Verification of ω_b, ω_d in XTOR-K

This formalism is also used in this thesis to verify the particle trajectories advanced numerically in 6D in XTOR-K by comparing their eigenfrequencies Ω_2, Ω_3 to the ones obtained with the angle-action approach for circular geometry. The eigenfrequencies are numerically computed by taking the Fourier transform of $\theta(t)$ in the simulation to obtain Ω_2 (θ being defined modulo 2π), and by doing a linear regression of $\varphi(t)$ to obtain Ω_3. This is presented in Chapter 5.

Characterization of the relevant invariants space

Another purpose of the angle-action formalism, is that it has defined the proper 3D phase space in which the resonant interaction needs to be studied. The eigenfrequency Ω_3 not being continuous across the trapped-passing boundary, it is then useful that the trapped and passing domain are clearly separated in hybrid simulations diagnostics. The particle distribution and the wave-particle energy are then projected on a 3D space labelled by their pitch angle, the passing-trapped boundary being then clearly defined. The second dimension is chosen to be either the radial position r or P_φ. The third dimension of this diagram can be chosen freely, and is chosen to be the particle energy E out of simplicity. Phase space diagnostics implemented during this thesis in XTOR-K are presented in Chapter 4.

Kinetic Poincaré plots

A final purpose of the angle-action formalism in this thesis is the construction of Kinetic Poincaré plots to visualize the temporal evolution of the island of resonance in phase space due to the wave-particle interaction. The modification of the system Hamiltonian due to wave-particle interaction can be formalized with angle-actions coordinates for a given resonant harmonic $\mathbf{n}$ as

$$H(\boldsymbol{\alpha},\mathbf{J},t) = H_{eq}(\mathbf{J}) - \tilde{h}(t)\cos(\Theta) \tag{2.55}$$

$$\Theta = \mathbf{n}\cdot\boldsymbol{\alpha} - \int_0^t \omega(t')dt' \tag{2.56}$$

$$C = \sum_{i,k} n_i n_k \frac{\partial^2 H_{eq}}{\partial J_i \partial J_k} \tag{2.57}$$

with $h(t)$ the amplitude of the perturbed hamiltonian, that oscillates with the phase Θ. C

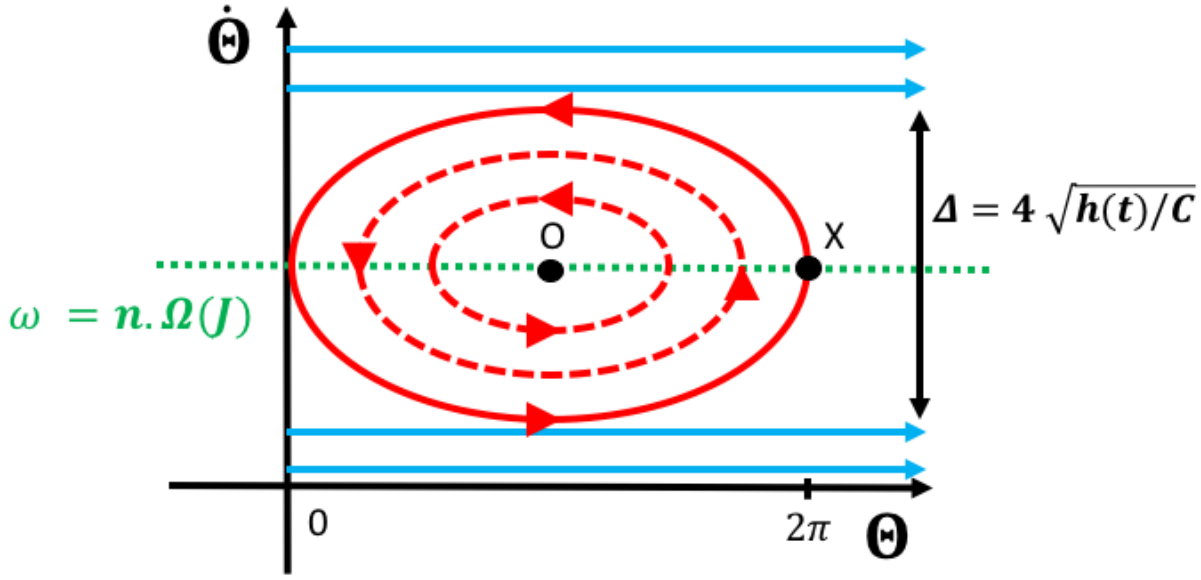

Figure 2.8: Kinetic Poincaré plot displaying the island of resonance in phase space. This diagram is 2π periodic in Θ. The resonance location is displayed as the green line in the diagram. Particle passing orbits are illustrated by blue lines, that are actually curves in phase space, and trapped orbits by the red ellipses. The separatrix between trapped and passing orbits is the plain red ellipse. The O point corresponds to the center of the phase space island, and X its extremity on the separatrix. The width of the island is given by $\Delta = 4\sqrt{h(t)/C}$ by identification with to the nonlinear pendulum . The island of resonance is therefore expected to evolve dynamically in time.

is the Hamiltonian's curvature. The wave-particle interaction implies that the Hamiltonian is no longer solely a function of the invariants $\mathbf{J}$, the invariants are no longer conserved. The temporal dynamics of the island of resonance in phase space can then been obtained by plotting the trajectory of near resonance particles in the diagram $(\Theta, \dot{\Theta})$, in a similar fashion as for the Hamiltonian of the nonlinear pendulum. The trajectories of near resonance particles in this diagram are then decomposed into two populations, trapped trajectories in the phase space island, and passing trajectories outside of it. Such trajectories are presented on Figure (2.8). The numerical integration of Kinetic Poincaré plots in XTOR-K is under development, and described in greater length in Chapter 4.

2.4 Conclusion

In this chapter, the trajectories of charged particles in real space for a tokamak configuration have been described. Out of these trajectories, three invariants of motion have been identified, as well as three characteristic frequencies that decompose the particles' motion on three distinct time scales. From these properties, it has been demonstrated that the tokamak configuration is Poincaré integrable, which implies that the particle dynamics is reduced

to 3D manifolds, that are nested 3D KAM tori in the 6D phase space. The angle-action coordinates of these tori are explicitly derived. It is then shown that this Hamiltonian formalism is particularly well adapted for the study of the wave-particle resonance, which is a crucial mechanism of the fishbone instability. In particular, it gives the framework for the construction of a fishbone instability linear theory, as well as for the implementation in hybrid codes of relevant phase space diagnostics to follow in time and phase space the evolution of the wave-particle resonance.

Chapter 3

MHD and Kinetic-MHD theory

In tokamak plasmas, large scales instabilities involving significant portions of the core plasma can arise. These instabilities do not take their source in the local behavior of some charged particles in the 6D phase space, but rather from a collective motion of particles in the physical 3D space, generating an additional magnetic field that perturbs the magnetic configuration described in Chapter 2. Such instabilities can therefore be described, averaging the particle distribution function in the entire velocity space, by a fluid formalism known as the Magneto-Hydro-Dynamics (MHD) theory. This theory can be compared to a fluid description using Navier-Stokes equation, but for a fluid that is composed of different species of charged particles, that can interact with exterior electromagnetic fields, as well as generating perturbed ones through the charged particles motion. The equations describing the MHD theory can then be seen as a coupled set of Maxwell and Navier-Stokes equations.

However, the MHD formalism is not ideal to describe burning plasmas. These plasmas are composed of minority species that are supra-thermal. In the case of fusion born alphas, supra-thermal particles can be two hundred times more energetic than the bulk plasma, with $E_\alpha = 3.5$ MeV. At such temperatures, particles eigenfrequencies Ω_i, derived in Chapter 2, can be comparable with the frequencies of MHD instabilities. The fluid description breaks down under these conditions, since resonant processes occur between MHD instabilities and supra-thermal particles. A kinetic formalism is needed to describe the dynamics of these minority species. To this purpose, the nonlinear two fluid MHD code XTOR-2F [Lütjens and Luciani, 2010] has been extended to treat the Kinetic-MHD equations. A Particle In Cell module has been introduced to describe kinetic particles, and the two fluid equations have been modified to take into account the kinetic moments. The resulting hybrid nonlinear code is named XTOR-K [Leblond, 2011].

In this chapter, a brief introduction to the MHD formalism is given. The ideal MHD equations are detailed, and the notion of MHD equilibrium is presented. Then, the Kinetic-MHD code XTOR-K is presented. The derivation of its two fluid MHD equations is detailed. The numerical scheme used to couple the MHD and kinetic modules is then discussed. The management of the PIC noise in XTOR-K is also explained. Last, the linear theory of the internal kink in MHD is presented. The internal kink mode structure and dispersion relation are partially derived from the ideal MHD equations in cylindrical geometry. The dispersion relation is afterwards generalized with the inclusion of toroidal curvature, resistivity and two fluid effects. This dispersion relation will set the groundwork for the derivation of the fishbone dispersion relation in Chapter 4.

3.1 The MagnetoHydroDynamic formalism

3.1.1 Ideal one fluid MHD model

The ideal MHD equations are a set of equations obtained from Vlasov equation and Maxwell's equations. Moments of the Vlasov equation are computed to obtain the time evolution of the plasma density, velocity and scalar pressure. The ideal MHD set of equations are closed using a truncation procedure that sets to zeros moments with order superior to the plasma pressure. Details for the derivation of the ideal MHD equations can be found in [Freidberg, 2014], chapter 2.

Assumptions of MHD models

Before presenting the equations of this model, assumptions of MHD models are discussed here. Given that the MHD theory aims at describing macro-instabilities, the typical length scale $L_{MHD}^{-1} \propto \nabla$ is considered to be much larger than all length scales characterizing the particles at a microscopic level. In particular, $L_{MHD} >> \rho_L$, with ρ_L the particles' gyroradius or Larmor radius. This property enables to construct the small parameter $\rho^* = \rho_L / L_{MHD} << 1$, typical of highly magnetized plasmas.

The MHD spatial length scale also needs to verify $L_{MHD} >> \lambda_D = \sqrt{2\epsilon_0 k_B T_s / n_s e^2}$, where λ_D is the Debye length of the specie s. This quantity represents in a plasma the length after which particles do not feel the Coulomb interaction of other particles. This implies that a quasi-neutrality approximation can be made in MHD, so that $\sum_s q_s n_s = 0$.

The characteristic time evolution of MHD waves must be larger that the smallest time scale of the microscopic dynamics, which is the gyro-pulsation $\omega << \omega_c$. The phase velocity of MHD waves is also small regarding the speed of light, $\omega/k << c$. This implies that the displacement current $c^2 \partial_t \mathbf{E}$ in Maxwell's equations can be discarded.

For the MHD fluid description to be valid, kinetic and finite orbit effects must be negligible. Kinetic effects can either come from Landau resonances, when the MHD mode frequency verifies $\omega \sim \mathbf{k} \cdot \mathbf{v}$, or from resonances with the eigenfrequencies of the individual motion of particles, $\omega \sim \mathbf{n} \cdot \mathbf{\Omega}$. Therefore, MHD frequencies must always be much higher or much lower than these frequencies.

Considering the Landau resonances, the condition for avoiding them is $\omega >> \mathbf{k} \cdot \mathbf{v}$, since MHD modes exhibit small wave vectors. Regarding the eigenfrequencies resonances, they are generally avoided for thermal species, which are in the energy range 10^4 eV for tokamak plasmas. At this energy range, the particles gyrofrequency is much higher than those of MHD modes, and their bounce and precessional frequencies ω_b, ω_d are much lower. However, for particles with higher energies, in the range 10^6 eV, precessional and bounce frequencies are increased, due to their respective energy dependence, $E^{1/2}$ and E. At these energies, ω_b and ω_d lie in the range $10^4 - 10^5$ Hz. This frequency range is similar to those of some MHD instabilities, for example the internal kink $n = m = 1$. Moreover, particle orbit width becomes also non-negligible at these energies. The fluid MHD description therefore breaks down in this energy range, that is typical of alpha particles in burning plasmas. A hybrid Kinetic-MHD formalism must then be applied for these plasmas in order to simulate the modes dynamics. Such a formalism is presented in the next section.

One fluid ideal MHD equations

Now that the MHD assumptions has been stated, the ideal one fluid MHD model is presented. The thermal bulk plasma is assumed to only contain two species, electrons and one specie of ions, usually deuterium ions. Considering that the electron inertia can be discarded, the one fluid mass density is defined by $\rho = \rho_i$, its scalar pressure by $p = p_i + p_e$, and its averaged velocity by $\mathbf{v} = \mathbf{v}_i$. The subscript i and e stand respectively for bulk ions and electrons. The time evolution of these quantities are given by

$$\frac{\partial \rho}{\partial t} + \nabla \cdot (\rho \mathbf{v}) = 0 \tag{3.1}$$

$$\rho \left[\frac{\partial \mathbf{v}}{\partial t} + (\mathbf{v} \cdot \nabla)\mathbf{v} \right] = \mathbf{J} \times \mathbf{B} - \nabla p \tag{3.2}$$

$$\frac{d}{dt}\left(\frac{p}{\rho^\gamma} \right) = 0 \tag{3.3}$$

with $\gamma = 5/3$ the ratio of specific heats. The Ohm's law describing the electric field is obtained through the electron momentum equation. Since the electron inertia can be discarded, Ohm's law reduces in ideal MHD to

$$\mathbf{E} = -\mathbf{v}_\perp \times \mathbf{B} \tag{3.4}$$

This equation implies that the magnetic flux through a given surface is a constant of motion, the plasma is attached to the magnetic field and evolves with it. This is known as the frozen-in law. Considering the following Maxwell's equations

$$\nabla \cdot \mathbf{B} = 0 \tag{3.5}$$

$$\nabla \times \mathbf{B} = \mu_0 \mathbf{J} \tag{3.6}$$

$$\nabla \cdot \mathbf{E} = -\frac{\partial \mathbf{B}}{\partial t} \tag{3.7}$$

the set of equations (3.1, 3.2, 3.3, 3.4, 3.5, 3.6, 3.7) fully defines the one fluid ideal MHD equations, being a set of 14 equations with 14 unknowns $(\rho, \mathbf{v}, p, \mathbf{B}, \mathbf{J}, \mathbf{E})$. These 14 unknowns constitute the MHD fields.

3.1.2 The MHD equilibrium

The numerical simulation of MHD fields constitutes an initial value problem. An equilibrium needs to be defined before the simulation of MHD instabilities can be performed. Such an equilibrium is characterized by setting the fluid velocity $\mathbf{v}$ and the time derivatives to zero in the MHD equations. It is then equivalent to assume that no waves propagate in the plasma. The equilibrium is formally expressed as

$$\mathbf{J} \times \mathbf{B} = \frac{(\nabla \times \mathbf{B})}{\mu_0} \times \mathbf{B} = \nabla p \tag{3.8}$$

This equation highlights the fact that in a tokamak, at equilibrium, the relaxation of the pressure gradient is prevented by the confinement effects of the magnetic field. Solving this equation for an arbitrary poloidal shaping represents a complex task since the magnetic field is not solely an external field determined by the poloidal coils. Its poloidal component depends on the poloidal magnetic flux ψ, magnetic flux on which depends also the pressure profile, since ψ is the natural radial variable of the system. Finding the MHD equilibrium of a given axisymmetric configuration therefore implies to solve for ψ an equation implicit in ψ.

The MHD equilibrium is better defined by highlighting the dependencies over the poloidal magnetic flux, recasting equation 3.8 as

$$\nabla \cdot \frac{1}{R^2}\nabla\psi = -\partial_\psi p(\psi) - \frac{1}{R^2} I\partial_\psi I(\psi) \tag{3.9}$$

This formulation of the equilibrium is called the Grad-Shafranov equation. It can be solved numerically by specifying input pressure and current profiles on a uniform radial grid. From these inputs, the free functions $\partial_\psi p$ and $I\partial_\psi I(\psi)$ are computed numerically with a finite difference scheme. The radial grid ψ can then be found numerically by a series of complex iterations, detailed for example in [Lütjens et al., 1996]. The radial grid solution of the Grad-Shafranov equation has a priori no reason to have its center, the magnetic axis, located at the geometrical center of the poloidal shaping, nor to be uniformly spaced. It can in fact be shown that the magnetic axis is not located there, the magnetic axis being shifted from this geometrical center even for simple equilibria with circular cross sections. This shift is called the Shafranov shift. Figure (3.1) displays a poloidal section of a torus at equilibrium, with a set of magnetic surfaces solution of equation (3.9). This figure highlights the last closed surface ψ_{edge}, as well as the Shafranov shit Δ. The forces $\mathbf{F}_B$ and $\mathbf{F}_p$ are both directed radially along $\hat{\psi}$, and exactly cancel each other. In this thesis, the numerical code CHEASE

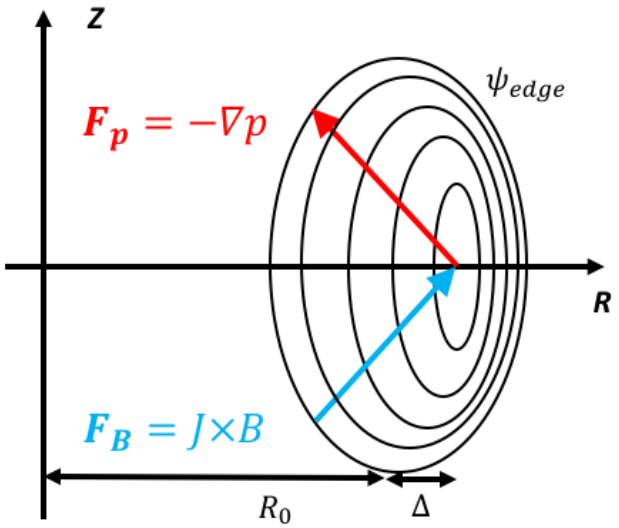

Figure 3.1: Illustration of a set of magnetic flux surfaces solution of the Grad-Shafranov equation. The equilibrium is exactly balanced by the forces $\mathbf{F}_B$ and $\mathbf{F}_P$. The Shafranov shift corresponds to the length Δ, and the last closed flux surface by ψ_{edge}.

[Lütjens et al., 1996] is used to generate the MHD equilbrium needed as an initial input for the Kinetic-MHD code XTOR-K.

3.2 The XTOR-K model for Kinetic-MHD

In this section, the general method for coupling the bulk MHD plasma to kinetic populations is discussed. The equations solved by the code XTOR-K and the self-consistent scheme to advance both MHD fields and kinetic particles are presented. The noise management in XTOR-K is also detailed.

3.2.1 Classical hybrid coupling between kinetic populations and bulk plasma

As first established in [Park et al., 1992], there exists two main coupling methods between bulk MHD plasma and kinetic or gyrokinetic populations of particles. A population k of kinetic particles is added to the bulk plasma, which is now denoted by the subscript b. Considering the one fluid ideal MHD equations in the previous section, and the first order fluid moment for a population k of kinetic particles, the equation of motion of the MHD fluid and of the kinetic population k are

$$\rho_b \frac{d\mathbf{v}_b}{dt} + \frac{\partial}{\partial t}[\rho_k v_{k,\parallel}]\hat{\mathbf{b}} = -\nabla p_b - \nabla \cdot \mathbf{P}_k + \mathbf{J} \times \mathbf{B} \tag{3.10}$$

$$\partial_t[\rho_k \mathbf{v}_k] = -\nabla \cdot \mathbf{P}_k + \mathbf{J}_k \times \mathbf{B} + q_k n_k \mathbf{E}_\perp \tag{3.11}$$

Notable approximations have been made in deriving these equations. The parallel electric field has been discarded in (3.11) due to the ideal MHD approximation. The perpendicular kinetic change of momentum $\partial_t(\rho_k \mathbf{v}_{k,\perp})$ has been neglected in 3.10. The time evolution of the magnetic field direction $\partial_t \mathbf{b}$ in 3.10 has also been discarded. These approximations are made to illustrate simply the different coupling methods, following [Park et al., 1992]. Such approximations are not made in the derivations of XTOR-K equations, since on one hand its MHD equations take into account both two fluid and resistive effects, and on the other hand, it is debatable to neglect $\partial_t(\rho_k \mathbf{v}_{k,\perp})$ and $\partial_t \mathbf{b}$ in 3.10.

The first coupling method uses the particle pressure $\mathbf{P}_k$ to couple the kinetic specie to the MHD equations. This equation of motion is obtained by subtracting the parallel component of equation (3.11) to equation (3.10), yielding

$$\rho_b \frac{d\mathbf{v}_b}{dt} = -\nabla p_b - (\nabla \cdot \mathbf{P}_k)_\perp + \mathbf{J} \times \mathbf{B} \tag{3.12}$$

The second coupling method uses the kinetic current inside the MHD equations, obtained by subtracting all components of 3.11 to 3.10, reading

$$\rho_b \frac{d\mathbf{v}_b}{dt} = -\nabla p_b + (\mathbf{J} - \mathbf{J}_k) \times \mathbf{B} - q_k n_k \mathbf{E}_\perp \tag{3.13}$$

In XTOR-K, the pressure coupling is preferred to the current coupling. However current terms are also present in the MHD equations of XTOR-K, since the terms $\partial_t(\rho_k \mathbf{v}_{k,\perp})$ and $\partial_t \mathbf{b}$ have not been neglected. Kinetic current terms also enter the MHD equations through the average velocity of electrons, due to the inclusion of two fluid effects. This tends to alter the clear division between the two different coupling schemes. In the following part, the derivations of XTOR-K equations are detailed.

3.2.2 Derivation of XTOR-K fluid equations

To take into account the kinetic effects of supra-thermal particles, XTOR-K uses a PIC module to advance kinetic particles in six dimensions, on electromagnetic fields that are derived from its fluid module. The equations are derived so that an arbitrary number of kinetic species can be considered, and not necessarily fast particles. Bulk species can also be simulated kinetically. In order to establish a self consistent description of MHD and kinetic effects, the equations of the two fluid XTOR-2F model [Lütjens and Luciani, 2010] need to be modified when considering additional kinetic species.

Considering a specie k of kinetic particles, its two first fluid moments read

$$\frac{\partial n_k}{\partial t} + \nabla \cdot (n_s \mathbf{v}_k) = 0 \tag{3.14}$$

$$\frac{\partial}{\partial t}(m_k n_k \mathbf{v}_k) + \nabla \cdot \mathbf{P}_k = q_k n_k (\mathbf{E} + \mathbf{v}_k \times \mathbf{B}) \tag{3.15}$$

where momentum exchange between kinetic particles and bulk ions and electrons have not been kept, since collisions are not yet implemented in XTOR-K. It should be noted here that the pressure tensor considered here stands for the total pressure. It includes isotropic partial pressure p_k, anisotropic partial pressure $\mathbf{\Pi}_k$, as well as velocity convection

$$\mathbf{P}_k = m_k n_k \mathbf{v}_k \otimes \mathbf{v}_k + p_k + \mathbf{\Pi}_k \tag{3.16}$$

The total pressure $\mathbf{P}_k$ is directly used in XTOR-K fluid equations. Particle density n_k, mean particle velocity v_k and total pressure $\mathbf{P}_k$ can be obtained by taking moments of the 6D distribution function F_k of the kinetic specie

$$F_k(\mathbf{r}, \mathbf{v}, t) = \sum_{i=1}^{N_k} \delta[\mathbf{r} - \mathbf{r}_{k,i}(t)] \delta[\mathbf{v} - \mathbf{v}_{k,i}(t)] \tag{3.17}$$

where N_k is the total number of physical particles in the kinetic specie k.

$$n_k(\mathbf{r}, t) = \int F_k(\mathbf{r}, \mathbf{u}, t) d^3\mathbf{u} = \sum_{i=1}^{N_k} \delta[\mathbf{r} - \mathbf{r}_{k,i}(t)] \tag{3.18}$$

$$\mathbf{v}_k(\mathbf{r}, t) = \int \mathbf{u}_k F_k(\mathbf{r}, \mathbf{u}, t) d^3\mathbf{u} = \sum_{i=1}^{N_k} \mathbf{u}_{k,i} \delta[\mathbf{r} - \mathbf{r}_{k,i}(t)] \tag{3.19}$$

$$\mathbf{P}_k(\mathbf{r}, t) = \int \mathbf{u}_k \otimes \mathbf{u}_k F_k(\mathbf{r}, \mathbf{u}, t) d^3\mathbf{u} = \sum_{i=1}^{N_k} \mathbf{u}_{k,i} \otimes \mathbf{u}_{k,i} \delta[\mathbf{r} - \mathbf{r}_{k,i}(t)] \tag{3.20}$$

The kinetic momentum and current density can be expressed as

$$\mathbf{J}^m_{kin}(\mathbf{r}, t) = \sum_k m_k n_k \mathbf{v}_k, \quad \mathbf{J}^q_{kin}(\mathbf{r}, t) = \sum_k m_k q_k \mathbf{v}_k \tag{3.21}$$

The only kinetic moments entering XTOR-K fluid equations are $\sum_k n_k$, $\sum_k \mathbf{P}_k$, $\mathbf{J}^m_{kin}$ and $\mathbf{J}^q_{kin}$. They are therefore the only moments computed by the code. The numerical projection of the kinetic moments will be discussed in the next section, together with the 6D particle advance.

Regarding the fluid module of XTOR-K, it has been chosen to maintain the definition of the MHD velocity as

$$\mathbf{v} = \mathbf{v}_E + u_{\parallel,i} \hat{\mathbf{b}} \tag{3.22}$$

used in XTOR-2F [Lütjens and Luciani, 2010]. It is important to note that such a choice is arbitrary, and implies specific bi-fluid terms in the fluid equations. Such a choice has been made to be as close as possible to the initial XTOR-2F equations. Considering that the quasi-neutrality of the plasma needs to be preserved, the electron density is not considered as a variable in XTOR-K and is then defined as

$$n_e = Z_i n_i + \sum_k Z_k n_k \tag{3.23}$$

where Z_k is the charge of the k kinetic specie, and Z_i the charge of the fluid bulk ion. The electron mean velocity $\mathbf{u}_e$ is, using the total current $\mathbf{J} = \nabla \times \mathbf{B}/\mu_0$

$$\mathbf{u}_e = \frac{Z_i n_i \mathbf{u}_i + \mathbf{J}^q_{kin}}{n_e} - \frac{\mathbf{J}}{e n_e} \tag{3.24}$$

The averaged velocity of a bulk specie s can be expressed by a drift ordering with the small parameter $\rho^* << 1$ [Hazeltine and Meiss, 2003]

$$\mathbf{u}_s = \mathbf{u}_{s,\parallel} + \mathbf{v}^{(1)}_{\perp,s} + \mathbf{v}^{(2)}_{\perp,s} \tag{3.25}$$

with the first order drift velocity being the sum of the cross field and diamagnetic drift velocities

$$\mathbf{v}^{(1)}_{\perp,s} = \frac{\mathbf{E} \times \mathbf{B}}{B^2} + \frac{\mathbf{B} \times \nabla p_s}{n_s Z_s e B^2} \tag{3.26}$$

and the second the sum of the polarization, frictional force induced and the viscous stress induced drift velocities. The second order of the drift ordering is neglected in XTOR-K fluid equations. Considering equation (3.25) and the MHD velocity chosen in equation (3.22), the averaged bulk ion and electron velocities are

$$\mathbf{u}_i = \mathbf{v} + \mathbf{v}^*_i \tag{3.27}$$

$$\mathbf{u}_e = \mathbf{v} + \left[\left(\frac{Z_i n_i}{n_e} - 1\right) u_{i,\parallel} + \left(J^q_{kin,\parallel} - \frac{\mathbf{J}_\parallel}{e n_e}\right)\right] \hat{\mathbf{b}} + \mathbf{v}^*_e \tag{3.28}$$

Equation (3.28) has been obtained by taking the parallel component of (3.24), and the intrinsic perpendicular component of the averaged electron velocity. It is interesting to note that the usual assumption $Z_i n_i \sim n_e$ has not been made here. This is because the kinetic species considered in XTOR-K are not necessarily supra-thermal species. In this context, the kinetic density n_k cannot be discarded regarding the bulk densities. Therefore, the term $Z_i n_i / n_e - 1$ is not null in XTOR-K equations.

The continuity equation and the momentum equation of a bulk specie s can be respectively expressed as

$$\frac{\partial n_s}{\partial t} + \nabla \cdot (n_s \mathbf{u}_s) = 0 \tag{3.29}$$

$$m_s n s \left(\frac{\partial \mathbf{u}_s}{\partial t} + (\mathbf{u}_s \cdot \nabla)\mathbf{u}_s\right) = Z_s e n_s (\mathbf{E} + \mathbf{u}_s \times \mathbf{B}) - \nabla p_s - \nabla \cdot \mathbf{\Pi}_s + \mathbf{R}^s \tag{3.30}$$

with $\mathbf{R}_s$ is the momentum transfer on the specie s. For bulk ion and electrons, it can be expressed as

$$\mathbf{R}^e = -\mathbf{R}_i = -n_e e[\eta_\parallel \mathbf{J}_\parallel + \eta_\perp \mathbf{J}_\perp] \tag{3.31}$$

with $\eta_\parallel$ and $\eta_\perp$ the parallel and perpendicular plasma resistivity.

XTOR-K ion continuity equation

In XTOR-K, the time advance of the kinetic density is obtained by the kinetic particle advance. Therefore only the time evolution of the bulk ion density is needed. Using equations (3.27,3.29), the ion continuity equation implemented in XTOR-K can be obtained as

$$\partial_t n_i = -\nabla(n_i \mathbf{v}) - \frac{1}{e Z_i} \nabla p_i \cdot \nabla \times \frac{\mathbf{B}}{B^2} + \nabla \cdot D_\perp \nabla n_i + S \tag{3.32}$$

where S and D are source and transport terms that arise from the inclusion of viscous drift. The source term is a free parameter, but it is usually set such as $S = -\nabla \cdot D_\perp \nabla n_i(t = 0)$.

XTOR-K parallel equation of motion

Since the MHD parallel velocity is simply the parallel velocity of bulk ions (equation 3.22), the parallel fluid equation of motion only needs to take into account the ion momentum equation. Using the ion continuity equation (3.29) and the parallel ion momentum equation (3.30) gives

$$\hat{\mathbf{b}}\cdot\left[m_i n_i\frac{\partial}{\partial t}\mathbf{u}_i + mi_i n_i(\mathbf{u}_i\cdot\nabla)\mathbf{u}_i\right] = -\nabla_\parallel p_i - \hat{\mathbf{b}}\cdot\nabla\cdot\mathbf{\Pi}_i + q_i n_i E_\parallel + \hat{\mathbf{b}}\cdot\mathbf{R}_i \tag{3.33}$$

The Ohm's law used in XTOR-K fluid equations is identical to the one used in [Lütjens and Luciani, 2010], with

$$\mathbf{E} = -\mathbf{v}\times\mathbf{B} - \frac{1}{en_e}\hat{\mathbf{b}}\Big(\hat{\mathbf{b}}\cdot\nabla p_e + \hat{\mathbf{b}}\cdot\nabla\cdot\mathbf{\Pi}_e\Big) + \eta_\parallel\mathbf{J}_\parallel + \eta_\perp\mathbf{J}_\perp \tag{3.34}$$

Concerning the fluid equation of motion, a ion gyroviscous cancellation arises between some ion diamagnetic terms and the anisotropic partial ion pressure, such as $d\mathbf{v}_i^*/dt = -\nabla\cdot\mathbf{\Pi}_i$ [Hazeltine and Meiss, 2003]. Using the gyroviscous cancellation and the parallel component of equation (3.34), equation (3.33) can be recast as, using the average ion velocity (equation 3.27)

$$\hat{\mathbf{b}}[\partial_t\mathbf{v} + (\mathbf{v}\cdot\nabla)\mathbf{v} + (\mathbf{v}_i^*\cdot\nabla)\mathbf{v}_\perp] = \frac{\nabla_\parallel p_i}{m_i n_i} - \frac{Z_i\nabla_\parallel p_i}{m_i n_e} - \frac{(\nabla\cdot\mathbf{\Pi}_e)_\parallel}{m_i n_e} + \frac{e\eta_\parallel J_\parallel}{m_i}\Big[\frac{n_e}{n_i} - Z_i\Big] \tag{3.35}$$

In order to modify as less as possible the existing equations in XTOR-2F, the left hand side of this equation needs to rewritten using the identity $\mathbf{x}\partial_t\mathbf{y} = \partial_t(\mathbf{xy}) - \mathbf{y}\partial_t\mathbf{x}$. Noting that

$$\partial_t\hat{\mathbf{b}} = \frac{(\partial_t\mathbf{B})_\perp}{B} = -\frac{\nabla\times\mathbf{E}_\perp}{B} \tag{3.36}$$

where Faraday equation has been used. The electric field rotational can computed from Ohm's law. Therefore, the left hand term of equation (3.35) can be developed as

$$\hat{\mathbf{b}}\cdot[\partial_t\mathbf{v} + (\mathbf{v}\cdot\nabla)\mathbf{v} + (\mathbf{v}_i^*\cdot\nabla)\mathbf{v}_\perp] = \partial_t u_{i,\parallel} + (\mathbf{v}\cdot\nabla)u_{i,\parallel} + \frac{1}{B}\mathbf{v}_\perp\cdot(\nabla\times\mathbf{E})_\perp \tag{3.37}$$

Adding the effects of ion viscous drift, the complete parallel equation of motion implemented in XTOR-K is

$$\partial_t u_{i,\parallel} + [(\mathbf{v}\cdot\nabla)\mathbf{v} + (\mathbf{v}_i^*\cdot\nabla)\mathbf{v}_\perp]_\parallel = \frac{1}{B}\mathbf{v}_\perp\cdot(\nabla\times\mathbf{E})_\perp - \frac{\nabla_\parallel p_i}{m_i n_i} - \frac{Z_i\nabla_\parallel p_e}{m_i n_e} - \frac{(\nabla\cdot\mathbf{\Pi}_e)_\parallel}{m_i n_e} \tag{3.38}$$

The term $(\nabla\cdot\mathbf{\Pi}_e)_\parallel$ is neglected for now in XTOR-K.

XTOR-K perpendicular equation of motion

Turning to the perpendicular equation of motion, summing the equations of motions of electrons, ions and kinetic particles gives

$$(\mathbb{I} - \hat{\mathbf{b}}\otimes\hat{\mathbf{b}})\Big[\sum_{s=i,e} m_s n s_s\partial_t\mathbf{u}_s + \sum_{s=i,e} m s_s n_s(\mathbf{u}_s\cdot\nabla)\mathbf{u}_s + \partial_t\Big(\sum_k m_k n_k\mathbf{u}_k\Big) - \mathbf{J}\times\mathbf{B} + \sum_{s=i,e}\Big(\nabla p_s + \nabla\cdot\mathbf{\Pi}_s\Big) + \sum_k\nabla\cdot\mathbf{P}_k\Big] = 0 \tag{3.39}$$

where collisions contributions are null since $\mathbf{R}_i + \mathbf{R}_e = 0$. It is reminded that collisions are not taken into account in the kinetic particle momentum equation (3.15). Using the vectorial relation

$$(\mathbb{I} - \hat{\mathbf{b}} \otimes \hat{\mathbf{b}})\partial_t \mathbf{x} = \partial_t \mathbf{x}_\perp + (\mathbf{x} \cdot \hat{\mathbf{b}})\partial_t \hat{\mathbf{b}} + (\mathbf{x} \cdot \partial_t \hat{\mathbf{b}})\hat{\mathbf{b}} \tag{3.40}$$

and equation (3.36), the equation (3.39) can be reformulated as

$$\begin{aligned}\sum_s m_s n_s \partial_t \mathbf{u}_{i,\perp} + \sum_s m_s n_s (\mathbf{u}_s \cdot \nabla)\mathbf{u}_{s,\perp} + \partial_t\Big(\sum_k m_k n_k \mathbf{u}_{k,\perp}\Big) - \\ \frac{1}{B}\Big[\sum_s m_s n_s u_{s,\parallel}(\nabla \times \mathbf{E})_\perp + (\sum_s m_s n_s \mathbf{u}_{s,\perp} \cdot (\nabla \times \mathbf{E})_\perp)\hat{\mathbf{b}}\Big] = \\ \mathbf{J} \times \mathbf{B} - \sum_{s=i,e}\Big(\nabla p_{s,\perp} + (\nabla \cdot \mathbf{\Pi}_s)_\perp\Big) + \Big(\sum_k \nabla \cdot \mathbf{P}_k\Big)_\perp\end{aligned} \tag{3.41}$$

The electron inertia can be neglected in the left hand side of equation (3.41) since $m_e << m_{i,k}$. Kinetic particles are considered here to be of ionic type. Considering equations (3.27) and (3.21), and using the gyroviscous cancellation of the bulk ion specie $d\mathbf{v}_i^*/dt = -\nabla \cdot \mathbf{\Pi}_i$, the left hand side of equation (3.41) $+\nabla \cdot \mathbf{\Pi}_i$ reads

$$\begin{aligned}\sum_{s=i,e} m_s n_s \partial_t \mathbf{u}_{i,\perp} + \sum_{s=i,e} m_s n_s (\mathbf{u}_s \cdot \nabla)\mathbf{u}_{s,\perp} + \nabla \cdot \mathbf{\Pi}_i + \partial_t\Big(\sum_k m_k n_k \mathbf{u}_{k,\perp}\Big) = \\ \rho_i \partial_t \mathbf{v}_\perp + \Big[\rho_i(\mathbf{v} \cdot \nabla)\mathbf{v} + \rho_i(\mathbf{v}_i^* \cdot \nabla)\mathbf{v}_\perp\Big]_\perp + \partial_t \sum_k \mathbf{J}^m_{kin,\perp}\end{aligned} \tag{3.42}$$

Finally, combining equations (3.41) and (3.42), the perpendicular fluid equation of motion implemented in XTOR-K is

$$\begin{aligned}\rho_i \partial_t \mathbf{v}_\perp + \Big[\rho_i(\mathbf{v} \cdot \nabla)\mathbf{v} + \rho_i(\mathbf{v}_i^* \cdot \nabla)\mathbf{v}_\perp\Big]_\perp + \partial_t \sum_k \mathbf{J}^m_{kin,\perp} - \\ \frac{1}{B}\Big[(\rho_i u_{i,\parallel} + J^m_{kin,\parallel})(\nabla \times \mathbf{E})_\perp + [\rho_i \mathbf{v}_\perp + \rho_i \mathbf{v}_i^* + \mathbf{J}^m_{kin}] \cdot (\nabla \times \mathbf{E})_\perp)\hat{\mathbf{b}}\Big] = \\ \mathbf{J} \times \mathbf{B} - \Big(\nabla p_i + \nabla p_e + \nabla \cdot \mathbf{\Pi}_e + \nabla \cdot \mathbf{P}_k + \nabla \nu_\perp \nabla(\mathbf{v}_\perp + \mathbf{v}_i^*)\Big)_\perp\end{aligned} \tag{3.43}$$

The term $(\nabla \cdot \mathbf{\Pi}_e)_\perp$ is neglected for now in XTOR-K.

Electron and ion temperature evolution in XTOR-K

The same closure procedure as in [Lütjens and Luciani, 2010] is used for XTOR-K. The second order moment in XTOR-K two fluid equations reads

$$\frac{dS_s}{dt} + \frac{\nabla \cdot \mathbf{Q}_s}{p_s} = 0 \tag{3.44}$$

with S_s the specie entropy, and $\mathbf{Q}_s$ the specie heat flux, defined as

$$S_s = \frac{1}{\gamma - 1} \ln \frac{p_s}{n_s^\gamma}, \qquad \mathbf{Q}_s = \frac{5 p_s}{2 q_s B^2} \mathbf{B} \times \nabla T_s \tag{3.45}$$

with γ the ratio of specific heat, equal to $5/3$ in a hot plasma. The total temporal temperature derivative of each specie s can be directly rewritten in terms of its entropy one as

$$\frac{dT_s}{dt} = \frac{2}{3} T_s \frac{dS_s}{dt} + \frac{2}{3}\frac{T_s}{n_S}\frac{dn_s}{dt} \tag{3.46}$$

Then, using the specie continuity equation and equation (3.44), the vectorial relations $\nabla \cdot (\mathbf{A}\times\mathbf{B}) = (\nabla\times\mathbf{A})\cdot\mathbf{B} - \mathbf{A}\cdot(\nabla\times\mathbf{B})$ and $\nabla\times\nabla x = 0$, the specie temperature time evolution reads

$$\partial_t T_s = -\mathbf{u}_s\cdot\nabla T_s - \frac{5}{3}\frac{T_s}{q_s}\nabla T_s\cdot\nabla\times\frac{\mathbf{B}}{B^2} - \frac{5}{3}T_s\frac{\mathbf{B}}{q_s n_s B^2}\cdot(\nabla T_s\times\nabla n_s) - \frac{2}{3}T_s\nabla\cdot\mathbf{u}_s \quad (3.47)$$

To close XTOR-K set's of fluid equations, the evolution of both the electron and ion temperature are required. The inclusion of kinetic species induces a kinetic term in the averaged electron velocity (equation [3.28]), since the quasi-neutrality assumption $n_e = Z_i n_i + \sum_k Z_k$ needs to be preserved.

Inserting equation (3.27) in equation (3.47), the ion temperature evolution implemented in XTOR-K is

$$\partial_t T_i = -\frac{2}{3}T_i\nabla\cdot\mathbf{v} - \mathbf{v}\cdot\nabla T_i - \frac{T_i}{Z_i e}\left(\frac{2\nabla p_i}{3n_i} + \frac{5\nabla T_i}{3}\right)\cdot\nabla\times\frac{\mathbf{B}}{B^2} \quad (3.48)$$

Inserting equation (3.28) in equation (3.47), the electron temperature evolution implemented in XTOR-K is

$$\begin{aligned}\partial_t T_e = &-\frac{2}{3}T_e\nabla\cdot\mathbf{v} - \mathbf{v}\cdot\nabla T_e + \frac{T_e}{e}\left(\frac{2\nabla p_e}{3n_e} + \frac{5}{3}\nabla T_e\right)\cdot\nabla\times\frac{\mathbf{B}}{B^2}\\ &-\frac{2}{3}BT_e\nabla_\parallel\left(\frac{e(Z_i n_i - n_e)u_{i,\parallel} + J^q_{kin,\parallel} - J_\parallel}{en_e B}\right) - \left(\frac{e(Z n_i - n_e)u_{i,\parallel} + J^q_{kin,\parallel} - J_\parallel}{en_e}\right)\nabla_\parallel T_e \quad (3.49)\end{aligned}$$

with $J_\parallel = (\nabla\times\mathbf{B})\cdot\mathbf{b}/\mu_0$. Equations (3.32), (3.38), (3.43),(3.48) and (3.49) are then the complete set of fluid equations solved by XTOR-K, including kinetic moments contributions.

3.2.3 Newton-Krylov/Picard algorithm in XTOR-K

In XTOR-K, it has been chosen to describe the kinetic species using a full-f method. It implies that the phase space position $(\mathbf{r},\mathbf{v})$ of every particle among the kinetic species distribution function is evolved in time. The choice of a full f method was motivated by the simplicity of its implementation in a hybrid code, compared to a δf method. The particle time advance is performed in 6D by using the classical Lorentz equation

$$\dot{\mathbf{r}}_k = \mathbf{v}_k, \qquad \dot{\mathbf{v}}_k = \frac{q_k}{m_k}[\mathbf{E} + \mathbf{v}_k\times\mathbf{B}] \quad (3.50)$$

The particle advance is done numerically by applying a Boris-Buneman scheme, that is detailled in [Leblond, 2011]. For simplicity, the basis used for this time advance is the orthogonal set $(\mathbf{e}_R, \mathbf{e}_{\varphi^*}, \mathbf{e}_Z)$, with $\mathbf{e}_R$ and $\mathbf{e}_Z$ respectively the directions of the tokamak R and Z axis, and $\mathbf{e}_{\varphi^*}$ the counter toroidal direction regarding the basis used for the MHD fields, $(\mathbf{e}_\psi, \mathbf{e}_\theta, \mathbf{e}_\varphi)$.

The particle distribution function is computed with a Particle In Cell (PIC) module. A finite number of markers N, macro-particles, is used to represent the distribution function F_k. In XTOR-K, the weight from one marker to another is chosen to be constant. In order to simulate N_{phys} physical particles, the weight of the jth marker ω_j is $\omega_j \equiv \omega_{PIC} = N_{phys}/N$, such as

$$F_k(\mathbf{r},\mathbf{v}) = \sum_i^{N_{phys}} \delta(\mathbf{r}-\mathbf{r}_i)\delta(\mathbf{v}-\mathbf{v}_i) = \sum_j^N \omega_j\delta(\mathbf{r}-\mathbf{r}_j)\delta(\mathbf{v}-\mathbf{v}_j) \quad (3.51)$$

The noise level introduced by a PIC module with constant weighting is $\epsilon_{noise} \propto 1/\sqrt{N}$ [Aydemir, 1994].

Particle sub-time step

The physical richness of having a "full orbit, full-f" code has unfortunately its computational downsides. Given that the particle advance is not gyro-kinetic, particles need to be advanced using a sub-time step regarding the time step used for the evolution of the MHD fields. This sub-time step needs to resolve the particle's gyration. Theoretically speaking, because of the circle's squaring, only four sub-time step per gyration are needed. However, parametric studies in [Leblond, 2011] showed that approximatively 12 points by gyration are required for a good conservation of the particles invariants. This imposed a sub-time step of order $\delta_{t,k} \sim 10^{-3}\tau_A \sim 10^{-10}$ seconds for light ions such as alpha particles. The Alfvén time is defined by $\tau_A = \sqrt{\mu_0\rho}/B_0R_0$. For ITER relevant magnetic equilibria, the Alfvén time is of order 10^{-7} seconds. The fluid time step in XTOR-K is usually set at $\delta_{t,MHD} \sim \tau_A$. Therefore, $\sim 10^3$ sub-time steps are required to advance kinetic particles over one fluid time step.

The ratio between the electron and ion frequencies is $|\omega_{c,e}/\omega_{c,i}| = m_e/m_i \sim 10^{-3}$. Kinetic advance of electrons would require sub-time steps three orders of magnitude below those of ions. Therefore the full orbit full f simulation of kinetic electrons is not numerically realistic yet for reasonable simulation times. However, a gyro-kinetic description of kinetic electrons would waive the requirement of having such low electron sub-time step.

Since a full-f method is used, every macro-particle of the kinetic distribution needs to be advanced in time. Moreover, $10^7 - 10^8$ macro-particles are required in the PIC module to have a reasonable level of noise. These two points imply that that the particles advance represent the most costly operation in a XTOR-K fluid time step, superior to the MHD advance. The PIC module therefore needs to be highly parallelized, to decrease the computational time of a hybrid simulation.

Moments projection

Similarly to the particle advance, the particles moments are projected on the direct grid (R, φ^*, Z). To simplify the interpolation of the particles position on this grid, a Fourier transform in the toroidal direction in performed. In the poloidal plane (R, Z), macro-particles are projected on the grid using bilinear projection. The weighting factor $S_{i,j}$ at a grid point (R_i, φ_l^*, Z_j) for a macro-particle with coordinate (R_k, Z_k) is

$$S_{i,j}(R_k, Z_k) = \omega_{PIC}\sigma_H(R_{i+1}-R_k)\sigma_H(R_k-R_i)\sigma_H(Z_{j+1}-Z_k)\sigma_H(Z_k-Z_j)(1+R_k-R_{i+1})(1+Z_k-Z_{j+1}) \tag{3.52}$$

Assuming that n_{max} toroidal grid points are used, the kinetic moments used in XTOR-K fluid equations at a grid point (R_i, Z_j) are

$$n_k(R_i, Z_j) = \sum_{k=1}^{N} S_{i,j}(R_k, Z_k) \tag{3.53}$$

$$\mathbf{v}_k(R_i, Z_j) = \sum_{k=1}^{N} \mathbf{u}_k S_{i,j}(R_k, Z_k) \tag{3.54}$$

$$\mathbf{P}_k(R_i, Z_j) = \sum_{k=1}^{N} \mathbf{u}_k \otimes \mathbf{u}_k S_{i,j}(R_k, Z_k) \tag{3.55}$$

The moment $\mathbf{v}_k$ is not computed in XTOR-K, but it illustrates how the moments $\mathbf{J}^m_{kin}$ and $\mathbf{J}^q_{kin}$ are computed.

The self-consistent Kinetic-MHD advance in XTOR-K

For a self-consistent advance of both MHD fields and kinetic particles, a Newton-Krylov/Picard algorithm is used in XTOR-K. It uses the implicit Newton-Krylov scheme described in [Lütjens and Luciani, 2010].

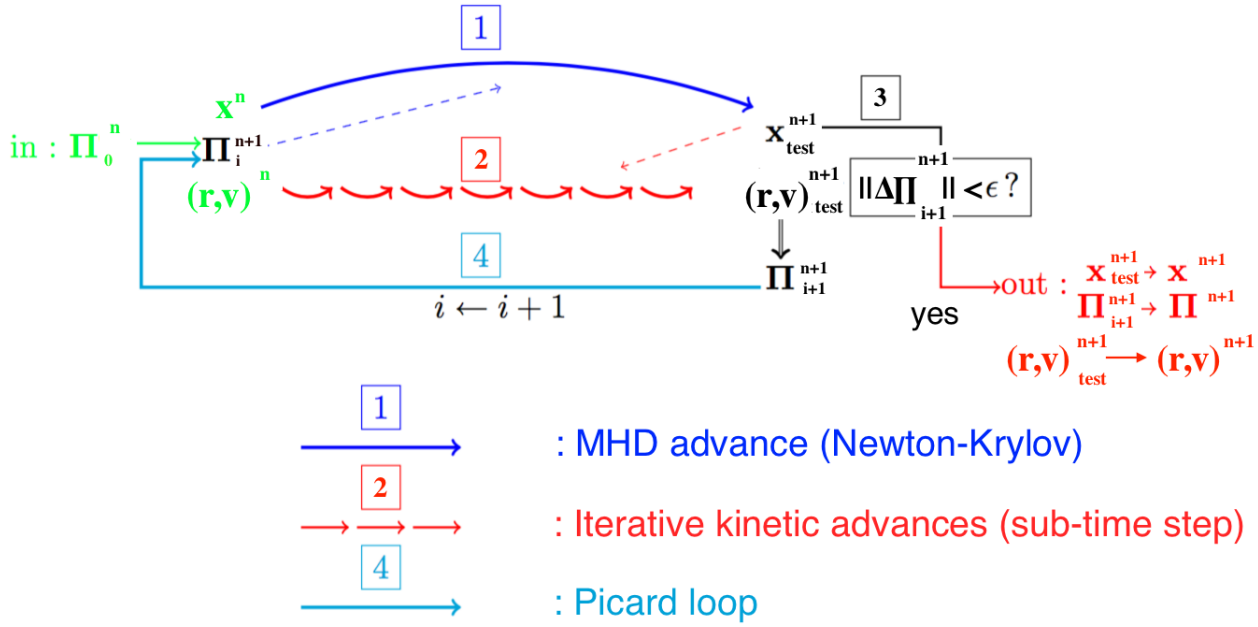

Figure 3.2: The Newton-Krylov/Picard schem. It enables to advance self-consistently kinetic particles and MHD fields.

The Newton-Krylov/Picard scheme is summarized on Figure 3.2. A brief explanation of this scheme is discussed here over one fluid time step. Let us consider the n^{th} fluid iteration. At the beginning of this iteration, the MHD fields are noted $\mathbf{x}^n$, the kinetic moments $\mathbf{\Pi}^n$ and the phase space position of all macro-particles $(\mathbf{r},\mathbf{v})^n$. In order to obtain all theses quantities at the $n+1^{th}$ fluid iteration, a Picard loop is performed. The algorithm of this loop is explained here in details for the ith Picard iteration

- Step [1] : The Newton-Krylov algorithm is used to advance XTOR-K fluid equations. The MHD fields used are $\mathbf{x}^n$. The particles moments used are $\mathbf{\Pi}_i^{n+1}$, obtained at the previous Picard iteration. If i = 0, $\mathbf{\Pi}_0^{n+1}$ is initialized by extrapolation of the kinetic moments $\mathbf{\Pi}^n$ and $\mathbf{\Pi}^{n-1}$. This initialization enables to reduce the number of Picard iterations required over one fluid iteration. The MHD fields $\mathbf{x}_{test}^{n+1}$ are obtained at the end of the MHD advance.

- Step [2] : The particle advance is done from the initial phase space positions $(\mathbf{r},\mathbf{v})^n$. It is performed by successive advances over a kinetic sub-time step. The electromagnetic fields used in Lorentz equation are interpolated between the MHD fields $\mathbf{x}_{test}^n$ and $\mathbf{x}_{test}^{n+1}$. Once the advance has reached a fluid time step, the new phase space positions $(\mathbf{r},\mathbf{v})_{test}^{n+1}$ are obtained. From these positions, the new kinetic moments $\mathbf{\Pi}_{i+1}^{n+1}$ are interpolated on the (R,φ^*,Z) grid.

- Step [3] : The quantity $\Delta\mathbf{\Pi}_{i+1}^{n+1} = \mathbf{\Pi}_i^{n+1} - \mathbf{\Pi}_{i+1}^{n+1}$ is computed. The kinetic moment used in the total pressure tensor $\mathbf{P}_k$. If $||\delta\mathbf{\Pi}_i^n|| < \epsilon$, the Picard algorithm has converged. Therefore, at the $n+1^{th}$ fluid step, the MHD fields are $\mathbf{x}^{n+1} = \mathbf{x}_{test}^{n+1}$, the phase space position $(\mathbf{r},\mathbf{v})^{n+1} = (\mathbf{r},\mathbf{v})_{test}^{n+1}$ and the kinetic moments $\mathbf{\Pi}^{n+1} = \mathbf{\Pi}_{i+1}^{n+1}$.

If $||\delta\mathbf{\Pi}_i^n|| > \epsilon$, the Picard algorithm has not converged. The quantities $\mathbf{x}_{test}^{n+1}$ and $(\mathbf{r},\mathbf{v})_{test}^{n+1}$ are not retained. The algorithm goes to step [4]. The quantity ϵ is a small parameter set in advance at the beginning of the simulation.

- Step [4] : The kinetic moments $\mathbf{\Pi}_{i+1}^{n+1}$ are injected back into step [1]. One complete fluid iteration has been done.

3.2.4 Management of the noise level in XTOR-K

Since a full f method is used in XTOR-K, the code is considerably more affected by the noise brought by the PIC module than other hybrid codes using a δf scheme. According to [Aydemir, 1994], the noise in a δf method is reduced by a factor $\delta f_k/F_k << 1$, where $F_k = F_{eq,k} + \delta f_k$. Therefore, several points need to be verified carefully when performing Kinetic-MHD simulations with a full f method. First, the dominant modes simulated must not be affected by the number of macro-particles N in the simulation. Second, the noise level must evolve as $1/\sqrt{N}$ when the number of macro-particles is increased [Aydemir, 1994]. The noise level can be evaluated by the harmonic with lowest energy in the simulation.

On Figure 3.3, magnetic energies obtained from the same XTOR-K simulation, with different number of macro-particles, are presented. The harmonics $n = 1$ correspond to the dominant modes, in their linear phase. The harmonics $n = 3$ correspond to the harmonics with lower energy in each simulation. It can be seen on Figure 3.3 that the dominant

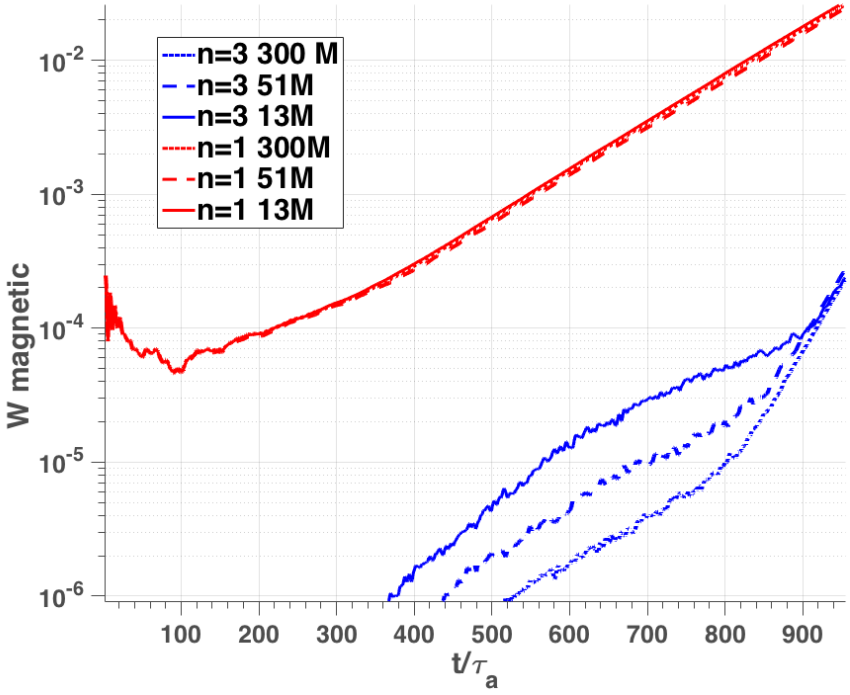

Figure 3.3: Magnetic energies of the $n = 1$ and $n = 3$ modes simulated in XTOR-K. The number of macro-particles have been varied from one simulation to an other. Up to $t/\tau_A = 900$, the $n = 3$ modes are still below the noise level. At $t/\tau_A = 900$, these modes rise above the noise level. It is noted that the noise level from one simulation to another indeed varies as $1/\sqrt{N}$. This is particularly visible at $t/\tau_A = 600$. The $n = 1$ dominant modes are not affected by the number of macro-particles.

$n = 1$ modes are not affected by the number of macro-particles used. The $n = 3$ modes

are below their respective noise level up to $t\tau_A = 900$. Their noise level can be compared for example at $t/\tau_A = 600$. Let us denote E_N the noise level observed for each simulation, with N the number of macro-particles. At $t/\tau_A = 600$, $E_{300} = 2.10^{-6}$, $E_{51} = 5.10^{-6}$ and $E_{13} = 1.05 \times 10^{-5}$. It can be observed that $E_{51}/E_{300} = 2.5 \sim \sqrt{300/51} = 2.4$ and that $E_{13}/E_{51} = 2.1 \sim \sqrt{51/13} = 1.98$. The noise level indeed varies has $1/\sqrt{N}$. After $t/\tau_A = 900$, all the $n = 3$ harmonics are beyond their noise level, they get pumped by toroidal coupling with the $n = 1$ harmonics.

A last point needs to be verified when performing a hybrid simulation with XTOR-K. The noise level needs to be below the local minima of the unstable modes that are studied in the nonlinear phase. As an example, kinetic energies of a XTOR-K simulation at the beginning

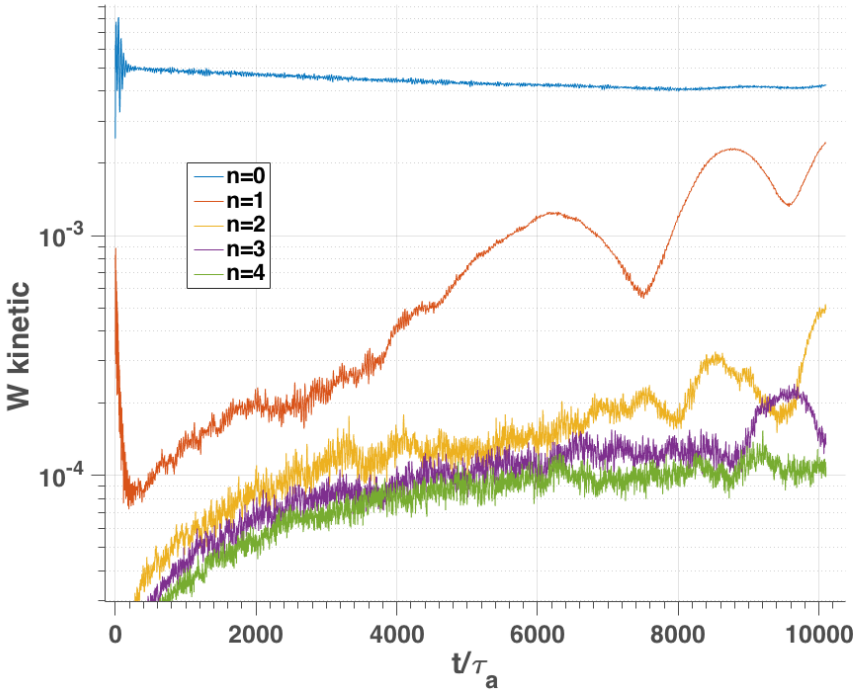

Figure 3.4: Kinetic energies obtained from a hybrid simulation in its nonlinear phase. The PIC noise is particularly high in this simulation, the linear phase of the unstable modes $n = 1$ are below the noise level. In its nonlinear phase, the $n = 1$ modes exhibit local minima. The number of macro-particles N needs to be tuned so that the local minima lie above the noise level.

of the nonlinear phase are plotted on Figure 3.4. According to the $n = 4$ modes, the noise level of the simulation in terms of kinetic energy is 10^{-4}. The dominant modes $n = 1$ exhibit oscillations in the nonlinear phase, with the lowest local minima value being $W = 5.10^{-4}$. In this simulation, 300 million macro-particles are used. If 13 million of macro particles would have been used, the local minima $W = 5.10^{-4}$ would have lied below the noise level, which is not acceptable.

It has been chosen to set the noise level well below the $n = 1$ modes smallest minima for two reasons. First, modes with lower energies such as the $n = 2$ can become of interest in the simulation. Therefore, their local minima, which will be below those of the $n = 1$ modes, need also to be resolved. Second, phase space diagnostics are used in this simulation. They permit to see the time evolution of the wave-particle resonance and its structure in phase space. These diagnostics are presented in Chapter 4. A high number of macro-particles are

required for these diagnostics. It enables to obtained a refined resolution in phase space in order to see the thin wave-particle resonant structures.

3.3 Linear stability of the internal kink in MHD

Now that the XTOR-K code has been presented in details, the structure and the dispersion relation of the $n = m = 1$ internal kink MHD is discussed. This discussion is needed here for two reasons. First, the fishbone instability studied in this thesis is a $n = m = 1$ Kinetic-MHD mode, that gets destabilized due to the resonant interaction between a $n = m = 1$ internal kink and energetic particles eigenfrequencies. Before addressing the issue of the fishbone instability, the nature of the internal kink instability needs to be presented.
Second, a linear theory for the fishbone instability needs to be derived. The code XTOR-K has been implemented recently, it needs to be verified against linear theory before being used to simulate the fishbone instability. In order to derive such a linear theory, which is the matter of Chapter 4, a dispersion relation for the internal kink is required.

In this section, the ideal MHD equations are firstly linearized. The energy principle is presented, in order to assess the stability of an arbitrary magnetic configuration. Using the energy principle formalism, the mode structure and the dispersion relation of the ideal MHD internal kink in cylindrical geometry is derived from [Freidberg, 2014]. Afterwards, the internal kink mode structure and its the dispersion relation is generalized to two fluid resistive MHD equations, including toroidal curvature. This dispersion relation constitutes the groundwork of the fishbone dispersion relation derived in the next chapter.

3.3.1 The Energy Principle

Linearization of the MHD equations

In order to perform a linearization of the ideal MHD equations (equations 3.1 - 3.7), all MHD fields can be separated into an equilibrium and a perturbed part. Noting $P(\mathbf{r}, t)$ a given field, it can be expressed as $P(\mathbf{r}, t) = P_0(\mathbf{r}) + P_1(\mathbf{r})e^{-i\omega t}$, where ω the complex frequency of an arbitrary instability. All MHD fields possess an equilibrium part, except the MHD velocity since at MHD equilbrium, $\mathbf{v} = 0$. When a macroscopic instability occurs, the plasma experiences, at a given time t and location r inside the torus, a shift $\boldsymbol{\xi}(\mathbf{r}, t)$ from its equilibrium position. This shift is called the MHD displacement and verifies $\dot{\boldsymbol{\xi}}(\mathbf{r}, t) = \mathbf{v}(\mathbf{r}, t)$. Using these notations, the MHD equations can be linearized

$$p_1 = -\boldsymbol{\xi} \cdot \nabla p - \gamma p \nabla \cdot \boldsymbol{\xi} \tag{3.56}$$

$$\mathbf{B}_1 = \nabla \times (\boldsymbol{\xi} \times \mathbf{B}) \tag{3.57}$$

$$-\omega^2 \rho \boldsymbol{\xi} = \mathbf{F}(\boldsymbol{\xi}) \tag{3.58}$$

$$\mathbf{F}(\boldsymbol{\xi}) = \frac{1}{\mu_0}\big[(\nabla \times \mathbf{B}_1) \times \mathbf{B} + (\nabla \times \mathbf{B}) \times \mathbf{B}_1\big] + \nabla(\boldsymbol{\xi} \cdot \nabla p + \gamma p \nabla \cdot \boldsymbol{\xi}) \tag{3.59}$$

The linear stability analysis in MHD therefore reduces to an eigenvalue/eigenvector problem according to equation (3.58), with eigenvalue ω^2 and eigenvector $\boldsymbol{\xi}$. In ideal MHD, $\omega^2 \in \mathbb{R}$. During plasma discharges and MHD numerical simulation, several eigenfunctions $\boldsymbol{\xi}$ with corresponding eigenvalues ω^2 can co-exist. However, only those with the smaller ω^2 are of interest, i.e. with highest growth rates, since they will dominate the dynamics. The linear stability problem is then solved by finding eigenfunctions $\boldsymbol{\xi}$ solutions of (3.58) that minimizes the eigenvalues ω^2.

The present formulation of the eigenvector/eigenvalue problem does not detail a systematic scheme for finding the solutions of (3.58) with minimum eigenvalues. It enables only to obtain the eigenvalue corresponding to a given test eigenfunction $\boldsymbol{\xi}_0$. This is only useful when the global structure of the unstable mode is already known. However, in order to properly assess the linear stability of a given magnetic configuration, the eigenvector/eigenvalue problem needs to be solved entirely. To this end, a variational formalism is now presented.

The Energy Principle

The eigenvector/eigenvalue problem can be reformulated into the Energy Principle [Freidberg, 2014], chapter 8.7. By forming $-1/2 \int_V d^3\mathbf{r}\ \boldsymbol{\xi}^* \cdot$ on (3.58), the instability total energy can be expressed as

$$\mathbf{E}(\boldsymbol{\xi}, \boldsymbol{\xi}^*) = K(\boldsymbol{\xi}, \boldsymbol{\xi}^*) - \delta W(\boldsymbol{\xi}, \boldsymbol{\xi}^*) = 0 \tag{3.60}$$

where K stands for the kinetic energy of the instability

$$K(\boldsymbol{\xi}, \boldsymbol{\xi}^*) = \frac{1}{2} \int_V d^3\mathbf{r}\ \rho\omega^2 |\boldsymbol{\xi}|^2 \tag{3.61}$$

and δW its potential energy.

$$\delta W(\boldsymbol{\xi}, \boldsymbol{\xi}^*) = -\frac{1}{2} \int_V d^3\mathbf{r}\ \boldsymbol{\xi}^* \cdot \mathbf{F}(\boldsymbol{\xi}, \boldsymbol{\xi}*) \tag{3.62}$$

The eigenfunctions of interest are those which minimize the potential energy. Considering a test solution $\boldsymbol{\xi}_s$ for a given magnetic configuration, it needs to verify that $\forall \delta\boldsymbol{\xi} \in \mathbb{R}^3, \delta W(\boldsymbol{\xi}_s + \delta\boldsymbol{\xi}) = \delta W(\boldsymbol{\xi}_s)$. Given that the potential energy is a complex function of the MHD displacement, it is useful to choose a variational parameter that eases the minimization procedure, by taking advantage of the potential energy structure for an arbitrary magnetic configuration. Once the potential energy has been minimized for a given magnetic configuration, its linear stability can be directly assessed by the sign of δW since

$$\omega^2 = \frac{\delta W(\boldsymbol{\xi}, \boldsymbol{\xi}^*)}{\frac{1}{2}\int_v d^3\mathbf{x}\ |\boldsymbol{\xi}|^2} \tag{3.63}$$

Given that $|\boldsymbol{\xi}|^2$ is purely positive, the sign of ω^2 is entirely determined by the potential energy, so that the considered magnetic configuration is unstable when $\delta W < 0$, and stable otherwise. This is however only true for the one fluid ideal MHD equations

The potential energy needs to be reformulated in a way that highlights its simple dependence over a variational parameter. This reformulation also enables to highlight the physical processes that are stabilizing or destabilizing MHD waves. Following the complete derivation presented in [Freidberg, 2014] chapter 8.5.3, δW can be expressed as

$$\delta W(\boldsymbol{\xi}, \boldsymbol{\xi}^*) = \frac{1}{2} \int_V d\mathbf{r} \left[\frac{|\mathbf{B}_{1,\perp}|^2}{\mu_0} + \frac{B^2}{\mu_0} |\nabla\cdot\boldsymbol{\xi}_\perp + 2\boldsymbol{\xi}_\perp\cdot\kappa|^2 + \gamma p |\nabla\cdot\boldsymbol{\xi}|^2 - 2(\boldsymbol{\xi}_\perp\cdot\kappa)(\boldsymbol{\xi}_\perp\cdot\nabla p) - J_\parallel(\boldsymbol{\xi}_\perp^*\times\mathbf{b})\mathbf{B}_{1,\perp} \right] \tag{3.64}$$

The three first terms of the potential energy being strictly positive, they represent the stabilizing terms. These terms relax perturbations imposed to the equilibrium by propagating MHD waves. The only terms that do not have a priori a clear sign are the last two. They constitute the terms that can drive MHD instabilities. The physical meaning of each terms is explained as follow :

1^{st} term : It stands for the energy required to bend the field lines, driving the shear Alfvén wave at the Alfvén velocity $V_a = B_0/\sqrt{\mu_0 \rho}$. This velocity, or order $10^7 m.s^{-1}$ in tokamaks, is associated to the Alfvén time by $\tau_A = V_A/R_0$, or order $10^{-7} - 10^{-6}$ s.
2^{nd} term : It represents the energy required to compress the field lines, driving the compressional Alfvén waves, that propagates either at the Alfvén velocity, or at the sound velocity $c_s = \sqrt{\gamma p/\rho}$.
3^{rd} term : It is associated to the energy required to compress the plasma, driving the sound wave that propagates at the sound velocity.
4^{th} and 5^{th} term : They represent respectively the pressure and current terms, that drives MHD instabilities.

It can be noted that the parallel MHD displacement $\xi_\parallel$ only appears in the third term of the potential energy. Therefore, using it as the variational parameter enables to simplify greatly the amount of analytical calculations required to minimize the potential energy. It can be shown that minimizing δW against $\xi_\parallel$ is equivalent to choose perturbations such that the plasma becomes incompressible, i.e. $\nabla \cdot \xi = 0$ [Freidberg, 2014] chapter 8-9.

To summarize, the general procedure to assess the linear stability goes as follow. In a first step, the potential energy needs to be explicitly derived for the considered magnetic configuration. Then, the potential energy is minimized against $\xi_\parallel$ so that the plasma becomes incompressible with $\nabla \cdot \boldsymbol{\xi} = 0$. If necessary and/or possible, the potential energy is minimized further with an other components of the MHD displacement. Finally, the eigenfunction obtained through this variational formalism is injected inside the potential energy. The sign of δW then assesses the linear stability, and equation (3.63) is the dispersion relation of the instability.

3.3.2 Stability of the internal kink in cylindrical geometry

The energy principle formalism is now applied to the tokamak configuration, for the study of the internal kink. The derivation with toroidal curvature is beyond the scope of this discussion, and can be found in [Bussac et al., 1975]. The present derivation will be performed in cylindrical geometry.

In order to describe a configuration still relevant to the tokamak configuration with circular cross section and large inverse aspect ratio, a cylinder of length $L = 2\pi R_0$ is considered, with outer radius $r = a$. Periodic boundary conditions are used to mimic a tokamak configuration. The equilibrium magnetic field of such a configuration is $\mathbf{B} = B_\theta \hat{\theta} + B_\varphi(r)\hat{\varphi}$, $\hat{\varphi}$ being here the direction along the cylinder axis. The safety factor is simply $q(r) = rB_\varphi/(R_0 B_\theta)$. This configuration is periodic along θ and φ, so the MHD displacement can be described by $\boldsymbol{\xi}(\mathbf{r}) = \boldsymbol{\xi}(r)e^{i(m\theta - n\varphi)}$. The wave vector has been here assumed to be of the form $\mathbf{k} = m\hat{\theta}/r - n\hat{\varphi}/R$. The derivation of δW firstly considers arbitrary poloidal and toroidal harmonics, and then focuses on the $n = m = 1$ internal kink. Given the relative complexity of the magnetic field, it is convenient to use the following basis vectors

$$\begin{array}{rclcl} \hat{b} & = & \frac{1}{B}(B_\theta \hat{\theta} + B_\varphi \hat{\varphi}), & \hat{\theta} = \frac{1}{B}(B_\theta \hat{b} + B_\varphi \hat{\eta}) \\ \hat{\eta} & = & \frac{1}{B}(B_\varphi \hat{\theta} - B_\theta \hat{\varphi}), & \hat{\varphi} = \frac{1}{B}(B_\varphi \hat{b} - B_\eta \hat{\varphi}) \end{array} \tag{3.65}$$

The displacement vector can then be expressed as $\boldsymbol{\xi}(r) = \xi_r(r)\ \hat{r} + \eta(r)\ \hat{\eta} + \xi_\parallel(r)\hat{b}$. The derivation that will follow is present in [Freidberg, 2014], chapter 11-5. The steps of the derivation are presented to give some intuition of the internal kink structure.

Minimization of δW with respect to $\xi_\parallel$ and η

In order to get an expression for $\xi_\parallel$ from $\nabla \cdot \xi = 0$, the following notations are used : $F = \mathbf{k} \cdot \mathbf{B} = (B_\varphi/R_0)(m/q - n)$, $G = (m/r)B_\varphi + (n/R)B_\theta$

$$\nabla_\parallel \xi_\parallel = -\nabla_\perp \cdot \boldsymbol{\xi}_\perp \Leftrightarrow \xi_\parallel = \frac{iB}{F} \nabla \cdot \xi_\perp \tag{3.66}$$

It is noted here that $\xi_\parallel$ is only defined for $F(r) \neq 0$. The parallel displacement becomes singular at the resonant surface r_s. This surface is defined by $\mathbf{k} \cdot \mathbf{B}(r_s) = 0$, which implies $q(r_s) = m/n$ for a tokamak configuration. But it can be shown that $\xi_\parallel$ can be extended by continuity at this surface, the plasma compressibility making a vanishing contribution to δW.

It can be shown that δW is further minimized by

$$\eta = \frac{iR^2}{B_\varphi n^2 r} \left[G(r)[r\xi_r]' - \frac{2nB_\theta}{R} \xi_r \right] \tag{3.67}$$

Minimized expression of δW for the $n = m = 1$ internal kink

Using equations (11.89) and (11.90) in [Freidberg, 2014], it can then be shown that the potential energy for this configuration is

$$\frac{\delta W}{2\pi^2 R/\mu_0} = \int_0^a dr \, \left[f(r)|\xi_r'|^2 + g(r)|\xi_r|^2 \right] + \left[\frac{n^2\epsilon^2 B_\varphi^2 - m^2 B_\theta^2}{n^2\epsilon^2 + m^2} \right]_a |\xi_r(a)|^2 \tag{3.68}$$

with

$$f(r) = \frac{r\epsilon^2 B_\varphi^2 \Big(1/q - n/m\Big)^2}{1 + \epsilon^2 n^2/m^2} \tag{3.69}$$

$$g(r) = \frac{\epsilon^2 B_\varphi^2}{1 + \epsilon^2 n^2/m^2} \left[\frac{2\mu_0 p'}{B_\varphi^2} \frac{n^2}{m^2} + \frac{1}{r} \Big(\frac{1}{q} - \frac{n}{m} \Big)^2 (m^2 - 1 + n^2\epsilon^2) + \frac{2n^2\epsilon^2}{r m^2 (1 + \epsilon^2 n^2/m^2)} \Big(\frac{n^2}{m^2} - \frac{1}{q^2} \Big) \right] \tag{3.70}$$

Since only internal modes are of interest in this thesis, $\xi(a) = 0$ has been chosen as boundary condition. This is equivalent to neglect external kink modes. Using the notation $\delta W_P \mu_0 / 2\pi^2 R = \int dr (B_\varphi^2)/(1 + \epsilon^2 n^2/m^2) W(r)$, an expansion of W can be performed regarding the small parameter $\epsilon = r/R$, such as $W = W_2 + W_4 + \mathcal{O}(\epsilon^6)$. The lowest order of this expansion reads

$$W_2(r) = \frac{\epsilon^2}{r} \Big(\frac{1}{q} - \frac{n}{m} \Big)^2 \left[r^2 |\xi'|^2 + (m^2 - 1)|\xi|^2 \right] \tag{3.71}$$

Therefore, at leading order, all perturbations are stable for $m > 1$ since $W_2(r) > 0$. This result implies that the $m = 1$ mode is always the most unstable for this configuration. Turning now to the internal kink $n = m = 1$, it is possible to construct eigenfunctions that minimize further the potential energy so that

$$W_2(r) = r\epsilon^2 \left(\frac{1}{q} - 1 \right)^2 |\xi_r'|^2 = 0 \tag{3.72}$$

This equation implies that at its lowest order, denoted $\xi_{r,0}$, the radial eigenfunction of the $n = m = 1$ internal kink reads

$$\xi_{r,0} = \xi_0 \sigma_H (r_s - r) \tag{3.73}$$

with σ_H the Heaviside function, and ξ_0 the radial displacement at $r = 0$. $\xi_{r,0}$ is not constant all over the cylinder since at $r = r_s$, $1 - q(r_s) = 0$ for the $n = m = 1$ instability. Therefore W_2 vanishes for $r > r_s$. Using this eigenfunction, the potential energy needs to be expressed at the next order in ϵ

$$W_4(r) = -\xi_{r,0}^2 \epsilon^2 \beta \left(\epsilon^2 \frac{3q+1}{\beta r q^2}[1-q] - \frac{p'}{p} \right) \tag{3.74}$$

The minimized potentiel energy δW_{min} then reads

$$\delta W_{min} = \frac{2\pi^2 R_0}{\mu_0} \int_0^{r_s} B_\varphi^2(r) W_4 dr \tag{3.75}$$

The internal kink $n = m = 1$ is therefore unstable when $\delta W_{min} < 0 \Leftrightarrow W_4(r) > 0$. Given that inside the cylinder, as in a tokamak, $p'(r) < 0$ since all the profiles are peaked, the internal kink is always unstable when $1 - q(r) > 0$. It implies that existence of a $q = 1$ surface is a sufficient condition to trigger this instability. Moreover, the dependencies of W_4 over p' and $1-q$ show that the internal kink is at the same time a current and pressure driven instability.

Mode structure and growth rate

In order to obtain the precise mode structure of the internal kink, as well as its dispersion relation, it is necessary to minimize the instability total energy $E = K - \delta W$. This is necessary since the next order contribution in ϵ to ξ_r, $\xi_{r,2}$, becomes singular near the resonant surface $r = r_s$. It implies that the kinetic energy varies significantly in this region, called the inertial layer. First, the potential energy is minimized at next order in ϵ, ϵ^4. Considering equation (3.68) and applying the variational principle with respect to $\xi_r \to \xi_r + \delta\xi_r$, δW is minimized through

$$\delta(\delta W)_\xi \approx \int dr \, \Big[(f\xi')' - g\xi \Big] \delta\xi = 0 \tag{3.76}$$

which gives the Euler-Lagrange equation

$$(f\xi')' - g\xi = 0 \tag{3.77}$$

Given that the expansions of f, g and ξ with respect to ϵ are $f(r) = f_2(r) + \mathcal{O}(\epsilon^4)$, $g(r) = g_4(r) + \mathcal{O}(\epsilon^6)$ and $\xi(r) = \xi_{r,0} + \xi_{r,2} + \mathcal{O}(\epsilon^4)$, the next order MHD displacement $\xi_{r,2}$ is given by

$$\frac{d}{dr}\left(f_2(r) \frac{d\xi_2}{dr}(r) \right) = \xi_0(r) g_4(r) \tag{3.78}$$

with

$$f_2(r) = \frac{r\epsilon^2 B_\varphi^2}{q^2}(1-q^2), \;\; g_4(r) = B_\varphi^2(r) W_4(r) \tag{3.79}$$

which gives an expression at second order for ξ at both sides of the inertial layer

$$\begin{array}{rcll} \frac{d\xi_2}{dr}(r) & = & \frac{q^2\xi_0}{r\epsilon^2[1-q(r)]^2 B_\varphi^2(r)} \int_0^{r_s} B_\varphi^2(r') W_4(r') dr', & r < r_s \\ & = & \frac{q^2\alpha}{r\epsilon^2[1-q(r)]^2 B_\varphi^2(r)}, & r > r_s \end{array} \tag{3.80}$$

α being here a constant yet to be determined. The derivative of $\xi_{r,2}$ is in fact diverging in the inertial layer, the kinetic energy cannot be considered constant there as it is the outer region $r < r_s$, E needs to be minimized. Assuming that the internal kink is unstable with $\omega^2 = -\gamma^2$ the mode growth rate, the kinetic energy reads

$$K = -2\pi^2 R \int dr \; r\rho\gamma^2 \Big[|\xi_\parallel|^2 + |\xi_r|^2 + |\eta|^2 \Big] \tag{3.81}$$

In the inertial layer $r \sim r_s$, it can be assumed that $\xi << r_s\xi'$ due to the brutal shift in the displacement vector at the lowest order. Such an assumption implies that in K, the term $|\xi_r|^2$ is neglected, and that

$$\xi_\parallel \approx \frac{iB}{rF}\Big[1 - \frac{G^2}{B^2k_0^2}\Big]\xi_r' = \frac{iF}{Bk_0^2}\xi_r' \approx ir\frac{B_\theta}{B}\xi_r' \propto \epsilon\xi_r' \tag{3.82}$$

$|\xi_\parallel|^2$ being of order ϵ^2, it can also be neglected. The only term remaining in (3.81) is therefore $|\eta|^2$, which reads under the previous assumption

$$\eta \approx \frac{iG}{Bk_0^2}\xi_r' \approx ir\frac{B_\phi}{B}\xi_r' \approx ir\xi_r' \tag{3.83}$$

Therefore, inside the inertial layer $r \sim r_s$, the instability kinetic energy is

$$K \approx -2\pi^2 R\int dr\ \rho\gamma^2 r^3|\xi_r'|^2 \tag{3.84}$$

At order 2 in ϵ in the inertial layer, $W_2 = r^3F^2|\xi_r'|^2/R_0^2$. The potential energy then is

$$\delta W = \frac{2\pi^2 R_0}{\mu_0}\int dr\ r^3F^2|\xi_r'|^2 \tag{3.85}$$

Therefore, at lowest order, using the Alfvén velocity and the Alfvén time $v_A = B_\varphi^2/\sqrt{\mu_0\rho}$ and $\tau_A = R_0/v_A$

$$K - \delta W = 0 \Leftrightarrow \int dr\frac{B_\varphi^2}{\mu_0}r^3\left(\Big[(\gamma\tau_A)^2 + \frac{R_0^2F^2}{B_\varphi^2}\Big]|\xi_r'|^2\right) = 0 \tag{3.86}$$

where F^2 can be expanded around the inertial layer following $r = r_s + x$ at first order as $F^2(R_0^2/B_\varphi^2) \approx x^2q'^2(r_s) = x^2s(r_s)^2/r_s^2$. s is the local magnetic shear defined by $s(r) = rq'(r)/q(r)$. Assuming that at lowest order in ϵ $B_\varphi \approx B_\varphi(r=0) = B_0$, the Euler equation for (3.86) reads at lowest order in ϵ

$$\begin{aligned}(d/dx)\Big[r_s^3\big(\tau_A^2\gamma^2 + x^2s^2/r_s^2\big)|\xi'|^2\Big] &= 0\\ \Leftrightarrow (d\xi_r/dx) &= cst/\Big[1 + (s^2x^2/\tau_A^2\gamma^2r_s^2)\Big]\\ \Leftrightarrow \xi_r &= K_1 + K_2\arctan\big(sx/\tau_A\gamma r_s\big)\end{aligned} \tag{3.87}$$

Matching this expression with the boundary conditions $\lim_{x\to-\infty}\xi(x) = \xi_0,\ \lim_{x\to+\infty}\xi(x) = 0$, the complete radial mode structure of the $n = m = 1$ internal kink finally is

$$\xi_r = \xi_0\left[\frac{1}{2} - \frac{1}{\pi}\arctan\Big(\frac{sx}{\tau_A\gamma r_s}\Big)\right] \tag{3.88}$$

The mode structure is displayed on Figure (3.5). The MHD displacement $\boldsymbol{\xi}$ of the internal kink is predominantly a core radial displacement ξ_r, shaped at first order as a Heaviside function $\xi_{r,0}$ centered on the resonant location $q(r_s) = 1$. The next order correction $\xi_{r,2}$ tends to smooth the discontinuity at the resonant surface. According to equation (3.88), $\xi_{r,2}$ becomes important for large growth rates, large resonant position r_s, and low magnetic shear at the resonant surface. Since for parabolic q profile, $s(r_s) = 2[1-q(0)]$, $\xi_{r,2}$ becomes also important when the on-axis safety factor is close to $m/n = 1$. On Figure 3.5, a parabolic q profile has been used, with the following parameters $r_s = 0.5$, $\gamma\tau_A = 1.10^{-2}$, $q_0 = 0.8$.

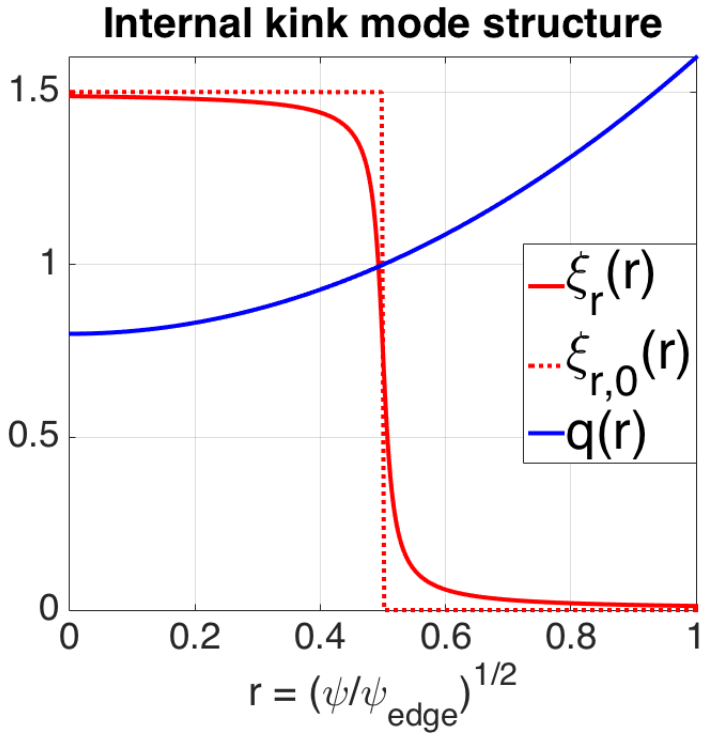

Figure 3.5: Compared values for the safety factor q, the total displacement ξ_r, and the lowest order displacement $\xi_{r,0}$, as functions of the normalized radial flux component $r = \sqrt{\psi/\psi_{edge}}$, where ψ_{edge} is the magnetic flux at the edge of the cylinder

The growth rate and the α constant are found by matching (3.80) and the derivative of (3.88) at $x \to \infty$, far from the $q = 1$ surface which is

$$\lim_{x\to\infty} \frac{d\xi_r}{dr} = -\frac{\xi_0 \tau_A \gamma r_s}{\pi s x^2} \tag{3.89}$$

giving

$$\gamma\tau_A = -\frac{\pi R_0^2}{s r_s^2 B_\varphi^2(r_s)} \int_0^{r_s} B_\varphi^2(r) W_4(r) dr, \qquad \alpha = \frac{\xi_0 R_0^2}{B_\varphi^2(r_s)} \int_0^{r_s} B_\varphi^2(r) W_4(r) dr \tag{3.90}$$

Since it can be shown that $\gamma\tau_A \propto 1/n$, the $n = m = 1$ instability is then the dominant one in the cylindrical configuration. A similar result can be shown in toroidal geometry [Bussac et al., 1975]. Finally, the link between the minimized potential energy, δW_{min}, and the mode normalized growth rate with $\lambda_H = \tau_A \gamma$, can be made by direct comparison of equations (3.75) and (3.90), yielding the one fluid ideal MHD dispersion relation

$$\delta W_{min} = -\frac{2\pi}{\mu_0} \frac{\xi_0^2}{R_0^2} R_0 r_0^2 s_0 B_\varphi^2(r_s^2) \lambda_H = -\frac{2\pi}{\mu_0} \xi_0^2 R_0 s_0 B_\theta^2 \lambda_H \tag{3.91}$$

This relation holds also for toroidal geometry, assuming large inverse aspect ratio.

3.3.3 Generalization of the internal kink relation dispersion

Effects of toroidal curvature

The inclusion of toroidal curvature was first performed in [Bussac et al., 1975], and then later in [Connor and Hastie, 1985], where monotonic q profiles were assumed. It does not change

the eigenfunction $\boldsymbol{\xi}$ found in cylindrical geometry. However, toroidal curvature affects the dispersion relation of the internal kink, as

$$\lambda_H = \gamma\tau_A = -3\pi s(r_s)\big(1-q(0)\big)\frac{r_s^2}{R_0^2}\left(\frac{13}{144}-\beta_p(r_s)^2\right) \tag{3.92}$$

where $\beta_p = 2\mu_0 p/B_\theta^2$ is the poloidal beta. Contrarily to cylindrical geometry, the internal kink is not always unstable when there exists a $q=1$ surface inside the torus. The poloidal beta needs to be as well beyond the threshold value $\beta_{p,res} = 13/144$.

A 3D representation of the internal kink mode structure has been displayed on Figure (3.6) in toroidal geometry. The color gradient refers to the core magnetic surfaces as red, and to the edge magnetic surfaces as blue. The $n=m=1$ mode is pushing radially outward the magnetic axis, with a structure 1,1 periodic in the poloidal and toroidal directions. The green lines represent the helicoidal structure of the magnetic field in the torus, at different poloidal positions of the magnetic surface labelled in green. The red lines display the same thing at the plasma core.

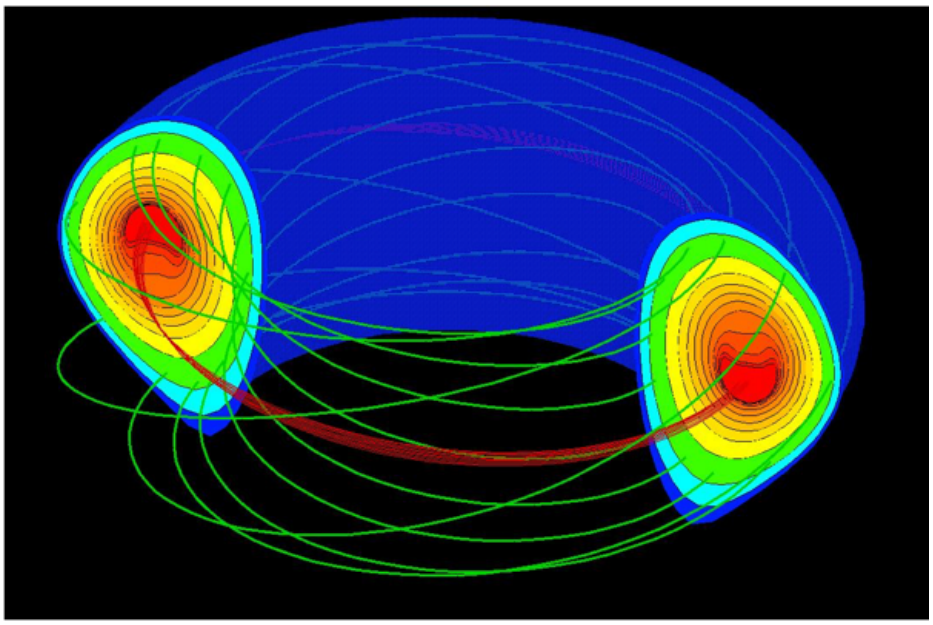

Figure 3.6: 3D representation of the $n=m=1$ internal kink mode structure

Effects of finite resistivity

Relaxing the ideal MHD approximation implies that the frozen-in law is not verified anymore, Ohm's having the additional contribution $\eta\mathbf{J}$, where η is the plasma resistivity. Resistive effects induce magnetic reconnection inside the inertial layer. The mode eigenfunction is only modified by the fact that the ideal growth rate is replaced by the resistive one. The mode eigenvalue ω^2 is modified when considering kinetic effects. Considering the normalized growth rate λ_H of ideal MHD, the kink instability dispersion relation becomes in resistive MHD [Ara et al., 1978]

$$\omega\tau_A I_R(\omega) = i\lambda_H \tag{3.93}$$

where the resistive contribution $I_R(\omega)$ is given by

$$I_R(\omega) = \frac{8\Gamma[(\Lambda^{3/2}+5)/4]}{\Lambda^{9/4}\Gamma[(\Lambda^{3/2}-1)/4]},\ \Lambda = \frac{\omega\tau_A S^{1/3}}{s(r_s)^{2/3}} \tag{3.94}$$

S is the Lundquist number defined by $S = \tau_R/\tau_A$, and τ_R is the resistive time given by $\tau_R = \mu_0 r_s^2/\eta$. The main effect of resistivity on the internal kink mode is that it is always unstable, even in toroidal geometry with $\beta_p < 13/144$. For example, at ideal MHD marginal stability $\lambda_H = 0$, it can be shown that the growth rate is $\gamma\tau_A = S^{-1/3}$. Also, when the resistive effects are included, $\omega \in \mathbb{C}$.

Two fluid effects

When two fluids are considered in the MHD momentum equation, one for thermal ions and the other for thermal electrons, it can be shown [Ara et al., 1978] that the dispersion relation, in presence of resistive effects, reads

$$\sqrt{\omega(\omega-\omega_{*i})}\frac{8\Gamma[(\Lambda^{3/2}+5)/4]}{\Lambda^{9/4}\Gamma[(\Lambda^{3/2}-1)/4]} = i\lambda_H, \Lambda = [\omega(\omega-\omega_{*i})(\omega-\omega_{*e})]^{1/3}\tau_A\frac{S^{1/3}}{s(r_s)^{2/3}} \tag{3.95}$$

This dispersion relation will serve as a basis for the fishbone linear model developed in Chapter 4.

3.4 Conclusion

In this chapter, the XTOR-K code has been presented. This code is used in this thesis to simulate the nonlinear phase of the fishbone instability. This is the matter of Chapter 6. The derivation of its fluid equations including kinetic moments has been detailed. The projection of the particle moments has been explained, as well as the self-consistent scheme used to couple MHD advance and particle advance. Methods to manage the noise brought by the PIC module have also been discussed.
Afterwards, the energy principle has been used to partially derive the mode structure and the dispersion relation of the $n = m = 1$ internal internal kink instability from the one fluid ideal MHD equations in cylindrical geometry. The derivation was performed to give some intuition on the obtained mode structure and dispersion relation. The complete derivation is performed in [Freidberg, 2014] chapter 11-5. The internal kink dispersion relation is then generalized for the two fluid resistive MHD equations including toroidal curvature. This generalization has been done by using results from [Bussac et al., 1975][Ara et al., 1978].
This complete internal kink dispersion relation constitutes the groundwork for the derivation of the fishbone linear theory performed in Chapter 4.

Chapter 4

Theoretical and numerical developments for the study of the fishbone instability

In this thesis, theoretical and numerical developments were required before studying the alpha fishbone instability with XTOR-K. The implementation of the Kinetic-MHD code XTOR-K is fairly recent. It therefore needs to be validated before performing long nonlinear simulations with XTOR-K. Two methods can be used to validate XTOR-K's implementation. A benchmarking of the code can be done, using results from other linear or nonlinear hybrid codes. A linear verification of XTOR-K can also be performed by deriving a linear Kinetic-MHD theory. Few examples of alpha fishbone simulations exist in the literature [Cheng, 1991][Fu et al., 2006][Hu et al., 2006], contrarily to other Kinetic-MHD instabilities, such as TAEs. Since the alpha fishbone is the subject of this thesis, it has been preferred to develop a linear theory for this instability. The Kinetic Energy principle is used to derive a fishbone dispersion relation, similarly as in other linear theories such as [Porcelli et al., 1994]. The linear theory developed in this thesis [Brochard et al., 2018] is presented in the first section of this chapter.

New numerical developments were also required to be implemented in the code XTOR-K. Energetic particles in a tokamak are not at thermodynamic equilibrium. They cannot be described in velocity space by a Maxwellian. It can be shown [Devaney and Stein, 1971][Stix, 1972] that their distribution function is a slowing-down distribution. Slowing-down distributions in a tokamak can either be isotropic or anistropic, depending on the nature of the energetic particles. Fast ions distributions generated by non-inductive heating techniques are anisotropic, whereas alpha particles distributions generated by fusions reactions are isotropic. Both kind of slowing down distributions have been implemented in XTOR-K. In addition to these realistic distribution functions, phase space diagnostics were also implemented in XTOR-K. Their purpose is to locate in the 3D invariants space where the wave-particle resonances $\omega - \mathbf{n} \cdot \mathbf{\Omega} = 0$ arise, and to observe the time evolution of such structures during the nonlinear phase of the fishbone instability. A diagnostic computing Kinetic Poincaré plots has also been partially implemented in XTOR-K. These numerical developments are detailed in the second section of this chapter.

4.1 Linear model for the Kinetic-MHD fishbone instability

In this section, the linear theory of the fishbone instability is derived. First, the fishbone dispersion relation is derived from the Kinetic Energy Principle. Then, the kinetic contribution λ_K in the fishbone dispersion relation is derived from the Hamiltonian formalism in angle-action coordinates presented in Chapter 2. Afterwards, the analytical/numerical computation of λ_K is discussed. Finally, the method used to solve the fishbone dispersion relation is detailed.

4.1.1 The Kinetic Energy Principle

The Energy Principle presented in Chapter 3 needs to be extended when considering an additional population of fast particles to the equilibrium. In presence of fast particles, an additional force $\mathbf{F} = -\nabla \cdot \mathbf{P}_h$ is exerted on the plasma, with $\mathbf{P}_h$ the fast particles pressure tensor. According to the kinetic energy principle, the potential energy becomes

$$\delta W = \delta W_{MHD} + \delta W_K \tag{4.1}$$

where δW_{MHD} is the same quantity as in equation (3.62)

$$\delta W_{MHD} = -\frac{1}{2}\int_V d^3\mathbf{x}\ \boldsymbol{\xi}^* \cdot \left(\mu_0 \tilde{\mathbf{J}} \times \mathbf{B} + \mu_0 \mathbf{J} \times \tilde{\mathbf{B}} - \nabla \tilde{p}_b\right) \tag{4.2}$$

and δW_k the potential energy associated to the fast particles

$$\delta W_K = \frac{1}{2}\int_V d^3\mathbf{x}\ \boldsymbol{\xi}^* \cdot \tilde{\mathbf{P}}_h \tag{4.3}$$

$p_b = p_i + p_e$ is the isotropic bulk plasma pressure, and $\mathbf{J}$ the total plasma current. The tilde symbol denotes perturbed quantities regarding the MHD equilibrium. In the present derivation, resistive and two fluid effects are taken into account. However, these effects do not modify the potential energy δW_{MHD} obtained in one fluid ideal MHD, since they do not introduce additional forces to the bulk momentum equation. An identical expression for the total potential energy is used in [Porcelli et al., 1994] equation (64).

The perturbed fast particles pressure tensor can be expressed, following [Antonsen, 1982], as

$$\tilde{\mathbf{P}}_h = \tilde{p}_{\perp,h}\mathbb{I} + (\tilde{p}_{\parallel,h} - \tilde{p}_{\perp,h})\mathbf{bb} + (p_{\parallel,h} - p_{\perp,h})(\tilde{\mathbf{b}}\mathbf{b} + \mathbf{b}\tilde{\mathbf{b}}) + \tilde{\mathbf{B}}_\parallel \frac{\partial \mathbf{P}_h}{\partial \mathbf{B}} \tag{4.4}$$

with $\mathbf{b}$ the magnetic field equilibrium direction, $\tilde{\mathbf{B}}_\parallel$ the perturbed parallel magnetic field. $\tilde{p}_{\perp,h}$ and $\tilde{p}_{\parallel,h}$ are the perturbed perpendicular and parallel scalar pressure of kinetic species, that can be expressed as

$$\tilde{p}_{\perp,h} = m_h \int d^3\mathbf{v}\ v_\parallel^2 \tilde{f}_h, \qquad \tilde{p}_{\parallel,h} = m_h \int d^3\mathbf{v}\ v_\perp^2 \tilde{f}_h \tag{4.5}$$

with $\tilde{f}_h$ the perturbed distribution function of the kinetic species, solution of the linearized Vlasov equation. In the rest of this section, only the diagonal terms of $\tilde{\mathbf{P}}$ are retained.

In equation 4.1, the contribution of fast particles does not only enter the term δW_K. Since $\mathbf{J}$ stands for the total current, it also includes the contribution of kinetic species. Therefore,

the bulk MHD term implicitly depends on the kinetic particle pressure. This dependence is brought by the modification of the MHD equilibrium due to the inclusion of kinetic particles, $p \rightarrow p_b + p_h$. Therefore, in general, the term δW_{MHD} cannot be computed without taking into account the contribution of kinetic particles.

However, when $p_h << p_{tot} = p_b + p_h$, the contribution of fast particles to δW_{MHD} can be neglected. δW_{MHD} can therefore be computed with the contribution of the bulk plasma only. The internal kink dispersion relation in equation (3.95) is modified by the inclusion of fast particles [Coppi et al., 1988],[Porcelli et al., 1994],[Zonca and Chen, 2014]. It becomes the fishbone dispersion relation

$$\mathcal{D}(\omega, n_{h,0}) = [M\omega(\omega - \omega_{*i})]^{1/2} I_R(\omega) - i\omega_A[\lambda_H + \lambda_K(\omega, n_{h,0})] = 0 \tag{4.6}$$

where I_R is the resistive contribution in equation 5.11, and $n_{h,0}$ is the on-axis density of fast particles. M is the inertial enhancement factor. An expression for this term can be found in [Merle, 2012], equation (5.35). In this linear model, it is assumed that the plasma is compressible, which implies [Merle, 2012] that $M = 3$. The relation between δW and λ is given in equation (3.90).

The fishbone dispersion relation is used to compute the complex frequency $\omega = \omega_r + i\gamma$ for a given Kinetic-MHD equilibrium. Since it is considered that $p_h << p_{tot}$, the MHD equilibrium used to compute λ_H and λ_K does not take into account fast particles. The CHEASE code is used to generate this MHD equilibrium. The one fluid ideal growth rate λ_H is computed with XTOR-K, by excluding fast particles, resistive effects, bi-fluid effects. It is then equivalent to the growth rate described in equation (3.92) [Bussac et al., 1975]. The equilibrium computed by CHEASE is chosen to have circular magnetic flux surfaces. It enables to simplify the the analytical derivation of λ_K. This derivation is now presented.

4.1.2 Linear solution of Vlasov equation $\tilde{f}_h$

In order to obtain an analytical expression for λ_K, it is needed to obtain an expression for the perturbed distribution function $\tilde{f}_h$ in equation (4.5). Let F_h be the distribution function of fast particles such as $F_h = F_{eq,h} + \tilde{f}_h$, $F_{eq,h}$ being the equilibrium distribution function. Vlasov equation can be written as, assuming no collisions between particles and the bulk plasma

$$d_t F = \partial_t F - \{H, F\} = 0 \tag{4.7}$$

where H is the Hamiltonian of fast particles. The Poisson's brackets $\{\cdot, \cdot\}$ are defined in the angle/action formalism presented in Chapter 2 as

$$\{A, B\} = \frac{\partial A}{\partial \boldsymbol{\alpha}} \cdot \frac{\partial B}{\partial \mathbf{J}} - \frac{\partial B}{\partial \boldsymbol{\alpha}} \cdot \frac{\partial A}{\partial \mathbf{J}} \tag{4.8}$$

Linearizing (4.7)

$$\partial_t \tilde{f}_h - \{\tilde{h}, F_{eq,h}\} - \{H_{eq}, \tilde{f}_h\} = 0 \tag{4.9}$$

Since $F_{eq,h}$ and H_{eq} are equilibrium quantities, they only depend on the actions $\mathbf{J}$. Using (4.8) in (4.9)

$$\partial_t \tilde{f}_h - \frac{\partial \tilde{h}}{\partial \boldsymbol{\alpha}} \cdot \frac{\partial F_{eq}}{\partial \mathbf{J}} + \frac{\partial \tilde{f}_h}{\partial \boldsymbol{\alpha}} \cdot \frac{\partial H_{eq}}{\partial \mathbf{J}} = 0 \tag{4.10}$$

A Fourier expansion of a perturbed quantity $\tilde{g}$ can be done using angle-action variables

$$\tilde{g}(\boldsymbol{\alpha}, \mathbf{J}, t) = \sum_{\mathbf{n}} g_{\mathbf{n}\omega}(\mathbf{J})\ e^{i(\mathbf{n}\cdot\boldsymbol{\alpha} - \omega t)} \tag{4.11}$$

where $\mathbf{n} = (n_1, n_2, n_3)$ is the wave-vector in the angle/action formalism. Applying this Fourier expansion to (4.10), the resonant solution of Vlasov equation in Fourier space is

$$\tilde{f}_{\mathbf{n}\omega} = -\frac{\mathbf{n} \cdot \partial F_{eq,h}/\partial \mathbf{J}}{\omega - \mathbf{n} \cdot \mathbf{\Omega}} \tilde{h}_{\mathbf{n}\omega} \tag{4.12}$$

Considering that $F_{eq,h}$ is solely a function of the invariants ($H_{eq} = E, \mu, P_\varphi$), its derivative with respect to $\mathbf{J}$ expands as

$$\mathbf{n} \cdot \frac{\partial F_{eq,h}}{\partial \mathbf{J}} = \mathbf{n} \cdot \left[\frac{\partial H_{eq}}{\partial \mathbf{J}} \frac{\partial F_{eq}}{\partial H_{eq}} + \frac{\partial \mu}{\partial \mathbf{J}} \frac{\partial F_{eq}}{\partial \mu} + \frac{\partial P_\varphi}{\partial \mathbf{J}} \frac{\partial F_{eq}}{\partial P_\varphi} \right] = \frac{\partial F_{eq,h}}{\partial H_{eq}} \left[(\mathbf{n} \cdot \mathbf{\Omega} - \omega) + \omega - \omega_+ - \omega_* \right] \tag{4.13}$$

where ω is artificially introduced to later dissociate $\tilde{f}$ into a resonant and a fluid part. ω_+ and ω_* are defined as

$$\omega_+ = n_1 \frac{q_s}{m_s} \frac{\partial F_{eq,h}/\partial \mu}{\partial F_{eq,h}/\partial H_{eq}}, \qquad \omega_* = -n_3 \frac{\partial F_{eq,h}/\partial P_\varphi}{\partial F_{eq,h}/\partial H_{eq}} \tag{4.14}$$

with q_s the particle's charge and m_s the particle's mass. It is assumed in this model that the perpendicular potential vector is negligible, considering $A_\perp \ll A_\parallel$. The perturbed Hamiltonian reads, using equation (2.18)

$$\tilde{h} = q_s(\phi - v_\parallel A_\parallel) \tag{4.15}$$

with ϕ the electric potential. The ideal MHD assumption implies $E_\parallel = 0$. Resistive effects are taken into account in the term $I_R(\omega)$ of equation (4.6). Introducing the time integral of the electrical potential $\chi(\mathbf{x}, t) = \int_0^t \phi(\mathbf{x}, t')dt'$, it leads to

$$E_\parallel = -\nabla_\parallel \phi - \partial_t A_\parallel = 0 \Leftrightarrow A_\parallel = -\nabla_\parallel \chi \tag{4.16}$$

The perturbed Hamiltonian can then be expressed as

$$\tilde{h} = q_s[\partial_t \chi + v_\parallel \nabla_\parallel \chi] = q_s[d_t \chi - (\mathbf{v}_d \cdot \boldsymbol{\nabla})\chi] \tag{4.17}$$

where $d_t\chi = (\partial_t + \mathbf{v} \cdot \boldsymbol{\nabla})\chi, \mathbf{v} = v_\parallel \mathbf{b} + \mathbf{v}_d$, v_d being the drift velocity of fast particles. $d_t\chi$ can be expressed, using the angle-action Hamiltonian approach, as

$$d_t \chi = \partial_t \chi - \{H_{eq}, \chi\} = \partial_t \chi + \mathbf{\Omega} \cdot \frac{\partial \chi}{\partial \boldsymbol{\alpha}} \tag{4.18}$$

Therefore, inserting (4.18) into (4.17) and Fourier expanding $\tilde{h}$

$$\tilde{h}_{\mathbf{n}\omega} = i(\mathbf{n} \cdot \mathbf{\Omega} - \omega) q_s \chi_{\mathbf{n}\omega} - [q_s(\mathbf{v}_d \cdot \boldsymbol{\nabla})\chi]_{\mathbf{n}\omega} \tag{4.19}$$

Then, inserting (4.19),(4.13) into (4.12), one obtains $\tilde{f}_{\mathbf{n}\omega} = \tilde{f}^{res}_{\mathbf{n}\omega} + \tilde{f}^{fl}_{\mathbf{n}\omega}$, with

$$\tilde{f}^{res}_{\mathbf{n}\omega} = \frac{\partial F_{eq}}{\partial H_{eq}} \frac{\omega - \omega_+ - \omega_*}{\omega - \mathbf{n} \cdot \mathbf{\Omega}} [q_s(\mathbf{v}_d \cdot \boldsymbol{\nabla})\chi]_{\mathbf{n}\omega}, \quad \tilde{f}^{fl}_{\mathbf{n}\omega} = \frac{\partial F_{eq}}{\partial H_{eq}} \left[i(\mathbf{n} \cdot \mathbf{\Omega} - \omega_+ - \omega_*) q_s \chi_{\mathbf{n}\omega} - [q_s(\mathbf{v}_d \cdot \boldsymbol{\nabla})\chi]_{\mathbf{n}\omega} \right] \tag{4.20}$$

It is reminded from Chapter 2 that $\Omega_1 = \omega_{c,s}$. The fast particles gyrofrequency is several orders of magnitude larger that their bounce/transit and precessional frequency, as well as the mode pulsation $Re[\omega]$. Therefore, the Kinetic-MHD mode cannot resonate with Ω_1, n_1 is set to zero. It implies that $\omega_+ = 0$.

A $n = m = 1$ mode is of interest in this derivation, in order to describe the fishbone

instability. Perturbed quantities such as the electrostatic potential can be expressed as $\phi(\mathbf{r}) = \phi(r)e^{-i(\theta-\varphi)}$. Performing a Fourier expansion

$$\phi_{\mathbf{n}} = \frac{1}{(2\pi)^2}\int d\alpha_2 d\alpha_3 \ \phi(r)e^{-i(\theta-\varphi+n_3\alpha_3+n_2\alpha_2)} \tag{4.21}$$

It is assumed in this derivation that the position vector $\mathbf{r}$ corresponds to the particles' guiding center. The subscript G designing the guiding center is dropped from simplicity. It is also assumed that particles have thin orbit widths around their reference magnetic surface $\bar{\psi}$. In Chapter 5, it is shown that for alpha particles, the thin orbit width approximation is valid up to $E = 1$ MeV. In this derivation, the reference flux surface $\bar{\psi} = \langle\psi\rangle$ is the time averaged flux surface of the particle.

Using equations (2.38)(2.50), the toroidal and poloidal angles can be expressed as $\varphi = \alpha_3 - \epsilon_b q(\bar{\psi})\hat{\theta} - \hat{\alpha}$, $\theta = \hat{\theta} + \epsilon_b\alpha_2$. It is reminded that $\hat{\theta}$ and $\hat{\alpha}$ are periodic functions of α_2. $\epsilon_b = 1$ for passing particles and 0 for trapped particles. Replacing these expressions for φ and θ in equation (4.21), the only non vanishing component of $\phi_{\mathbf{n}}$ along the integration over α_3 is $n_3 = n = 1$. Therefore, the general resonance condition reads

$$\omega - \sum_{n_2}\sigma_c\Big[n_2 + \epsilon_b q(\bar{\psi})\Big]\omega_b - \omega_d = 0 \tag{4.22}$$

It is reminded that $\sigma_c = \pm 1$ for co/counter passing particles. Since the frequencies ω_b, ω_d depend on the three invariants of motion (E, P_φ, μ), the solutions of this resonance condition are surfaces in phase space. On Figure (4.1) the resonant planes have been displayed, considering every harmonic n_2. The analytical expressions for ω_b, ω_d are obtained assuming circular flux surfaces (A.18), (A.7), (B.11), (B.14). These planes have been computed for alpha particles on a ITER-like MHD equilibrium, at a fixed $\bar{\psi}$ position. Only three surfaces, one for trapped particles with $n_2 = 0$ and two for passing ones with $n_2 = -1$ (co-passing and counter-passing), contribute to the resonant term. All the other n_2 harmonics are therefore neglected, the general resonance condition for the $n = m = 1$ internal kink can then be restricted to

$$\omega + \sigma_c\epsilon_b[1 - q(\bar{\psi})]\omega_b - \omega_d = 0 \tag{4.23}$$

Regarding the fluid term in equation (4.20), it is not necessary to use the angle/action formalism to describe it. This formalism is better adapted to the study of resonant terms. It is therefore more convenient to come back to real space. Noticing that in Fourier space $\mathbf{v}\cdot\nabla = i\mathbf{n}\cdot\mathbf{\Omega}$ and that $\{\chi, P_\varphi\} = i\chi_{\mathbf{n},\omega}$

$$\tilde{f}^{fl} = q_s\frac{\partial F_{eq}}{\partial H_{eq}}\left[v_\parallel\nabla_\parallel\chi - \omega_*\{\chi, P_\varphi\}\right] \tag{4.24}$$

The first term of this expression is directly linked to the kinetic tearing term in [Edery et al., 1992]. As a current term, it needs to be incorporated in δW_{MHD}.

In order to derive explicitly $\tilde{f}$, an expression of χ as a function of $\boldsymbol{\xi}$, the MHD displacement, is needed. In this derivation, $\boldsymbol{\xi}$ is taken at the lowest order in $\epsilon = \bar{r}/R$. $\bar{r}$ is the radial position associated to $\bar{\psi}$. For $n = m = 1$, as discussed in Chapter 3 equation(3.73), $\boldsymbol{\xi} = \xi_0\sigma_H(r_{q=1} - \bar{r})e^{-i(\theta-\varphi+\omega t)}\mathbf{e}_r$. Following the drift ordering in MHD assumption, at lowest order in ρ^*

$$\mathbf{v}_\perp = \mathbf{v}_{E\times B} \Leftrightarrow -i\omega\xi_0 B_0 e^{-i(\theta-\varphi+\omega t)} = i\omega\partial_\theta\chi/\bar{r} \Leftrightarrow \chi = -i\xi_0 B_0\bar{r}e^{-i(\theta-\varphi+\omega t)} \tag{4.25}$$

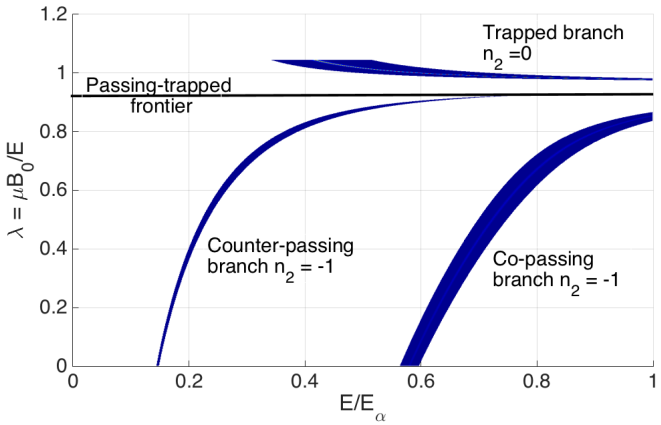

Figure 4.1: Curves of resonance between fast particles and the internal kink in the energy - pitch angle diagram at a fixed $\bar{\psi}$ position. Three branches of resonance are available, one for trapped particle resonating with the precessional frequency, and two for passing particles resonating with combinations between transit and precessional frequencies, considering co and counter passing particles.

It is possible to obtain explicit expressions for both the resonant and fluid perturbed distribution using the definition of the drift velocity

$$\mathbf{v}_d = \frac{2E}{m_s\omega_{c_s}B}\mathbf{B}\times\left[\left(1-\frac{\lambda}{H^*}\right)\boldsymbol{\kappa}+\frac{\lambda}{2H^*}\nabla\ln B\right] \tag{4.26}$$

where $\lambda = \mu_0 B_0/H_{eq}$ stands for the generalized pitch angle, and B_0 the magnetic field at $\bar{r}=0$, $H^* \equiv B_0/B(\bar{r},\theta) = R/R_0 = 1+\bar{r}/R_0\cos\theta$, ω_c the particle's gyrofrequency and $\boldsymbol{\kappa} = (\mathbf{b}\cdot\nabla)\mathbf{b}$ the magnetic curvature.

It is reminded here that a MHD equilibrium with circular flux surfaces is used in this derivation. The flux surfaces used are also concentric, which is an approximation. This is not the case in the MHD equilibrium computed by CHEASE. Therefore, at first approximation, the quantities R_0 and B_0 used in λ_K are defined at the magnetic axis computed by CHEASE. At low β, (4.26) reduces to

$$\mathbf{v}_d = \frac{E\sigma}{m_s\omega_{c,s}BH^*}\mathbf{B}\times\nabla\ln B \tag{4.27}$$

with $B = B_0R_0/R$, $\sigma = 2-\lambda/H^*$ and $\mathbf{B} = (B_0/H^*)(\mathbf{e}_\phi + (\bar{r}/Rq)\mathbf{e}_\theta)$. Therefore

$$\nabla\ln B = \left[\frac{\sin\theta}{R_0}\mathbf{e}_\theta - \frac{\cos\theta}{R_0}\mathbf{e}_r\right] \tag{4.28}$$

Then

$$\mathbf{v}_d\cdot\boldsymbol{\nabla} = -\frac{\sigma E}{q_sB_0R_0}\left(\sin\theta\partial_r + \frac{\cos\theta}{\bar{r}}\partial_\theta\right) \tag{4.29}$$

For the resonant term, inserting (4.25) in (4.20)

$$(\mathbf{v}_d\cdot\boldsymbol{\nabla})\chi = \frac{\sigma E\xi_0}{q_sR_0}e^{i(\alpha_3+q\hat{\theta}-\omega t)} \tag{4.30}$$

The Fourier coefficient being given by the inverse Fourier transformation

$$g_{\mathbf{n}\omega} = \int\frac{d\alpha_1}{2\pi}\frac{d\alpha_2}{2\pi}\frac{d\alpha_3}{2\pi}e^{-i\mathbf{n}\cdot\boldsymbol{\alpha}}g \tag{4.31}$$

two cases need to be considered in computing the resonant term. First, for trapped particles, only the triplet $\mathbf{n}_t = (0, 0, 1)$ contributes, therefore

$$[q_s(\mathbf{v}_d \cdot \boldsymbol{\nabla})\chi]_{\mathbf{n}_t\omega} = \frac{E\xi_0}{R_0}\int \frac{d\alpha_2}{2\pi}\sigma e^{iq\theta} = \frac{E\xi_0}{R_0}\sigma I_q \tag{4.32}$$

where $I_q =< \cos\theta >_{\alpha_2} +(1-q) < \theta \sin\theta >_{\alpha_2}$, whose derivation is given in annex A. For passing particles, only the triplet $\mathbf{n}_p = (0, -1, 1)$ contributes, therefore

$$[q_s(\mathbf{v}_d \cdot \boldsymbol{\nabla})\chi]_{\mathbf{n}_p\omega} = \frac{E\xi_0}{R_0}\int \frac{d\alpha_2}{2\pi}\sigma e^{iq\theta+(1-q)\alpha_2} = \frac{E\xi_0}{R_0}\sigma I_{q,p} \tag{4.33}$$

Given the α_2 dependence in $I_{q,p}$, the obtention of an analytical expression for this term is quite difficult. However, performing a series expansion of $\exp[(1-q)\alpha_2]$, where $1-q$ is considered as a small parameter given that the studied MHD instability is the internal kink, trapped and passing contributions are identical at lowest order. Therefore the analytical expression for I_q is used for both trapped and passing particles. The resonant perturbed distribution function then reads

$$\tilde{f}^{res}_{\mathbf{n}\omega} = E\frac{\partial F_{eq}}{\partial H_{eq}}\frac{\omega-\omega^*}{\omega+\delta_p\sigma_\parallel(1-q)\omega_b-\omega_d}\frac{\xi_0}{R_0}I_q(\bar{r},\lambda) \tag{4.34}$$

Regarding the fluid term, using the expression of Poisson's brackets in regular toroidal coordinates [Brizard and Hahm, 2007], one finds

$$\{\chi, P_\varphi\} = -\frac{\mathbf{b}}{eB_0}\cdot\nabla\chi\times\nabla P_\varphi = \frac{\bar{r}}{q}\hat{r}\cdot(\mathbf{b}\times\nabla\chi) \tag{4.35}$$

The fluid contribution, or interchange contribution by comparison with [Edery et al., 1992], yields

$$\tilde{f}^{int} = -\xi_0\frac{\partial F_{eq}}{\partial\bar{r}}e^{i(\varphi-\theta)} \tag{4.36}$$

This term is identical to the adiabatic term from [Coppi et al., 1990], as well as to the more general expression in eq. (71) of [Porcelli et al., 1994] in the limit of thin particles' orbits.

An explicit expression for the precessional frequency ω_d is needed in (4.34). It can be found in annex B for a reference magnetic surface defined by $\bar{\psi} = \langle\psi\rangle = m(Rv_\parallel - \langle Rv_\parallel\rangle_{\alpha_2})/Ze$.

It should be noted that such a choice for $\bar{\psi}$ does not allow all the physics related to the inertial layer to be retained, since the MHD displacement $\boldsymbol{\xi}$ is naturally a function of ψ, not $\bar{\psi}$. Therefore, using a step function for $\boldsymbol{\xi}$, inertial enhancement and global stability effects recovered in [Graves, 2013], where ψ was chosen as radial variable, are not included in this model. However, for fast particles at low energies ($\sim$ 100keV-1Mev), orbit widths are relatively small (see Chapter 5), which means that considering $\boldsymbol{\xi}(r) = \boldsymbol{\xi}(\bar{r})$ should not impact significantly the solution of the fishbone dispersion relation.

4.1.3 Derivation of the kinetic contribution λ_K

Now that the perturbed fast particle distribution function has been derived, the derivation of δW_K is performed. Considering the momentum equation of fast particles, discarding their inertia on the basis of their dilution in the whole plasma, $\tilde{\mathbf{J}}_h \times \mathbf{B} = \nabla\cdot\tilde{\mathbf{P}}_h$. Since $\boldsymbol{\xi} = (\mathbf{b}/B)\times\nabla\boldsymbol{\chi}$, δW_K can be written as

$$\delta W_K = -\frac{1}{2}\int d^3\mathbf{x}\ \tilde{\mathbf{J}}_{\perp h}\cdot\nabla\boldsymbol{\chi}^*, \qquad \mathbf{J}_{\perp h} \equiv \int d^3\mathbf{v}\tilde{f}_h q_s\mathbf{v}_d \tag{4.37}$$

It is noted here that the parallel component of the fast particles current has also to be taken into account. This term is incorporated into the functional δW_{MHD} so that the current considered in δW_{MHD} stands for the total current. This parallel current is negligible regarding the total current since $p_h << p_{tot}$. Using equation (3.90) the kinetic contribution λ_K in equation (4.6) can be written as

$$\lambda_K = \frac{1}{\xi_0^2 s_0 R_0 B_p^2} \int d^3\mathbf{x} d^3\mathbf{v} \tilde{f}_h [e(\mathbf{v}_d \cdot \nabla)\boldsymbol{\chi}^*] \tag{4.38}$$

Therefore, using this expression, the resonant perturbation in Fourier space equation (4.34) and applying Parseval's theorem to (4.20)

$$\lambda_K^{res} = \frac{1}{s_0 R_0 B_p^2} \int d^3\mathbf{x} d^3\mathbf{v} \frac{\partial F_{eq}}{\partial E} \frac{\omega - \omega_*}{\omega + \epsilon_b \sigma_c (1-q)\omega_b - \omega_d} \frac{\sigma^2 E^2}{R_0^2} I_q^2 \tag{4.39}$$

In order to compute λ_K^{res}, it is useful to express its resonant denominator as a polynomial of $v = \sqrt{2E/m_s}$. Explicit expressions for ω_b and ω_d can be found in (A.7), (A.18), (B.14), (B.11). In the rest of the derivation, the notations I_b and I_d are used instead of $I_{b,p/t}$ and $I_{d,p/t}$ to simplify the notations. Therefore, expliciting ω_*

$$\lambda_K^{res} = \frac{1}{s_0 R_0 B_p^2} \int d^3\mathbf{x} d^3\mathbf{v} \frac{\sigma^2 E^2 I_q^2}{\lambda R_0^2 I_d} \left(\frac{\partial F_{eq}}{\partial \bar{r}} \frac{R_0}{E_b} - \frac{\partial F_{eq}}{\partial E} \frac{x\hat{\omega}}{q} \right) \frac{1}{\hat{v}^2 + v_1 \hat{v} + v_2} \tag{4.40}$$

with $\hat{v} = v/v_b$, $\hat{\omega} = \omega/\bar{\omega}_d$ $r_0 = \bar{r}_{q=1}$, $x = \bar{r}/r_0$ and

$$\bar{\omega}_d = \omega_d(\bar{r} = r_0, \lambda = (1-\epsilon)^{-1}, E = E_b) = \frac{E_b}{q_s B_0 r_0 R_0} \tag{4.41}$$

This quantity is the precessional frequency of deeply trapped particles at energy E_b located on the resonant surface $r_{q=1}$. The coefficients of the polynomial are

$$v_1(\bar{r}, \lambda) = 2\epsilon_b \sigma_c [1 - q(\bar{r})] \frac{q_s B_0 r_0 x}{q^2(\bar{r}) \lambda m_s v_b I_b(r, \lambda)} \tag{4.42}$$

$$v_2(\bar{r}, \lambda, \omega) = -\frac{\hat{\omega} x}{q(\bar{r}) \lambda I_d(r, \lambda)} \tag{4.43}$$

v_b and E_b correspond to the birth velocity and energy of the fast particles, considering that F_{eq} is a slowing-down function. The fluid contribution to λ_K can be developed as

$$\lambda_K^{int} = -\frac{1}{s_0 R_0 B_p^2} \int d^3\mathbf{x} d^3\mathbf{v} \frac{\partial F_{eq}}{\partial \bar{r}} \frac{\sigma E}{R_0} e^{-i\theta} \tag{4.44}$$

In this derivation, it is chosen to describe the 6D phase space with the coordinates $(\bar{r}, \theta, \varphi, E, \lambda, \Phi)$, Φ being the gyro-angle. The Jacobian $\mathcal{J}_{6D}$ of this change of variables is therefore needed. In toroidal geometry, assuming large aspect ratio

$$\int d^3\mathbf{x} = 2\pi R_0 \int_0^a \bar{r} d\bar{r} \int_0^{2\pi} d\theta \tag{4.45}$$

Now, using $(v_\parallel, v_\perp, \Phi)$ coordinates

$$\int d^3 v = \int 2\pi v_\perp dv_\parallel dv_\perp = 2\pi \int \sum_{\sigma_c} E^{1/2} \left(\frac{2}{m} \right)^{1/2} \left(\frac{\lambda}{H^*} \right)^{1/2} \mathcal{J}_{2D} dE d\lambda \tag{4.46}$$

$\mathcal{J}_{2D}$ is the Jacobian of the change of variable $(v_\parallel, v_\perp) \to (E, \lambda)$. Since $v_\parallel = \sigma_c(2E/m_s)^{1/2}(1-\lambda/H^*)^{1/2}$, $v_\perp = (2\lambda E/m_s H^*)^{1/2}$

$$\frac{\partial v_\parallel}{\partial E} = \sigma_\parallel (2Em)^{-1/2}(1-\lambda/H^*)^{1/2}, \qquad \frac{\partial v_\parallel}{\partial \lambda} = -\sigma_\parallel (2Em)^{1/2}\Big[(2H^*)^{-1}(1-\lambda/H^*)^{-1/2}\Big] \quad (4.47)$$

$$\frac{\partial v_\perp}{\partial E} = (\lambda/2m_s E H^*)^{1/2}, \quad \frac{\partial v_\perp}{\partial \lambda} = (E/2m_s \lambda H^*)^{1/2} \quad (4.48)$$

yielding

$$\mathcal{J}_2 D = \frac{1}{2m_s}\frac{1}{(\lambda H^*)^{1/2}(1-\lambda/H^*)^{1/2}} \quad (4.49)$$

Therefore, using the following identity,

$$\int_{-\pi}^{\pi} d\theta \int_0^H d\lambda = \int_0^{(1-\epsilon)^{-1}} d\lambda \int_{-\theta_0}^{\theta_0} d\theta \quad (4.50)$$

The Jacobian $\mathcal{J}_{6D}$ is obtained as

$$\int d^3\mathbf{x} d^3\mathbf{v} = \int_0^{r_0} d\bar{r} \int_0^{(1-\epsilon)^{-1}} d\lambda \int_0^{\infty} dE \mathcal{J}_{6D}(\bar{r}, \lambda, E) \quad (4.51)$$

$$\mathcal{J}_{6D} = \sum_{\sigma_\parallel = \pm 1} \pi^2 R_0 \left(\frac{2}{m_s}\right)^{3/2} \bar{r} \int_{-\theta_0}^{\theta_0} \left(1 - \frac{\lambda}{H^*}\right)^{-1/2} d\theta E^{1/2} \quad (4.52)$$

where the sum over the parallel velocity is two for trapped particles. Regarding the different terms of λ_K, considering only even terms in θ and the bounce-averaging formalism developed in annex A, one gets

$$\lambda_K^{res} = \frac{2\pi^3 \epsilon_0}{s_0 r_0 B_{p,0}^2}\left(\frac{2}{m}\right)^{3/2} \sum_{\sigma_c = \pm 1} \int_0^{r_0} \bar{r} d\bar{r} \int_0^{(1-\epsilon)^{-1}} d\lambda \frac{\sigma^2 I_b I_q^2}{\lambda I_d} \int_0^{\infty} E^{5/2} \frac{\partial_{\bar{r}} F_{eq}/E_b - \bar{r}\hat{\omega}\partial_E F_{eq}/q r_0 R_0}{\hat{v}^2 + v_1 \hat{v} + v_2} dE \quad (4.53)$$

$$\lambda_K^{int} = -\frac{4\pi^3 \epsilon_0}{s_0 r_0 B_{p,0}^2}\left(\frac{2}{m}\right)^{3/2} \int_0^{r_0} \bar{r} d\bar{r} \int_0^{(1-\epsilon)^{-1}} d\lambda \sigma I_b I_c \int_0^{\infty} E^{3/2} \frac{\partial F_{eq}}{\partial \bar{r}} dE \quad (4.54)$$

where $I_c =< \cos\theta >_{\alpha_2}$, $I_b =< 1 >_{\alpha_2}$. It can be shown that these two expressions are similar to δW_1 and δW_2 in [Porcelli et al., 1994] equations (71-72). However, a difference arises when considering deeply passing particles in the integrand of (4.53). The term σ^2/λ is used instead of λ. This difference appears more clearly in equation (11) of [Porcelli, 1991].

4.1.4 Computation of the kinetic term λ_K

The terms in (4.53-4.54) need to be computed for a given MHD equilibrium and a mode frequency $\omega = \omega_r + i\gamma$. The different integrals in these terms are not independent, they need to be computed in chain. The energy integral contains the wave-particle resonance $\omega - \mathbf{n}\cdot\mathbf{\Omega}$. This integrand tends to diverge for finite MHD growth rates when particles are located near the resonant planes. Therefore, its computation cannot be simply handled by a trapezoidal method. It would miss the imaginary contribution due to the poles of this integral. It would also introduce important error on the real part of this integral. For both these reasons, this integral needs to be solved by taking into account its poles carefully.

Integration contour $\mathcal{C}$ of the energy integral

For simplicity, the integrand's numerator of the energy integral is noted $f(\bar{r}, \lambda, E)$. The energy integral can then be expressed as

$$I_{res} = \int dE \frac{f(\bar{r}, \lambda, E)}{\hat{v}^2 + v_1(\bar{r}, \lambda)\hat{v} + v_2(\bar{r}, \lambda, \omega)} = \int d\hat{v} \frac{2}{m_s v_b^2} \frac{\hat{v} f(\bar{r}, \lambda, E)}{(\hat{v} - v_+)(\hat{v} - v_-)} \tag{4.55}$$

$$v_\pm(\bar{r}, \lambda, \omega) = -\left[v_1 \pm \sqrt{v_1^2 - 4v_2}\right]/2 \tag{4.56}$$

To compute the complex integral I_{res}, an integration contour $\mathcal{C}$ needs to be defined. This contour must not encounter the poles for a given ω, otherwise $\lambda_K(\omega)$ cannot be computed accurately. Moreover, the fishbone dispersion relation (4.6) is an implicit function of ω. In order to find the solution of (4.6), λ_K needs to evaluated for different test complex frequencies ω_{test}. Therefore, the contour $\mathcal{C}$ needs also to be defined so that it still does not encounter a pole when ω is evolved arbitrarily.

It can be shown from equation (4.56) and (4.43) that the poles are always complex when $\gamma \neq 0$, and that their imaginary parts have opposite signs. The sign of the imaginary part of the poles is also reversed when γ changes sign, since $v_2 \propto \omega$.

Considering these properties for the poles, the integration contour $\mathcal{C}$ is chosen to be the real axis when $\gamma > 0$. When γ changes sign, the poles cross the real axis. In order to avoid singularites, the contour $\mathcal{C}$ is deformed as shown on Figure (4.2) Vertical parts of the contour on both sides of the poles cancel each other. The half circles of the contour add/substract an extra $i\pi$ to the imaginary pole contributions. An identical contour is used in [Merle, 2012].

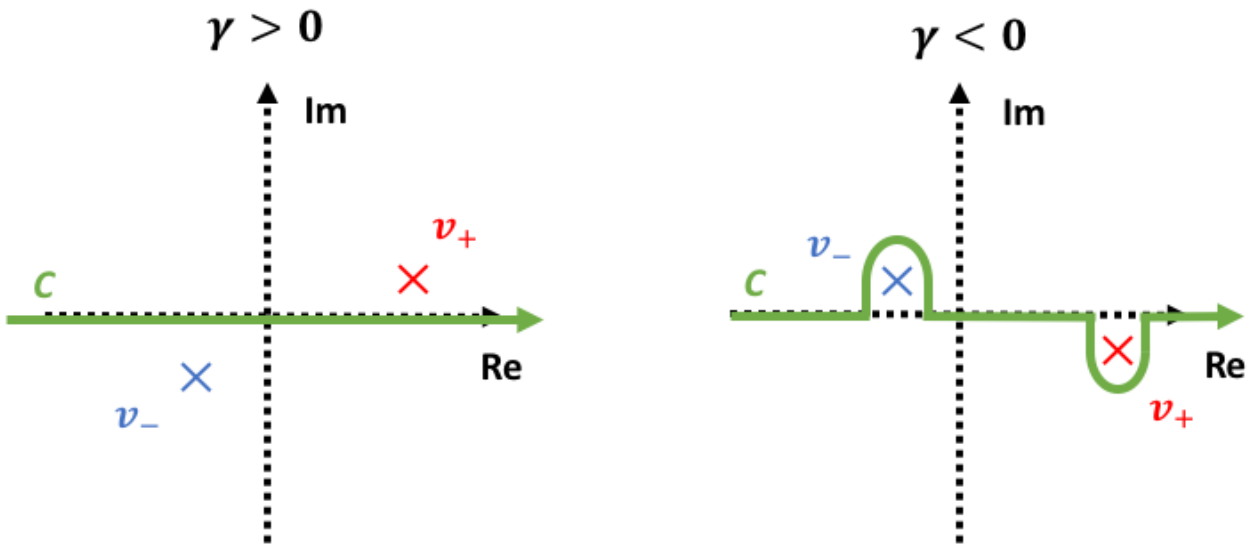

Figure 4.2: Integration contour of the resonant integral in the complex plane, the red cross standing for v_+ and the blue one for v_-. When $\gamma > 0$, the contour is simply taken to be the real axis, as displayed on the left figure. When γ changes sign, the poles cross the contour, it then needs to be deformed as shown on the right figure.

Computation of the energy integral for a slowing-down distribution

In the fishbone linear model, the distribution function of interest is the isotropic slowing-down function. Its expression is [Stix, 1972][Devaney and Stein, 1971]

$$F_{eq,SD}(\bar{r},v) = \frac{n_h(\bar{r})}{v_b^3 C}\frac{\sigma_H(v_b - v)}{\hat{v}^3 + (v_c/v_b)^3} \tag{4.57}$$

with $\hat{v} = v/v_b$ and where the normalization factor C is

$$C = \frac{4\pi}{3}\ln\left[1 + \left(\frac{v_b}{v_c(\bar{r})}\right)\right] \tag{4.58}$$

$n_h(r)$ is the density profile of fast particles, denoted at $r = 0$ as $n_{h,0}$. v_c is the critical speed of fast particles at which they give as much energy to the bulk ions as to the bulk electrons via Coulombian collisions. This velocity can be expressed as

$$v_c(\bar{r}) = \left(\frac{3\sqrt{\pi}m_e}{4m_s}\right)^{1/3}\sqrt{\frac{2k_B T_e(\bar{r})}{m_e}} \tag{4.59}$$

with m_e the electron mass and T_e the electron temperature profile. Inserting this equilibrium function in the energy integral

$$I_{res} \propto \int_0^1 d\hat{v}\frac{\hat{v}^n}{(\hat{v}^3 + (v_c/v_b)^3)(\hat{v} - v_+)(\hat{v} - v_-)} \tag{4.60}$$

Only the terms depending on v in the integrand of the energy integral have been displayed

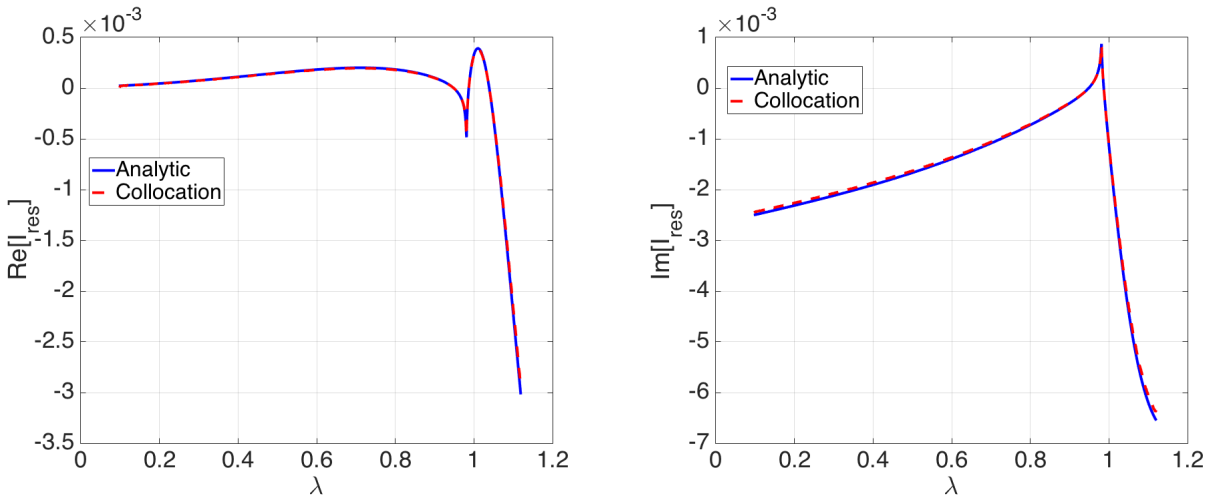

(a) (b)

Figure 4.3: Comparison of the analytical and numerical computation of the resonant velocity integral, for both real (a) and imaginary (b) contributions. These curves are obtained by varying the pitch angle onto its entire domain of definition, at fixed $\bar{r} = 0.3\bar{r}_{q=1}$

on (4.60). n=6 for the term proportional to $\partial_{\bar{r}}F_{eq}$ and $n = 4$ for the term proportional to $\partial_E F_{eq}$ in (4.53). When an ordering can be formed such as $(v_c/v_b)^3 \gg \hat{v}^3$ or $(v_c/v_b)^3 \ll \hat{v}^3$ for most $\hat{v}$ relevant to the slowing-down distribution function, a direct analytical calculation of I_{res} is performed. This is done by neglecting either $\hat{v}^3$ or $(v_c/v_b)^3$ in $\hat{v}^3 + (v_c/v_b)^3$ in (4.60). Explicit expressions can be found in annex C.1 in both cases. However, a numerical integration needs to be performed when an ordering does not exist. In this case, the numerical

method used is the collocation method. It takes into account properly the poles and retrieves correct expressions for both the real and imaginary contribution. The collocation method is detailed in annex C.2.

The collocation method has been tested on a Kinetic-MHD equilibrium where the ordering $(v_c/v_b)^3 << \hat{v}$ is achieved. The particles considered are alphas with birth energy $E_b = 3.5$ MeV, and the on-axis electron temperature is $T_{e,0} = 10$ keV. Therefore, $(v_c/v_b)^3 = 8.10^{-3}$. The complex MHD frequency considered is $\omega\tau_A = (2 + 0.5i)10^{-2}$. Figure 4.3 shows that the analytical and numerical methods agree rather well, ensuring the good implementation of both of them.

Computation of the radial and pitch angle integrals

The radial and pitch angle integrals can be computed using a simple trapezoidal method. For a fixed $\bar{r}$, the pitch angle integral is computed by calculating $I_{res}(\bar{r}, \lambda)$, and then the same is done at all $\bar{r}$.

An artificial singularity requires special care in the pitch angle integral. When the resonance condition is normalized to express it as an unitary second order polynome, it adds a factor $1/I_d(\bar{r}, \lambda)$ to the integrand of the pitch angle integral. I_d vanishes when the precessional drift of fast particles is reversed. Given the complex expression of I_d in (B.11-B.14), finding the couples $(\bar{r}, \lambda)$ solution of $I_d(\bar{r}, \lambda) = 0$ is not a direct operation. These couples are then found using a dichotomy method. Then, the pitch angle grid is designed such that the singularities lie at equal distance of two grid points, minimizing the error.

4.1.5 Non-perturbative resolution of the fishbone dispersion relation

The fishbone dispersion relation (4.6) is an implicit function of the mode frequency ω, since the kinetic contribution λ_K depends on ω. Finding ω solution of $\mathcal{D}(\omega, n_{h,0})$ at a given $n_{h,0}$ requires a specific numerical method. Some linear codes adopt a perturbative method to solve this equation [Nabais et al., 2015]. However, such a method is only valid when the MHD frequency of the internal kink is weakly affected by the inclusion of the fast particles. In the case of the fishbone instability, the mode complex frequency evolves significantly when particles are included, even for $p_h << p_{tot}$.

Therefore, a non-perturbative scheme needs to be implemented to solve (4.6). Some numerical techniques have been developed for the purpose of locating the zeros of an analytic function [Davies, 1986]. They can be used to solve $\mathcal{D}(\omega, n_{h,0}) = 0$, as it is done in [Merle, 2012] for the MIKE code that solves the electronic fishbone dispersion relation.

In this fishbone linear model, a simpler method is used to solve 4.6. For a given $n_{h,0}$, the term $\mathcal{D}(\omega, n_{h,0})$ is computed on a grid in the complex plane (ω_r, γ), in which the solution of 4.6 is assumed to lie. Then, on the same grid, the quantity $1/|\mathcal{D}|^2(\omega, n_{h,0})$ is computed. The solutions of (4.6) appears then as maxima on the grid (ω_r, γ). When a hybrid simulation is performed with XTOR-K, the instability with the largest growth rate dominates the others in the linear phase. Therefore, in order to verify the code XTOR-K, the growth rate obtained from a hybrid simulation is compared to the solution of 4.6 with the highest growth rate γ.

Solutions obtained from 4.6 for a given Kinetic-MHD equilibrium are displayed on Figure

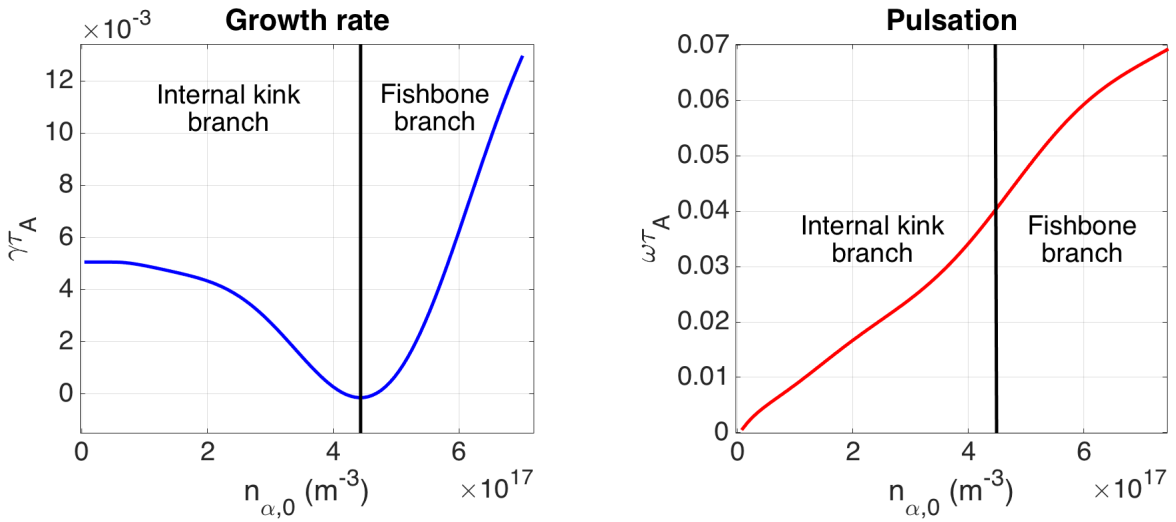

(a) (b)

Figure 4.4: Complex frequencies solutions of the fishbone dispersion relation, for a test example MHD equilibrium. (a) The instability growth rate. (b) The mode pulsation. The two branches obtained in [Wu et al., 1994] are retrieved. The internal kink branch at low fast particle density, where the mode is stabilized by the alpha particles, and the fishbone branch, where a new Energetic Particle Mode is destabilized at higher fast particle density.

(4.4). The mode pulsation and growth rate are functions of $n_{h,0}$. An isotropic slowing-down distribution function of with birth E_b =3.5 MeV has been used to describe fast particles. The MHD equilibrium computed by CHEASE is an ITER-like equilibrium with circular flux surfaces.

As it was expected from earlier numerical works [Wu et al., 1994] and experimental results [Nave et al., 1991], the fishbone dispersion relation exhibits two branches of solution. One for the internal kink mode, and an other for the fishbone mode. The internal kink branch is stabilized at low fast particles density. At the fishbone threshold $n_{\alpha,0} = 4.4.10^{17} m^{-3}$, the fishbone instability dominates the internal kink, and grows well above the initial growth rate without fast particles, whereas the internal kink is fully stabilized. These results highlight the necessity of using a non-perturbative method to solve the fishbone dispersion relation.

4.2 Numerical developments in XTOR-K

In this section, the implementations made in XTOR-K to study the fishbone instability are presented. First, the introduction of an anisotropic slowing-down distribution function in XTOR-K is discussed. Then, the implementation of phase space diagnostics is detailed.

4.2.1 Coherent implementation of fast particles distributions between CHEASE and XTOR-K

In order to study the impact of fast particles onto the MHD stability in a hybrid code such as XTOR-K, two implementations need to be performed. The first one is the implementation of a new particle initialization in XTOR-K, to obtain a slowing-down distribution in velocity space. When including kinetic particles in XTOR-K, an additional pressure is added to the total pressure. Therefore, the MHD equilibrium needs to be modified. The second implementation is the introduction of the additional scalar pressure induced by fast particles in

the code CHEASE.

The following slowing-down distribution function has been implemented in XTOR-K

$$F_{SD,ani}(r,v,\lambda) = \frac{n_h(r)}{C}\frac{\sigma_H(v_b - v)}{v^3 + v_c^3(r)} e^{-\left[\frac{\lambda-\lambda_0}{\Delta\lambda}\right]^2} \tag{4.61}$$

where the anistropy is characterized by a Gaussian function. The isotropic distribution is recovered when $\Delta\lambda \to +\infty$. The scalar pressure associated to (4.61) is firstly derived, then the particle initialization procedure in XTOR-K will be discussed.

Modification of the scalar pressure in CHEASE

Considering the change of variable $(v_x, v_y, v_z) \to (v, \lambda, \Phi)$, following the same procedure as in (4.46)

$$\int d^3v = 2\pi \int_0^{H^*_{max}} \frac{d\lambda}{H^*[1-\lambda/H^*]^{1/2}} \int_0^{\infty} v^2 dv \tag{4.62}$$

$H^*_{max}(r) = B_0/B_{min}(r)$ is the maximum pitch angle value for a given magnetic flux surface denoted by r. The normalization factor C is defined by $n_h(r) = \int d^3v F_{SD,ani}$. Considering $\lambda' = \lambda/H^*$, it can then be expressed as

$$C = \frac{2\pi}{3}\ln\left[1 + \left(\frac{v_\alpha}{v_c}\right)^3\right] \int_0^1 d\lambda' \frac{e^{-[(\lambda' H - \lambda_0)/\Delta\lambda]^2}}{[1-\lambda']^{1/2}} \tag{4.63}$$

In the particular case of an isotropic distribution, $\Delta\lambda \to +\infty$, the pitch angle integral value is 2.

The scalar pressure due to the fast particles can be obtained from the CGL stress tensor $\mathbf{P}_h = P_\parallel \mathbf{bb} + P_\perp(\mathbb{I} - \mathbf{bb})$

$$p_h = \frac{P_\parallel + 2P_\perp}{3} = \frac{m}{3}\left[\int d^3v\ v_\parallel^2 F + \int d^3v\ v_\perp^2 F\right] \tag{4.64}$$

The parallel velocity of fast particles can be expressed with (2.11), leading to

$$p_{h,\parallel} = n_h E_b^2 \frac{2I_{v2}}{I_v I_\lambda} \int_0^1 [1-\lambda']^{1/2} e^{-[\lambda' H^* - \lambda_0]/\Delta\lambda} d\lambda' \tag{4.65}$$

$$p_{h,\perp} = n_h E_b^2 \frac{2I_{v2}}{I_{v1} I_\lambda} \int_0^1 \frac{\lambda'}{[1-\lambda']^{1/2}} e^{-[\lambda' H^* - \lambda_0]/\Delta\lambda} d\lambda' \tag{4.66}$$

where

$$I_{v1} = \ln\left[1 + \left(\frac{v_\alpha}{v_c}\right)^3\right],\ I_{v2} = \int_0^1 \frac{\hat{v}^4}{\hat{v}^3 + \hat{v}_c^3} dv\ I_\lambda = \int_0^1 d\lambda' \frac{e^{-[(\lambda' H^* - \lambda_0)/\Delta\lambda]^2}}{[1-\lambda']^{1/2}} \tag{4.67}$$

Therefore, in a equilibrium code that solves the Grad-Shafranov equation for an anisotropic plasma, adding these parallel and perpendicular fast particle scalar pressure to the bulk pressure will ensure to work with a consistent MHD equilibrium when a significative fraction of energetic particles is introduced. The pitch angle integral I_λ can be computed numerically through a trapezoidal method. It can be shown by direct calculations that the velocity integral I_{v2} yields

$$\int_0^1 \frac{v^4}{v^3 + a^3} dv = -\frac{\pi a^2}{6\sqrt{3}} + \frac{1}{6}\left[3 + a^2\left(2\sqrt{3}\arctan\left[(1-2a^{-1})/\sqrt{3}\right] + 2\ln(1+a) - \ln(1-a+a^2)\right)\right] \tag{4.68}$$

However, the equilibrium code CHEASE is implemented to solve Grad-Shafranov equation for an isotropic plasma. The method used to obtain a coherent equilibrium with fast particles can be described as follow. The isotropic fast particle scalar pressure is added to CHEASE. This scalar pressure is obtained by imposing $\Delta\lambda \to +\infty$ and reads

$$p_{h,iso} = n_h(r) E_\alpha \frac{2I_{v2}(r)}{I_{v1}(r)} \tag{4.69}$$

The fast particles are then initialized according to (4.61). Then a hybrid simulation is launched, during which the MHD fields are projected on the harmonic $n = 0$ at each fluid time step. After a sufficient number of fluid advances, the initially ill-defined equilibrium computed with CHEASE has relaxed towards an equilibrium coherent with an anisotropic distribution of fast particles.

When an isotropic slowing-down distribution function of fast particles is used in XTOR-K, such a procedure is not required. The equilibrium computed by CHEASE is already correct. It is noted that in (4.69), $2I_{v2}/I_{v1}$ can be seen as a temperature profile by direct comparison with the isotropic maxwellian distribution function.

Initialization in XTOR-K for slowing-down distribution functions

Now that the method for obtaining a coherent MHD equilibrium with fast particles have been detailed, the initialization of an anisotropic slowing down distribution function in XTOR-K is discussed. A Monte-Carlo method is used to populate the 6D phase space with particles. The initialization of particles is decomposed in two steps.

First, particles are initialized in position space. The poloidal and toroidal angles of each particles is chosen randomly in the interval $[0, 2\pi]$. Sobol operators are used in XTOR-K to generate random numbers. To initialize the radial coordinate of kinetic particles, the density profile n_h is used as a probability density function. The radial coordinate of each particle is chosen randomly inside n_h, by inverting this profile.

In velocity space, particles can be characterized using the triplet $\mathbf{v} = (v, \lambda', \Phi)$. The velocity vector associated to this triplet is

$$\mathbf{v} = v\left[\sqrt{1-\lambda}\hat{\mathbf{b}} + \sqrt{\lambda'}(\cos\Phi \mathbf{e}_{1,\perp} + \sin\Phi \mathbf{e}_{2,\perp})\right] \tag{4.70}$$

where $(\mathbf{b}, \mathbf{e}_{1,\perp}, \mathbf{e}_{2,\perp})$ is a direct orthogonal basis. $\mathbf{b}$ is the local direction of the magnetic field at the position $\mathbf{r} = (r, \theta, \varphi)$. The probability density function for each of these coordinates needs to be defined for an anisotropic slowing-down distribution function. Considering (4.61) and (4.62)

$$\int d^3\mathbf{v} F_{SD,ani} = \int_0^{2\pi} d\Phi \int_0^1 g(r,\theta,\lambda')d\lambda' \int_0^{+\infty} h(r,v)dv \tag{4.71}$$

$$g(r,\theta,\lambda') = \frac{\exp[-(\lambda' B_0/B(r,\theta) - \lambda_0)/\Delta\lambda]}{\sqrt{1-\lambda'}}, \qquad h(r,v) = \frac{\sigma_H(v_b - v)}{\ln(1+[v_b/v_c(r)]^3)(v^3 + v_c^3(r))} \tag{4.72}$$

The probability density function of the gyroangle Φ is uniform. For each particle, the gyroangle is chosen randomly in $[0, 2\pi]$. The coordinates λ' and v need to be initialized randomly according to their respective probability density functions $g(r,\theta,\lambda')$ and $h(r,v)$. This can be performed by inverting theses functions, choosing randomly a value in the interval in which the inverse functions are defined, and getting the corresponding coordinates (λ', v). For λ',

this operation is performed numerically in XTOR-K by inverting the arrays $X = \lambda', Y = g(r)$. For the norm velocity of particles, an analytical expression of the inverse function h can be obtained directly

$$v = h^{-1}(Y, r) = \frac{v_c(r)}{v_\alpha}\left[e^{Y \ln[1+v_c^{-3}(r)]}\right]^{1/3} \tag{4.73}$$

Once the coordinates $(r, \theta, \varphi, v, \lambda', \Phi)$ have been obtained for every particle in the simulation,

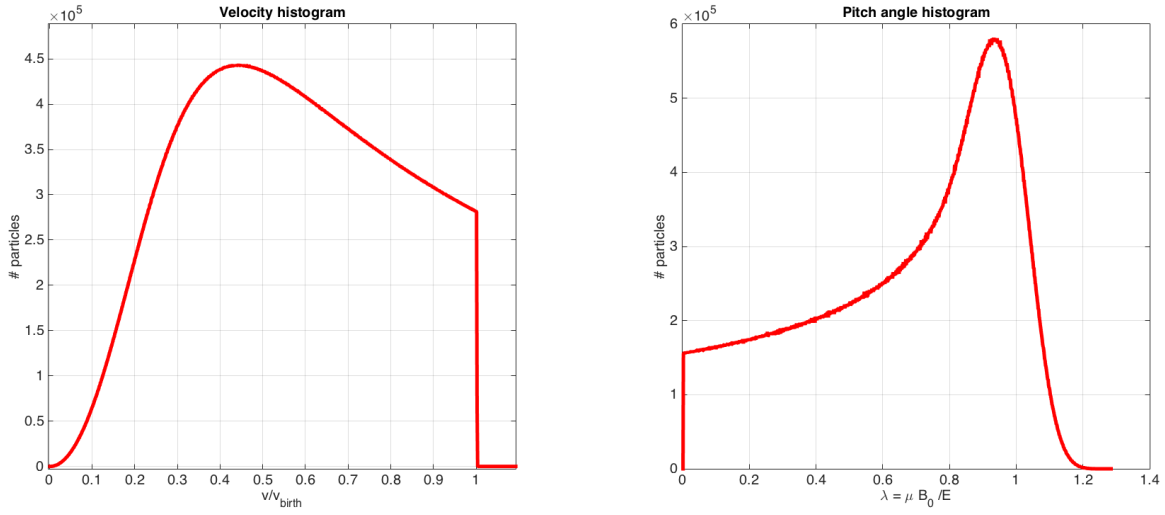

(a) (b)

Figure 4.5: (a) Histogram of the kinetic particles velocity. (b) Histogram of the kinetic particles pitch angle

they are transferred to the coordinates $(R, \varphi^*, Z, v_R, v_{\varphi^*}, v_Z)$ used for the particle advance. On Figure 4.5, histograms of the particles velocity and pitch angle $\lambda = \mu B_0/E$ obtained from XTOR-K are presented. An isotropic slowing distribution function of particles with birth energy $E_b = 3.5$ MeV has been used, and the on-axis electron temperature is $T_{e,0} = 20$ keV.

4.2.2 Implementation of phase space diagnostics

Finding the resonant planes in phase space where the wave-particle energy exchange occur is essential for diagnosing Kinetic-MHD simulations. In the nonlinear phase of such simulations, the resonance condition $\omega - \mathbf{n} \cdot \mathbf{\Omega} = 0$ can evolve significantly. This is due to variation of the mode frequency, and/or to evolution of the particles resonant frequencies, the particles invariants not being invariant anymore. A diagnostic computing the wave-particle energy exchange between kinetic particles and the MHD fields enables to follow the position of the resonance in time. A discussion on the nonlinear evolution of the resonance condition can be found in [Zonca et al., 2015], appendix A-2.

Moreover, fast particles can be transported out of their initial orbit, due to wave-particle energy exchange in these resonant zones of phase space. Following the time evolution of both the particle distribution and of the resonance is then of crucial interest in the nonlinear phase of hybrid simulations to understand the physical processes at play.

The total energy density of fast particles is noted $\mathcal{E}_k$. Its time evolution is

$$\partial_t \mathcal{E}_k = \sum_k \mathbf{v}_k \cdot [m_k \partial_t \mathbf{v}] \tag{4.74}$$

using Lorentz equation, this leads to

$$\partial_t \mathcal{E}_k = \mathbf{J}_k \cdot \mathbf{E} \tag{4.75}$$

The total energy of the system bulk + fast particles is composed of the electromagnetic fields' energy, the bulk particles kinetic energy and of the fast particles kinetic energy. The total energy density reads

$$\mathcal{E} = \frac{\epsilon_0 E^2}{2} + \frac{B^2}{2\mu_0} + \sum_i \frac{m_i}{2} v_i^2 + \mathcal{E}_k \tag{4.76}$$

Since the total energy of the system is conserved, the quantity $\mathbf{J}_k \cdot \mathbf{E}$ then stands for the power transferred from kinetic particles to the rest of the plasma. When it is positive, it implies that kinetic particles are taking energy away from the plasma, and giving it away when it is negative.

The total energy-exchange of fast particles needs to be computed on specific phase space grids in order to highlight the resonant processes. Since the resonance condition is solely a function of the particles invariants, this can be done by computing $\mathbf{J}_k \cdot \mathbf{E}$ on the 3D grid labelled by (E, λ, P_φ). It is also convenient to use the grid (E, λ, r), where r labels a magnetic flux surface, in order to study the resonant transport of fast particles. The implementation of the wave-particle energy exchange diagnostic in XTOR-K is now discussed. The instantaneous power exchange of a single kinetic particle located in phase space at $(\mathbf{r}_k, \mathbf{v}_k)$ is

$$w_k(\mathbf{r}_k, \mathbf{v}_k) = q_k \mathbf{v}_k \cdot \mathbf{E}(\mathbf{r}_k) \tag{4.77}$$

w_k is projected onto the grids (E, λ, r) or (E, λ, P_φ) by tri-linear interpolations. Denoting the coordinates r and P_φ by A, the total power is

$$W(E_m, \lambda_n, A_p) = \sum_k^N w_k S_L(E_k, E_m) S_L(\lambda_k, \lambda_n) S_L(A_k, A_p) \tag{4.78}$$

for N macro-particles, with the weighting factor

$$S_L(X, X_i) = \sigma_H(X - X_i)\sigma_H(X_{i+1} - X)\frac{X_{i+1} - X}{\delta X} + \sigma_H(X - X_{i-1})\sigma_H(X_i - X)\frac{X - X_{i-1}}{\delta X} \tag{4.79}$$

The distribution function of kinetic particles on these grids is simply given by

$$F(E_m, \lambda_n, A_p) = \sum_k^N S_L(E_k, E_m) S_L(\lambda_k, \lambda_n) S_L(A_k, A_p) \tag{4.80}$$

In Kinetic-MHD simulations, fast particles resonate with MHD modes with finite pulsation ω. The energy exchange in XTOR-K is time averaged at least over one rotation time of the MHD mode, $T_{MHD} = 2\pi/\omega$. Several are preferred in general to average out the inherent noise brought by the PIC module.

On Figure 4.6 and Figure 4.7, results obtained with these diagnostics are presented, for a nonlinear hybrid simulation performed with XTOR-K. On Figure 4.6, the wave-particle energy exchange for respectively trapped particles and passing particles have been plotted on the diagram (E, λ) at a fixed P_φ. Resonant structures can be observed in both trapped and passing diagrams. The transport of particles associated to these resonant structures is displayed on Figure (4.7). The perturbed distribution squared has been plotted on the same diagram.

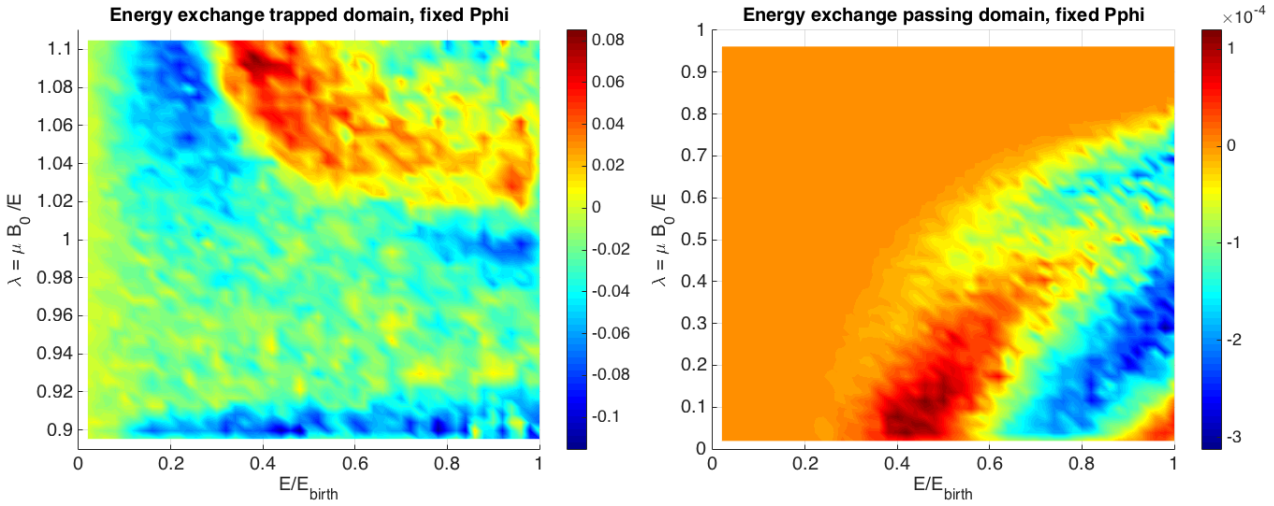

(a) Trapped particle domain (b) Passing particle domain

Figure 4.6: Wave-particle energy exchange $-\mathbf{J}_k \cdot \mathbf{E}$ in the diagram (E, λ) at fixed P_φ, in arbitrary units.

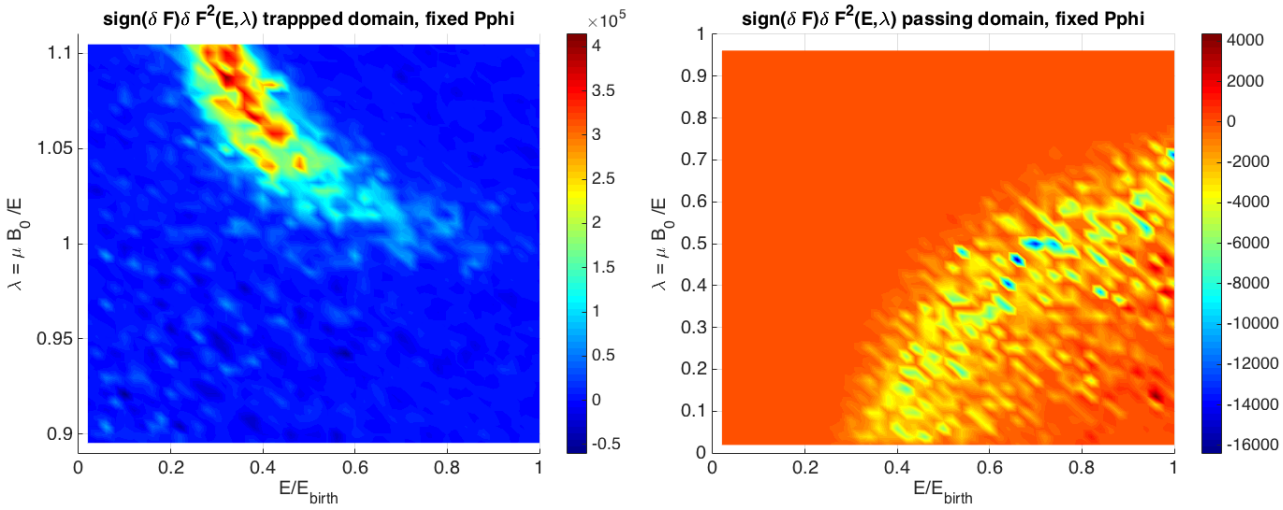

(a) Trapped particle domain (b) Passing particle domain

Figure 4.7: Perturbed distribution function squared in the diagram (E, λ) at fixed P_φ

4.2.3 Implementation of Kinetic Poincaré plots in XTOR-K

In addition to the energy exchange diagnostic, a Kinetic Poincaré diagnostic can be very useful to study the evolution of the resonant island in phase space. Such a diagnostic has been developed for the code XHMGC [Briguglio et al., 2014][Briguglio et al., 2017]. A similar method has been implemented in XTOR-K. It consists in following resonant particles in the phase space diagram $(\Theta, \dot{\Theta})$ that was presented in Chapter 2.3. The quantity Θ is defined in (2.57). As done in [Briguglio et al., 2014], $\dot{\Theta}$ can be replaced by P_φ for simplicity.

In XTOR-K, this diagnostic is still under development. Preliminary results have though already been obtained. The implementation of this diagnostic, and the method to use it is discussed here. First, the resonant zones of phase space need to identify, in order to decide which particles to follow in the diagram (Θ, P_φ). Then, for a given $P_{\varphi,res}$ lying on a wave-particle resonant surface, it is chosen to follow particles with the same energy and pitch angle, on a range of P_φ around the resonant surface.

The phase Θ depends on the nature of the resonance considered in the angle-action formalism. For the alpha fishbone instability, only two resonances are of interest. The precessional resonance with $\mathbf{n} = (0, 0, 1)$, and the passing resonance $\mathbf{n} = (0, -1, 1)$ (see Figure 4.1).

$$\Theta_{precessional}(\boldsymbol{\alpha}, t) = \alpha_3 - \int_0^t \omega(t')dt' \tag{4.81}$$

$$\Theta_{passing}(\boldsymbol{\alpha}, t) = \alpha_3 - \alpha_2 - \int_0^t \omega(t')dt' \tag{4.82}$$

In the Kinetic Poincaré diagnostic implemented in XTOR-K, both resonances can however be treated similarly. Along the trajectory of resonant particles, a dot in the diagram (Θ, P_φ) is plotted every time their poloidal angle $\theta = 0$ on the low field side. The same procedure is used in [Briguglio et al., 2014]. At $\theta = 0$, as displayed on Figure (2.6), the angle $\alpha_2 = 0$. The angle α_3 can be written as (2.50) $\alpha_3 = \varphi + F(\alpha_2)$ with F a periodic function of α_2. When computing Θ at $\theta = 0$, $F(\theta = 0)$ is a constant, so Θ can be defined for both resonances as

$$\Theta(t) = \varphi - \int_0^t \omega(t')dt' \tag{4.83}$$

As of now in XTOR-K, the Kinetic Poincaré diagrams can only be obtained for one resonant particle. Being able to use an arbitrary number of particles is currently being implemented, and constitutes a mandatory feature to observe the dynamics of the resonant island. Yet, a one-particle diagram gives a general idea of the island behavior. On Figure 4.8, an example of a one particle Kinetic Poincaré diagram is displayed. It has been obtained from a nonlinear hybrid simulation performed with XTOR-K.

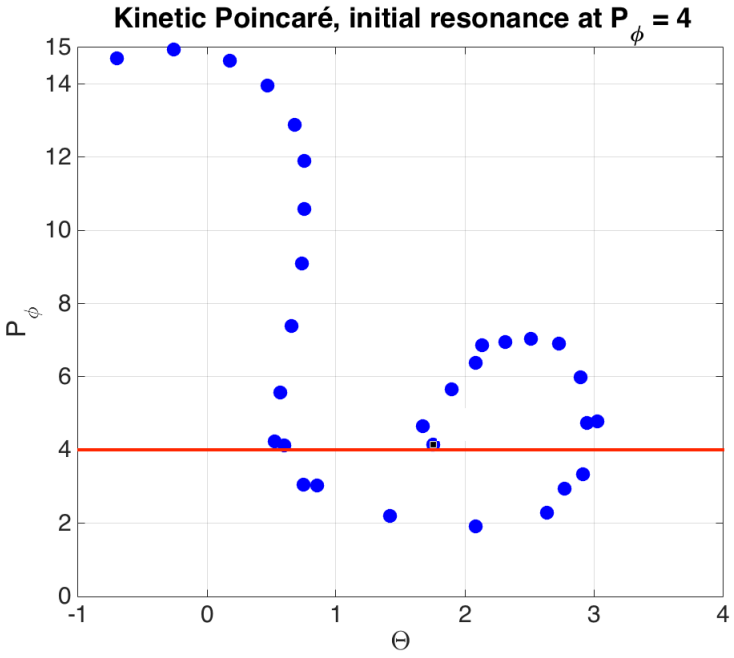

Figure 4.8: Trajectory of a resonant particle in the Kinetic Poincaré diagram (Θ, P_φ). The precessional resonance is located at $P_\varphi = 4$, marked by the red line. The considered particle was initially trapped in a resonant island, and escaped at larger P_φ.

4.2.4 Conclusion

In this chapter, the linear theory of the fishbone instability has been derived. A fishbone dispersion relation has been obtained, considering an isotropic slowing distribution function of fast particles. It incorporates some specificities regarding earlier linear models. The resonant contribution of passing particles is taken into account [Cheng, 1992][Fu et al., 2006], and non-resonant terms are included in the kinetic contribution λ_K to the fishbone dispersion relation [Nabais et al., 2015]. This fishbone linear model will enable to verify linearly the code XTOR-K in Chapter 5. The implementation of realistic fast particles distribution function in XTOR-K has also been presented. It will permit the study of the alpha fishbone instability in Chapter 5 and 6. The implementation of phase space diagnostics has also been discussed in this chapter. They are used in chapter 6 to study the behavior of fast particles in the nonlinear phase of the alpha fishbone instability.

Chapter 5

Linear verification of XTOR-K and application to ITER linear stability

The advantage of having a linear model when possessing a global nonlinear hybrid code is double. On one hand, the fishbone linear model can be used to assess at minimal computational cost the linear stability of simple equilibria against the fishbone instability. Assessing the linear stability of a given equilibrium with a hybrid code such as XTOR-K requires of order $10^4 - 10^5$ computing hours, whereas the fishbone linear model only requires a few minutes. Therefore, the fishbone linear model lowers drastically the amount of computational time needed to obtain the threshold $\beta_{h,res}/\beta_{tot}$ at which the fishbone instability dominates the internal kink instability. The assessment of the fishbone threshold with hybrid codes requires several simulations with different kinetic particle densities.

On the other hand, the linear model can be used to proceed to the linear verification of hybrid codes such as XTOR-K. It enables to validate the correct implementation of kinetic modules in nonlinear MHD codes. Such a verification permits two studies. First, the fishbone linear model uses intrinsic assumptions that prevents it from estimating the linear stability of complex Kinetic-MHD equilibria, with for example non-circular magnetic surfaces and highly energetic kinetic particles. Once verified, the code XTOR-K can be used instead of this model to assess the linear stability of complex equilibria. This is done for the ITER 15 MA equilibrium in this chapter. Second, when verified, nonlinear hybrid codes can be used to study the nonlinear phase of the fishbone instability, in which resonant transport and mode chirping occur. Such a study is performed in Chapter 6.

In this chapter, the eigenfrequencies of kinetic particles in XTOR-K are first compared to those obtained from the angle-action formalism. Then, the Kinetic-MHD equilibrium on which the code XTOR-K can be verified by the fishbone linear model is defined, taking into account the model restrictive assumptions. Afterwards, the linear verification of XTOR-K is presented, and the importance of the linear model specificities is highlighted. Finally, the code XTOR-K is used to find the fishbone thresholds of two Kinetic-MHD equilibria relevant to the ITER 15 MA scenario. It is found that the fishbone thresholds lie well below the expected β_α/β_{tot} for this scenario. The ITER 15 MA scenario is then likely to be unstable against the alpha fishbone instability.

5.1 Verification of the particles' characteristics frequencies

The fishbone instability is characterized by resonant processes between the mode ω and the particles eigenfrequencies ω_b, ω_d. The first step of XTOR-K's linear verification is then the comparison between the eigenfrequencies computed from the code, and those obtained from the angle-action formalism (A.7), (A.18), (B.11), (B.14). In a previous work [Leblond, 2011], it has been shown that in XTOR-K simulations, the invariants of motion are well conserved when particles are advanced on a Grad-Shafranov equilibrium. As a result, it is expected that the particles eigenfrequencies, directly linked to the invariants of motion by the angle-action formalism, are correct. However, it is worth verifying that it is numerically the case, since slight divergences in these frequencies values would induce significative differences regarding the overall characteristics of the fishbone instability, such as its growth rate, rotation frequency and/or position of resonances in phase space.

In order to work out numerical values for ω_b, ω_d from particle orbits obtained with XTOR-K, the 6D particle advance in the code has been taken out into a separated module. This module is used to advance particles on MHD equilibria computed by the CHEASE code. Particles are initialized for a given set of invariants $(E, \lambda, \langle\psi\rangle)$, which facilitates the comparison with the angle-action formalism. The particles' eigenfrequencies in XTOR-K are obtained from the time evolution of their poloidal and toroidal angles.

The bounce/transit frequency ω_b is computed using a Fourier transform of $\theta(t)$, since the poloidal angle is computed modulo 2π in the code. Typical θ time evolutions for passing and trapped particles are given in Figure 5.1. The precessional frequency ω_d can be ob-

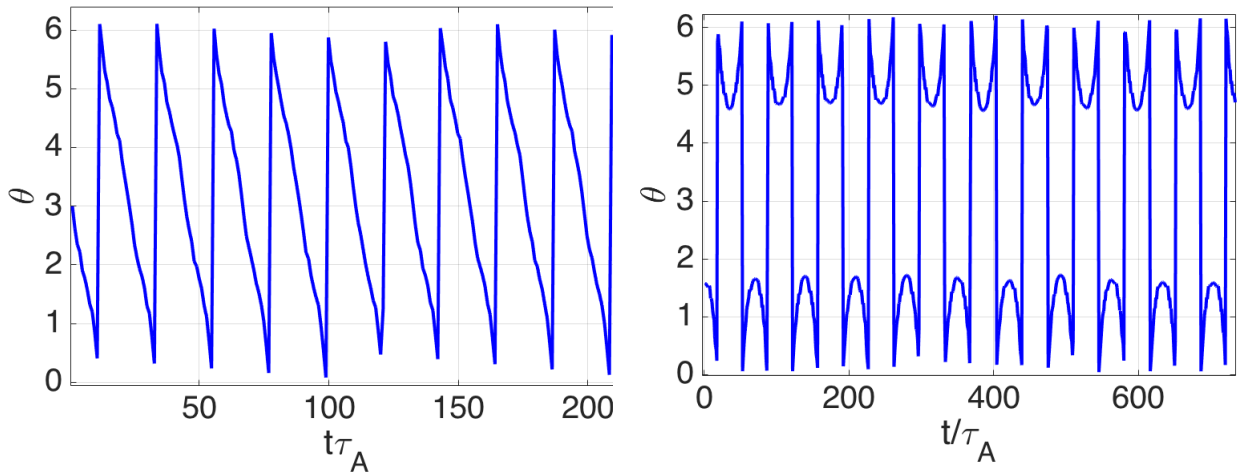

(a) (b)

Figure 5.1: Poloidal angle time evolution for passing particles (a), and trapped particles (b). θ is given modulo 2π.

tained from the toroidal angle using equation (2.50). For trapped particles, ω_d is obtained by performing a linear regression on $\varphi(t)$, since $\varphi \propto \omega_d t$. For passing particles, the precessional frequency is computed by subtracting $q(\bar{\psi})\omega$ from the slope of $\varphi(t)$. However, since $\omega_b \gg \omega_d$, the computation of ω_d is quite challenging since it involves a precise measurement of $q(\bar{\psi})$, which is not always possible for deeply passing particles. Therefore, the eigenfrequency $\Omega_3 = q(\bar{\psi})\omega_b + \omega_d$ in XTOR-K is directly compared with the value predicted by the

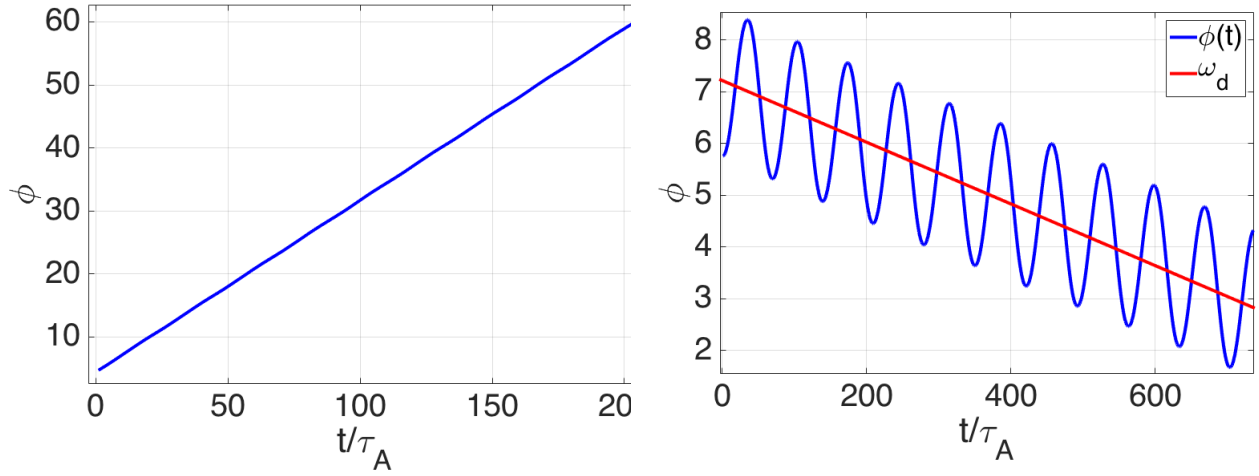

(a) (b)

Figure 5.2: Toroidal angle time evolution for passing particles (a), and trapped particles (b). On (b), the precessional frequency (red curve) is obtained by a linear fit of $\varphi(t)$

angle-action formalism. Typical φ time evolutions can be found in Figure 5.2.

The theoretical expressions of ω_b, ω_d have been derived using a thin orbit width approximation. Therefore, the particles' eigenfrequencies in XTOR-K need to be verified at low energy, since the particles' orbit width is proportional to $\sqrt{E}$. It is then chosen to advance particles with energy $E = 100$ keV. Particles are chosen all over the pitch angle range, for different radial positions inside the $q = 1$ surface. Particles with radial positions beyond $q = 1$ are not of interest since they cannot interact resonantly with the mode.

Figure 5.3 displays the values of ω_b, ω_d computed from the angle-action formalism and particles' trajectories in XTOR-K. The trapped and the passing domains have been separated on this figure. The agreement between the numerical and theoretical values is satisfactory, for all radial positions considered and all over the pitch angle range. Particles' eigenfrequencies are therefore well described by XTOR-K.

5.2 Valid Kinetic-MHD equilibrium for XTOR-K's linear verification

As mentioned in Chapter 4, a number of assumptions have been used in the derivation of the analytical model. They are restricting the Kinetic-MHD equilibria that can be considered with the fishbone linear model. The most restrictive assumptions are the circular magnetic surfaces, a small inverse ratio aspect at $q = 1$, thin orbit widths and low kinetic pressure regarding total pressure $p_h \ll p_{tot}$.

Some of these constraints can be easily applied, for example by configuring a circular MHD equilibrium with CHEASE verifying $a \ll R_0$. However, the parameters space in which the two others assumptions are valid needs to be found. It is shown in this section that the birth energy E_b of the slowing-down distribution function used is a crucial parameter for meeting the model assumptions. Once the ideal birth energy has been found, it must also be determined if an ordering between the critical and birth velocity of the slowing-down distri-

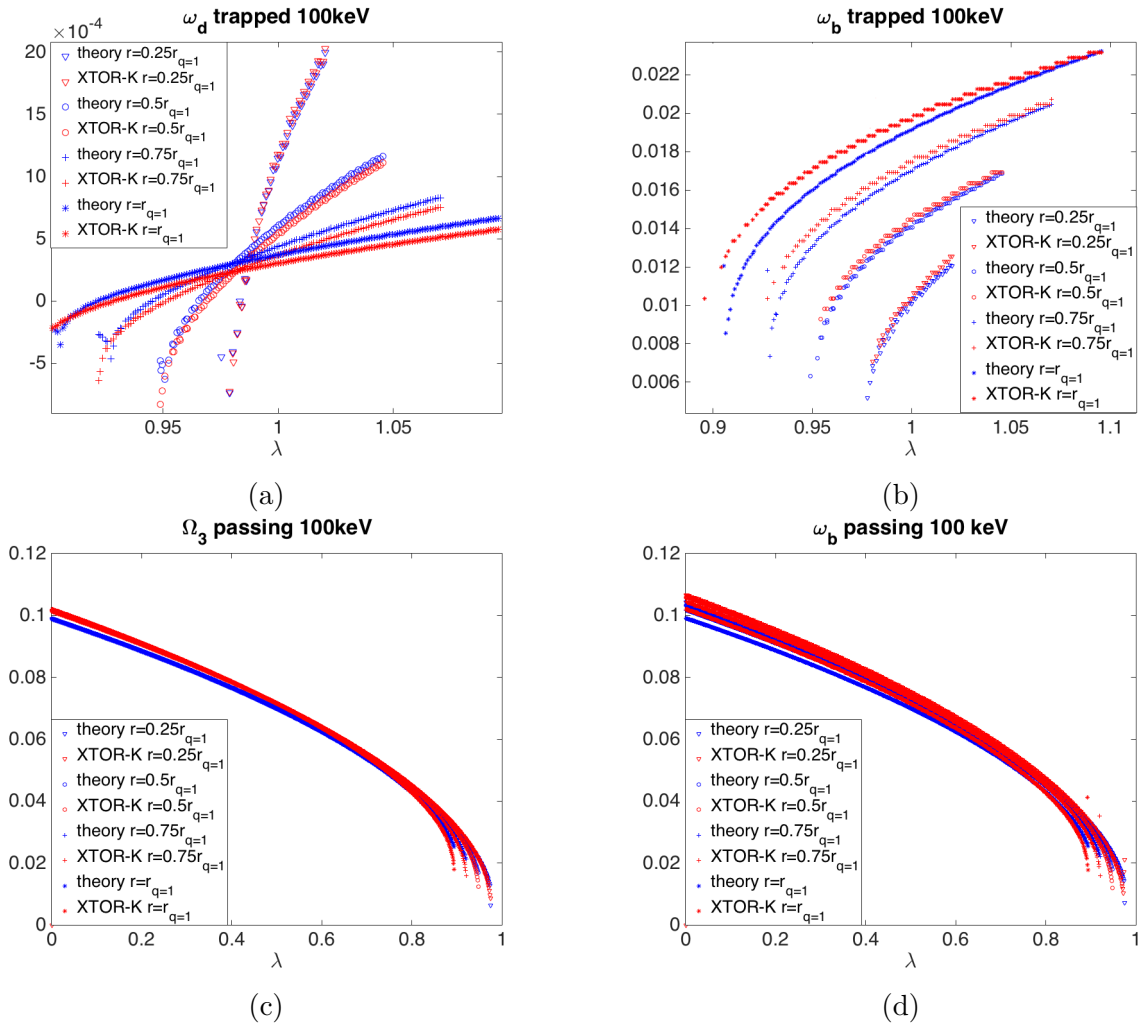

Figure 5.3: (a) Precessional frequencies. (b) Bounce frequencies in the trapped domain. (c) Third eigenfrequencies Ω_3. (d) Transit frequencies in the passing domain. Blue points are obtained from the theoretical expressions of ω_b, ω_d, and the red points are computed from XTOR-K. The frequencies are plotted at different radial positions $\bar{\psi}$ against their pitch angle λ for $E = 100$ keV. Frequencies are normalized at the Alfvén time τ_A.

bution can be obtained. If not, the fishbone dispersion relation will be computed with the collocation method.

5.2.1 Limit brought by high birth energies

When the particles' energy is increased, their trajectory in the poloidal plane evolves from thin banana orbits to large potato orbits, as displayed on Figure 5.4. Therefore, there exists an energy threshold beyond which a thin orbit width approximation cannot be used to describe fast particles.

Such a threshold is defined here as the energy beyond which the eigenfrequencies derived by the linear theory do not match those obtained from XTOR-K. The frequencies ω_b, ω_d computed from XTOR-K are assumed to be correct at all energies. Such an assumption is acceptable since the particle advance is not restricted at high particle energy in XTOR-K, and because eigenfrequencies obtained from the code have been verified at low energy.

On Figure (5.5), precessional and bounce frequencies obtained at $E = 3.5$ MeV and $E = 1$

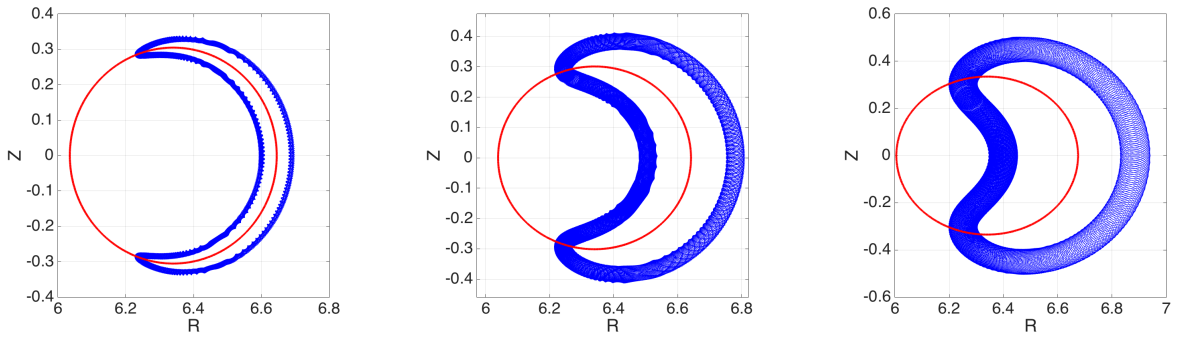

Figure 5.4: Trajectories in the poloidal plane for trapped particles. Particles have the same $\bar{\psi}$ and λ, but were launched at different energies to highlight orbit width effects. (a) 100 keV, (b) 1MeV, (c) 3.5 MeV. The red circle on these figures represent the reference flux surface $\bar{\psi}$ of the particles.

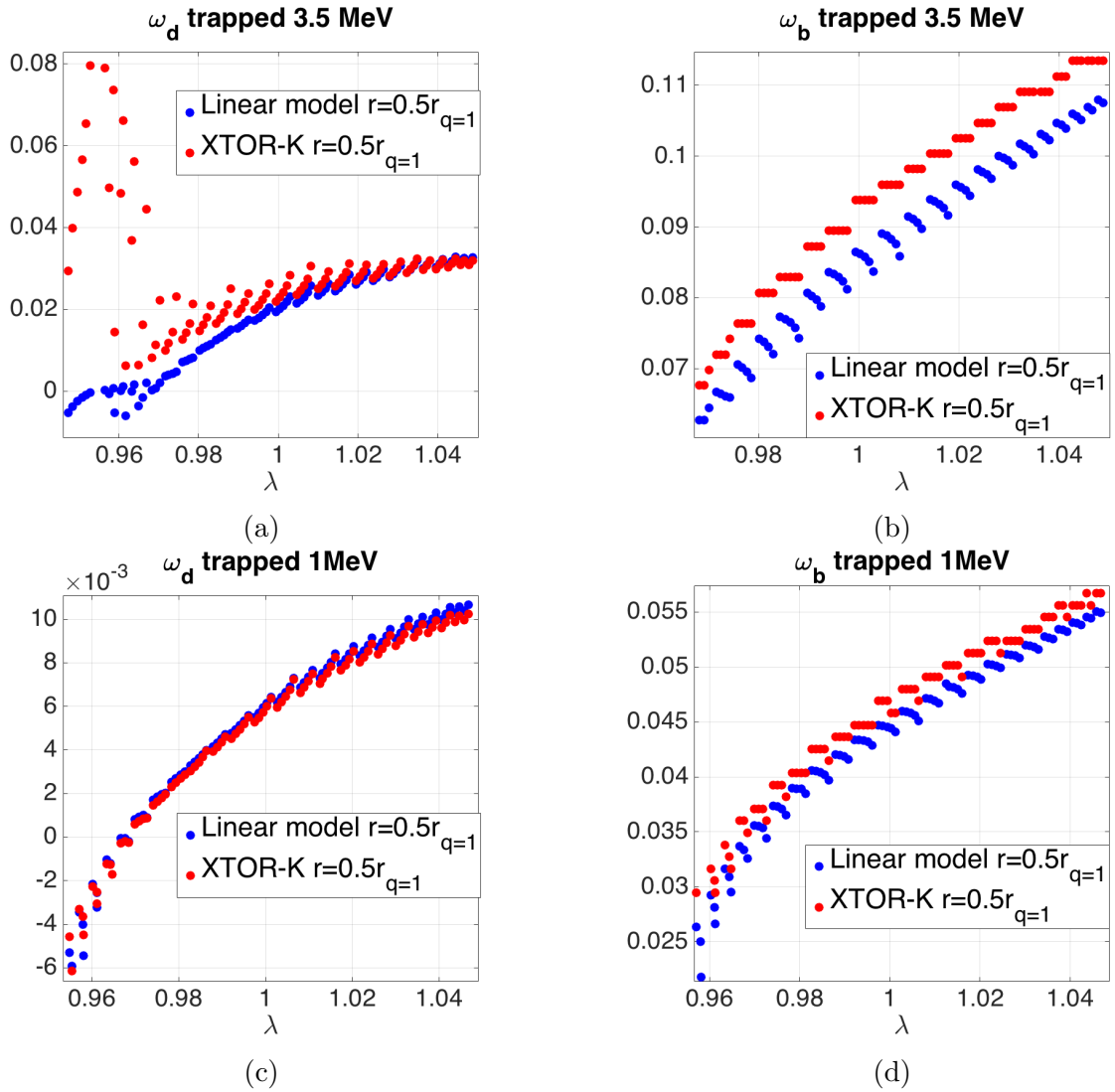

Figure 5.5: Comparison of the frequencies ω_b, ω_d at different energies between the linear model (blue points) and XTOR-K (red points), at r=$0.5r_{q=1}$ against pitch angle. Results at 3.5 MeV are displayed respectively on (a) for the precession, and in (b) for the bounce. Same results are shown in (c) and (d) at 1 MeV. Frequencies are normalized at the Alfvén time τ_A

MeV are displayed. Only the trapped domain is shown here to simplify this discussion, results from the passing domain being redundant. At $E = 3.5$ MeV, the bounce frequencies of the linear model remain somewhat valid. However, the theoretical precessional frequencies do not recover those obtained from XTOR-K, especially near the trapped-passing boundary. Therefore, a realistic slowing-down distribution of alpha particles with birth energy $E_b = 3.5$ MeV cannot be described by the fishbone linear model.

However, at intermediate particle energy $E = 1$ MeV, the theoretical precessional and bounce frequencies are found to be still in good agreement with XTOR-K's at $\hat{\psi} = 0.5\hat{\psi}_{q=1}$. At lower radial position close to the magnetic axis, some particles at 1 MeV exhibit non-standard orbits, and are then badly described by the thin orbit width approximation. However, the proportion of particle with non-standard orbits is found to be weak regarding particles with standard ones. Therefore, the thin orbit width approximation still holds for slowing-down distribution function with birth energy $E_b = 1$ MeV. For birth energies higher than 1 MeV, it has been observed that the theoretical frequencies ω_d, ω_b are not recovered by XTOR-K. $E_b = 1$ MeV is therefore the threshold birth energy regarding the thin orbit width assumption.

5.2.2 Limit brought by low birth energies

At first sight, regarding the thin orbit width assumption, it seems that a slowing-down distribution function with a birth energy as low as possible is a good candidate for a linear verification. However, at lower energy, much larger kinetic densities are required to destabilize significantly the fishbone instability. Since the kinetic pressure needs to verify $p_h \ll p_{tot}$ in the fishbone linear model, a birth energy in an intermediate regime needs to be used to satisfy both assumptions.

In order to find the ideal birth energy, two sets of linear simulations have been done with XTOR-K. Both sets consider an isotropic slowing distribution function of alpha particles at kinetic densities just high enough to trigger the fishbone instability. The first set considers a birth energy $E_b = 100$ keV, and the second one $E_b = 1$ MeV. The ratio p_h/p_{tot} for both sets of simulations is displayed on Figure (5.6).

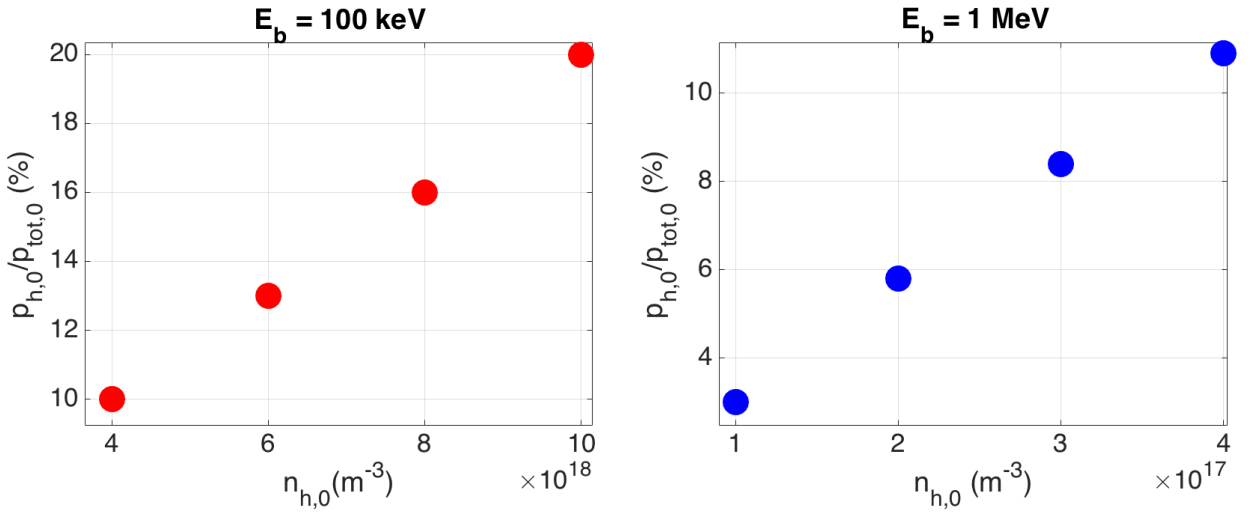

(a) (b)

Figure 5.6: On-axis ratio between the kinetic and total pressure, for different kinetic pressures at which the fishbone instability is significantly perturbed. (a) Case at 100 keV, (b) Case at 1 MeV.

For the case with $E_b = 100$keV, the fishbone instability begins to appear at $n_{h,0} = 4.10^{18} m^{-3}$. At this density, the on-axis pressure ratio $p_{h,0}/p_{tot,0}$ is about 10 %, which is already too large regarding the limit $p_h/p_{tot} \ll 1$. The complex frequencies $\omega + i\gamma$ cannot be expected to be similar between XTOR-K and the fishbone linear model for $E_b = 100$ keV. The birth energy of the slowing-down distribution function needs to be further increased in order to obtain lower pressure ratio.

For the set $E_b = 1$ MeV, the fishbone instability is appearing at $n_{h,0} = 1.10^{17} m^{-3}$, with a corresponding pressure ratio $p_h/p_{tot} = 4\%$. It satisfies the condition $p_h/p_{tot} \ll 1$. At the maximum on-axis density considered for this set, the low kinetic pressure condition is not as well respected, with $p_h/p_{tot} = 11\%$. Compared results between XTOR-K and the fishbone linear model can be expected to diverge above $n_{h,0} = 4.10^{17}\mathrm{m}^{-3}$.

Therefore, an isotropic slowing-down distribution function with birth energy $E_b = 1$ MeV is an ideal candidate to verify XTOR-K with the fishbone linear model. It meets simultaneously the thin orbit width and the low kinetic pressure assumptions.

5.2.3 Computational method used for λ_K

Now that the relevant birth energy E_b has been defined, the quantity $(v_c/v_b)^3$ needs to be evaluated. As explained in 4.1.4, the computation of λ_K in the linear model (4.60) depends on the value of this ratio. If an ordering between the two velocities can be found, the energy integral of λ_K is computed analytically. Otherwise, the collocation method needs to be used. The only free parameter remaining in the ratio $(v_c/v_b)^3$ is the electron temperature. For realistic tokamak plasmas, this parameter lies between 10-30 keV.

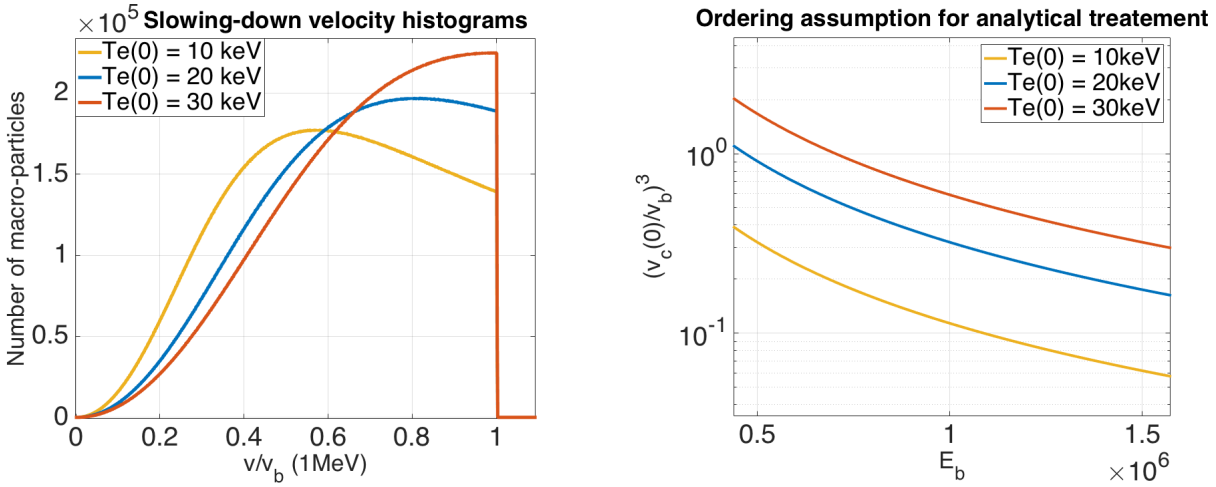

(a) (b)

Figure 5.7: (a) Velocity histogram of slowing-down distribution functions for different on-axis electron temperature. (b) Cubic ratio between the critical velocity and the birth velocity, as a function of the birth energy for different on-axis electronic temperatures

Figure (5.7) (a) displays the velocity histograms of the slowing-down distribution functions for various electron temperatures. Most particles' velocity range in $\hat{v} \in [0.4, 1]$. Unfortunately, as displayed on Figure (5.7) (b), for realistic electron temperatures, an ordering as $(v_c/v_b)^3 \ll \hat{v}^3$ or $(v_c/v_b)^3 \gg \hat{v}^3$ cannot be formed. At the lowest temperature considered T_e

= 10 keV, the ordering $(v_c/v_b)^3 \ll \hat{v}^3$ is only marginally satisfied at $\hat{v} = 1$, not for lower velocities. At higher temperatures, there is no energy range on which an ordering can be formed. Therefore, the electron bulk temperature cannot be tuned in order to use an analytical method for I_{res} in (4.60). The bulk temperature is then set to $T_i(0) = T_e(0) = 20$ keV to describe an ITER-like equilibrium and the collocation method is used to compute I_{res}.

5.2.4 Valid equilibrium for linear verification

The Kinetic-MHD equilibrium defined for the linear verification of XTOR-K is presented here. As explained above, a MHD equilibrium with circular cross sections is used, with dimensions and magnetic field identical to those of ITER, $R_0 = 6.2m, a = 2m, B_0 = 5.3T$. By imposing a $q = 1$ surface at $s = \sqrt{\psi/\psi_{edge}} = 0.4$, this ITER-like geometry has a small inverse aspect ratio on $q = 1$ as $\epsilon_{q=1} \equiv \epsilon_0 \sim 0.11 \ll 1$, which is required by the linear model.

The safety factor profile is also chosen to have an on-axis value $q_0 = 0.95$ close to 1, which is an other requirement of the fishbone linear model. The kinetic density profile is chosen to be steep in order to trigger the fishbone instability at low kinetic pressure, with $p_h \ll p_{tot}$. It is possible since $\lambda_K \propto \partial_r F_e q \propto \partial_r n_h$ in (4.53). The density profile is $n_\alpha(s) = n_{\alpha,0}(1 - s^2)^6$, with s the normalized radial coordinate $s = \psi/\psi_{edge}$. Kinetic particles are chosen to be alpha particles.

The equilibrium alpha distribution function is represented on Figure 5.8, in the (E, λ) diagram at a fixed radial position, for both trapped and passing populations. The number of particles in this diagram is peaked on the trapping-passing $\lambda = B_0/B_{max}(r)$ boundary.

The bulk part of the equilibrium has been designed such that it is unstable against the $n = m = 1$ resistive internal kink mode. Diamagnetic effects have not been considered in the bulk. The growth rate of the instability without alpha particles is $\gamma\tau_A = 1.7\ 10^{-3}$. This choice has been made such that it is possible to observe the expected stabilization of the instability at low density of fast particles.

5.3 Quantitative verification

5.3.1 Quantitative match for the linear frequencies of the internal kink

Now that a suitable equilibrium has been defined, the complex frequencies $\omega = \omega + i\gamma$ obtained from XTOR-K and the fishbone linear model are presented. The fishbone dispersion relation (4.6) is solved with different on-axis kinetic densities $n_{\alpha,0}$, and several hybrid simulations are performed with XTOR-K for the corresponding $n_{\alpha,0}$. Results are presented on Figure 5.9. As expected theoretically and experimentally [White et al., 1990], [Wu et al., 1994][Nave et al., 1991], both models recover the two branches of solution, as in 4.1.5. The internal kink branch, dominant at low kinetic density, corresponds to the stabilization of the internal kink MHD mode. The fishbone branch dominates the kink mode above the fishbone beta threshold $\beta_{h,th}/\beta_{tot} = 5\%$. The fishbone mode is destabilized by the resonant drive introduced by kinetic particles. It is further destabilized with increasing fast particles beta, contrarily to the kink branch.

Regarding the pulsations, the two branches exhibit different behaviors. The mode pulsation on the kink branch is one order of magnitude below than on the fishbone branch. Still

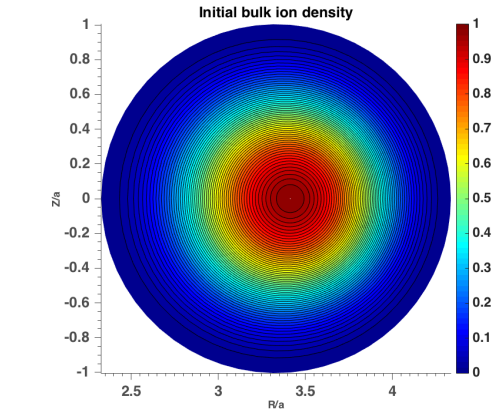

(a)

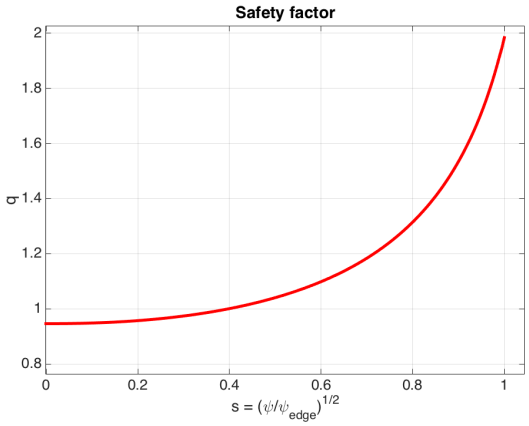

(b)

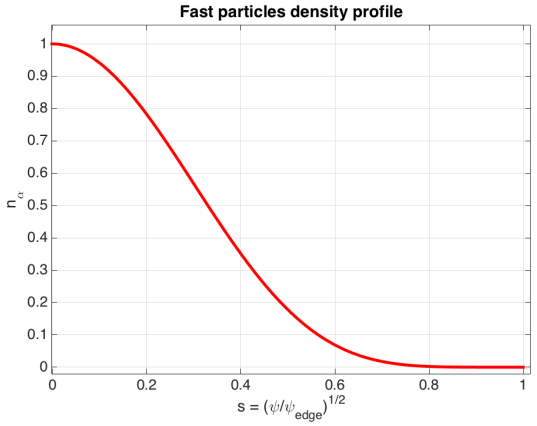

(c)

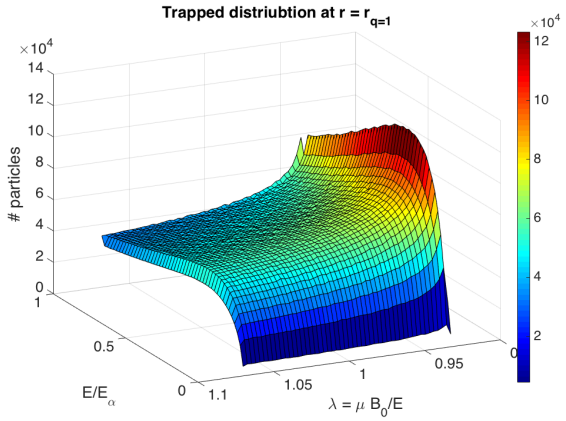

(d)

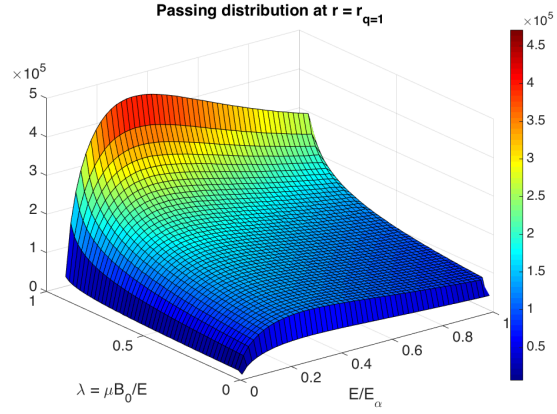

(e)

Figure 5.8: Kinetic MHD equilibrium used for linear verification. (a) Bulk ion density in the poloidal plane, exhibiting the equilibrium geometry. (b) Parabolic q profile with $q_0 = 0.95$ and $q_{95} = 2$. (c) Peaked alpha density profile. (d)-(e) Alpha distribution function in the (E, λ) in the trapped (d) and passing (e) domains, at $r = r_{q=1}$.

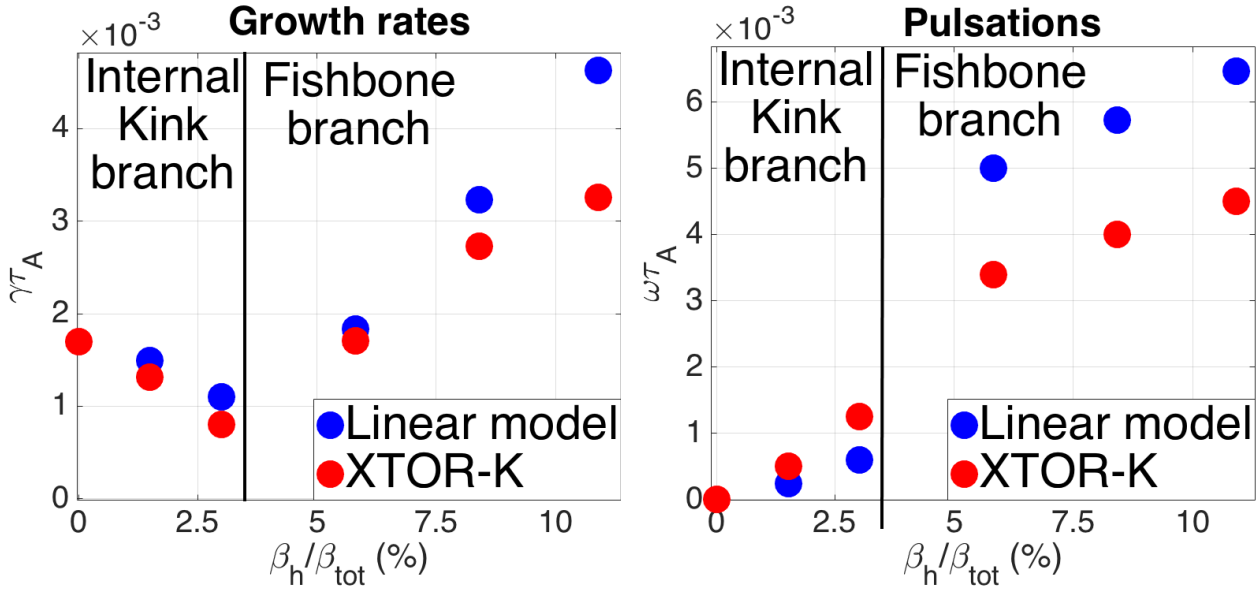

(a) (b)

Figure 5.9: Compared complex frequencies against the beta ratio β_h/β_{tot}. Values from the linear model in blue, and from XTOR-K in red. Growth rates are shown in (a), pulsations in (b). A quantitative agreement is obtained between the hybrid code and the linear theory.

on the kink branch, the instability rotates mainly because of the diamagnetic effect carried by the fast alpha-like particles. Instead, on the fishbone branch, the rotation is due to both the diamagnetic effect and the resonant interaction between the $n = m = 1$ mode and the fast particles eigenfrequencies. On the fishbone branch, due to the resonant interaction, the mode pulsation tends to scale as the precessional frequency of deeply trapped particles. On Figure (5.9), $\omega\tau_A \sim 5.5 \times 10^{-3}$ and on Figure (5.5) (c), $\omega_d\tau_A = 6.10^{-3}$ for $\lambda \sim 1$.

The kink branch still exists beyond the critical kinetic beta, but has a lower growth rate than the fishbone branch. The fishbone linear model shows that fast particles fully stabilize the internal kink mode at higher kinetic beta. In XTOR-K, only the instability with the largest growth rate can be observed, which is why Figure 5.9 does not show overlap between the two branches.

The agreement between the fishbone linear model and the linear simulation phases of XTOR-K is satisfactory at lower densities. Both models recover the same critical kinetic beta at which the fishbone branch dominates the kink branch. On the fishbone branch, the two models begin to diverge with increasing kinetic density. On Figure (5.9), at the highest kinetic beta, the pressure ratio is $p_h/p_{tot} = 11\%$, which begins to be too large regarding the assumption $p_h \ll p_{tot}$. At this kinetic pressure, δW_{MHD} cannot be computed without including the kinetic contribution to the total current $\mathbf{J}$. The divergence between XTOR-K and the fishbone linear model at higher kinetic beta is then due to the restrictive assumptions of the linear model.

Therefore, a linear verification of the hybrid code XTOR-K has been provided by the linear theory. It ensures that the kinetic PIC module and its coupling with the fluid equations has been correctly implemented.

5.3.2 Relevance of the linear model specificities

The specificities introduced in the fishbone linear model have revealed to be essential to provide a precise verification of XTOR-K. Figure 5.10 displays the complex frequencies that would have been obtained from the fishbone linear model without those specificities. The features removed from the linear model on this figure are respectively the resonant contribution of passing particles, and the non-resonant kinetic contribution (4.54) to the fishbone dispersion relation (4.6). Results obtained using Porcelli's expression in [Porcelli, 1991] have also been plotted on Figure (5.10).

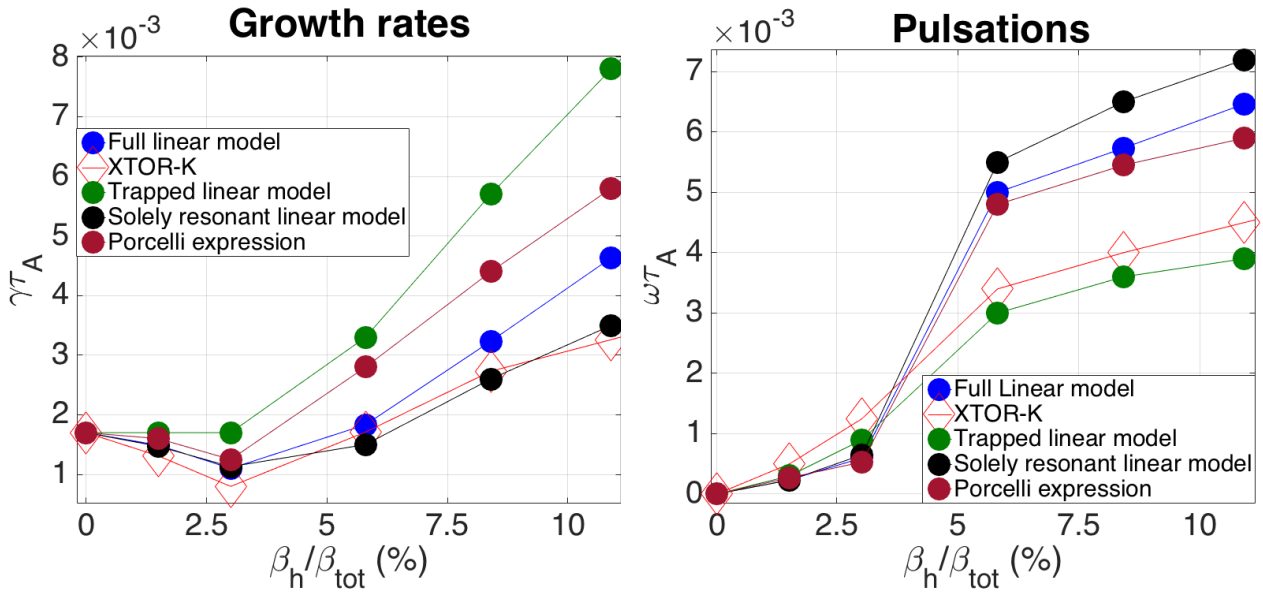

(a) (b)

Figure 5.10: Compared results between different theoretical linear models and XTOR-K regarding the mode growth rates (a) and pulsations (b). Red diamonds : XTOR-K, blue points : the full fishbone linear model, green points : the full linear model without the resonant passing contribution, black points : the full linear model without the non-resonant contribution and brown points : Porcelli's model expression [Porcelli, 1991].

From this figure, it can be observed that without the passing resonant contribution (green points), the pulsations obtained are closer to XTOR-K's values than with the complete model. However, the growth rates obtained in this limit are more than twice as high as XTOR-K's growth rates. Since the linear model needs to recover precise values for the total complex frequencies, the inclusion of the resonant contribution of passing particles is necessary for the linear verification of XTOR-K by the fishbone model. Similarly, the inclusion of the non-resonant contribution is necessary for the linear verification. Without this contribution (black points), the growth rates computed are closer to XTOR-K's, but the pulsations are twice as large as those obtained with the hybrid code.

Results obtained between the complete fishbone linear model (blue points) and the Porcelli's model are quite similar. Complex frequencies for the Porcelli's model have been obtained by replacing the term σ^2/λ in equation (4.53), by λ according to equation (11) in [Porcelli, 1991]. The growth rates computed from this model are somewhat larger than those of the fishbone model, whereas the pulsations obtained are almost identical. The fishbone model derived in Chapter 4 is therefore preferred for verifying linearly the hybrid code XTOR-K.

5.3.3 Quantitative match for positions of resonances in phase space

Finally, the linear verification of XTOR-K is completed by comparing the positions of the precessional resonance in the 3D invariants space. The position of the resonance in the linear theory is obtained by solving numerically the equation $\omega - \omega_d(E, \lambda, \bar{r}) = 0$ using (B.11). This equation is solved at a fixed radial position $\bar{r}$, and the solution is a curve in the (E, λ) diagram. The resonance is found in XTOR-K by using the diagnostics implemented in 4.2.2. During the linear phase of the fishbone instability, the perturbed kinetic distribution function δF is expected to be maximal around the resonance position, according to equation (4.12).

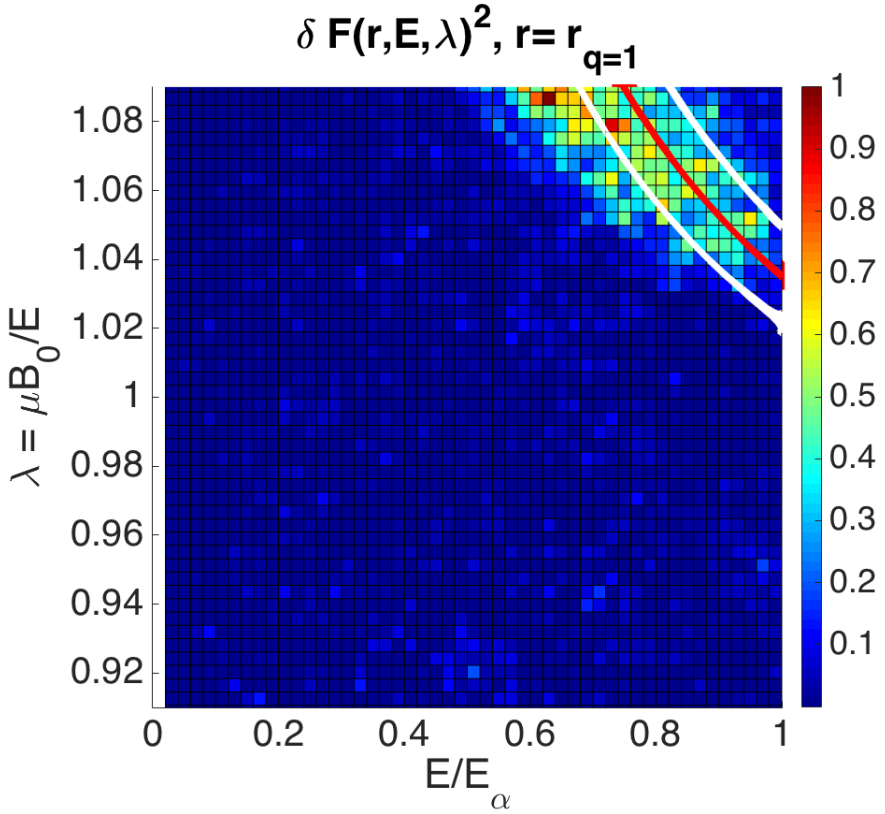

Figure 5.11: Perturbed kinetic distribution function squared δF^2 obtained from a XTOR-K simulation. It is taken at the late linear phase of the fishbone instability, and projected on the (E, λ) on the radial slice $r \in [r_{q=1} - \delta r, r_{q=1} + \delta r]$. The red and white curves corresponds to the theoretical position of the precessional resonance at different radial positions. Red for $r = r_{q=1}$, and white for $r = r_{q=1} \pm \delta r$. The resonant structure acquired from XTOR-K is coherent with the theoretical position of the resonance.

On Figure (5.11), the results obtained from the linear theory and XTOR-K phase space diagnostics are presented. They have been acquired by considering the beta ratio $\beta_h/\beta_{tot} = 8\%$ (see Figure (5.9)). For this simulation, the mode pulsation is $\omega\tau_A = 4.10^{-3}$. This value has been used to solve $\omega = \omega_d$. The color dots on this figure correspond to the perturbed kinetic distribution function squared δF^2, computed on the (E, λ) diagram between the two radial grid points on which lies the $q = 1$ surface $r_{q=1}$. It is noted that the (E, λ) diagram considered lies in the trapped domain, since only the precessional resonance is of interest here. On Figure (5.11), δF corresponds to the perturbed distribution function taken at the end of the linear phase, before the fishbone mode saturates. This simulation has been continued further in the nonlinear phase, it will be discussed in Chapter 6.

The red curve on Figure (5.11) is the solution of $\omega - \omega_d(E, \lambda, r_{q=1})$ in the (E, λ) diagram. Since δF^2 has been computed in XTOR-K for kinetic particles with radial positions such as $r \in [r_{q=1} - \delta r, r_{q=1} + \delta r]$, it is necessary to evaluate the error bars associated to this radial interval. These error bars can be provided by the linear theory, solving $\omega - \omega(E, \lambda, r_{q=1} - \delta r)$ and $\omega - \omega(E, \lambda, r_{q=1} + \delta r)$ in the (E, λ) diagram. The solutions of these equations are illustrated by the white curves on Figure (5.11). The theoretical position of the resonance is almost identical to the resonance's position obtained from XTOR-K, the structure observed on the δF^2 diagnostic lying nearly entirely inside the white curves.

The linear verification of XTOR-K by the fishbone linear model has now been fully addressed. Complex mode frequencies and resonance position obtained with the hybrid code match quantitatively those computed from the linear model.

5.4 Stability of the ITER equilibrium against the alpha fishbone instability

XTOR-K can now be used on equilibria that are beyond the scope of the fishbone linear model. In this section, the linear stability of the ITER 15 MA scenario against the alpha fishbone is studied with XTOR-K. Such a study has already been carried out in two previous works [Hu et al., 2006][Fu et al., 2006], respectively through linear theory and hybrid simulations performed with the nonlinear code M3D-K. Results acquired from XTOR-K simulations are compared to these previous works.

5.4.1 Equilibrium used

This study is based on profiles inspired from integrated simulations performed with the code Corsica [Imbeaux et al., 2015] on the ITER 15 MA case. Profiles have been adjusted at the plasma edge to obtained null pressure gradient, needed for initial values codes such as XTOR-K. The current profile has been modified in order to obtain parabolic q profile with on-axis value below unity, which facilitates the study of $n = m = 1$ modes. Also, the plasma resistivity has been decreased from $S = 3.10^9$ to $S = 1.10^7$ in order to resolve the mode inertial layer. Such a layer gets too thin for ITER relevant Lundquist numbers, and cannot be resolved by the radial resolution used in these XTOR-K simulations. 200 grid points are used in the radial direction. The on-axis ion/electron bulk temperatures are set at 20 keV, the bulk density at 10^{20} m^{-3}. In the different simulations performed, the only free parameters are the on-axis kinetic density, and the shape of the current profile. They are used respectively to explore the different instability branches, and to set the on-axis safety factor . Bulk diamagnetic effects have not been added to these hybrid simulations. The kinetic density profile is the same as the one used for the linear verification. Such a profile is rather peaked, its relevance is discussed in the latter part of this chapter. An isotropic slowing distribution function with birth $E_b = 3.5MeV$ is used to describe alpha particles. On Figure 5.12, several features of the Kinetic-MHD equilibrium are presented.

5.4.2 Results for flat q profile and peaked alpha density profile

Two sets of simulations have been performed for this analysis. Different q profiles have been used, with on axis values of 0.9 and 0.95, same edge safety factor and same radial position for the $q = 1$ surface, $s_{q=1} = 0.35$. It ensures to only study the impact of the on-axis safety

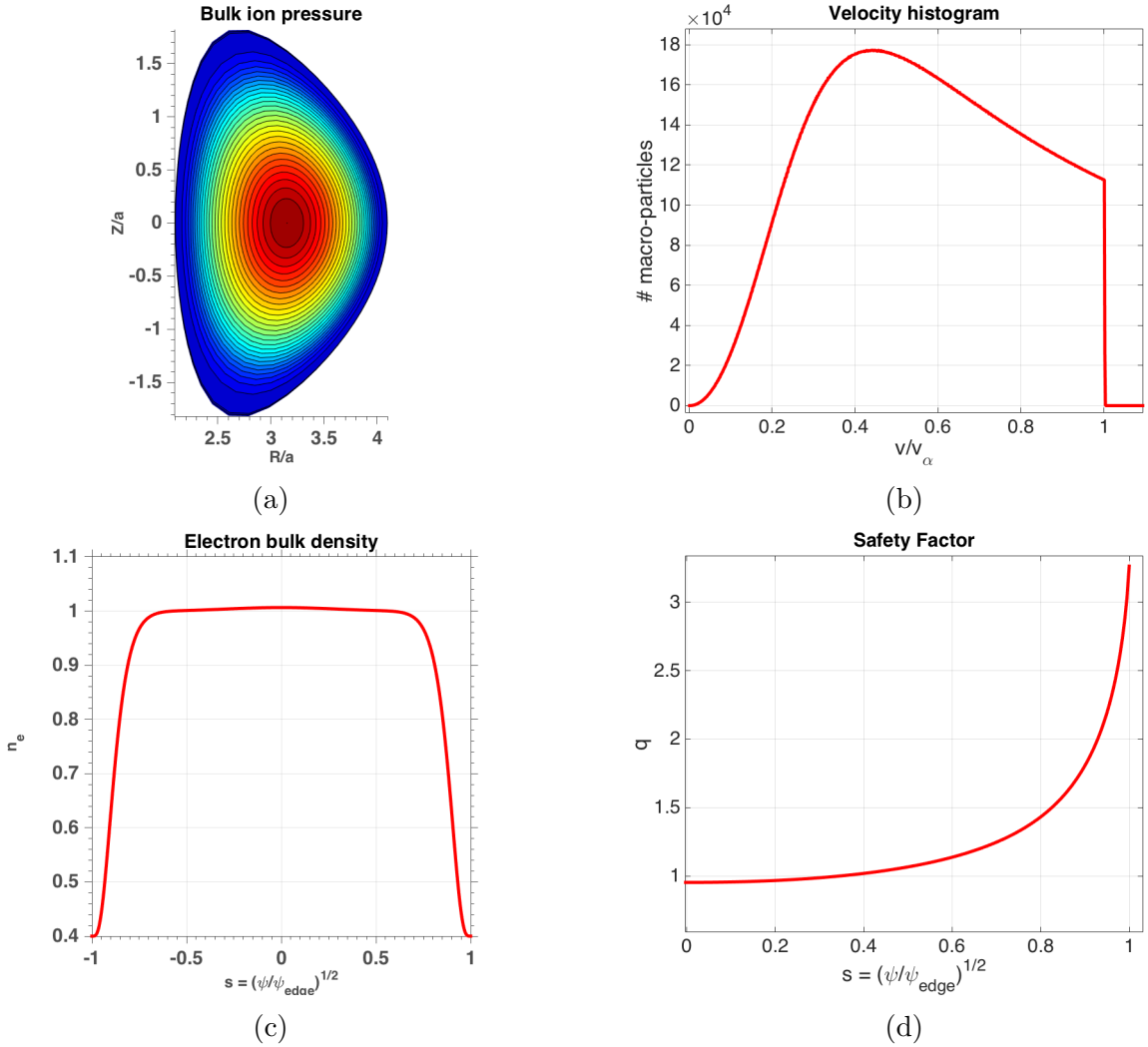

Figure 5.12: Kinetic-MHD equilibrium defined for the ITER 15 MA case. (a) The bulk ion pressure in the poloidal plane, which highlights the equilibrium geometry. (b) The alpha distribution function velocity histogram, for $E_b = 3.5$ MeV and $T_{e,0} = 20keV$. (c) The electron bulk density profile. (d) The q profile, that is chosen to be parabolic with on axis values below unity

factor when varying the q profiles. The alpha beta is evolved from 0 to 12% of the total plasma beta. Such a range is lower than the expected beta ratio [iTER physics basics, 2000] on ITER, where depending on the on-axis temperature, $\beta_\alpha/\beta_{tot} \in [15\%, 20\%]$. This is not restrictive since the point of these linear simulations is to find the fishbone threshold in beta ratio. For both cases studied, they lie below $\beta_h/\beta_{tot} = 12\%$

As discussed in 4.1.5 and 5.3.1, results shown on Figure 5.13 recover the characteristics of the interaction between fast particles and 1,1 modes. A kink and a fishbone branch appear in both cases. Points displaying null growth rates on Figure (5.13) (a) do not necessarily describe stable configurations. Points marked with null frequencies are those where no modes emerge from the noise level after $t = 4000\tau_A$. Such points can be indeed stable, or unstable with a growth rate low enough to prevent them from raising above the noise level after $4000\tau_A$. This kind of situation is depicted on Figure 5-16, where magnetic energies from cases $\beta_\alpha/\beta_{tot} = 6\%$ and 8% with $q_0 = 0.95$ are compared. The $n = 1$ harmonic at $\beta_\alpha/\beta_{tot} = 8\%$ emerges from the noise and becomes unstable. The $n = 1$ harmonic at $\beta_\alpha/\beta_{tot} = 6\%$ does not rise above the noise level defined by the harmonics $n = 2, n = 3$.

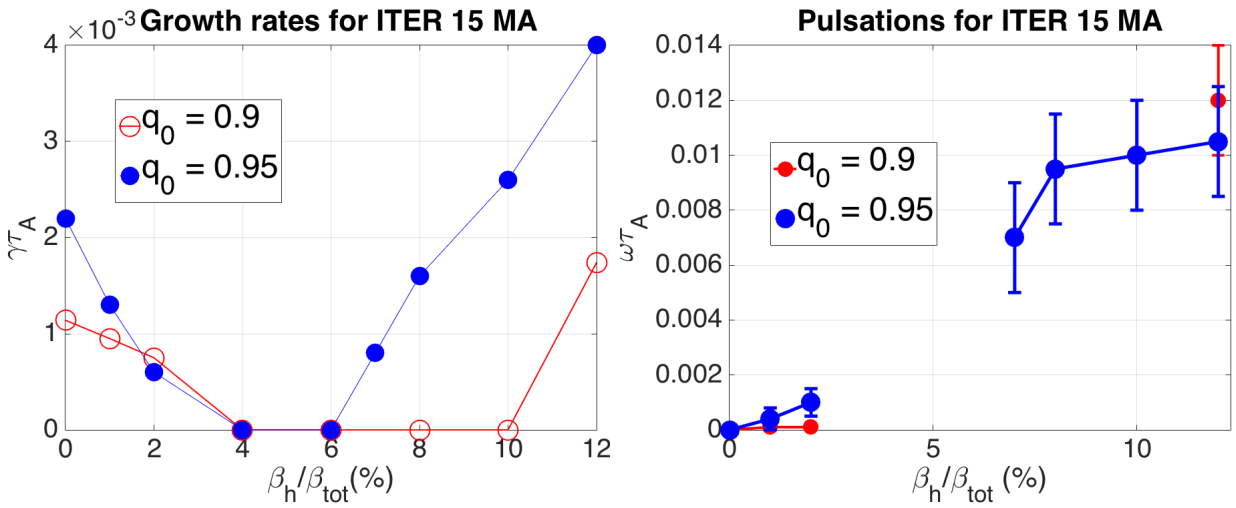

(a) (b)

Figure 5.13: Instability growth rates (a) and pulsations (b) for the ITER 15 MA case, with in red results with $q_0 = 0.9$, and in blue $q_0 = 0.95$

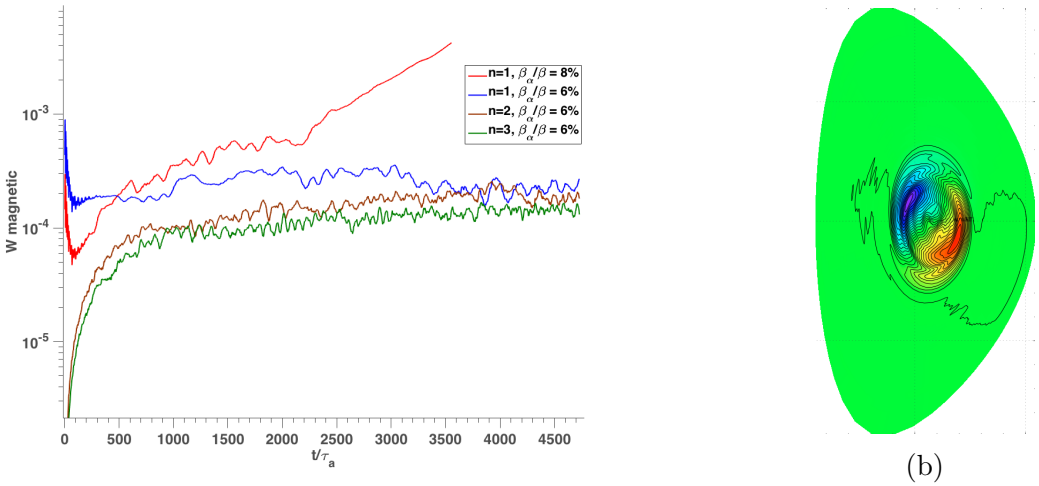

(a) (b)

Figure 5.14: (a) Magnetic energies of $m = 1$ modes, for several n harmonics and beta ratio. (b) Perturbed electronic temperature in the poloidal plane during the linear phase, that exhibits the inherent noise level

These results show that the fishbone threshold is a decreasing function of the on-axis safety factor. For $q_0 = 0.95$, the threshold is located at $\beta_h/\beta_{tot} = 5\%$, while for $q_0 = 0.9$, the fishbone branch starts around 10%. Given the low variation applied on q_0, the fishbone threshold is quite sensitive to the safety factor used. The growth rates without alpha particles are different between the two set of simulations studied. The fluid growth rate derived in [Bussac et al., 1975] scales like $1 - q_0$, which explains the factor two of difference between the growth rates without fast particles.

The error bars on Figure 6.20 (b) are due to the noise level in the ITER simulations. The mode pulsation is obtained in XTOR-K by computing $\omega = \omega_{E\times B} - \omega_{lab}$. $\omega_{E\times B}$ refers to the cross field rotation of the whole plasma, and can be easily computed. ω_{lab} refers to the rotation rate of the mode instability. It is computed by locating the maxima of a perturbed

quantity on the flux surface $q = 1$, at a given toroidal position. Figure (5.14) (b) shows for example the perturbed electron temperature at $\varphi = 0$ in the linear phase of the simulation. It can be seen on this figure that a certain level of noise is present, the 1,1 mode structure not being symmetric. It prevents a precise localization of the perturbed quantity maximum. Therefore, it induces an error on the measurement of ω, quantified by the error bars on Figure (6.20) (b).

5.4.3 Comparison of XTOR-K's results with earlier works

The results obtained with XTOR-K hybrid simulations reveal that both Kinetic-MHD equilibria studied become unstable against the fishbone instability at low kinetic beta. For the two sets of simulations performed, the fishbone thresholds lie below the expected $\beta_\alpha/\beta_{tot} = 15 - 20\%$ beta ratio in [iTER physics basics, 2000], by a factor up to 3 for the set $q_0 = 0.95$. The alpha fishbone instability is therefore likely to be unstable on the ITER 15 MA scenario, according to the simulations presented.

However, earlier results find the fishbone instability to be either unstable [Hu et al., 2006] or stable Fu et al. [2006] on the ITER 15 MA scenario. The equilibrium parameters used in these works need to be presented and compared to those used in XTOR-K, to assess in greater depth the linear stability of the ITER configuration.

Results from [Hu et al., 2006] have been obtained with a linear model fairly similar to the one developed in 4.1. Complex geometries are allowed in this model, and kinetic effects of the bulk plasma are derived, to take into account the kinetic bulk ion inertia enhancement. Such bulk kinetic effects are not taken into account in XTOR-K's alpha fishbone simulations. The equilibrium used in this work is quite similar to those defined in 5.4.1, with for example parabolic q profiles with $q_0 = 0.9$. A notable difference though is the alpha density profile used in this work. It is not defined arbitrarily as defined in 5.4.1, but obtained by balancing the source of fusion born alpha particles and their loss due to thermalization. These results show, for the unique beta ratio of 7% considered, that there exists a threshold on β_{tot}, keeping β_α/β_{tot} constant, above which the equilibrium is fishbone unstable. In 5.4.2, for $q_0 = 0.9$, the fishbone is triggered at a beta ratio around 10% for a fixed β_{tot}. Therefore, results obtained between XTOR-K on the ITER 15 MA scenario are in good agreement with those in [Hu et al., 2006].

However, global hybrid simulations performed with M3D-K [Fu et al., 2006] do not agree with such results. In this work, for $q_0 = 0.95$ and $\beta_h/\beta_{tot} = 15\%$, the internal kink is only stabilized, with a growth rate that is 50% below the one without fast particles. In comparison, at 12% of beta ratio and $q_0 = 0.95$, XTOR-K simulations show that the internal kink is fully stabilized and that the fishbone instability is triggered. Such a discrepancy with the results obtained in 5.4.2 and those of [Hu et al., 2006] can be explained by a number of points. First, the total beta used in M3D-K ITER simulation is $\beta_{tot} = 6.5\%$, and only $\beta_{tot} = 5.75\%$ in XTOR-K. It can then be expected that the $q = 1$ poloidal beta is higher in M3D-K, which implies that the internal kink without fast particles is more unstable in M3D-K's simulations. A higher alpha density than in XTOR-K's simulations is then required to fully stabilize the kink.

Moreover, as shown in Figure 5.15, the normalized alpha density gradient used in M3D-

K is much lower that those taken in [Hu et al., 2006] and XTOR-K, by a factor of 3 when considering a q=1 radius around $s = \sqrt{\psi/\psi_{edge}} = 0.4$. As shown in equation (4.53), the kinetic drive is directly proportional to the alpha density gradient. Therefore the fishbone threshold is a decreasing function of ∇n_α. Given that in the corresponding XTOR-K simulation, the beta ratio threshold is $\sim 10\%$, the threshold in [Fu et al., 2006] should lie $\sim 30\%$. It explains why only a stabilization effect is recovered at $\beta_h/\beta_{tot} = 15\%$ for the ITER 15 MA case in [Fu et al., 2006].

It is interesting to note that the arbitrarily defined alpha density profile used with XTOR-K is quite similar to the one obtained with realistic density of alpha particles, when considering $s_{q=1} \sim 0.4$. A realistic density profile for alpha particles can be derived with a source S_{fusion} due to fusion reactions, and a sink due to alpha thermalization such as

$$\frac{\partial n_\alpha}{\partial t} \equiv S_{fusion} - P_{thermalization} = \frac{n_i^2}{4}\langle\sigma v\rangle - n_\alpha \tau_{th} \tag{5.1}$$

At steady state, $\partial_t n_\alpha = 0$, and according to (5.1), $n_\alpha(r) = n_i^2\langle\sigma v(T_i(r))\rangle\tau_{th}(r)/4$, with τ_{th} the thermalization time, of order 1 second in ITER [iTER physics basics, 2000]. This thermalization time scales radially as $\tau_{th}(r) \propto T_e(r)^{3/2}$ when considering flat bulk density. The reaction rate scales as $\langle\sigma v(T_i)\rangle \propto e^{0.1T_i(r)}$ for $T_i \in$ [10 keV ,20 keV] [Wesson and Sen, 1989]. Therefore, the alpha density radial dependency is $n_\alpha(r) \propto T_e(r)^{3/2} e^{[0.1T_i(r)]}$. The realistic alpha gradient is plotted in green on Figure (5.1). The ad hoc profile used in XTOR-K's simulation is then well suited to analyze the ITER 15 MA scenario linear stability against the alpha .

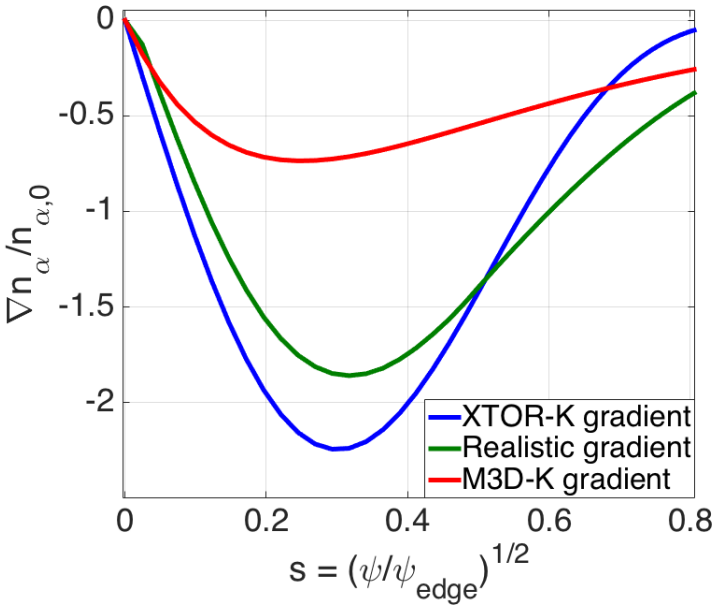

Figure 5.15: Compared normalized alpha particle gradients between different linear study of the fishbone instability on the ITER 15 MA case. In red the gradient used in M3D-K's simulations, in green the realistic gradient computed from the bulk electronic and ionic temperature, and in blue the one used in XTOR-K's simulations.

It can then be concluded that the ITER 15 MA scenario is indeed likely to be unstable against the alpha fishbone, since a ITER relevant alpha density profile has been used in XTOR-K's linear simulations.

5.5 Conclusion

The linear verification of the hybrid code XTOR-K by the fishbone linear model developed in 4.1 has been detailed in this chapter. First, the particles eigenfrequencies in XTOR-K have been verified through theoretical expressions obtained from the angle-action formalism. Then, taking into account the restrictive assumptions of the linear model, a suitable Kinetic-MHD equilibrium has been defined for XTOR-K's linear verification. Results for the complex frequencies $\omega + i\gamma$ obtained with XTOR-K are in good quantitative agreement with those computed from the fishbone linear model. Such results confirm the correct implementation of kinetic modules in XTOR-K. Furthermore, the specificities retain in the linear model have revealed to be essential for the verification of XTOR-K. Finally, the linear verification has been completed by identifying the zones of resonant interaction in the 3D invariants space. The theoretical position of the precessional resonance was found to be consistent with the resonant structure obtained from XTOR-K's phase space diagnostics.

The linear verification of XTOR-K has enabled to conduct a series of linear hybrid simulations on the ITER 15 MA scenario. The fishbone instability was studied for ITER relevant parameters. It was shown that the fishbone kinetic beta thresholds lie well below the operational alpha beta expected on ITER [iTER physics basics, 2000]. These results obtained with XTOR-K are then discussed with previous studies performed on the ITER 15 MA scenario. It is noted that the alpha density gradient used in XTOR-K's simulations is relevant to the realistic alpha density on ITER. It is then concluded that the alpha fishbone instability is likely to be triggered on the ITER tokamak.

Chapter 6

Fishbone-induced transport of fast particles

In the previous chapter, it has been established that the alpha fishbone instability will likely be triggered during burning plasmas experiments on the ITER tokamak. Therefore, first principle simulations in the nonlinear phase of the fishbone instability are essential. They can be used to predict and control the redistribution of fast particles occurring during fishbone oscillations. Such simulations can also evaluate to which extent kinetic particles affect the sawteeth period. At the present time, self-consistent hybrid simulations over an entire sawtooth cycle are requiring a too long computational time. Yet, it is possible to assess with reasonable computing time the particles resonant transport during fishbone oscillations appearing before a sawtooth crash. In this chapter, the aim is then to study particle transport during alpha fishbone oscillations prior to complete magnetic reconnection. This study is performed by simulating the instability in its nonlinear phase using the code XTOR-K, linearly verified in the previous chapter. For this study, isotropic slowing-down distribution functions of alpha particles have been imposed at the beginning of the simulations. The assumption of taking an imposed distribution, and not one generated by a source of alpha particles and collisions between kinetic particles and the bulk plasma will be discussed in this chapter. Characteristic resonant transport and thermalization times will be compared.

As described in the literature, two nonlinear regimes exist for the fishbone instability. The first one is the low kinetic drive limit, where the considered equilibrium is close to the fishbone threshold [Berk et al., 1999] [Odblom et al., 2002] [Breizman and Sharapov, 2011] [Idouakass, 2016], where $|\gamma - \gamma_L| \ll \gamma_L$. γ and γ_L are respectively the fishbone linear growth rates for a given equilibrium, and at the fishbone threshold. For this regime, the resonant islands in phase space are evolving on a characteristic time τ_{NL} much smaller than the bounce time inside these islands τ_B. This regime is likely to arise when MHD activity occurs while fast particles begin to be generated by fusion reactions. The other regime is the strong kinetic drive limit, where the considered equilibrium is far away from the fishbone threshold, $\gamma > \gamma_L$ [Zonca et al., 2015][Vlad et al., 2013]. There, the evolution time of the resonance structure is equivalent or smaller to the bouncing time in the structure, $\tau_{NL} \sim \tau_B$. This regime arises when MHD activity is triggered after the formation of a stationary fast particle distribution function, with a kinetic beta well above the fishbone threshold. XTOR-K solves the extended MHD equations in 3D toroidal geometry and self-consistently advances kinetic particles in 6D inside the whole torus. Therefore, it takes into account all nonlinearities. For this reason, it is an ideal tool for the study of the fishbone instability in any regime.

In this chapter, the nonlinear phase of the alpha fishbone instability is firstly studied on

an ITER-like equilibrium, similar to the one used for the linear verification. This equilibrium is expected to lie in the strong kinetic drive limit. In the nonlinear phase, the simulation exhibits frequency chirping of the mode, associated with resonant particle transport. Detrapping of resonant particles in phase space is also observed in this simulation. Then, the alpha fishbone instability is studied on the ITER 15 MA scenario. Two simulations are performed in each of the nonlinear regimes. Results obtained from the strong kinetic drive limit are coherent with the ITER-like nonlinear simulation. A weak redistribution of alpha particles out of $q = 1$ is predicted by the simulation. A total transport of order 5% of the initial distribution is observed over several fishbone oscillations on the ITER 15 MA scenario. Preliminary results have been obtained for the low kinetic drive limit. They are found consistent with those of previous works [Odblom et al., 2002][Idouakass, 2016].

6.1 ITER-like case far from fishbone threshold

For the first nonlinear simulation of fishbone oscillations performed with XTOR-K, it has been chosen to consider a simple equilibrium whose linear phase can be predicted by the fishbone linear model. The fishbone threshold can therefore be predicted easily, so that the instability indeed lies on the desired nonlinear regime. Moreover, it also enables to know in advance the phase space zones in which the mode will resonate with kinetic particles. Indeed, for an equilibrium with circular flux surfaces, equations (A.7),(A.18),(B.11),(B.14) are characterizing the particles eigenfrequencies ω_b, ω_d in the 3D invariants space.

The Kinetic-MHD equilibrium described in this nonlinear simulation is then chosen to be the same as in 5.2.4. The only exception is that the on-axis ion bulk density is of $2.10^{19}\mathrm{m}^{-3}$ rather than 3.10^{19}. Such a modification enables to lower the linear growth rate without fast particles to $\gamma_{MHD}\tau_a = 7.10^{-4}$. The fishbone threshold then arises at lower kinetic beta. It permits to conduct a nonlinear simulation in the strong drive limit with a relatively small beta ratio of $\beta_\alpha/\beta_{tot} = 8\%$. This is preferable for a nonlinear simulation since the noise brought by the PIC module is smaller in that case. 300 millions macro-particles are used in the simulation to ensure that the noise level is not critical. Only four n harmonics are retained in the fluid part, with 20 poloidal modes, given that the instability of interest is a $n = m = 1$ mode.

6.1.1 Nonlinear dynamics of the MHD fields

The modes' time evolution are presented in Figure 6.1. The noise level is well below the oscillations of the different energies, ensuring that the simulation is not limited by the PIC module. Four phases can be dissociated in this simulation. A first phase lasting until $t = 4000\tau_A$ is dominated by PIC noise. The modes energies are not yet larger than the noise level. Then, from $t = 4000\tau_A$ to $t = 9500\tau_A$, a fishbone linear phase is visible, with the 1,1 mode growing exponentially with $\gamma\tau_A = 1.1 \times 10^{-3}$, and a constant mode frequency $\omega\tau_A = 4.10^{-3}$ (Figure 6.2). The linear growth rate is far above the fishbone threshold predicted by the linear theory. The 2,2 and 3,3 modes are also getting pumped by toroidal coupling.

A nonlinear fishbone phase occurs afterwards. Two 1,1 mode amplitude roll-over arise at $t/\tau_A = 1.10^4,\ 1.2 \times 10^4$. These roll-over are identified as fishbone oscillations. As shown on Figure 6.2, this nonlinear phase is accompanied by down chirping of the 1,1 mode frequency. This nonlinear phase has been associated to the fishbone instability since the saturation observed differs from the classical internal kink case. For a 1,1 internal kink, in the nonlinear phase, magnetic reconnection at the resonant surface q=1 is causing the mode saturation.

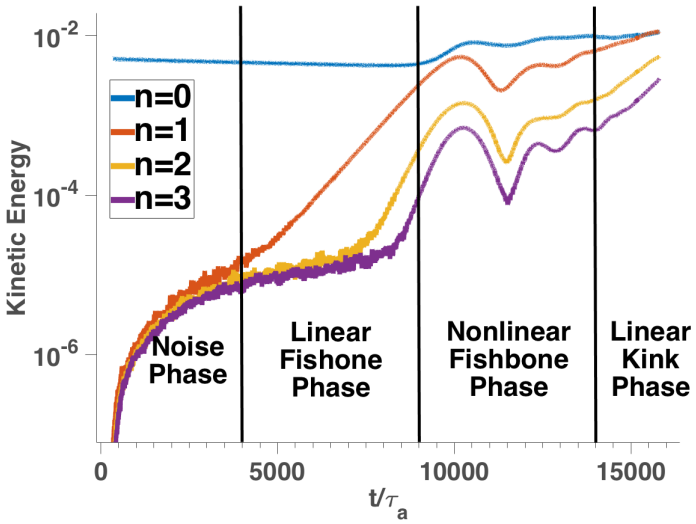

Figure 6.1: Kinetic energy of the toroidal harmonics, for all n resolved in the simulation. A linear phase is dominated by the 1,1 mode until $t = 9500\tau_A$. Then, a nonlinear phase occurs. It is characterized by two fishbones oscillations, identified during the 1,1 mode saturations at $t/\tau_A = 1.10^4, 1.2 \times 10^4$. It is followed by an linear internal kink phase at $t/\tau_A = 14000$.

In this case, as displayed on the Poincaré plots on Figure 6.3, magnetic reconnection does happen at the end of the linear phase and during saturation (Figure 6.3 (a) and Figure 6.3 (b)). A clear 1,1 island appears on the q=1 surface that lies at $r = 0.4$. However, because of its size, the observed island cannot alone explain the mode saturation, as well as the mode frequency down chirping. Moreover, mode chirping is a characteristic feature of the fishbone instability [Nave et al., 1991]. This point is further confirmed on Figure 6.4 (a), where the safety factor profile has been plotted at characteristic times of the simulation. During the fishbone phase, at $t = 1.1\ 10^4\tau_A$, the q profile is weakly flattened around $q = 1$. The saturated fishbone is observed in Figure 6.3 (b).

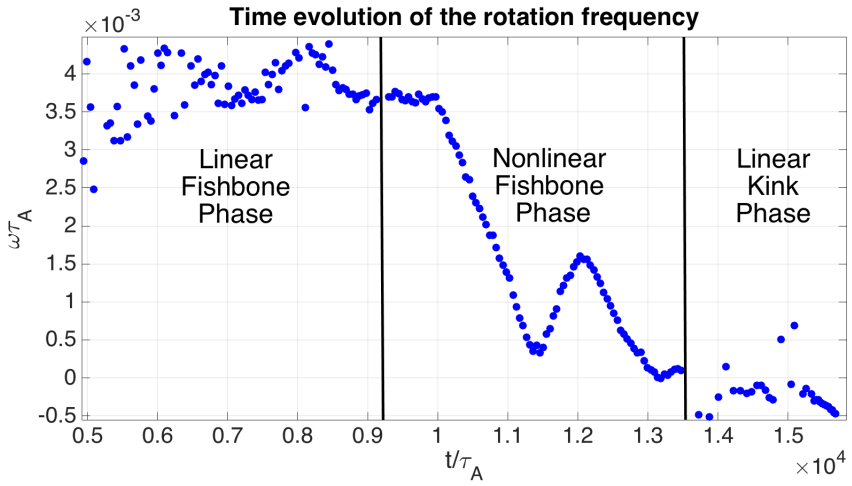

Figure 6.2: Time evolution of the 1,1 mode frequency. As expected the mode pulsation is almost constant during the linear phase, and then chirps down significantly during the fishbone phase. It is almost zero during the kink phase.

A linear internal kink phase appears after the mode frequency down chirping is over at $t/\tau_A = 1.4 \times 10^4$. In fact, as displayed on Figure 6.3 (c) (d), the 1,1 island has grown signifi-

cantly in this phase, and the core plasma begins to get evacuated by the $n = m = 1$ island. At the end of the simulation, the q profile (Figure 6.4) is largely flattened around q=1. This dynamics correspond to a standard resistive internal kink. The nonlinear simulation was stopped at this stage, since the simulation of an entire sawtooth cycle with kinetic particles requires a too long simulation time.

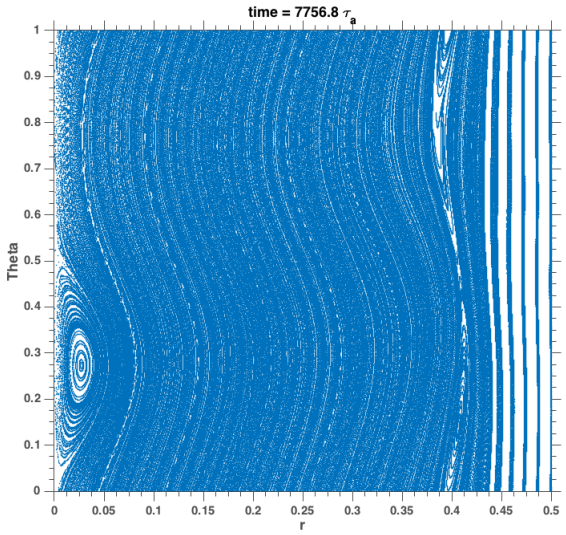

(a) $t = 7756.8\tau_A$

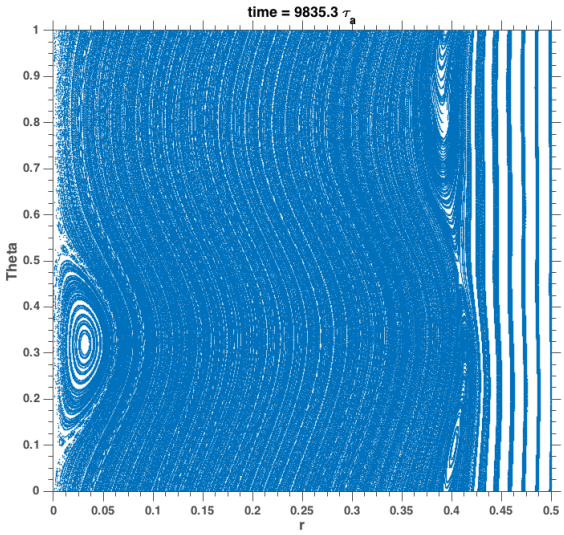

(b) $t = 9835.3\tau_A$

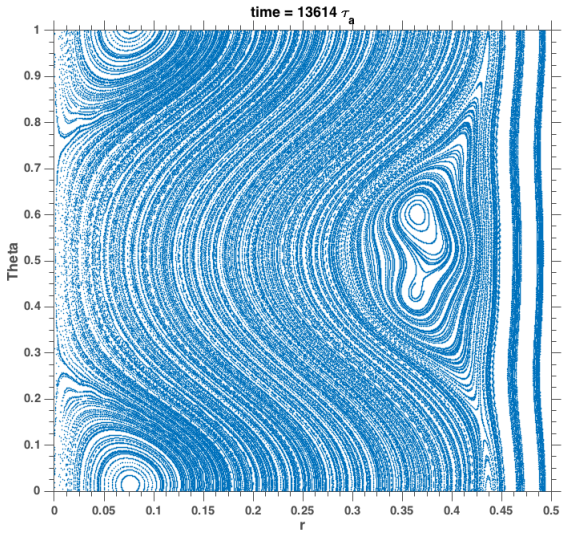

(c) $t = 13614\tau_A$

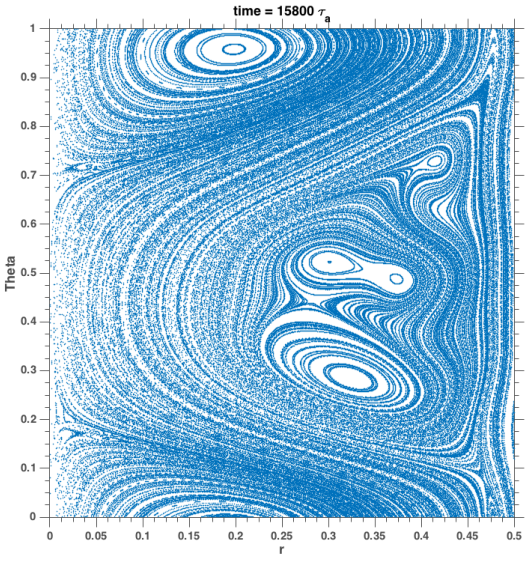

(d) $t = 15800\tau_A$

Figure 6.3: Poincare plots in the polar plane (r, θ) taken at selected times of the simulation. (a) End of the linear fishbone phase, a 1,1 island begins to grow on q=1. (b) Saturation of the 1,1 fishbone mode, the island on q=1 is somewhat larger.Be (c) Beginning of the linear kink phase, with the growth of a large $m = m = 1$ island. (d) End of the simulation, the core plasma begins to be evacuated by magnetic reconnection with the 1,1 island on $q = 1$.

Even if these fluid diagnostics enables to dissociate the different phases of the simulation, they do not however permit to understand the main mechanism at play during the nonlinear fishbone phase. A detailed study of the alpha-like particles distribution function dynamics in

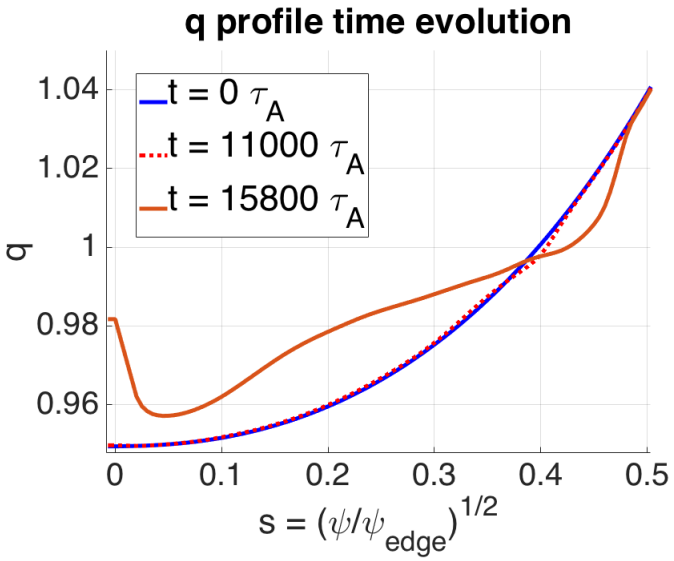

Figure 6.4: (a) Evolution of the safety factor profile. During the linear (blue line) and nonlinear (red dotted line) fishbone phase, the profile does not evolve much. It is only weakly flattened around $q = 1$ during the nonlinear phase. However, it is significantly flatten in the linear internal kink phase (brown line), which is characteristic of the beginning of magnetic reconnection.

invariants space is required. To this purpose, the phase space diagnostics presented in 4.2.2 are used.

6.1.2 Nonlinear evolution of the alpha distribution function in phase space

Before looking at the nonlinear time evolution of the wave-particle energy exchange and of the distribution function in the invariants space, it is very useful to know in advance in which zones of invariants space the resonances lie, and what kind of resonances are involved. It enables to dissociate the weakly nonlinear regime, where the resonances positions do not evolve, from the deep one where the resonances position change due to mode chirping and evolution of the invariants of motion. As it was explained above, equations (A.7),(A.18),(B.11),(B.14) can be used to obtain the initial resonance positions, since the Kinetic-MHD equilibrium considered has circular cross sections and a low slowing-down birth energy E_b =1 MeV. For this equilibrium, it was observed that mostly trapped particles interact resonantly with the 1,1 mode, through their precessional frequency. The passing resonance condition $\omega - [1 - q(\bar{\psi})\omega_b] - \omega_d$ is marginally met in invariants space in this case.

The resonance curves in the (E, λ) diagram at different radial positions are shown on Figure (6.5). The resonant curves lie at higher pitch angle and energy values when the radial position is increased, coherent with the fact that $\omega_d \propto E\lambda/r$ (see equations (B.11,B.14)). During mode down chirping, it is then expected that the resonances are all shifted at lower pitch angle and energy values. In this diagram, two zones have been identified. One where the kinetic trapped particles are very likely to resonate with the mode, and one where they are not. These curves will be useful when analyzing the time evolution of the wave particle resonance.

The time evolution of the perturbed kinetic particles density profile is plotted on the diagram $(s, t/\tau_A)$ on Figure (6.6). $s = \sqrt{\psi/\psi_{edge}}$ is the normalized radial position. Three cases

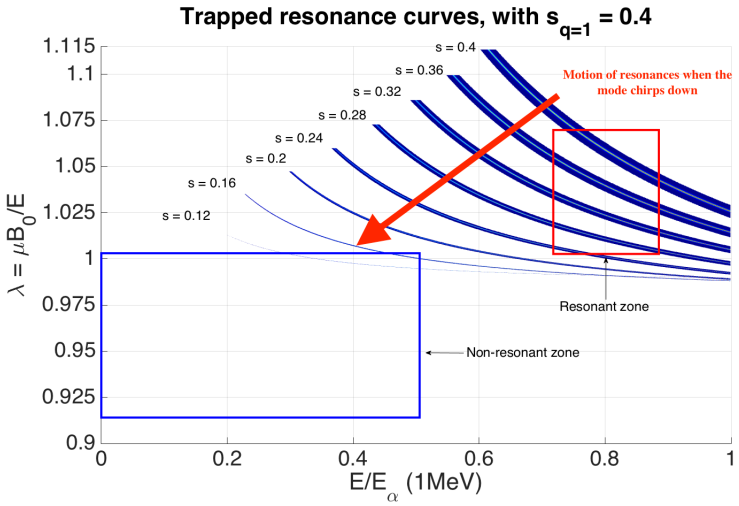

Figure 6.5: Positions of the precessional resonance on the (E, λ) diagram for trapped particles, at different radii. Two zones are identified, a zone free from resonances (blue) and one crossed by many resonances (red). When the MHD mode frequency chirps down, the resonant curves are displaced at lower energies and pitch angles.

have been considered on these diagrams. Figure 6.6 (a) displays the entire perturbed kinetic density, (b) the perturbed kinetic density of only trapped particles and (c) of only passing particles. It can be seen that particle transport from inside $s_{q=1} = 0.4$ to this surface occurs for all classes of particles during the first mode saturation. The particle transport is mostly dominated by trapped particles, as it was expected given the resonant patterns in Figure 6.5. Two peaks of transport are observed at $t/\tau_A = 1.10^4,\ 1.2 \times 10^4$. These peaks correspond to the fishbone oscillations that occur when the 1,1 mode saturates in the nonlinear fishbone phase (Figure (6.1)). Around 15% of the initial trapped distribution is transported towards q=1 during the fishbone oscillations, whereas only a few percents of passing particles are concerned. Since the equilibrium fraction of trapped particles scales as the inverse aspect ratio ϵ, only a few percents of all particles are transported from the core plasma towards $q = 1$.

During these oscillations, the MHD displacement is not large enough to explain the outward particle transport, and could not account for a transport of mostly trapped particles. An other mechanism must be introduced to explain this dynamics. The global transport is not shown in the linear internal kink phase, since there the MHD displacement pushes the entire plasma towards $q = 1$. The fluid transport cannot be dissociated from an other transport mechanism.

As expected from the resonant patterns in Figure (6.5), and from the experimental behavior of the fishbone instability [Nave et al., 1991], the mechanism at play here is the resonant transport of kinetic particles. Such a mechanism is clearly revealed in Figures (6.7) and (6.8). On Figure (6.7), the perturbed distribution function between the end of the fishbone phase and the beginning of the simulation is plotted on the (E, λ) diagram for two different radial slices, $r = 0.5 r_{q=1}$ (Figure 6.5 (a)) and $r = r_{q=1}$ (Figure 6.5 (b)). $r_{q=1}$ is the radial position of the $q = 1$ surface.

At $r = 0.5_{q=1}$, around 40% of the trapped particles are transported out of the radial slice in a zone of invariants space in which the precessional resonance lies, according to Figure (6.5). The resonant zone observed is larger than the initial resonant curve on Figure (6.5) for $s = 0.2$. It affects about a quarter of the (E, λ) diagram, with $E \in [0.4, 1]$, $\lambda \in [1, \lambda_{max}]$.

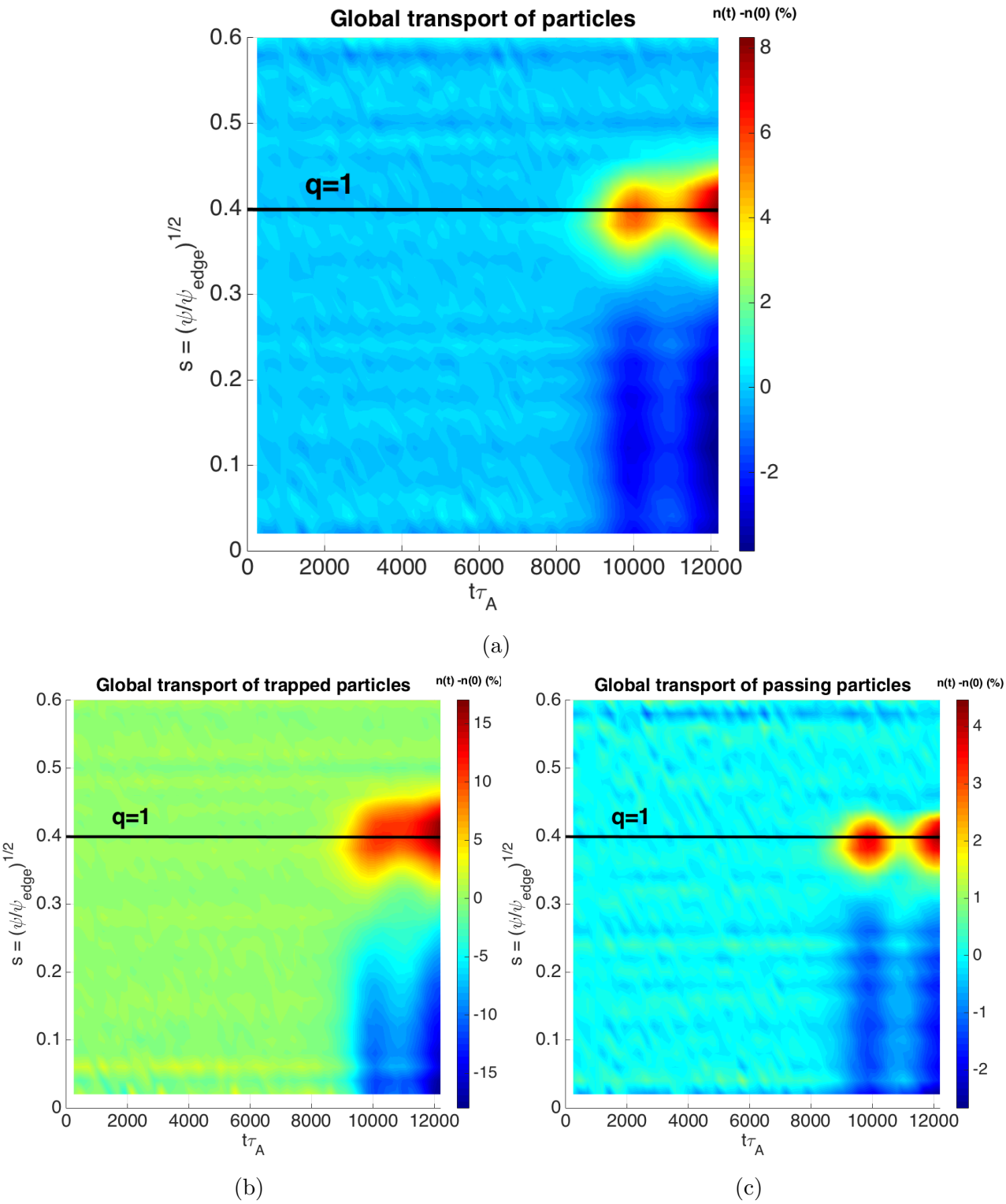

Figure 6.6: Global transport of particles on the $(s, t/\tau_A)$ diagram, with s the normalized radial position. The z axis corresponds to perturbed density in percentage between the time t and the initial density. (a) Transport of all kinetic particles in the simulation (b) Transport of trapped particles (c) Transport of passing particles

At q=1, in approximately the same zone of invariants space, a gain of 140% of the initial population is observed.

On Figure (6.8), the density profile of fast particles is plotted in the resonant and non-resonant

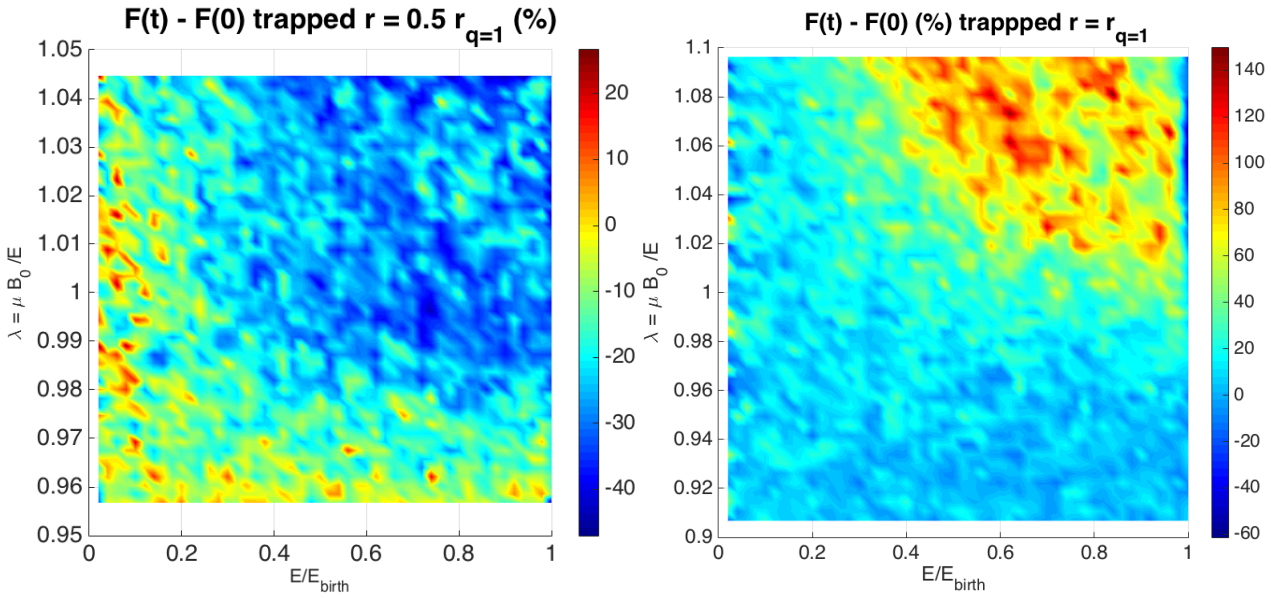

(a) (b)

Figure 6.7: Total transport on the (E, λ) diagram between the beginning and end of the simulation. The transport is presented at two different radii. (a) At the mid q=1 radius, it can be seen that particles located in the resonant zone are transported outward (40%). (b) At the q=1 surface, the density in the resonant zone has more than doubled (140%), particles coming from lower radial layers arriving to the q=1 surface.

zones of invariants space found in Figure (6.5). These figures clearly show a flattening of the density profile inside of q=1 where resonances can occur (a), at characteristic times coherent with the nonlinear fishbone phase. The flattening is not present in the second zone of invariants space (b), except at the very end of the simulation in the linear kink phase due to the MHD displacement that affects the entire plasma. Figures (6.6), (6.7) and (6.8) therefore show that an net outward radial transport of kinetic particles towards $q = 1$ is observed in the simulation. Fast particles cannot be transported further since they are transported through resonant interaction with the $n = m = 1$ mode. This mode vanishes beyond $q = 1$.

Partial mechanism explaining resonant transport

This nonlinear simulation lies in the strong kinetic drive limit, where $\tau_{NL} \sim \tau_B$. It means that the nonlinear evolution of the resonant island evolves on a time scale comparable to the bounce time of resonant particles inside this island. Therefore, resonant islands in this limit are virtual. The notion of island is used here to guide the discussion. A partial mechanism is proposed here to explain the role of virtual islands in the net outward radial resonant transport observed. This mechanism is proposed on the basis of observations made on this hybrid simulation, they will be detailed after this discussion. The part of mode frequency down chirping in this mechanism is highlighted.

The equations describing the nonlinear evolution of trapped particles due to the precessional resonance are presented here. They can be obtained by deriving the Hamilton-Jacobi equations of the perturbed Hamiltonian in equation 2.55

$$\frac{dP_\varphi}{dt} \equiv -\frac{\partial H}{\partial \alpha_3} = h(t) \sin \Theta \tag{6.1}$$

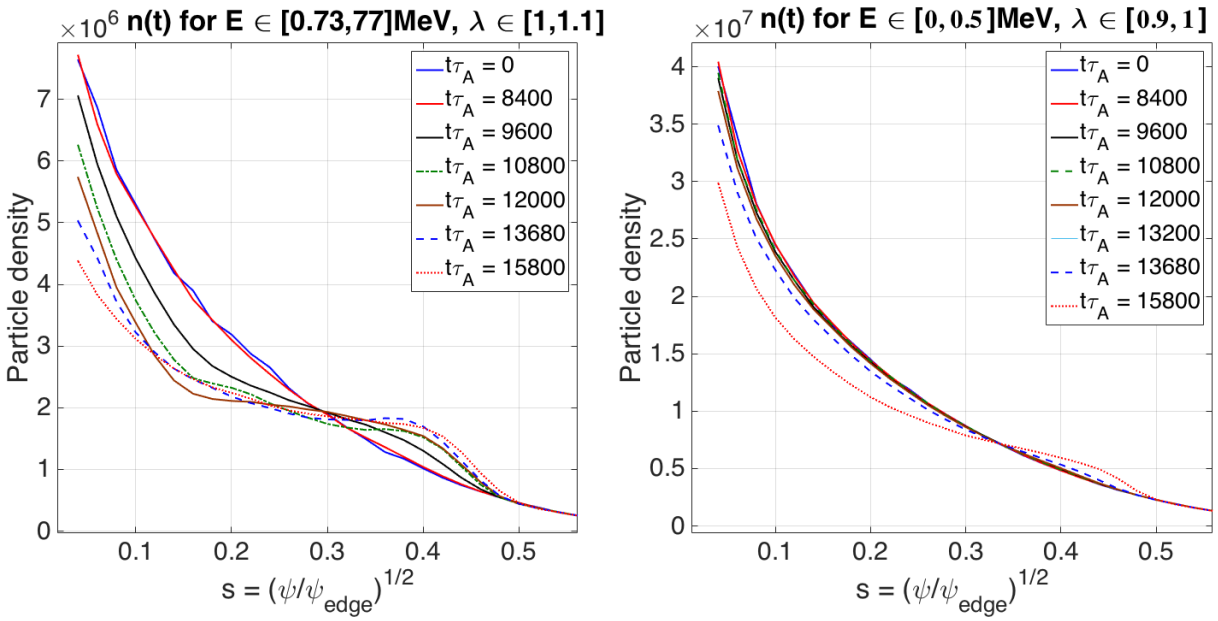

(a) (b)

Figure 6.8: 1D radial transport in the resonant and non-resonant zone of invariants space at different times. (a) Flattening of the particle density in the resonant zone (b) Particle density in the non-resonant zone. The density does not flatten here, except during the kink phase in which the strong MHD displacement transports all particles, resonant or not.

$$\frac{dE}{dt} \equiv \frac{\partial H}{\partial t} = -h(t)\omega(t)\sin\Theta + \frac{dh}{dt}\cos\Theta \tag{6.2}$$

$$\frac{d\Theta}{dt} \equiv \omega_d(E,\lambda,P_\varphi) - \omega \tag{6.3}$$

with the phase Θ described in equation (2.57), and $h(t)$ the width of the resonant virtual island. These equations give the time evolution of the particle invariants in the nonlinear fishbone phase. The virtual island is stationary when the frequency of the 1,1 mode ω does not evolve in time. In that case, considering the precessional resonance lies at $P_{\varphi 0}$ such as $\omega_d(E,\lambda,P_{\varphi 0}) = \omega$, to next order in δP_φ, equation (6.1.2) can be recast as

$$\frac{d\Theta}{dt} = \left.\frac{\partial \omega_d}{\partial P_\varphi}\right|_{E,\lambda,P_{\varphi 0}} (P_\varphi - P_{\varphi 0}) = \frac{\partial K}{\partial P_\varphi} \tag{6.4}$$

with

$$K = \left.\frac{1}{2}\frac{\partial \omega_d}{\partial P_\varphi}\right|_{E,\lambda,P_{\varphi 0}} (P_\varphi - P_{\varphi 0})^2 - h(t)\cos\Theta \tag{6.5}$$

$K = H - \omega P_\varphi$ can be seen as the new Hamiltonian in the referential of the internal kink wave ω. The virtual island is then described by $K = cst$ in the diagram (Θ, P_φ), as displayed on Figure (6.9) by the green curve.

The island is only virtual since the mode frequency is quickly evolving for the fishbone instability. K is not a constant of motion anymore. The fast chirping prevents particles from circling once on the island. At the beginning of the nonlinear fishbone phase, $\partial_t h$ can be neglected, but $\omega(t) \neq cst$. Combining equations (6.1-6.2), the nonlinear time evolution of the kinetic toroidal momentum can be recast as

$$\dot{P}_\varphi = -\frac{\dot{E}}{\omega} \tag{6.6}$$

In XTOR-K's conventions, P_φ increases when ψ and r increase. Since a net outward radial

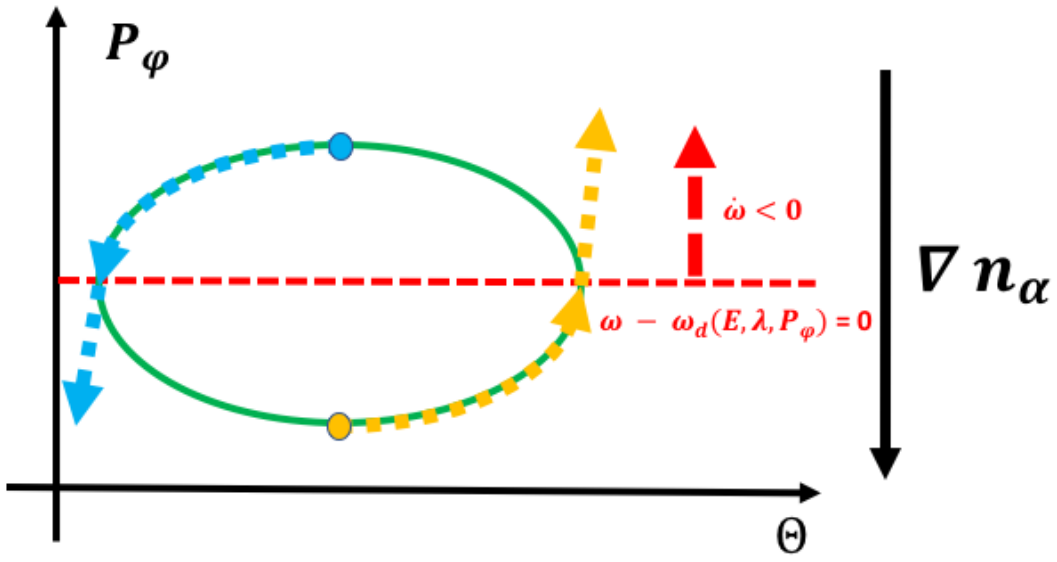

Figure 6.9: Sketch of the trajectory of a near resonance particles in the Kinetic Poincaré diagram (Θ, P_φ). The precessional resonance is the dotted red line. The green ellipse is the trajectory of the near resonance particle if both ω and ω_d remain constant. Particles are giving energy to the fields when they go up in P_φ with $\sin\Theta > 0$ (yellow curve), and are yielding energy when they go down in P_φ with $\sin\theta < 0$ (blue curve). Due to a gradient of particles in this diagram, more particles are going up than down. The mode down chirping pushes up the resonance, which prevents particles from cycling once in the island. It leads to a net transfer of energy to the fields and to outward radial transport.

transport is occurring, for most resonant particles, $\dot{P}_\varphi > 0$. The transport observed can only be explained if particles loose irreversibly energy to the fields, according to equation (6.6). The transport is also enhanced if the mode frequency chirps down, as it is noticed in this simulation. The sole existence of the precessional resonance cannot explain the fast particles transport. For a classical wave-particle resonance [O'Neil, 1965], resonant particles are circling inside an island in phase space. It is illustrated on Figure (6.9). The island of precessional resonance is plotted in the Kinetic Poincaré diagram (Θ, P_φ). If the resonance, the red dotted line, does not change position, particles are circling around the resonance on the green curve. According to equation (6.2), when $\partial_t h$ is neglected, particles are taking energy when $\sin\Theta < 0$, i.e when particle go down the island with $\dot{P}_\varphi < 0$, and are giving energy when $\sin\Theta > 0$ with $\dot{P}_\varphi > 0$. The net energy transfer over a bounce in the island is then zero.

In this simulation, the islands are virtual, resonant particles do not have time to circle entirely in the diagram (Θ, P_φ) since the initial position of the island of resonance is evolving too rapidly. On Figure (6.9), it is noted that the gradient of alpha-like particles is directed towards lower P_φ since $P_\varphi \propto +\psi$. Therefore, a potential mechanism explaining the resonant transport can be expressed as follows. When the precessional resonance initially arises, more particles are going up (yellow curve) the island structure than down (blue curve). Afterwards, mode down chirping occurs in the simulation. It displaces the position of the resonance. ω decreases due to chirping, so the value of the precessional frequency ω_d on the resonance

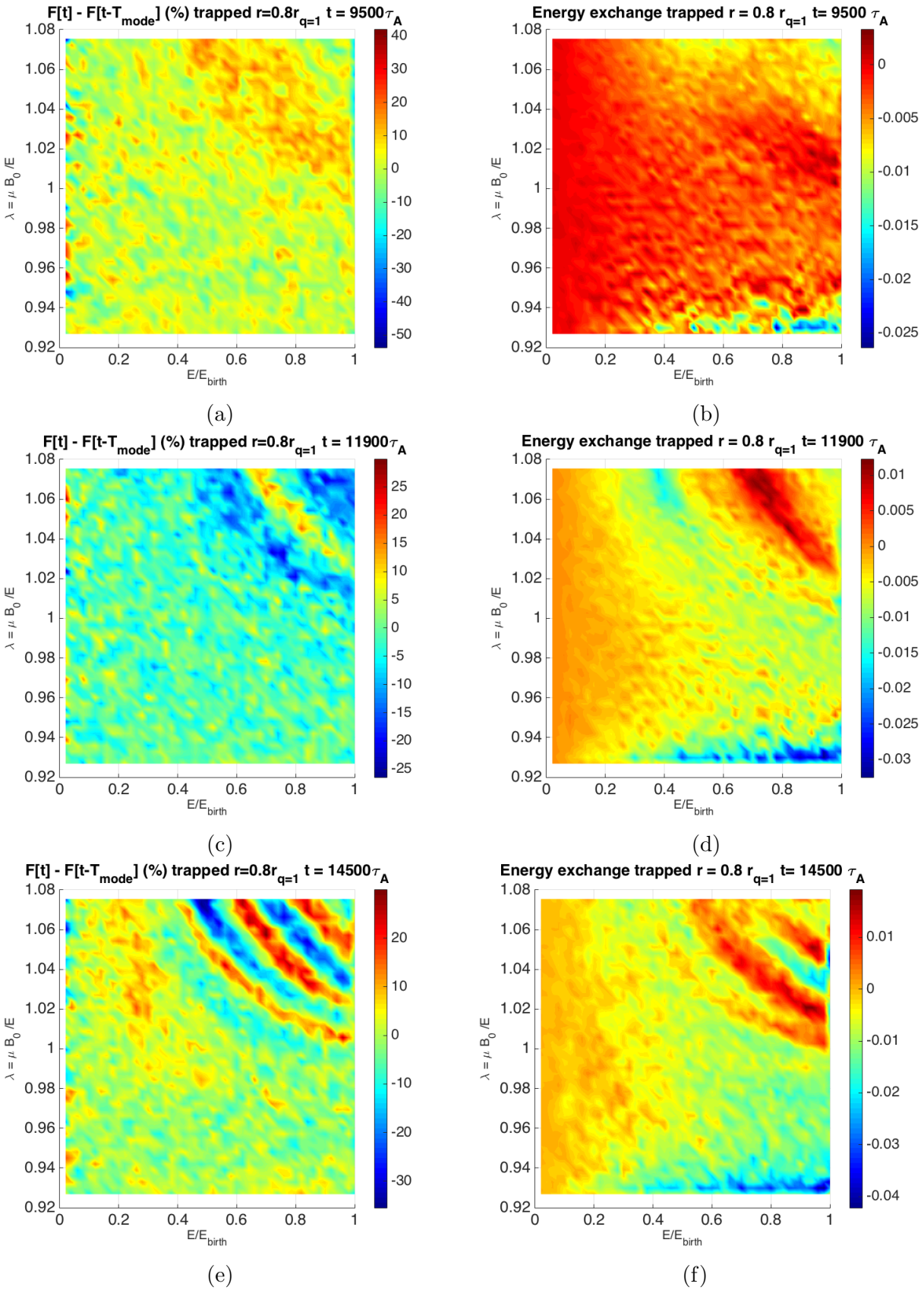

Figure 6.10: Time evolution of the precessional resonance in the (E, λ) diagram at $r = 0.8r_{q=1}$. The flux of particles on a mode rotation δF_T at a given time is plotted (left figures), together with the wave-particle energy exchange $-\mathbf{J}_h \cdot \mathbf{E}$ (right figures). On subfigures (a) and (b) (beginning of the nonlinear fishbone phase), it is noted that resonant transport arises prior to the mode frequency chirping. On subfigures (c),(d),(e) and (f) (middle and late nonlinear phase), it is observed that resonant structures with $\delta F_T > 0$ correspond to zones with $-\mathbf{J} \cdot \mathbf{E} > 0$, and vice-versa. Several resonance patterns are observed in the late nonlinear fishbone phase. This is due to the nonlinear evolution of the resonance positions, and of resonant structures arriving from inner radial layers.

needs to decrease too. Since $\omega_d \propto 1/r \propto 1/P_\varphi$ (equation B.11), the chirping tends to displace the resonance at higher P_φ, as displayed on Figure (6.9). Particles circling up the island are ejected at larger P_φ, and those circling down at smaller P_φ. Due to the direction of the density gradient, more particles are ejected radially outward than inward.

In order to validate such a partial mechanism, several behaviors need to be observed in the hybrid simulation. First, a net transport of resonant particles needs to be seen before the mode chirps down. It corresponds to the transport due to the combined effects of the direction of ∇n_α, and the initially constant position of the precessional resonance. Second, a time evolution of the resonance position needs to be observed, in a direction coherent with the frequency chirping. It indicates that the mode chirping indeed modifies the positions of the resonance, preventing them for circling completely in the (Θ, P_φ) diagram. Last, the de-trapping of a near-resonance particle in the Kinetic Poincaré diagram (Θ, P_φ) needs to be observed. However, such a partial mechanism does not explain why the chirping is occurring in first place. This will be addressed in the next section.

The proposed mechanism have been motivated by the observation of these different features in the hybrid simulation. These features are now detailed.

Time evolution of the wave-particle energy exchange and of particle transport

To investigate further the resonant transport of trapped particles, the time evolution of the wave-particle energy exchange and of the resonant flux of kinetic particles are plotted in the diagram (E, λ) near the $q = 1$ surface at $r = 0.8 r_{q=1}$ on Figure (6.10).

Subfigures (b),(d) and (f) correspond to the wave-particle energy exchange $-\mathbf{J}_h \cdot \mathbf{E}$ detailed in section 4.2.2. When $-\mathbf{J}_h \cdot \mathbf{E} > 0$, particles are yielding energy to the fields, and taking some away from the fields when $-\mathbf{J}_h \cdot \mathbf{E} < 0$. The wave-particle energy has been plotted at characteristic times of the nonlinear fishbone phase. (b) and (d) correspond to the two fishbone oscillations, (f) to the end of the nonlinear fishbone phase. On these subfigures, the wave-particle energy exchange is averaged in time over a mode period. Subfigures (a),(c) and (e) correspond to the resonant flux of particles over a mode period T as $\delta F_T(t) = F(t) - F(t-T)$. This quantity is plotted at the same times as subfigures (b), (d) and (f).

From Figure (6.10), several observations can be made. First, from (a), it can be noted that an outward resonant particle transport begins at $t/\tau_A = 9500$. About 10% of particles are transported over a mode period, in a resonant zone coherent with Figure (6.5) regarding the radial slice $s = 0.24 - 0.28$. Particles come from inner radial layers. This resonant transport is associated to a small energy loss from the particles to the fields $-\mathbf{J}_h \cdot \mathbf{E} > 0$, according to Figure (6.10) (b). As observed on Figure (6.2), the fishbone frequency only chirps down at $t/\tau_A = 1.10^4$, $500\tau_A$ after the beginning of resonant transport. Therefore, the resonant transport of fast particles begins before the mode frequency chirps down, as expected by the partial mechanism detailed above. This point is further confirmed by Figure (6.8) (a), where it can be seen that the density profile begins to get flattened at $t/\tau_A = 9600$, prior to the mode frequency down chirping.

Moreover, it can also be observed on Figure (6.10) that an interplay exists between wave-particle energy exchange and resonant flux of fast particles. On Figure (6.10) (c) and (e), several flux structures are observed at $r = 0.8 r_{q=1}$. They correspond either to particles coming from inner radial layers and arriving at $r = 0.8 r_{q=1}$ ($\delta F_T > 0$), or to particles leaving the

radial layer $r = 0.8 r_{q=1}$ for outer radial layers ($\delta F_T < 0$). On Figure (6.10) (c), a structure $\delta F_T > 0$ is located at the middle of two structures $\delta F_T < 0$. On Figure (6.10) (d), three structures are also present in the same part of the (E, λ) diagram. One with $-\mathbf{J}_h \cdot \mathbf{E} > 0$, in between of two with $-\mathbf{J}_h \cdot \mathbf{E} < 0$. It is noted that the color bars on subfigures (c) and (d) do not have the same color when the quantity they are describing changes sign. The same behavior is observed between subfigures (e) and (f), with in this case three structures with $\delta F_T > 0$, and two with $\delta F_T < 0$. There is therefore a connexion between resonant transport of particles and wave-particle energy exchange on Figure (6.10). When $\delta F_T > 0$, $-\mathbf{J}_h \cdot \mathbf{E} > 0$, particles lose energy to the fields, and when $\delta F_T < 0$, $-\mathbf{J}_h \cdot \mathbf{E} < 0$, they gain energy from the fields. This dynamics is in agreement with equation (6.6), $\dot{P}_\varphi > 0$ when $\delta F_T < 0$ and particles yield energy to the fields. When $\delta F_T > 0$, $\dot{P}_\varphi < 0$ and particles extract energy from the fields.

A last observation is made regarding the nonlinear evolution of the resonance position observed on Figure (6.10). At the first fishbone oscillation on subfigures (a) and (b), only one resonant structure is present, at the position predicted by the linear theory (Figure 6.5, $s = 0.24 - 0.28$), since it is only the beginning of the nonlinear fishbone phase. The mode has not chirped yet, and the particles invariants are only beginning to evolve in time. A study on the particles invariants is conducted in the next section. Therefore, both ω and $\omega_d(E, \lambda, \bar{\psi})$ do not evolve much. However, on subfigures (c),(d),(e) and (f), several structures are present, and spans a larger zone of invariants space, such as $E \in [0.4, 1]$, $\lambda \in [1, \lambda_{max}]$. This larger zone corresponds to the total transport observed on Figure (6.7). The extension of the resonant zone to lower energies and pitch angles is coherent with the mode chirping, according to Figure (6.5). When the mode frequency ω is decreasing, it tends to shift all resonant curves in zone of invariants space with lower energies and pitch angle. This confirms further the partial mechanism for resonant transport described above.

However, the chirping mechanism cannot explain why resonant structures are observed at higher energies and pitch angles than the initial resonance position for a given radial layer. An additional mechanism can explain this new resonant zone. The nonlinear evolution of the particles invariants can lead particles to populate these zone of invariants space. In order to investigate this assumption, the individual nonlinear behavior or near resonance particles is presented. The study of the individual behavior will also permit to see that particles behave in the (Θ, P_φ) diagram as presented in the partial mechanism proposed above.

6.1.3 Individual nonlinear behavior of near resonance particles

On (Figure 6.11), the time advance of a particle initialized with invariants (E, λ, P_φ) close to the linear resonance has been performed along the electromagnetic fields advanced self-consistently by XTOR-K. This time advance has been obtained by saving at each fluid time step of the hybrid simulation the 3D $(\mathbf{E}, \mathbf{B})$ fields. Then, the Boris kinetic advance is performed with a separate module. This procedure is similar to the one detailed in 5.1, but with time evolving electromagnetic fields. The nonlinear behavior of the near resonance particle detailed on (Figure 6.11) is similar to those of others near resonance trapped particles in the simulation.

As explained above, the resonant particle is indeed transported from its initial radial position towards the q=1 surface (Figure 6.11 (a) and (b)). At the same time, its triplet of invariants (c) and (e), that were naturally invariants in the linear phase until $t = 8000\tau_A$, are evolving notably in the fishbone phase. The toroidal kinetic momentum P_φ is increased drastically for $t/\tau_A \in [9.10^3, 10^4]$, which corresponds to the particle outward radial transport.

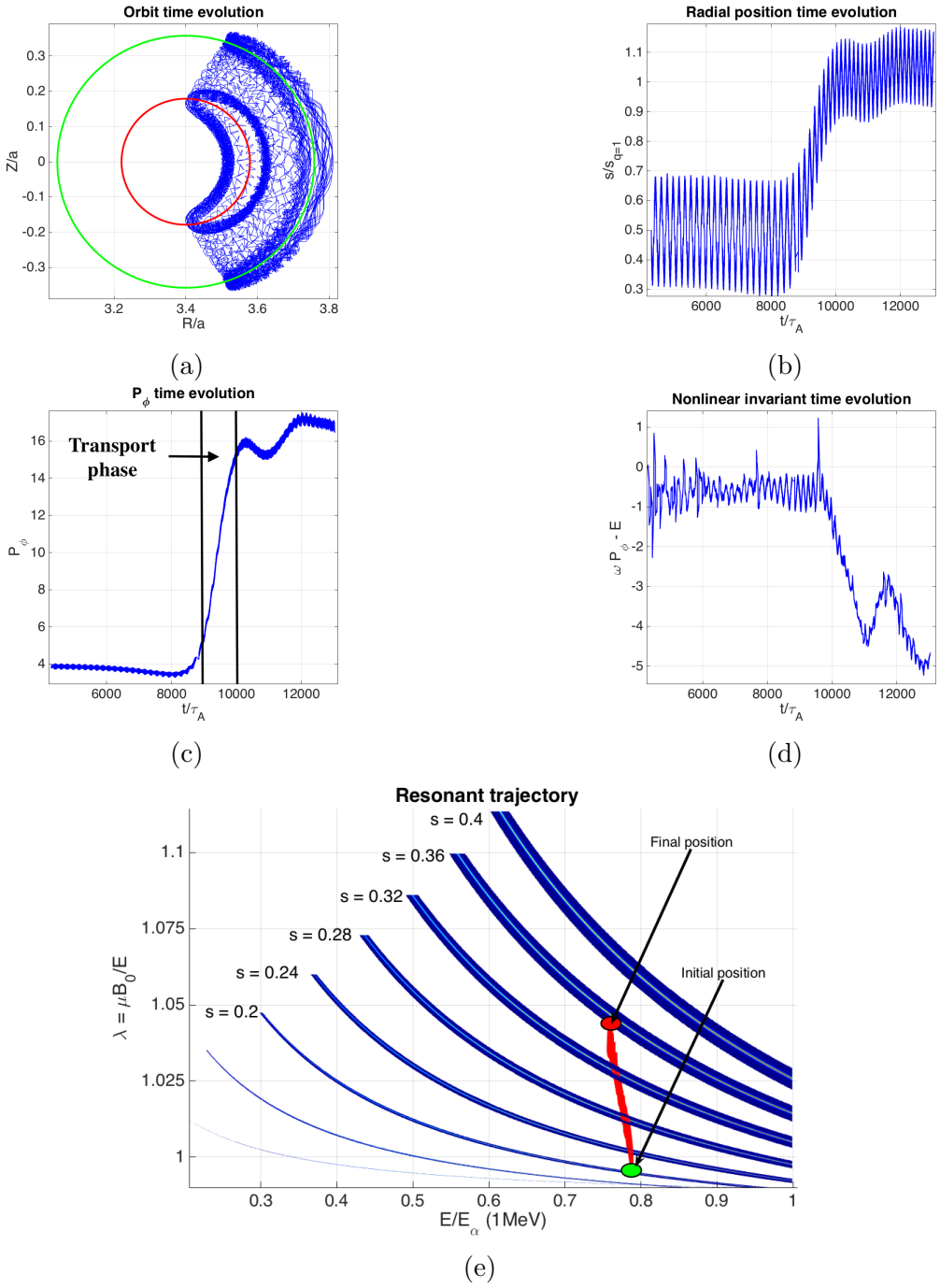

Figure 6.11: Time evolution of a near resonance trapped particle. (a) Particle's orbit, observing a net outward radial transport. The red and green circles correspond to the initial and final reference flux surface. The final one is $q = 1$. (b)Particle's radial position, normalized by the radial position of the $q = 1$ surface. The particle stops being transported at $q = 1$. (c) P_φ, whose invariance is greatly altered in the nonlinear fishbone phase. It increases significantly, due to radial transport, in a transport phase $t/\tau_A \in [9.10^3, 10^4]$. (d) Time evolution of the weakly nonlinear invariant $\omega P_\varphi - E$, showing that the resonant particle reacts to the mode chirping. (e) Nonlinear trajectory of a resonant particle in the (E, λ) diagram. Along this trajectory, the resonant particles is evolved to larger pitch angles

It is noted again here that the resonant particle starts being transported before the mode frequency chirps down, confirming further the partial mechanism presented.

The nonlinear trajectory of the resonant particle on the diagram (E, λ) is displayed on subfigure (e). Along this trajectory, the particle's energy is slightly lower, and its pitch angle is notably increased. The nonlinear evolution of λ therefore explains why resonant structures at larger pitch angles are observed on Figures (6.7) and (6.10).

Furthermore, Figure 6.11 (d) displays the time evolution of the term $\omega P_\varphi - E$, that is supposed to be an invariant of motion when the mode frequency is not evolving in time. Indeed, in that case, $\omega(t) = cst$, and equation (6.6) becomes $\omega P_\varphi - E = cst$. On Figure 6.11 (d), it can be seen that $\omega P_\varphi - E$ is no longer time invariant after $t/\tau_A \sim 9000$. Therefore the individual particles are indeed reacting to mode chirping.

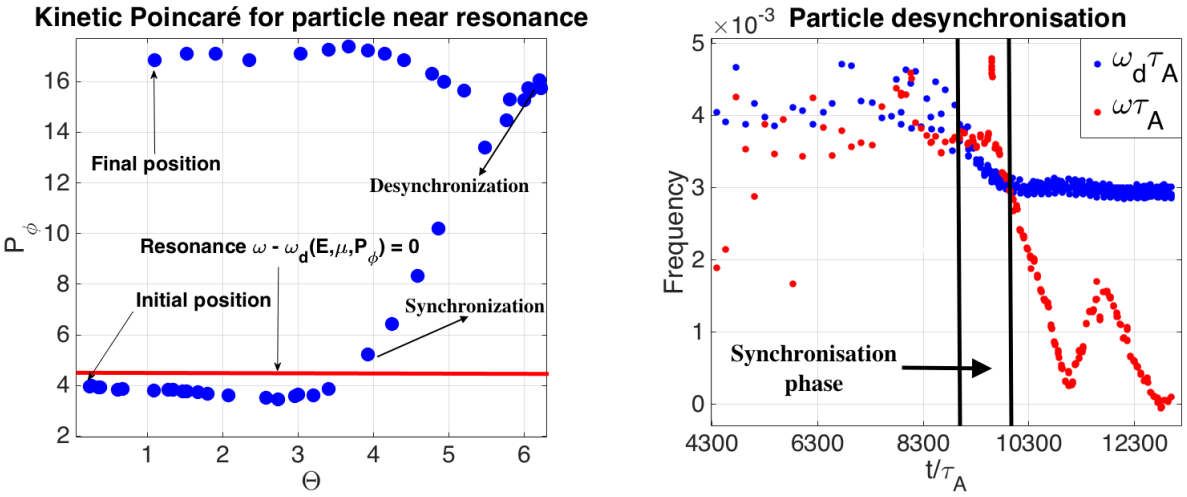

(a) (b)

Figure 6.12: (a) Kinetic Poincaré plot of a particle launched near the precessional resonance at $P_\varphi = 4.5$. The particle does not have time to circle in the virtual island that it is immediately transported at larger P_φ. (b) Compared time evolutions of the mode frequency and precessional frequency of a particle. The precessional frequency decreases slightly in amplitude when the mode is chirping, synchronizing with it over $t/\tau_A \in [9.10^3, 10^4]$. Afterwards, the particle desynchronizes with the mode. This synchronization phase corresponds on (a) to the de-trapping of the resonant particle.

Finally, the trajectory of the near resonance particle is plotted on the diagram (Θ, P_φ) on Figure (6.12) (a). The particle is initialized just below the precessional resonance condition at $P_\varphi = 4$. It is noted on this Figure that the resonant particle indeed does not have time to circle once in a phase space island. The island is virtual, and used here as a guidance. When the particle starts interacting with the mode via a precessional resoance, it is rapidly transported at higher P_φ. This behavior starts and ends during the transport phase highlighted on Figure (6.11) (c). Then, the resonant particle remains at a larger $P_\varphi = 16$, that corresponds to the $q = 1$ surface according to Figure (6.11) (b). The particle cannot interact with the mode anymore.
Moreover, on Figure (6.12) (b), the time evolutions of the mode frequency ω and of the resonant particle precessional frequency ω_d are compared. In the linear phase until $t/\tau_A = 9000$, the particle precessional frequency is comparable with ω since it is near the resonance position. Then, both frequencies are decreasing at the same pace for $t/\tau_A \in [9.10^3, 10^4]$ during a synchronization phase. This phase corresponds to the transport phase observed on Figures (6.11) (c) and (6.12) (a). Afterwards, both frequencies desynchronize, the precessional frequency remains constant and the mode frequency keeps on decreasing. The resonant trans-

port therefore arises during phase-locking, $\dot{\Theta} \equiv \omega - \omega_d \approx cst$ in the nonlinear fishbone phase. A similar behavior has been observed for electronic fishbones [Vlad et al., 2013].

Formulation of a complete mechanism for mode chirping and resonant particle transport

The observations made so far with the hybrid simulation has enabled to construct a partial mechanism explaining the net outward transport of particle due to resonant interaction and mode chirping. However, it does not explain why the mode frequency is chirping down initially. A more complete mechanism is proposed here, on the basis of the initial resonant transport prior to mode chirping, and to the linear fishbone dispersion relation (4.6).

When the particles are initially being displaced at $\omega(t) = cst$, prior to mode chirping, the density profile of fast particles is flattened in resonant zones of invariants space (see Figure 6.8 (a) $t/\tau_A = 9500$), due to the direction of the density gradient in the diagram (Θ, P_φ) (see Figure 6.9). In the fishbone dispersion relation (4.6), the kinetic contribution λ_K is mainly proportional to $\partial_r F_{eq}$ (see equation (4.53)), and then to ∇n_α. On Figures (5.9) (b) and (5.13) (b), it is observed that on the fishbone branch, the rotation frequency decreases when $n_{\alpha,0}$ is smaller. Since $\lambda_K \propto \nabla n_\alpha$, flattening the density profile in parts of invariants space is equivalent to lowering the amplitude of the density. Both operations decrease the kinetic drive brought by fast particles.

Therefore, the flattening of n_α tends to decrease ω, which starts the frequency down chirping. This chirping moves away the resonance position has described on Figure (6.7). Thus, the mode frequency down chirping flattens further n_α, as it can be seen on 6.8 (a) at $t/\tau_A = 1.2 \times 10^3$. It increases the down chirping until it stops at $t/\tau_A = 1.3 \times 10^4$ (see Figure (6.2)).

Conclusion on the ITER-like hybrid simulation

To conclude the analysis of this first hybrid simulation of the alpha fishbone instability, it has been observed that a net outward resonant transport of kinetic particles towards $q = 1$ is occurring. This transport affects merely a few percents of the initial distribution function, the redistribution of fast particles due to the fishbone instability is weak. The total resonant transport arises over a time $\Delta t \sim 3000\tau_A \sim 10^{-3}$s. The thermalization time of fast particles is of order $\tau_{th} \sim 10^{-1} - 1$s [iTER physics basics, 2000]. Therefore, using an imposed slowing distribution function was realistic since $\Delta t \ll \tau_{th}$.

A mechanism has been proposed to explain the particle transport during the fishbone instability. It highlights the role of the mode frequency down chirping, that prevents the precessional resonance position to remain stationary in the strong kinetic drive limit. This behavior was expected [Zonca et al., 2015]. The corresponding resonant island is therefore only virtual, resonant particles are yielding irreversibly energy to the fields and get transported. The hybrid simulation ends with a linear internal kink phase. The $m = n = 1$ island is growing significantly and starts the evacuate the plasma core. The simulation is ended here since the simulation of a complete sawtooth cycle with kinetic particles requires a too long computational time.

6.2 ITER 15 MA case far from the fishbone threshold

Now that fishbone oscillations have been analysed using XTOR-K with a simple Kinetic-MHD equilibrium, more complex equilibria relevant to the physics of burning plasmas are studied in this section. Results obtained from a nonlinear simulation on the ITER 15 MA equilibrium are discussed here. This simulation lies in the strong kinetic drive limit. It serves two purposes. First to generalize the results obtained with the previous simulation. Second, to study on a ITER relevant scenario the fishbone instability in its nonlinear phase, to predict the amount of resonant transport. This nonlinear simulation constitutes the prolongation in its nonlinear phase of the hybrid simulation presented in 5.4.2, with a beta ratio of $\beta_\alpha/\beta_{tot} = 12\%$ and $q_0 = 0.95$. It lies indeed in the strong kinetic drive limit, since its linear growth rate is $\gamma\tau_A = 4.10^{-3}$. It is far larger than the linear growth rate around the fishbone threshold, $\gamma_L\tau_A \sim 8.10^{-4}$ (see Figure (5.13 (a))).

6.2.1 Nonlinear dynamic of the MHD fields

Given the equilibrium shape, it has been chosen to increase to n=4 the number of resolved toroidal modes. Therefore, this simulation uses 201 radials points, 64 poloidal and 16 toroidal ones. The kinetic and magnetic energies of all $n = 0 - 4$ modes have been plotted on Figure (6.13), against their poloidal harmonic m. Both these figures show an expected behavior of

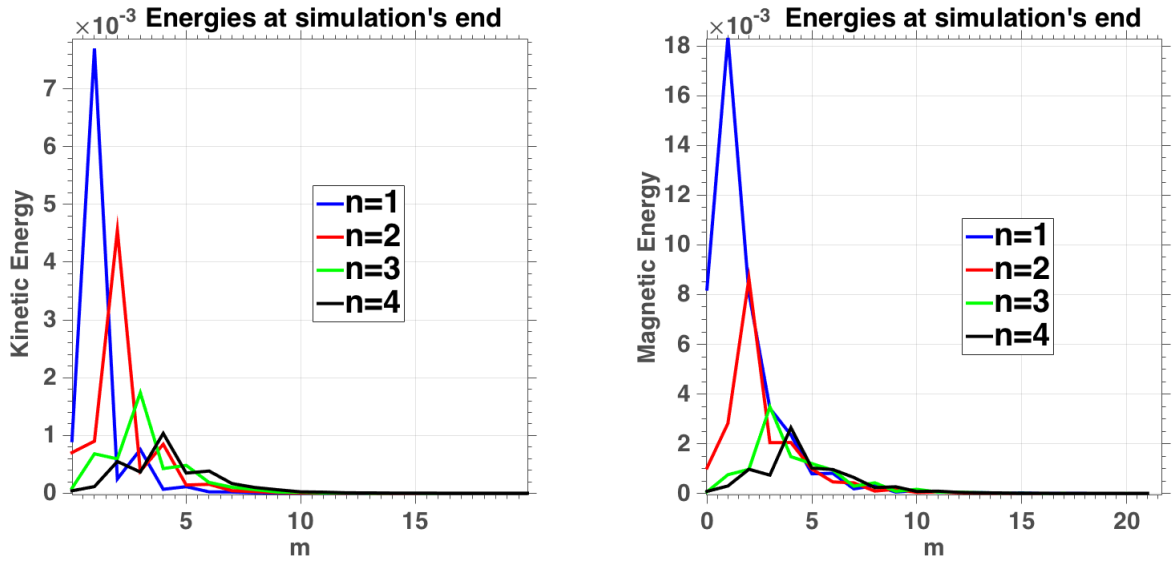

(a) (b)

Figure 6.13: Energies of the modes n resolved in the simulation as a function of the poloidal m harmonic, at the end of the simulation. Kinetic energies are displayed on (a) and magnetic energies on (b).

the mode energies. The energies of all n harmonics converge towards zero when $m \to m_{max}$. These results imply that the simulation is reasonably converged regarding the poloidal and toroidal resolutions.

The time evolution of the kinetic and magnetic energies of the n modes is displayed on Figure (6.14). Contrarily to the previous nonlinear case, a linear internal kink is not growing after the fishbone oscillations. The nonlinear fishbone phase is more complex from the MHD point of view. The linear fishbone phase ends around $t = 2500\tau_A$, the 1,1 mode amplitude roll-over afterwards. This roll-over is accompanied by the formation of a small 1,1 island as

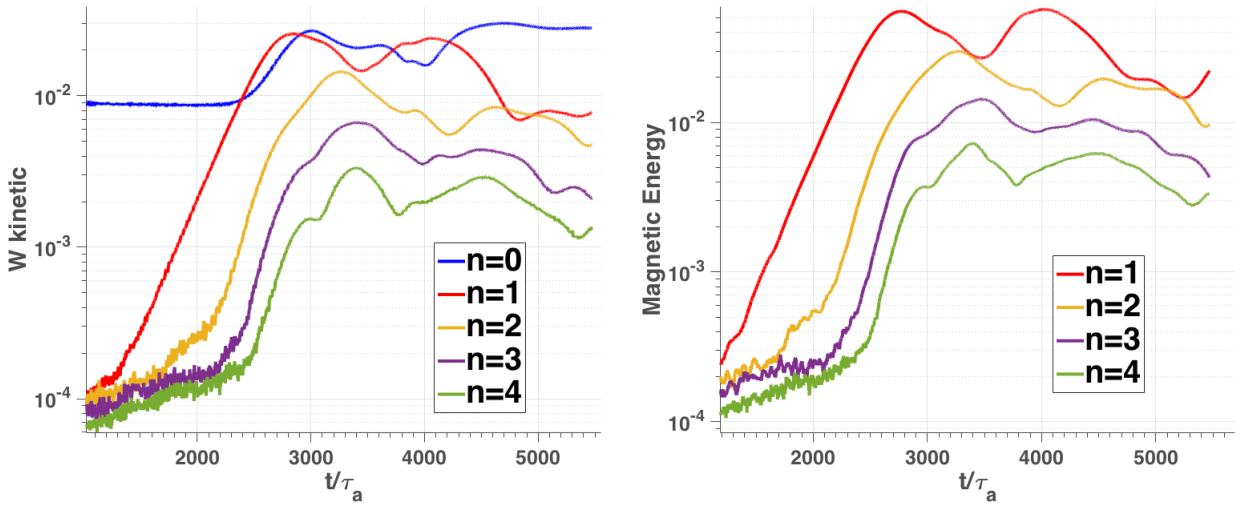

(a) (b)

Figure 6.14: Time evolution of the kinetic (a) and magnetic (b) energies of the n modes.

displayed on Figure 6.16 (a) , and by the beginning of a mode down chirping in Figure 6.15 at $t \sim 3000\tau_A$. This hints that the roll-over is partially due to resonant particle transport, as in the previous simulation. In this simulation, two roll-over of the 1,1 mode amplitude can be observed at $t/\tau_A = 3000$, $t/\tau_A = 4100$. They are associated to fishbone oscillations.

However, the mode down chirping is not as clear as before. The signal $\omega(t)$ is more affected by noise due to the difficult computation of $\omega(t) = \omega_{E\times B} - \omega_{lab}$ on a equilibrium with such an elongated shape. As discussed in 5.4.2 , ω_{lab} is computed by following the maxima of a perturbed field in the poloidal plane. The ITER shaping makes this task more difficult. It appears clearly however that the $E \times B$ rotation frequency decreases in time on Figure (6.15) (a), starting at $t = 3000\tau_A$. A clear down chirping of $\omega(t)$ arises around $t = 4000\tau_A$ on Figure (6.15) (b). This noisy mode frequency does not enable to study the trajectory of individual particles in the kinetic Poincaré diagram (Θ, P_φ).

The nonlinear behavior of the MHD fields in the nonlinear fishbone phase is significantly different than in the previous nonlinear simulation. Successive formations of 2,2, 3,3 4,4 and 5,5 islands arise on q=1. A 5,5 structure can be considered as problematic regarding the resolution of the simulation in the toroidal direction, since the harmonic $n = 5$ is not resolved. However, the sole formation of a 5,5 island structure on q=1 does not necessarily highlight a convergence issue. A n=5 structure on the q=1 surface can arise since a Poincaré plot is computed using

$$\frac{d\theta}{d\varphi} = \frac{\mathbf{B}\cdot\nabla\theta}{\mathbf{B}\cdot\nabla\varphi} \tag{6.7}$$

Performing algebraic operations between the toroidal and poloidal components of the magnetic field introduces coupling between the resolved modes. It can lead to a dominant 5,5 structure on the resonant q=1 surface. It shows that the formation of a 5,5 island is more related to the post-processing diagnostic computing the Poincaré plot, than to the simulation itself.

The q profile (Figure 6.17) oscillates during the nonlinear phase around its equilibrium position. It is not flattened around $q = 1$ at any point of the simulation, which would be a precursor of an internal kink instability.

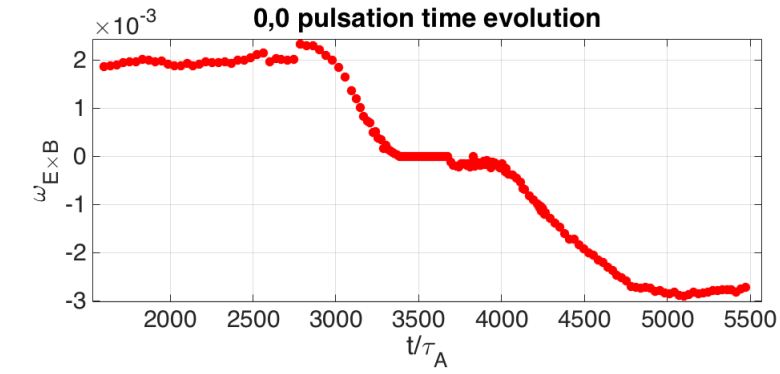

(a)

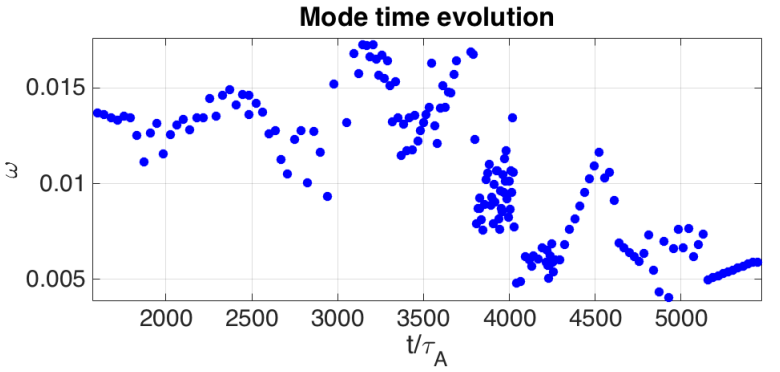

(b)

Figure 6.15: Time evolution of the $E \times B$ frequency (a) and of the mode frequency (b). These figures exhibits a general down chirping of the mode frequency, typical of fishbone oscillations. The signal $\omega(t)$ is affected by noise due to the complex shaping of the ITER configuration.

Moreover, again contrarily to the previous simulation, the mode structure of the instability evolves during the simulation, as displayed on Figure 6.18. After each roll-over of the 1,1 mode, its amplitude decreases, up to competing with the 2,2 mode. It leads to transitions between 1,1 and 2,2 structures during the entire simulation. This is an additional reason for the noisy $\omega(t)$ signal, since two maxima are present in the poloidal plane for $n = m = 2$. It is noted that a double step structure briefly appears near $t = 5150\tau_A$ (subfigure (e)) when the 1,1 mode amplitude grows again after the second saturation.

Even though the nonlinear evolution of the MHD fields is more complex in this simulation, the formation of magnetic islands cannot fully explain the mode roll-overs observed, and the mode down chirping.

6.2.2 Nonlinear evolution of the alpha distribution function in phase space

Similarly to the ITER-like case, a net outward resonant transport of alpha particles occurs during the nonlinear phase of this simulation. The overall transport is slightly higher for this ITER 15 MA case, as shown on Figure (6.19). This figure displays the perturbed alpha particles density on the $(s, t/\tau_A)$ diagram for all particles (a), only trapped particles (b), and only passing particles (c). In fact, in the core plasma, 25% of trapped particles are transported by fishbone oscillations beyond $q = 1$ (subfigure (b)), 3% of passing particles (subfigure (c))

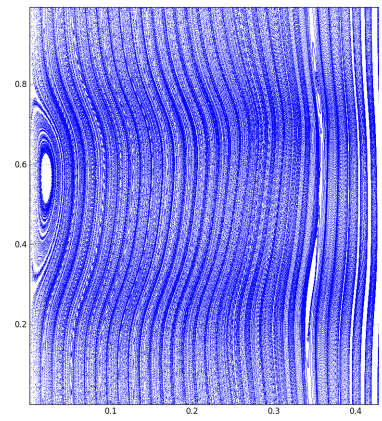

(a) $t = 2300\tau_A$

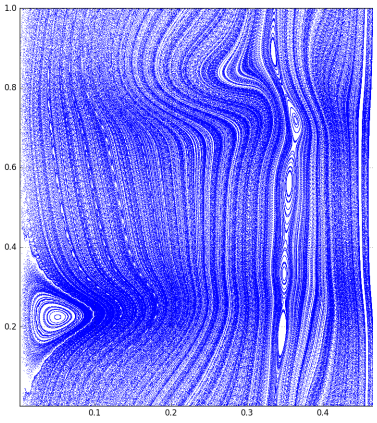

(b) $t = 3000\tau_A$

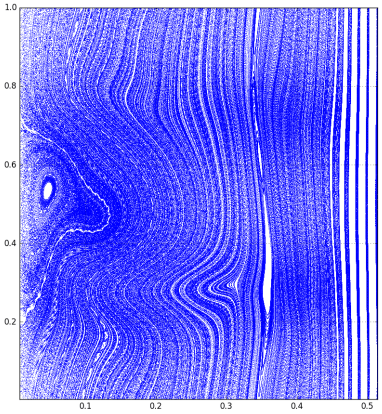

(c) $t = 3400\tau_A$

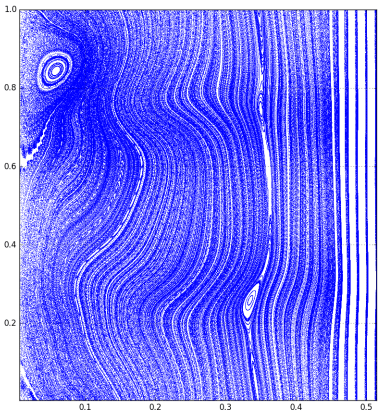

(d) $t = 4000\tau_A$

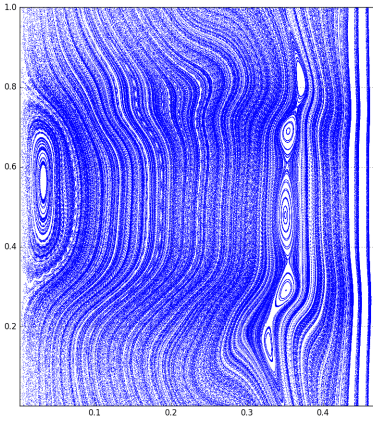

(e) $t = 4400\tau_A$

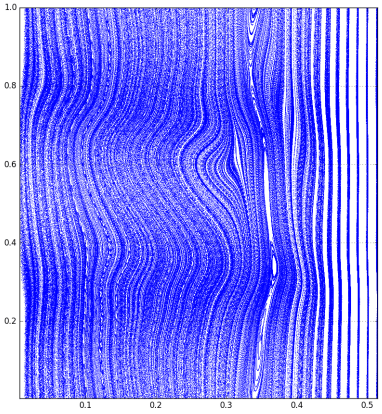

(f) $t = 4750\tau_A$

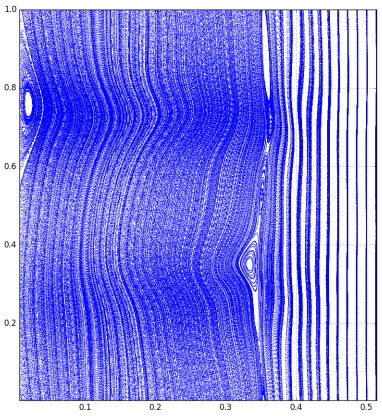

(g) $t = 5500\tau_A$

Figure 6.16: Poincaré plots in the polar (r, θ) plane taken at characteristic moments of the simulation. (a) End of the linear phase, generation of 2,2 islands. (b) Saturation of the 1,1 mode, formation of 5,5 islands. (c) Collapse of the 5,5 structure into a 2,2 one. (d) Second saturation of the 1,1 mode, with 3,3 islands on q=1. (e) Re-appearance of the 5,5 structure during the decline of the 1,1 mode. (f) Second collapse of the 5,5 structure into a 2,2. (g) End of the simulation, characterized by 3,3 islands on q=1

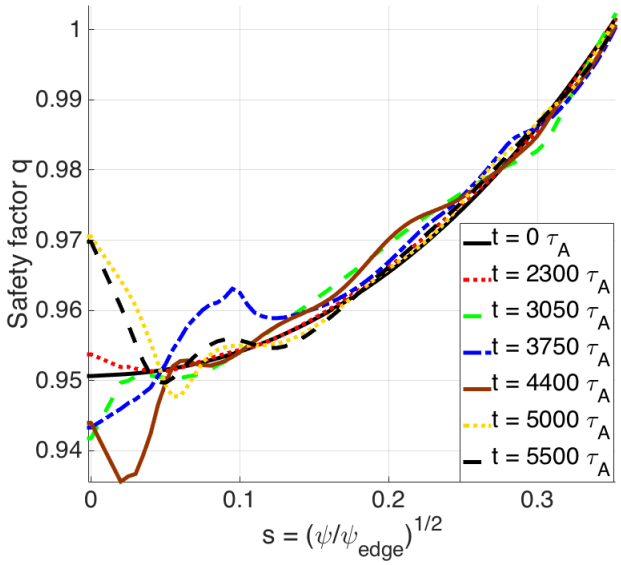

Figure 6.17: Time evolution of the q profile. During the simulation, the q profile oscillates around its initial equilibrium position. No flattening around $q = 1$ is observed.

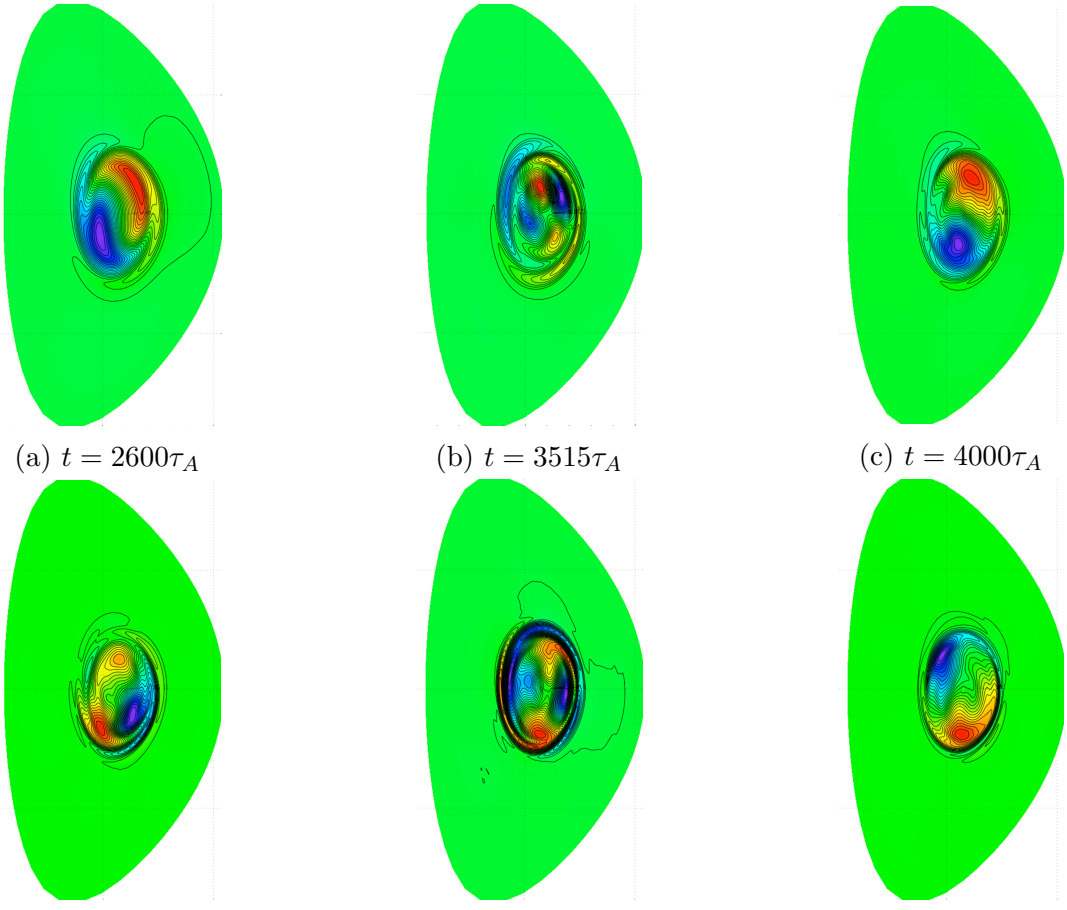

(a) $t = 2600\tau_A$ (b) $t = 3515\tau_A$ (c) $t = 4000\tau_A$

(d) $t = 4500\tau_A$ (e) $t = 5150\tau_A$ (f) $t = 5500\tau_A$

Figure 6.18: Time evolution of the mode structure in the poloidal plane (R, Z). The perturbed electron temperature is plotted here. The mode structure is initially of type $n = m = 1$ (a), and then oscillates between a 2,2 (b) (d) and a 1,1 (c) (f) type. On figure (e), the mode is characterized by a 2,2 and a double step structure.

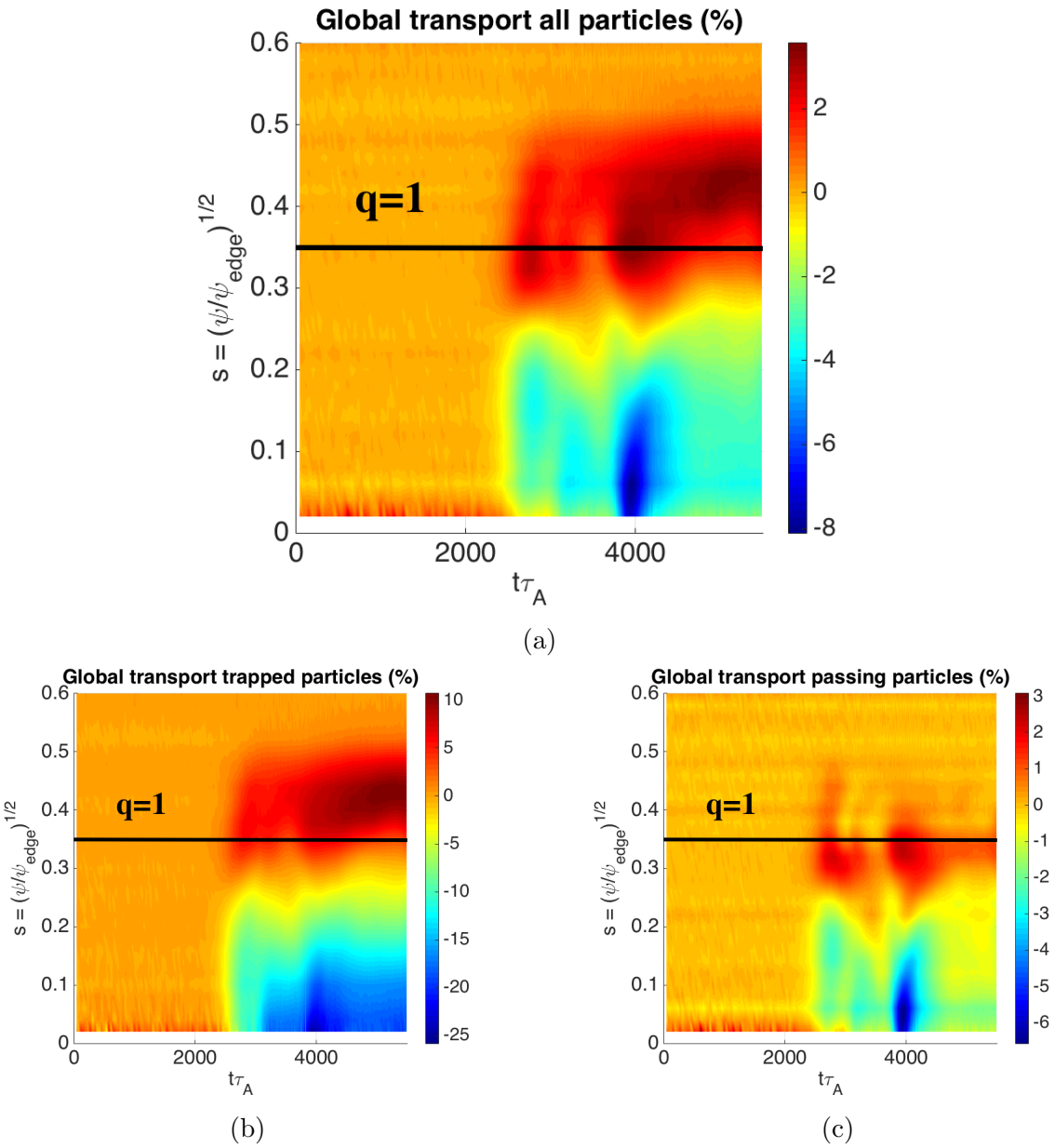

Figure 6.19: Global transport of particles in the diagram $(s, t/\tau_A)$ for all (a), trapped (b) and passing particles (c). Around 5% of all particles are transported by the fishbone in the core plasma, 25% and 3% respectively for trapped and passing particles.

and around 5% for all particles (subfigure (a)). In this simulation, the birth energy of fast particles is higher ($E_b = 3.5$ MeV). The particles have larger orbit width, which explains why they do not stop at $q = 1$ as in the ITER-like case. This point will be discussed further in the next section on the individual behavior of fast particles.

Morevover, on Figure (6.19) (a), two bursts of resonant transport can be observed at $t \sim 3000\tau_A$ and $t \sim 4000\tau_A$. They occur when the 1,1 mode amplitude roll-over on Figure (6.14) (a), during the fishbone oscillations. Furthermore, a notable distinction with the ITER-like case is that for passing particles, their initial density tends to be recovered at the end of the simulation. It is not the case for trapped particles, that remain at higher radial position. Given that the MHD displacement alone is not enough to explain the transient passing particles transport, resonant processes must also be at play for these particles.

This point is confirmed by Figure (6.20), where the available resonances for this equilibrium with a linear mode frequency of $\omega\tau_A = 1.3\ 10^{-2}$ are displayed. Since this non circular equilibrium with hot particles does not allow for an analytical prediction of resonant zones in invariants space, the same procedure as in 5.1 is applied to obtain the particles eigenfrequencies Ω_2, Ω_3. The equation $\omega - \mathbf{n}\cdot\mathbf{\Omega} = 0$ is then solved in the diagram (E, λ) at different radial positions. Only the harmonics $\mathbf{n} = (0, -1, 1)$ and $\mathbf{n} = (0, 0, 1)$ are studied, according to Figure (4.1). The precessional resonances obtained here (Figure (6.20) (a)) are quite similar

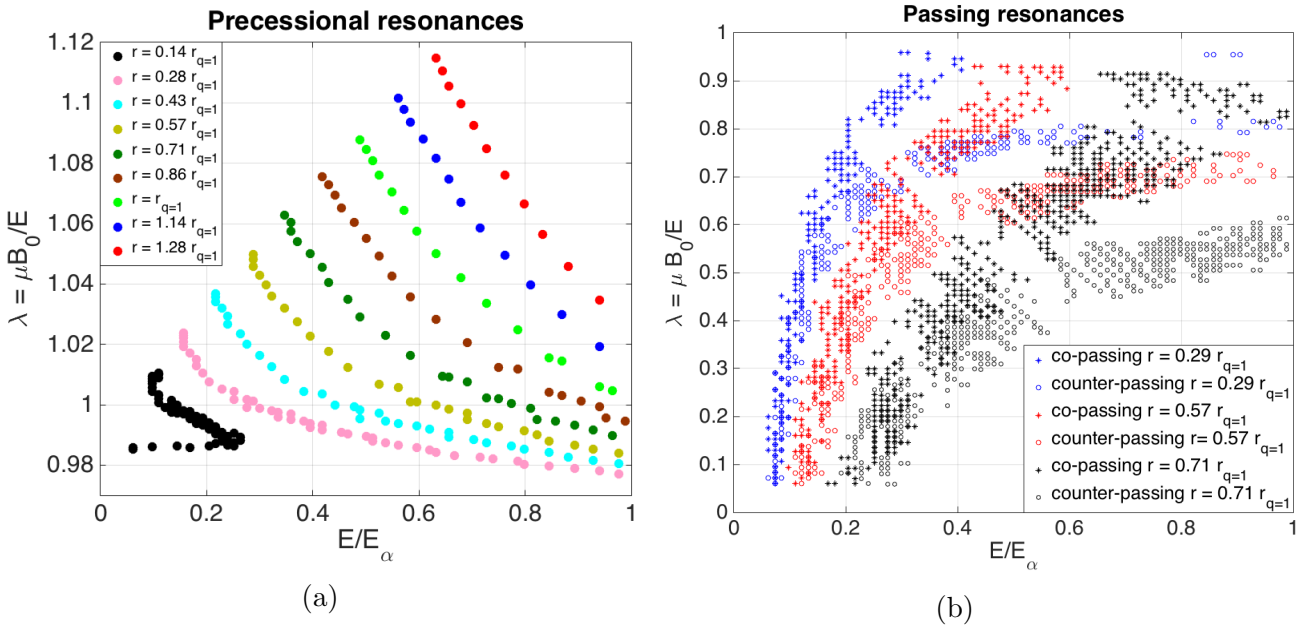

(a) (b)

Figure 6.20: Structure of the resonances for trapped and passing particles in the (E, λ) diagram. (a) Positions of the precessional resonance at different radii. (b) Positions of the co and counter passing resonances at different radii. There is no resonances available after $r = 0.71 r_{q=1}$.

to the ITER-like case. They have exactly the same dependencies over (E, λ, r).
However, for this equilibrium and mode rotation, the harmonics $\mathbf{n} = (0, -1, 1)$ also matters for both co and counter-passing particles, at specific radial positions below $r = 0.71 r_{q=1}$. The passing resonant curves are quite noisy on (Figure (6.20) (b)) since they have been obtained by advancing particles on only 5000 Alfvén times. It is not enough to compute bounce frequencies with a great precision. Yet, their pattern is somewhat similar to those obtained with the analytical theory on Figure (4.1).

Even if passing resonances do exist in this simulation, they do not transport particles as efficiently as the trapped resonance, according to Figure (6.19) (b) and (c). Resonant particle transport due to the precessional resonance is highlighted on Figures (6.21) and (6.22). On Figure (6.21), the perturbed distribution function between the beginning and the end of the simulation is plotted on the trapped (E, λ) diagram at several radial positions. These positions span over the radial interval on which particle transport occurs on Figure (6.19). The radial positions used are $r = 0.5 r_{q=1}$ on subfigure (a), $r = r_{q=1}$ on subfigure (b), and $r = 1.43 r_{q=1}$ on subfigure (c). In this simulation, radial surfaces beyond $q = 1$ are of interest since particles are transported beyond the inertial layer.

As in the ITER-like case, a net outward transport of trapped particles around the linear resonance zone is observed. Inside $q = 1$ at $r = 0.5 r_{q=1}$, 50% of the initial distribution is

transported to larger radial layers. The linear resonance at $r = 0.5r_{q=1}$ (Figure (6.20)) lies inside the transport zone. This transport zone is here again much larger that the initial resonance position. It is explained by the mode down chirping and the evolution of the particles invariants, as discussed in the resonant transport mechanism presented in the previous section.
According to Figure (6.21) (b), some resonant particles are stopped at the q=1 surface, whereas some others are transported further. On this figure, the resonant transport zone is also larger than the linear resonance position at $r = r_{q=1}$. The resonant transport may not be over in this simulation since the mode frequency has not decreased to zero, as it is the case in the ITER-like simulation.
Particles are transported up to $r = 1.43r_{q=1}$, where a particle gain of $\sim 50\%$ is observed.

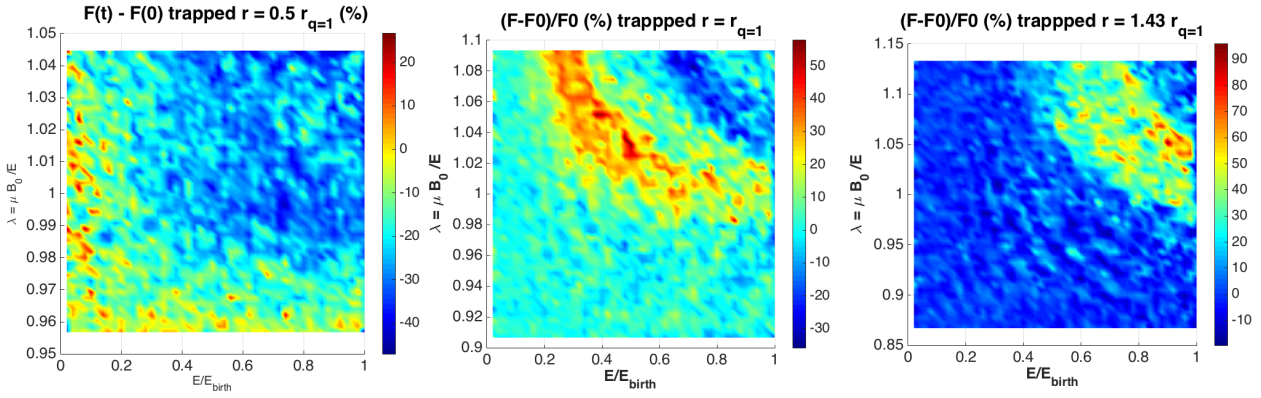

(a) (b) (c)

Figure 6.21: Total time evolution of the alpha distribution function in the (E, λ) diagram at different radii. (a) At $r = 0.5r_{q=1}$, particles are mostly transported to higher radial layers in the resonant zones of the diagram. (b) At the q=1 surface, particles are coming from lower radial layers and transported to higher ones, due to the positions in phase space of the different resonances. (c) At $r = 1.43r_{q=1}$, particles are solely coming from lower layers, since the particles cannot resonate with the 1,1 mode anymore at this radius.

An effective flattening of the alpha particle density profile in invariants space is also observed on Figure 6.22 (a). The kinetic density has been plotted at different times of the nonlinear fishbone phase, in a phase space region in which precessional resonances lie, according to Figure 6.20. The density flattening is up to 40% at the plasma core, at the end of the simulation. Furthermore, this flattening is observed to begin at $t = 2761\tau_A$. According to Figure (6.15) (a) and (b), the mode frequency has not evolved yet significantly at this time. The mode chirping occurs later around $t/\tau_A \sim 3000$. Therefore, resonant particles begin to be transported prior to the mode chirping, as described by the mechanism detailed in 6.1.
When a non-resonant zone of invariants space is considered (Figure (6.22) (b)), it appears that the alpha density profile is marginally flattened during the whole simulation. Such a weak flattening is not due to resonant processes, but to the MHD displacement of the 1,1 mode. It pushes all core particles towards $q = 1$.

Time evolution of the precessional and passing resonances

The time evolution of the resonances position is required to confirm that the mechanism described in 6.1 is also explaining the resonant transport in this simulation. To this effect, the particle flux δF_T and the wave-particle energy exchange $-\mathbf{J} \cdot \mathbf{E}$ are displayed on Figures (6.23) and (6.24). On figure (6.23), these quantities are computed on the trapped (E, λ)

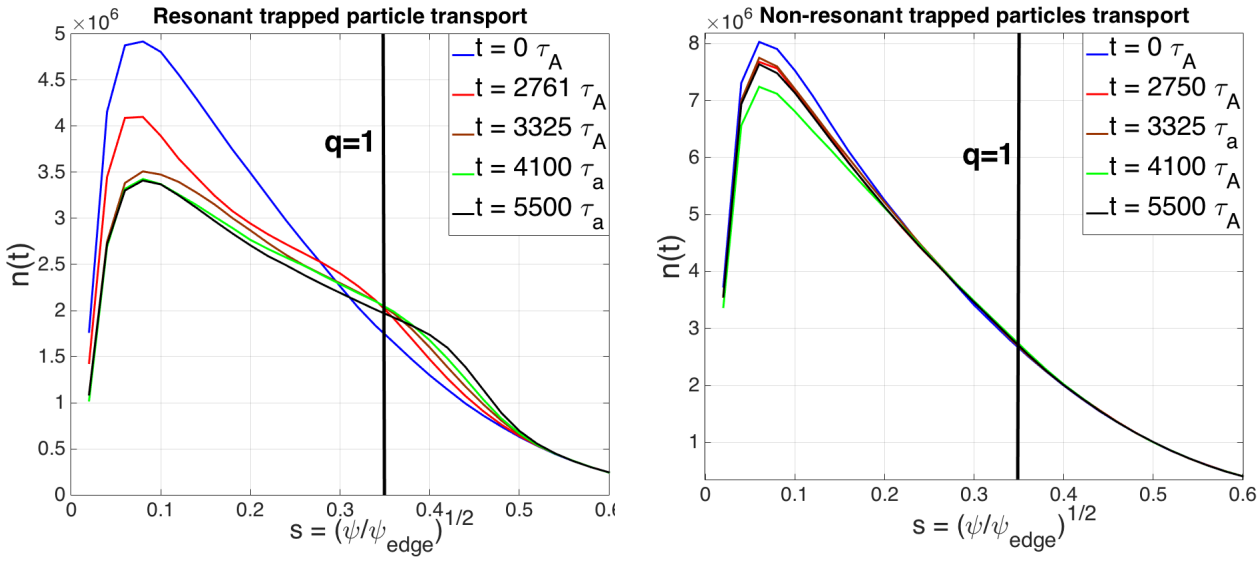

(a) (b)

Figure 6.22: Evolution of the particle density in resonant (a) and non-resonant (b) zones of phase space at characteristic time. A large flattening is observed in resonant zone, due to wave-particle interaction. In the non linear zone, the density is slightly modified due to the MHD displacement.

diagram at $r = r_{q=1}$, for the precessional resonance $\mathbf{n} = (0, 0, 1)$. On Figure (6.24), δF_T and $-\mathbf{J}\cdot\mathbf{E}$ are computed on the passing (E, λ) diagram at $r = 0.71 r_{q=1}$, for the passing resonance $\mathbf{n} = (0, -1, 1)$.

On Figure (6.23), the precessional resonance is observed just before the mode frequency chirps down at $t = 2710\tau_A$ (a) and (b), during the first fishbone oscillation at $t = 3500\tau_A$ (c) and (d), and at the second fishbone oscillation at $t = 3900\tau_A$ (e) and (f). On subfigure (a), it is noticed that the resonant transport arises before the mode chirping. This transport occurs on the initial resonance position at $q = 1$ displayed on Figure (6.20). On subfigure (b), the transport is associated to a small zone where $-\mathbf{J}\cdot\mathbf{E} > 0$.
Moreover, on subfigures (c),(d),(e) and (f), it is observed that the position of the precessional resonance evolves in time, and that new resonant structures arrive from inner radial layers, as in the previous simulation. On these subfigures, there is again the same connection between the sign of δF_T and $-\mathbf{J}\cdot\mathbf{E}$. Therefore, since the resonance position is evolving in time and that the zone of transport corresponds to the zone of wave-particle energy exchange, the same mechanism as in 6.1 is at play here for the precessional resonance.

On Figure 6.24, the passing resonance is displayed at later times than for the precessional resonance. At $t/\tau_A = 3900$ on (a) and (b) during the second fishbone oscillation, at $t/\tau_A = 4200$ on (c) and (d) which corresponds to the end of the second fishbone oscillation, and at $t/\tau_A = 4900$ on (e) and (f) near the simulation's end. The passing resonance is not displayed at earlier times because it does not occur. The same connection exists between δF_T and $-\mathbf{J}\cdot\mathbf{E}$, but the resonant structures do not evolve in time. Multiple resonances arise here as before. It is again due to a competition between particle transport from the considered radial position $r = 0.71 r_{q=1}$ and inner radial layers. The shape of the resonant structures is in good agreement with the resonances expected linearly on Figure (6.20) (b) for counter-passing particles.
The transport associated to the passing resonance is an order of magnitude weaker than

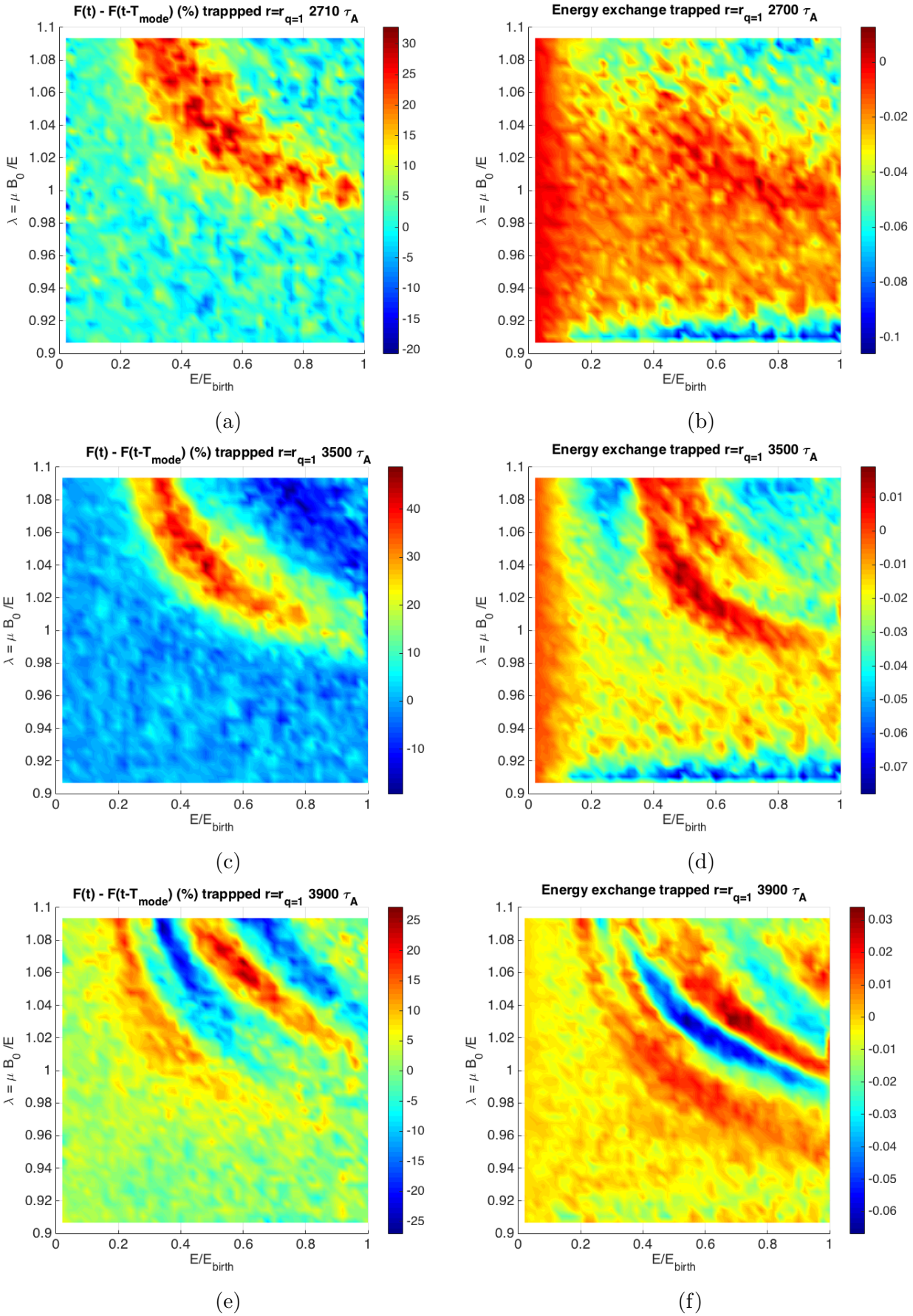

Figure 6.23: Time evolution in the trapped (E, λ) diagram of the particle resonant flux δF_T (left figures) and of the wave-particle energy-exchange $-\mathbf{J} \cdot \mathbf{E}$ (right figures), over a mode period at $r = r_{q=1}$. These quantities are plotted just before the first fishbone oscillation at $t = 2710\tau_A$ (a) and (b); after the first fishbone oscillation at $t = 3500\tau_A$ (c) and (d); and during the second fishbone oscillation at $t = 3900\tau_A$ (e) and (f).

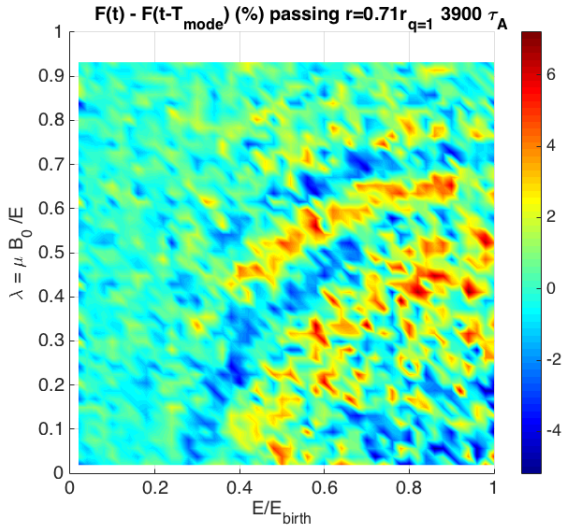

(a)

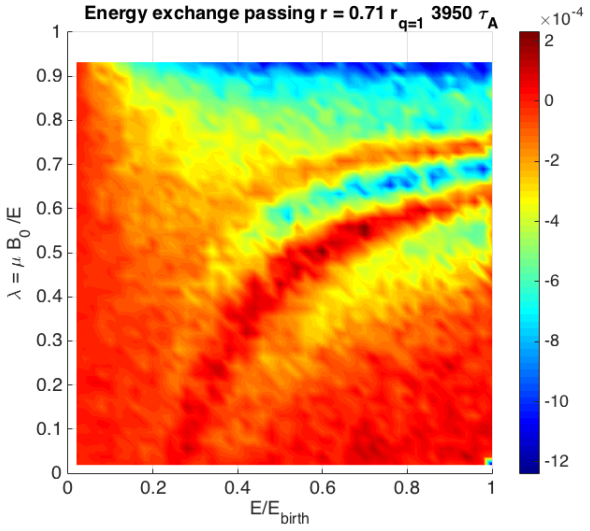

(b)

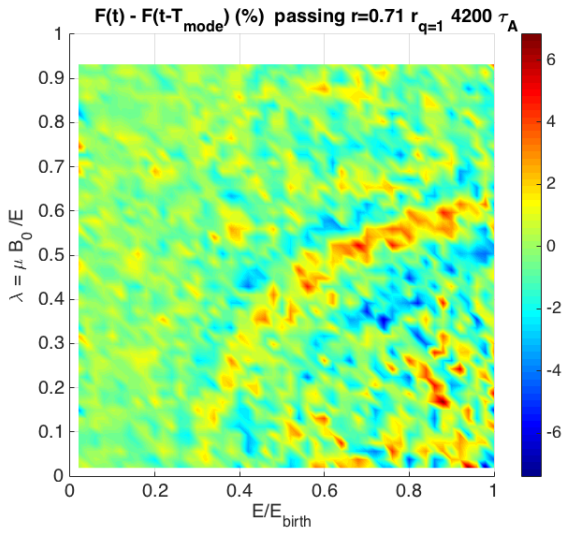

(c)

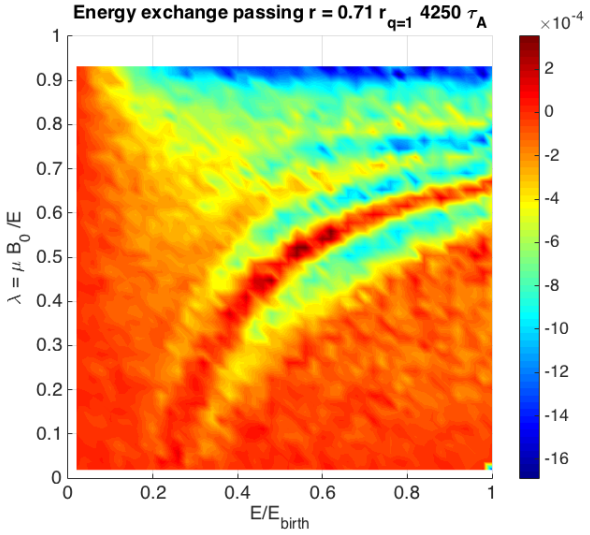

(d)

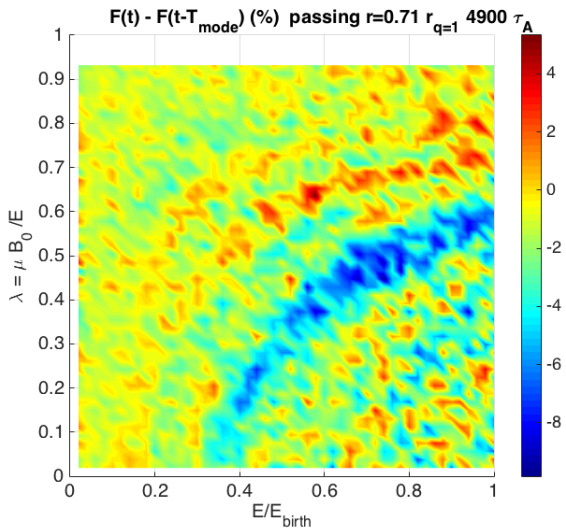

(e)

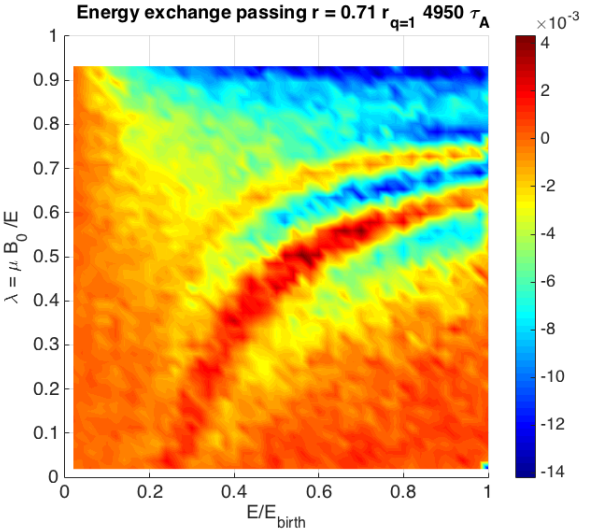

(f)

Figure 6.24: Time evolution in the passing (E, λ) diagram of the particle resonant flux δF_T (left figures) and of the wave-particle energy-exchange $-\mathbf{J} \cdot \mathbf{E}$ (right figures), over a mode period at $r = 0.71 r_{q=1}$. These quantities are plotted at the second fishbone oscillation at $t = 3900\tau_A$ (a) and (b); after the second fishbone oscillation at $t = 4200\tau_A$ (c) and (d); and near the end of the simulation at $t = 4500\tau_A$ (e) and (f).

the transport due to the precessional resonance. The mechanism behind the passing resonance is then different from the mechanism described in 6.1. In this scenario, resonant islands play some role since the resonances do not move. Following the trajectory of a resonant passing particle in the (Θ, P_φ) would help obtain some insights on the physics at play for this resonance. However, the signal $\omega(t)$ is too noisy to carry out such an analysis in this thesis.

6.2.3 Individual nonlinear behavior of near resonance particles

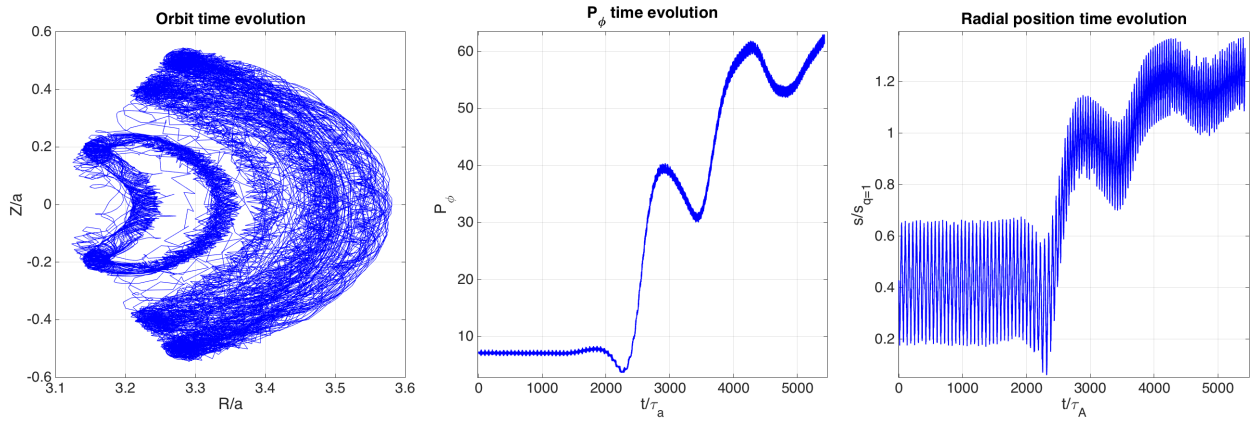

(a) (b) (c)

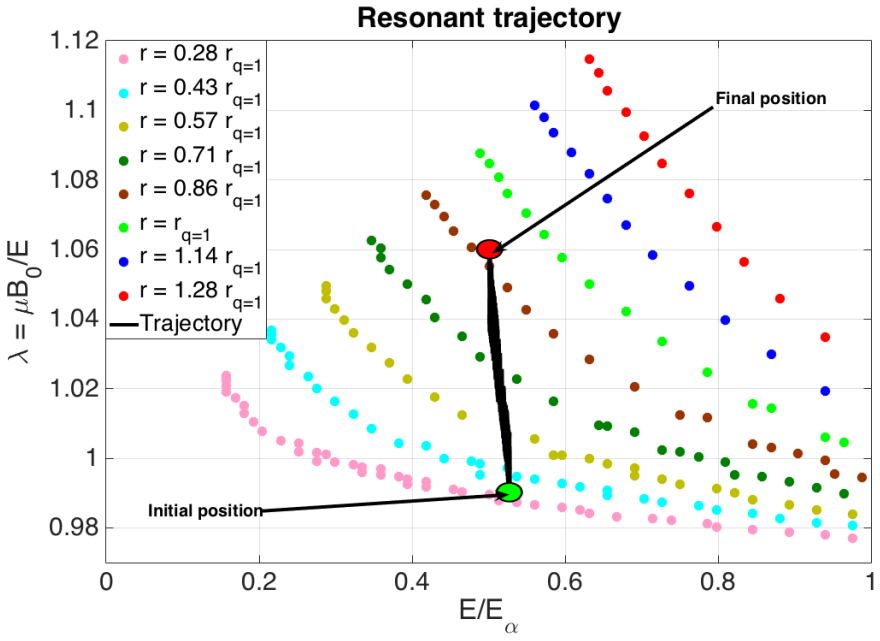

(d)

Figure 6.25: Time evolution of a trapped particle near linear resonance. (a) Trajectory in the poloidal plane (R,Z). (b) Time evolution of P_φ. (c) Time evolution of the radial position normalized to $r_{q=1}$. (d) Trajectory of the particle in the trapped (E, λ) diagram.

The individual nonlinear behavior of a near resonance trapped particle in this simulation is similar to the previous one, as observed on Figure (6.25). The considered particle is transported at a higher radial position as displayed on Figure (6.25) (a), (b) (c). On subfigure (a), the trajectory of the trapped particle is plotted in the poloidal plane. It is observed that the particle orbits on an outer reference flux surface at the end of the simulation.

On subfigure (b), it can be seen that P_φ increases rapidly at the end of the linear phase around $t \sim 2200\tau_A$. This is associated to the outward motion of the particle. Moreover, it is again noted that the transport occurs before the mode chirping. The mechanism detailed in 6.1 explains the transport associated to the precessional resonance.
On subfigure (c), the radial position is plotted, normalized to $r_{q=1}$. It is observed that the particle continues to resonate with the 1,1 mode until $r \sim 1.2 r_{q=1}$. As long as a part of the particle's orbit is inside the surface $q = 1$, it keeps on interacting with the mode.
On subfigure (d), the nonlinear trajectory of the resonant trapped particle in the diagram (E, λ) is plotted. As in the previous section, the particle gets transported to larger pitch angle values and slightly smaller energies.

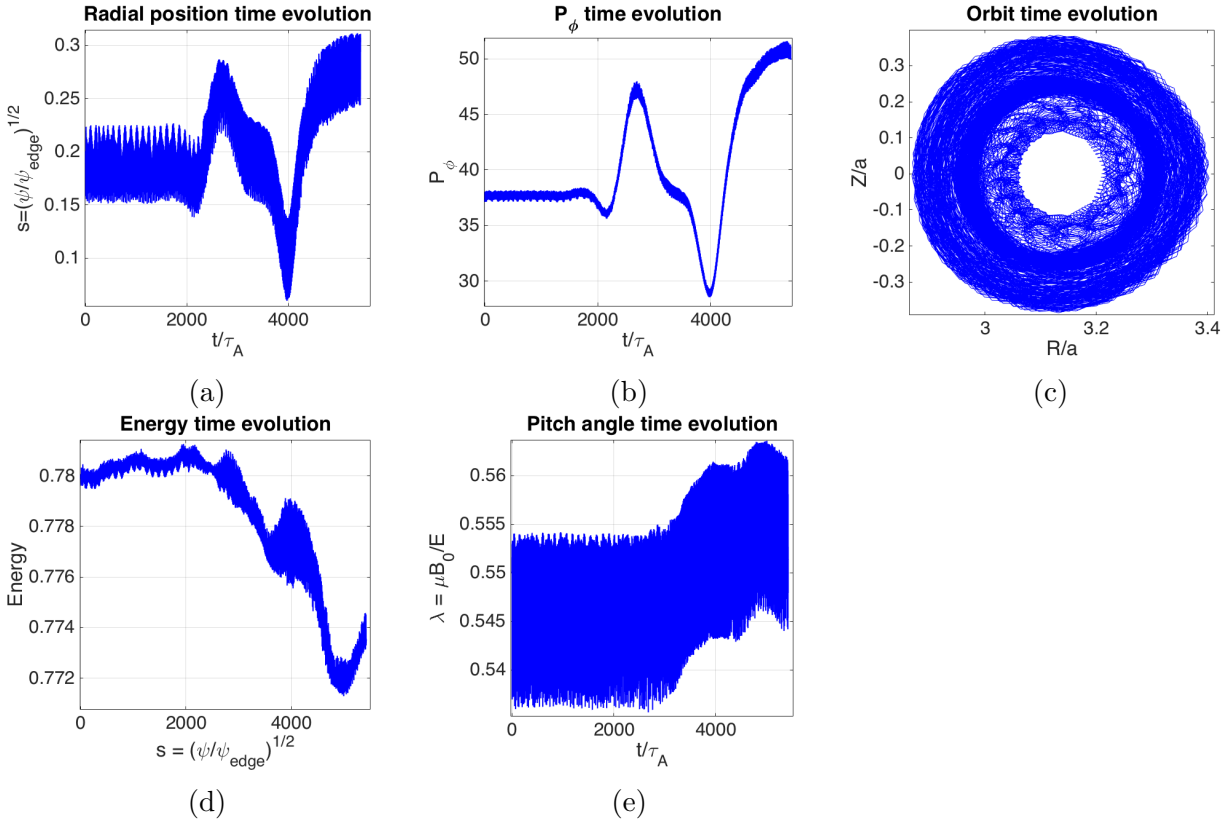

Figure 6.26: Time evolution of a counter-passing particle near linear resonance. (a) Time evolution of the radial position, normalized to $r_{q=1}$. (b) Time evolution of P_φ. (c) Trajectory in the poloidal plane (R,Z). (d) Time evolution of the particle's energy. (e) Time evolution of the pitch angle

Regarding the time evolution of a near resonance counter-passing particle (Figure 6.26), it is observed that its dynamics is affected by the mode. It is noted that the counter-passing particle is transported radially inward and outward during the simulation. This evolution can be observed on subfigures (a), (b) and (c). However, the net transport is still in the outward direction. This would need to be confirmed over longer simulation times. The particle's invariants are also affected by the mode. The energy of the co-passing particle (subfigure (d)) is lowered due to the interaction with the fields. Its pitch angle (subfigure (e)) is also slightly increased.

Interestingly, for the co-passing particle near resonance (Figure (6.27)), no net resonant transport is found in subfigures (a), (b) and (c). Moreover, the particle's invariants such as P_φ (subfigure (c)) and the particle's energy (subfigure (d)) oscillate in time, rather than

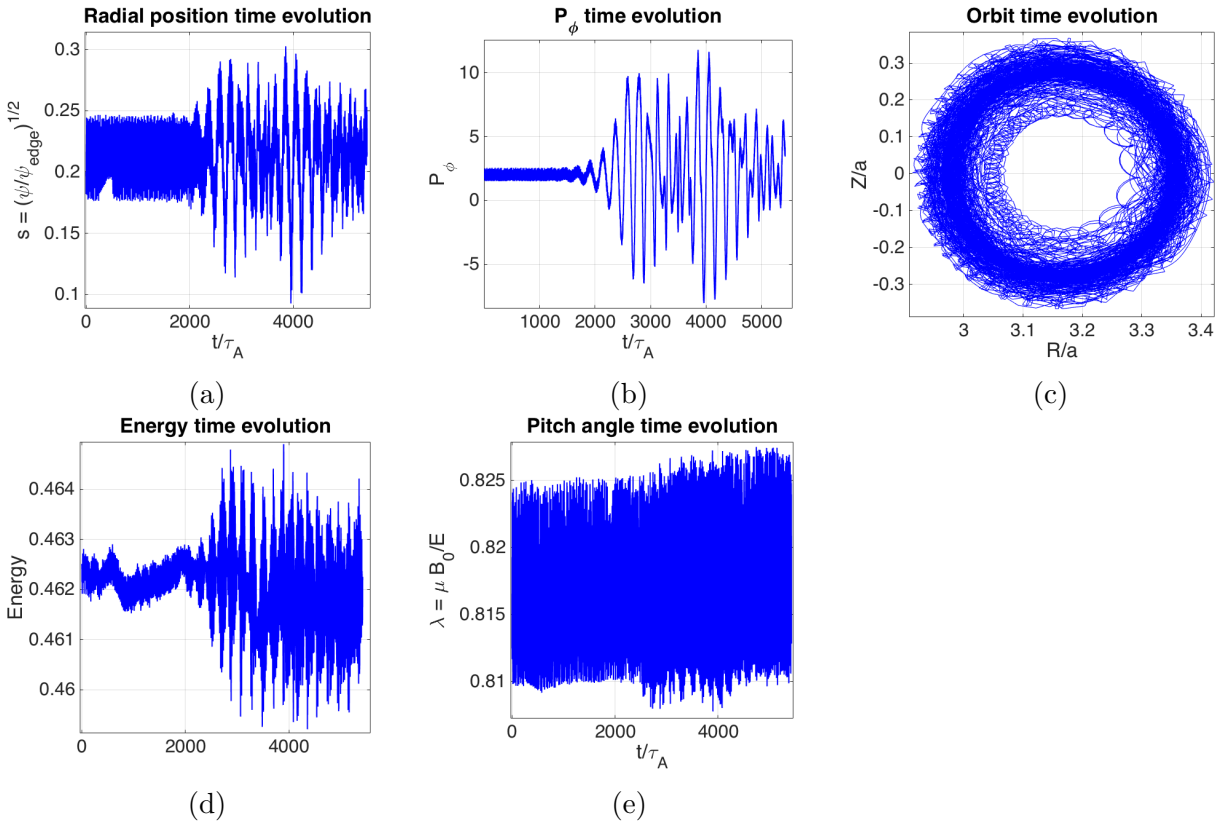

Figure 6.27: Time evolution of a co-passing particle near linear resonance. (a) Time evolution of the radial position, normalized to $r_{q=1}$. (b) Time evolution of P_φ. (c) Trajectory in the poloidal plane (R,Z). (d) Time evolution of the particle's energy. (e) Time evolution of the pitch angle

presenting a net evolution. It could be the sign that this particle is trapped in a phase space island. Plotting the trajectory of this particle in the (Θ, P_φ) diagram would help understanding this phenomena. However, this is beyond the scope of this thesis.

Conclusion on the ITER 15 MA hybrid simulation, in the strong kinetic drive limit

To conclude this study of the fishbone instability on the ITER 15 MA scenario, it can be said that two fishbone oscillations have been observed. They are associated to a weak redistribution of kinetic particles, around 5% of the core alpha particles, and to the down chirping of the 1,1 mode frequency.

Particles are transported on a characteristic time of order 10^{-3} seconds. The nonlinear fishbone phase lasts approximatively 3000 Alfvén times, with an Alfvén time $\tau_A = 5.10^{-7}$ seconds in the simulation. Again, this resonant transport time is a lot smaller than the typical thermalization time of fast particles in ITER, of order $10^{-1} - 1$ seconds [iTER physics basics, 2000]. The use of an imposed slowing-down distribution function for alpha particles is therefore justified.

The resonant transport of trapped particles follows the same mechanism as in the previous hybrid simulation. However, a different mechanism is at play for the passing particles, which is yet to be clarified. Moreover, the dynamics of co-passing and counter-passing particles are observed to be different.

At the end of the simulation, the growth of an internal kink is not observed. Therefore, it would be interesting to continue this simulation further, to see if others fishbone oscillations occur, or if an internal kink takes over.

6.3 ITER 15 MA case close to the fishbone threshold

A nonlinear simulation in the low kinetic drive limit has also been carried out on the ITER 15 MA scenario. It has been performed for the Kinetic-MHD equilibrium described in 5.4.2, with $q_0 = 0.95$, $\beta_h/\beta_{tot} = 7\%$. This equilibrium is close to the fishbone threshold since at $\beta_h/\beta_{tot} = 6\%$, the fishbone mode is not unstable (see Figure (5.13) (a)). The nonlinear simulation performed is still at a preliminary stage.

The time evolution of the kinetic energy of the $n = 0 - 4$ modes obtained so far is displayed on Figure 6.28. The 1,1 mode does not exhibit a clear linear phase, since a strong 1,1 perturbation has been imposed on the equilibrium. Given the low linear growth rate of this fishbone instability, this high perturbation has been used to reduce the computational time of the simulation. It enables to mainly focus on its nonlinear phase, that arises at $t = 6000\tau_A$.

During this nonlinear phase, the mode begins to saturate at a low energy level. The MHD displacement $\boldsymbol{\xi}$ associated to this energy level does not displace much the core plasma. Therefore, a strong resonant interaction cannot arise yet between the 1,1 mode rotation and the particles eigenfrequencies. No net resonant transport is observed. Frequency chirping has not been seen either during this simulation. It needs to be continued further, to see if a resonant transport can arise.

However, some preliminary comparisons with earlier works can be drawn from this early stage nonlinear simulation. The 1,1 mode energy saturates with increasing oscillations, that are not characteristic of the classical nonlinear collisionless damping described in [O'Neil, 1965]. A similar behavior of the 1,1 mode energy has been obtained in [Idouakass, 2016] chapter 5.2. Similar nonlinear increasing oscillations were observed in this work, from the simulation of a fishbone instability in the low kinetic drive limit.
In order to compare properly with this work, Kinetic Poincaré plots in resonant zones of phase space need to be computed. In [Idouakass, 2016] chapter 5, these plots highlight that when the 1,1 mode energy is at a minima, the phase space island is shifted by an additional phase of π in the diagram (Θ, P_φ). This phase slippage is found to explain the observed resonant transport of kinetic particles. Since no resonant transport has yet been observed in XTOR-K's nonlinear simulation, the kinetic Poincaré plots need to be computed at a later stage of the simulation.

Moreover, an other feature of fishbone instabilities in the low kinetic drive limit is also recovered in this simulation. In [Odblom et al., 2002] and [Idouakass, 2016] chapter 4.4, a double step structure is obtained on the 1,1 mode during the nonlinear evolution of the instability. Such a structure is observed in XTOR-K's simulation when the 1,1 kinetic energy reaches a local minima, as shown on Figure 6.29. On (a) and (d), the mode exhibits a classical 1,1 structure with a one step Heaviside side type MHD displacement. However, during (b) and (c), around the energy local minima, a second structure forms inside of q=1. It is characteristic of a double step MHD displacement.

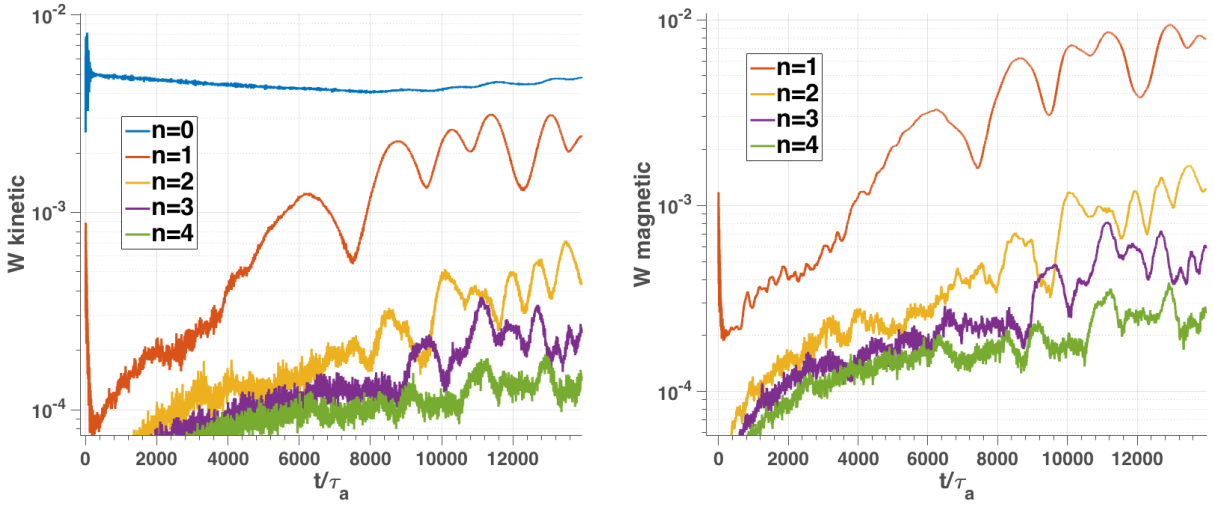

(a) (b)

Figure 6.28: Time evolution of the kinetic energies of the toroidal n modes near the fishbone threshold. This simulation does not have a clear linear phase. The beginning of the nonlinear phase features increasing oscillation of the 1,1 energy.

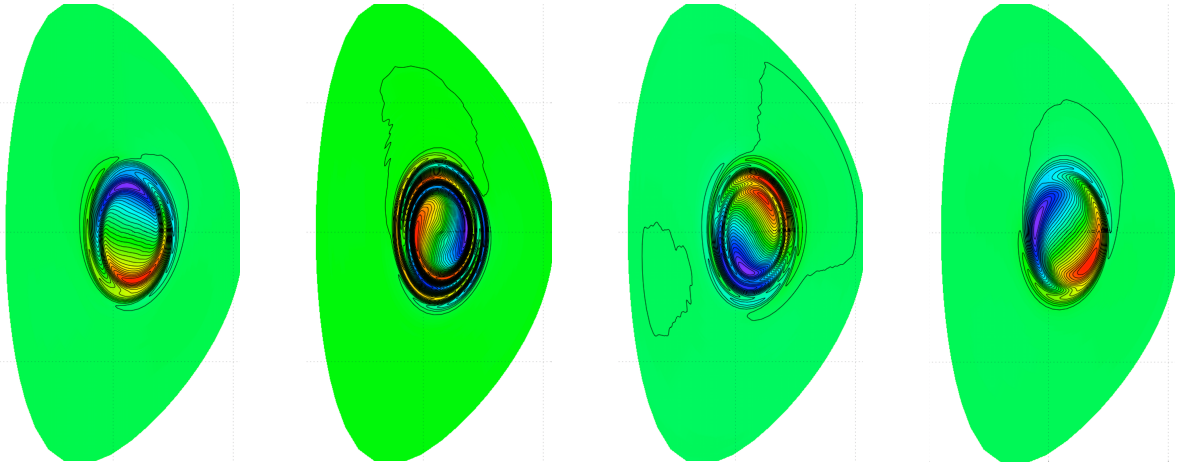

(a) $t = 8831\tau_A$ (b) $t = 9484\tau_A$ (c) $t = 9676\tau_A$ (d) $t = 9906\tau_A$

Figure 6.29: Evolution of the 1,1 mode structure during the bounces of the mode energy. A double step structure is found when the mode energy is at a minima.

6.4 Conclusion

To conclude this chapter on the analysis of particle transport during the nonlinear phase of the fishbone instability, it can be said that several milestones has been reached.

Firstly, a dynamics coherent with the experimental behavior of the fishbone instability has been recovered with XTOR-K. Simulations performed in the strong kinetic drive limit exhibit mode frequency down chirping, accompanied with resonant transport of mostly trapped particles. Simulations have been first carried out for a simplified ITER-like case, and then for an equilibrium more relevant to the ITER 15 MA scenario in terms of geometry, bulk equilibrium and alpha particle energies. Such a study is of crucial importance since it has been shown in Chapter 5 that this scenario will be likely to be unstable against the alpha fishbone instability. A quantification of the global particle transport due to fishbone oscil-

lations has been performed. It is found that over several oscillations, only up to 5% of the core alpha particles are transported outside of the q=1 surface. It implies that the fishbone instability does not decrease importantly the fusion performances due to alpha redistribution before their full thermalization onto the bulk. However, nonlinear simulations would need to be performed over more fishbone oscillations in order to generalize this result.

Moreover, a mechanism explaining the nonlinear interplay between mode down chirping and trapped particle transport has been proposed in the strong kinetic drive limit. A rapid dynamical evolution of the resonant island in phase space occurs at the end of the linear phase. It induces an asymmetric wave-particle energy exchange between resonant particles and the fields that is more beneficial for the fields. This asymmetry is explained by the direction of the kinetic density gradient in the (Θ, P_φ) diagram. An outward transport of fast particles is associated with this asymmetry, flattening in parts of phase space the alpha density profile. This flattening leads to mode down chirping since the kinetic drive in the fishbone dispersion relation is proportional to the alpha density gradient. When the mode frequency chirps down, it allows the precessional resonance to explore new zones of phase space, in which it continues to transport kinetic particles, which increases further the mode frequency down chirping.

Also, it has been found that the characteristic transport time of energetic particles is between two and three orders of magnitude below the total thermalization time of alpha particles onto the bulk plasma. Therefore, an imposed slowing-down distribution function can realistically describe a first series of fishbone oscillations.

Finally, a nonlinear simulation in the low kinetic drive limit has been performed. Preliminary results show increasing bouncing oscillations of the mode energy in the nonlinear phase, as well as a double step structure that appears when the mode energy is at a local minima. These features are present in existing literature [Odblom et al., 2002][Idouakass, 2016]. The mechanism coupling mode frequency down chirping and resonant particle transport is possibly different in this limit. Longer simulations, together with Kinetic Poincaré plots, are necessary to highlight the physics at play in the low kinetic drive limit.

Chapter 7

Conclusion and Perspectives

The ITER tokamak will be the first fusion device to confine burning plasmas over long durations. The alpha particles created by these plasmas are needed to maintain temperatures allowing fusion reactions to happen. Using a large fraction of non-inductive power to heat up the plasma in steady-state operations would severely reduce the enhancement factor of the device. It appears that alpha particles can resonantly interact with MHD instabilities. This interaction results in a new macroscopic instability named the alpha fishbone. The instability tends to transport alphas out of the core plasma. If energetic alphas in the MeV range are transported by the fishbone, they will not be able to transfer their energy to the core plasma. However, if understood and controlled, this instability could help transport the alpha particles that have partially thermalized on the bulk plasma. Thermalized alpha particles in the core plasma are impurities that decrease the fusion power.

Since DT operations on the ITER tokamak are still more than a decade away, nonlinear simulations of this instability are required to identify the scenarios in which the fishbone can occur, and estimate the amount of associated transport. The nonlinear coupling mechanism between mode chirping and resonant transport during fishbone activity needs also to be studied numerically. This would help designing scenarios taking advantage of the fishbone instability. First steps in this direction have been made in this thesis. Chapter 4 reports the implementation of realistic distribution function of energetic particles, slowing-down distributions, in the nonlinear hybrid code XTOR-K. Phase space diagnostics have also been implemented in the code. Their goal is to localize the regions of phase space in which wave-particle interaction and resonant particle transport arise. These implementations enable the fishbone instability to be simulated with XTOR-K, and diagnosed to gain a better understanding of the fishbone dynamics.

Since the kinetic module of XTOR-K has been recently implemented, a linear verification of the code was required before simulating the nonlinear phases of the fishbone instability. To this effect, a linear fishbone dispersion relation has been derived from the Kinetic Energy Principle. This model has the particularity to take into account the resonant effect of passing particles and non-resonant terms. It also solves non-pertrubatively the fishbone dispersion relation. Some minor differences were found between this model and the earlier one on which its derivation is built [Porcelli et al., 1994]. In chapter 5, results obtained from this fishbone dispersion relation and XTOR-K linear simulations are compared for simple Kinetic-MHD equilibria. They are in correct agreement regarding the values of the fishbone complex frequency obtained for different on-axis alpha densities. The phase space region in which wave-particle interaction arises in XTOR-K is also coherent with the position of the precessional resonance predicted by the linear theory. These results enable to verify linearly

the code XTOR-K, attesting the good implementation of its kinetic module. Since the linear model takes into account the effects of passing particles, the particle distribution function implemented in XTOR-K has not been restricted. Moreover, the specificities included in the linear model revealed to be decisive for the verification. Results obtained without resonant passing particles, or without non-resonant terms, did not agree as well with linear results obtained from XTOR-K. The fishbone dispersion relation has also been solved using the expressions presented in [Porcelli et al., 1994]. Results show that the complex frequencies are comparable between the two models. The linear theory developed in this thesis is slightly more in agreement with XTOR-K results than this other model.

As the XTOR-K code was verified linearly, it was then used to study the linear stability of the ITER 15 MA scenario against the alpha fishbone in Chapter 5. The linear model developed could not study this equilibrium due to its intrinsic assumptions over circular shaping and particles of intermediate energies. Linear simulations were performed for two sets of Kinetic-MHD equilibria relevant for the ITER 15 MA case. These sets use different ratio of $\beta_h/\beta_{tot} \in [0, 12\%]$, and two different on axis safety factor, $q_0 = 0.9,\ 0.95$. It was found that the threshold in beta ratio at which the fishbone instability occurs is $\beta_{h,th}/\beta_{tot} = 5\%$ for $q_0 = 0.95$, and $\beta_{h,th}/\beta_{tot} \sim 8 - 10\%$ for $q_0 = 0.9$. Since the expected beta ratio on ITER is $\beta_h/\beta_{tot} \sim 15 - 20\%$, it implies that for these equilibria, the ITER 15 MA scenario will be unstable against the fishbone instability. A discussion is provided in Chapter 5 on the comparison of these results with those of earlier studies. It is discussed why results obtained in [Fu et al., 2006] did not find that this configuration was unstable against the alpha fishbone. It appears that the alpha density gradient used was not peaked enough to destabilize the fishbone.

Nonlinear simulations were performed in the strong kinetic drive limit with XTOR-K in chapter 6. Two set of simulations were studied in this limit, one with a simplified circular ITER-like scenario, and one on the ITER 15 MA equilibrium defined in chapter 5 with $\beta_h/\beta_{tot} = 12\%$ and $q_0 = 0.95$. Results obtained from these two simulations were comparable. Down chirping of the fishbone frequency and resonant alpha particle transport were observed simultaneously. The global transport of alpha particles outside the $q = 1$ surface is found to affect only 5% of the initial distribution function over a few fishbone oscillations. The fusion performances of ITER will then not be too affected by this instability. A mechanism explaining the coupling between mode chirping and resonant transport has been proposed, using the phase space diagnostics. The time evolution of the wave-particle interaction and of the resonant transport show that particles start to be transported before the mode begins to chirp. This leads to the flattening of the alpha density in specific regions of phase space, lowering the kinetic drive of alpha particles. As highlighted by the developed linear theory, lowering the kinetic drive decreases the complex frequency of the mode. Mode roll-over and down frequency chirping are therefore induced by this transport. Given that the mode chirps down, the positions of the resonances are displaced in phase space. More alpha particles can then resonate with the mode, which induces their transport and chirps further down the mode frequency.

A nonlinear simulation was also performed near the fishbone threshold for the ITER 15 MA scenario, in the low kinetic drive limit. This simulation is still at a preliminary stage. The mode has not reached a high enough amplitude to resonate with alpha particles. However, the time evolution of the mode energy, and the onset of a transient double step structure, seems to be in agreement with results obtained from reduced Kinetic-MHD models [Odblom et al., 2002][Idouakass, 2016].

It order to further address the study of the alpha fishbone on ITER and other devices, several points will need to be tackled in the near future. Nonlinear simulations in the strong kinetic drive limit were only performed during a few fishbones oscillations. However, it is observed experimentally that many more oscillations can arise during plasma discharges. Longer simulation times are required to generalize the weak transport results obtained in this thesis. However, if more oscillations were to be described with XTOR-K, not taking into account collisions in the simulation could reveal problematic. The fishbone is flattening the alpha distribution function locally in phase space. Collisions might replenish these zones with alpha particles on longer simulations time, due to the thermalization of particles slightly more energetic and not in resonance with the mode. Partial thermalization would then compete with resonant transport. This could allow the fishbone to be excited again, and to flush the newly resonant particles in cycle. A collision operator has been recently implemented in XTOR-K and is currently being tested. Combining this operator with a realistic source of alpha particles at 3.5 MeV will allow simulations to take this effect into account. Comparing these simulations with the present ones, without any collisions, can determine if the resonant transport time and the partial thermalization time can indeed compete. Moreover, simulating a full cycle of fishbone oscillations followed by a sawtooth crash can help to understand what happens to the alpha distribution function on much longer times. These results would be convenient for assessing quantitatively the amount of alpha heating yielded to the plasma. However, such simulations are not at present tractable since they would require too long simulation times.

In addition to these developments, finalizing the implementation of Kinetic Poincaré plots in XTOR-K would help getting a more complete image of the mechanism coupling mode chirping and transport. The mechanism described in Chapter 6 only notes that a quick dynamical change affects the phase space island at the end of the linear phase. Observing the full dynamics of the island will permit to see how theses changes arise, and to determine how the fishbone instability could be used beneficially. Assuming that a quick island break up is a common feature of strong kinetic drive scenarios, the fishbone could be controlled by engineering in advance the position of the resonance in phase space. When the island breaks up, trapped particles around the resonance are rapidly being transported.

To conclude, simulations in the low kinetic drive limit need to be continued and performed for other equilibria with XTOR-K. The nonlinear behavior of phase space islands is expected to be different in this limit. Resonant particles are more likely to be trapped inside the mode. When the fishbone frequency is chirping down, the island location is displaced at larger radial positions. Particles trapped in the mode would then be transported along with the resonance. The total amount of alpha transported in this limit could therefore be different from the strong kinetic drive case.

Appendix A

Bounce-averaging formalism

In this section, bounce-averaging calculations are detailed for both passing and trapped particles. It is assumed that the MHD equilibrium used has circular flux surfaces, with low Shafranov shift. Any bounce-averaged quantity $\langle F \rangle$ is calculated through

$$\langle F \rangle = \int_{\mathcal{C}} \frac{F}{v_{\parallel}} dl \Big/ \int_{\mathcal{C}} \frac{dl}{v_{\parallel}} \tag{A.1}$$

where $\mathcal{C}$ is the path followed by the particle in the poloidal plane. The parallel velocity can be expressed as follows, considering $E = 1/2mv^2, \mu = mv_{\perp}^2/2B, \lambda = \mu B_0/E, H = R/R_0$

$$v_{\parallel} = \left(\frac{2E}{m}\right)^{1/2} \left(1 - \frac{\lambda}{H}\right)^{1/2} \tag{A.2}$$

where the electric potential has been neglected. Considering θ_0 the bounce angle for trapped particles and $\theta_0 = \pi$ for passing ones

$$\langle F \rangle = \int_{-\theta_0}^{\theta_0} F \Big(1 - \frac{\lambda}{H}\Big)^{-1/2} \frac{d\theta}{2\pi} \Big/ \int_{-\theta_0}^{\theta_0} \Big(1 - \frac{\lambda}{H}\Big)^{-1/2} \frac{d\theta}{2\pi} \tag{A.3}$$

using $\epsilon = r/R_0$, one has

$$\Big(1 - \frac{\lambda}{H}\Big)^{-1/2} = \Big(1 - \lambda + \epsilon\lambda\Big)^{-1/2} \left[1 - \frac{\sin^2(\theta/2)}{y^2}\right]^{-1/2} \tag{A.4}$$

with y^2 being expressed as

$$y^2(x, \lambda) = \frac{1 - \lambda + \epsilon\lambda}{2\epsilon\lambda} \tag{A.5}$$

Passing particles are distinguished from trapped particles by a simple condition on y^2. Trapped particles are characterized by the existence of two turning points in the poloidal plane where their parallel velocity is zero. Therefore, the condition on having trapped particles translates itself, according to (A.2), as $(1 - \lambda/H)^{1/2} = 0$, which implies, assuming $\lambda < 1/1 - \epsilon$, that $0 < y^2 < 1$. Passing particles are therefore characterized by $1 < y^2 < +\infty$.

From these conditions on y^2, the corresponding conditions on the pitch angle λ can be deduced. Respectively, for $y^2 = 0, 1, +\infty$, the corresponding λ are $\lambda = 1/1-\epsilon, \lambda = 1/1+\epsilon, \lambda = 0$. Therefore, for trapped particles, $1/1 + \epsilon < \lambda < 1/1 - \epsilon$, and for passing particles, $0 < \lambda < 1/1 + \epsilon$.

These expressions enable to write $\langle F \rangle$ as

$$\langle F \rangle = \int_{-\theta_0}^{\theta_0} F \Big(1 - y^{-2} \sin^2(\theta/2)\Big)^{-1/2} \frac{d\theta}{2\pi} \Big/ \int_{-\theta_0}^{\theta_0} \Big(1 - y^{-2} \sin^2(\theta/2)\Big)^{-1/2} \frac{d\theta}{2\pi} \tag{A.6}$$

Let us now derive expressions for $\langle \cos\theta \rangle, \langle \theta \sin \rangle$, $\langle v_\parallel^2 \rangle$, and $\langle \cos(q\theta) \rangle$ for both passing and trapped particles, which are appearing in the derivation of λ_K.

A.1 Passing particles

For passing particles, $\theta_0 = \pi$, the frequency to perform a poloidal revolution is defined as

$$\frac{\omega_b}{2\pi} = \frac{(2E/m)^{1/2}}{qR_0 I_{b,p}} \tag{A.7}$$

where

$$I_{b,p} = \int_{-\pi}^{\pi} \Big(1 - \frac{\lambda}{H}\Big)^{-1/2} \frac{d\theta}{2\pi} = 4(1-\lambda+\epsilon\lambda)^{-1/2} \int_0^{\pi/2} (1 - y^{-2}\sin^2\theta)^{-1/2} \frac{d\theta}{2\pi} = (1-\lambda+\epsilon\lambda)^{-1/2} \frac{2\mathbb{K}(1/y^2)}{\pi} \tag{A.8}$$

$\mathbb{K}$ being the elliptic integral of first kind. The definition of a bounce-averaged quantity is then

$$\langle F(\theta) \rangle_P = \int_0^{\pi/2} \frac{F(2\theta)(1 - y^{-2}\sin^2\theta)^{-1/2}}{\mathbb{K}(1/y^2)} d\theta \tag{A.9}$$

Therefore, knowing that

$$\cos 2\theta = 1 - 2\sin^2\theta = 2y^2\Big(1 - \frac{1}{y^2}\sin^2\theta\Big) + 1 - 2y^2 \tag{A.10}$$

it leads to

$$\langle \cos\theta \rangle_P = I_{c,p} = 2y^2 \frac{\mathbb{E}(1/y^2)}{\mathbb{K}(1/y^2)} + 1 - 2y^2 \tag{A.11}$$

where $\mathbb{E}$ is the elliptic integral of the second kind. Moreover, noticing that

$$\partial_\theta \Big[-4y^2(1 - y^{-2}\sin^2\theta)^{1/2} \Big] = 2\sin 2\theta (1 - y^{-2}\sin^2\theta)^{-1/2} \tag{A.12}$$

it implies, using an integration by parts

$$\int_0^{\pi/2} 2\theta \sin 2\theta (1 - y^{-2}\sin^2\theta)^{-1/2} d\theta = \Big[-4y^2\theta(1 - y^{-2}\sin^2\theta)^{1/2} \Big]_0^{\pi/2} + 4y^2 \int_0^{\pi/2} (1 - y^{-2}\sin^2\theta)^{1/2} d\theta \tag{A.13}$$

Therefore, it yields

$$\langle \theta \sin\theta \rangle_P = I_{s,p} = 4y^2 \left[\frac{\mathbb{E}(1/y^2)}{\mathbb{K}(1/y^2)} - \frac{\pi}{2\mathbb{K}(1/y^2)}(1 - y^{-2}) \right] \tag{A.14}$$

For $\langle v_\parallel^2 \rangle$, the derivation is straightforward

$$\langle v_\parallel^2 \rangle = \frac{4E\lambda\epsilon y^2}{m} \frac{\mathbb{E}(1/y^2)}{\mathbb{K}(1/y^2)} \tag{A.15}$$

Finally, in order to obtain $< \cos(q\theta) >_P$, one simply performs an expansion according to the small paramater $(1 - q)$, reading

$$\langle \cos(q\theta) \rangle_P = I_{q,p} = \langle \cos\theta \rangle_P + (1-q)\langle \theta \sin\theta \rangle_P = I_{c,p} + (1-q) I_{s,p} \tag{A.16}$$

A.2 Trapped particles

For trapped particles, θ_0 can have any value in the interval $[0, \pi]$. In order to have explicit expressions for bounce-averaged terms, it is needed to perform a change of variable. Considering the following one, $(1/y)\sin(\theta/2) = \sin u$, $\quad d\theta = \Big(2y/cos(\theta/2)\Big)\cos u \; du$ and knowing that $\cos(\theta/2) = (1 - y^2 \sin^2 u)^{1/2}$, and also noticing that $\theta \in [-\theta_0, \theta_0] \Leftrightarrow u \in [-\pi/2, \pi/2]$ since the existence of a bounce angle implies that $y^2 = \sin^2 \theta_0/2$, it leads to

$$I_{b,t} = 2\int_{-\theta_0}^{\theta_0} \Big(1-\frac{\lambda}{H}\Big)^{-1/2} \frac{d\theta}{2\pi} = \Big(1-\lambda+(r/R_0)\lambda\Big)^{-1/2} \int_0^{\pi/2} \frac{4y}{\cos(\theta/2)} \frac{du}{2\pi} = \Big(2\lambda\frac{r}{R_0}\Big)^{-1/2} \frac{2\mathbb{K}(y^2)}{\pi} \tag{A.17}$$

where the bounce frequency is given in this case by

$$\frac{\omega_b}{2\pi} = \frac{(2E/m)^{1/2}}{qR_0 I_{b,t}} \tag{A.18}$$

Moreover, knowing that $\cos\theta = 2(1 - y^2 \sin^2 u) - 1$

$$\int_{-\theta_0}^{\theta_0} \cos\theta \Big(1 - \frac{\lambda}{H}\Big)^{-1/2} d\theta = 4\Big(2\lambda\frac{r}{R_0}\Big)^{-1/2} \int_0^{\pi/2} \frac{\cos\theta}{\cos(\theta/2)} du = 4\Big(2\lambda\frac{r}{R_0}\Big)^{-1/2} [2\mathbb{E}(y^2) - \mathbb{K}(y^2)] \tag{A.19}$$

which gives

$$\langle \cos\theta \rangle_T = I_{c,t} = 2\frac{\mathbb{E}(y^2)}{\mathbb{K}(y^2)} - 1 \tag{A.20}$$

Performing the same integration by parts as before for $\langle \theta \sin\theta \rangle_T$, where this time the first term is dropped since $1 - y^{-2} \sin^2 \theta_0/2 = 0$

$$\int_{-\theta_0}^{\theta_0} \theta \sin\theta \Big(1 - \frac{\lambda}{H}\Big)^{-1/2} d\theta = 4\Big(2\lambda\frac{r}{R_0}\Big)^{-1/2} 4y^2 \int_{-\theta_0}^{\theta_0} \Big(1 - y^{-2}\sin^2(\theta/2)\Big)^{1/2} d\theta \tag{A.21}$$

Therefore, noticing that $\cos^2 u = y^{-2}(1 - y^2 \sin^2 u) + 1 - y^{-2}$

$$\langle \theta \sin\theta \rangle_T = I_{s,t} = \frac{4y^2}{\mathbb{K}(y^2)} \int_0^{\pi/2} \frac{\cos^2 u}{(1 - y^2 \sin^2 u)^{1/2}} du = 4\frac{\mathbb{E}(y^2)}{\mathbb{K}(y^2)} + 4(y^2 - 1) \tag{A.22}$$

For $\langle v_\parallel^2 \rangle$, it can be shown easily, using the same expression for $\cos^2 u$, that

$$\langle v_\parallel^2 \rangle = \frac{E\lambda\epsilon}{m} < \theta \sin\theta > \tag{A.23}$$

The expression of $\langle \cos q\theta \rangle$ is defined identically for both passing and trapped particles.

Appendix B

Derivation of the precessional frequency for an arbitrary reference magnetic surface

In this annex, explicit derivations of the precessional drift frequency of both trapped and passing particles are presented. These derivations are performed assuming a MHD equilibrium with circular flux surfaces and low Shafranov shift. Given that for passing particles, there is no bijection between their toroidal canonical momentum P_φ and the radius of their reference flux surface $\bar{r}$, the definition of their precessional drift frequency is not unique, and depends on the arbitrary choice made for the reference flux surface. First, a general definition of ω_d will be performed without specifying $\bar{\psi}$ the reference flux surface. Then, it will be applied to two definitions, present in the literature.

B.1 General expression of ω_d

Considering a general definition of the reference magnetic surface $\bar{\psi}$, as

$$\bar{\psi} = \psi_0 - \frac{P_\varphi}{Ze} \tag{B.1}$$

where ψ_0 is an arbitrary shift from the toroidal canonical momentum, the excursion from the reference magnetic surface reads

$$\hat{\psi} = \frac{mRv_\parallel}{Ze} - \psi_0 \tag{B.2}$$

The general definition for the precessional drift frequency is, given in equations (2.48-2.49)

$$\omega_d = \left\langle \mathbf{v}_d \cdot \nabla\varphi - q(\bar{\psi})\mathbf{v}_d \cdot \nabla\theta + \frac{dq}{d\psi}(\bar{\psi})\hat{\psi}\frac{d\theta}{dt} \right\rangle_{\alpha_2} \tag{B.3}$$

with

$$\mathbf{v}_d = -\frac{\sigma E}{ZeB_0R_0}(\sin\theta\ \mathbf{e}_r + \cos\theta\ \mathbf{e}_\theta) \tag{B.4}$$

Therefore, the first term in equation (B.3) is null, and the second one reads

$$\left\langle -q(\bar{\psi})\mathbf{v}_d \cdot \nabla\theta \right\rangle_\alpha = \frac{q(\bar{\psi})E}{ZeB_0R_0\bar{r}}\left[\lambda\langle\cos\theta\rangle_{\alpha_2} - \lambda\epsilon\langle\cos^2\theta\rangle_{\alpha_2} + 4\epsilon\lambda y^2\langle\cos\theta(1 - y^{-2}\sin^2\theta/2)\rangle_{\alpha_2}\right] \tag{B.5}$$

In the rest of this derivation, only the lowest order in ϵ is kept. Bounce-averaged quantities for terms with higher orders in ϵ are given in annex A. The last term in equation (B.3) can be recast as

$$\left\langle \frac{dq}{d\psi}(\bar{\psi})\hat{\psi}\frac{d\theta}{dt}\right\rangle_{\alpha_2} = \left\langle \frac{dq}{d\psi}(\bar{\psi})\hat{\psi}v_{\parallel}\nabla_{\parallel}\theta\right\rangle_{\alpha_2} = \left\langle \frac{dq}{d\psi}(\bar{\psi})\left[\frac{mRv_{\parallel}}{Ze}-\psi_0\right]v_{\parallel}\nabla_{\parallel}\theta\right\rangle_{\alpha_2} \tag{B.6}$$

Knowing that in a cylindrical limit and at leading order $\nabla_{\parallel} = \partial_{\varphi}/R_0 + R_0\partial_{\theta}/(q(\bar{\psi})R^2)$, it yields

$$\left\langle \frac{dq}{d\psi}(\bar{\psi})\hat{\psi}\frac{d\theta}{dt}\right\rangle_{\alpha_2} = 4\frac{dq}{d\psi}(\bar{\psi})\frac{\bar{r}\lambda E y^2}{q(\bar{\psi})ZeR_0}\Big[\frac{m}{4E\lambda y^2\epsilon}\langle v_{\parallel}^2\rangle_{\alpha_2} - \frac{2Ze}{R_0 m}\Big(\frac{m}{E\epsilon\lambda}\Big)^{1/2}\langle\psi_0\rangle_{\alpha_2}\Big] \tag{B.7}$$

The arbitrary reference flux surface $\bar{\psi}$ being linked to its reference radius as $\bar{\psi} = B_0\bar{r}^2/2q(\bar{r})$ without loss of generality, the derivative along ψ can be recast as

$$\frac{dq}{d\psi}(\bar{\psi}) = \frac{s(\bar{r})}{\bar{r}^2 B_0}, \qquad s(\bar{r}) = \bar{r}\frac{dq}{dr}(\bar{r})/q(\bar{r}) \tag{B.8}$$

Equation (B.7) can then be re-expressed as

$$\left\langle \frac{dq}{d\psi}(\bar{\psi})\hat{\psi}\frac{d\theta}{dt}\right\rangle_{\alpha_2} = \frac{q(\bar{r})\lambda E}{ZeB_0\bar{r}R_0}4s(\bar{r})y^2\Big[\frac{m}{4E\lambda y^2\epsilon}\langle v_{\parallel}^2\rangle_{\alpha_2} - \frac{2Ze}{R_0 m}\Big(\frac{m}{E\epsilon\lambda}\Big)^{1/2}\langle\psi_0\rangle_{\alpha_2}\Big] \tag{B.9}$$

The precessional drift frequency for an arbitrary reference flux surface is then, at lowest order in ϵ

$$\omega_d = \frac{q(\bar{r})\lambda E}{ZeB_0\bar{r}R_0}\left[\langle\cos\theta\rangle_{\alpha_2} + 4s(\bar{r})y^2\left(\frac{m}{4E\lambda y^2\epsilon}\langle v_{\parallel}^2\rangle_{\alpha_2} - \frac{2Ze}{R_0 m}\Big(\frac{m}{E\epsilon\lambda}\Big)^{1/2}\langle\psi_0\rangle_{\alpha_2}\right)\right] \tag{B.10}$$

B.2 Explicit expressions

B.2.1 Trapped particles

For trapped particles, the choice for ψ_0 does not matter since their reference flux surface is an invariant of motion. The choice of the reference flux surface is then unique and intersects the banana turning points in the poloidal plane as $\bar{\psi} = \psi = -P_{\varphi}/Ze$. The explicit expression for the precessional frequency is then, using annex A

$$\omega_d(\bar{r},\lambda,E) = \frac{q(\bar{r})\lambda E}{ZeB_0\bar{r}R_0}I_{d,t}(\bar{r},\lambda), \quad I_{d,t} = \left[2\frac{\mathbb{E}(y^2)}{\mathbb{K}(y^2)} - 1 + 4s(\bar{r})\Big(\frac{\mathbb{E}(y^2)}{\mathbb{K}(y^2)} + y^2 - 1\Big)\right] \tag{B.11}$$

B.2.2 Passing particles

Two definitions of the reference flux surface for passing particles are present in the literature. In [Nguyen, 2009], this surface is taken to be directly proportional to the canonical toroidal momentum, $\bar{\psi} = -P_{\varphi}/Ze$, where in this case $\psi_0 = 0$. This choice enables to simplify significantly the derivations using the angle-action formalism, and is closed to the intrinsic reference flux surface for passing particles near the passing-trapped frontier. The explicit expression for ω_d in this case is

$$\omega_d(\bar{r},\lambda,E) = \frac{q(\bar{r})\lambda E}{ZeB_0\bar{r}R_0}I_{d,p}(\bar{r},\lambda), \quad I_{d,p} = \left[2y^2\left(\frac{\mathbb{E}(1/y^2)}{\mathbb{K}(1/y^2)} - 1\right) + 1 + 4s(\bar{r})y^2\frac{\mathbb{E}(1/y^2)}{\mathbb{K}(1/y^2)}\right] \tag{B.12}$$

It is noted that this expression is identical in [Nguyen, 2009]. However, this definition is not the most practical.

Indeed, for energetic particles, the term mRv_φ is of the same order of magnitude than $Ze\psi$. Therefore, passing particles orbits can be quite distant from the latter definition of $\bar{\psi}$. If it is wished to compare theoretical values for ω_d with ones obtained from orbit codes, as it is done in Chapter 5 with XTOR-K, it prevents a precise comparison. Therefore, a wiser choice is to take the time average particle flux surface as reference, which is equivalent to take its average value along α_2

$$\bar{\psi} = \langle\psi\rangle_t = \frac{1}{Ze}[m\langle Rv_\parallel\rangle_{\alpha_2} - P_\varphi], \qquad \hat{\psi} = \frac{m}{Ze}[Rv_\parallel - \langle Rv_\parallel\rangle_{\alpha_2}] \tag{B.13}$$

Such a choice is also made in [Graves, 2013][Merle, 2012][Zonca et al., 2007]. It implies that $\psi_0 = m\langle Rv_\parallel\rangle_{\alpha_2}/Ze$, the explicit expression for ω_d then reads

$$\omega_d(\bar{r},\lambda,E) = \frac{q(\bar{r})\lambda E}{ZeB_0\bar{r}R_0}\left[2y^2\left(\frac{\mathbb{E}(1/y^2)}{\mathbb{K}(1/y^2)}-1\right)+1+4s(\bar{r})y^2\left(\frac{\mathbb{E}(1/y^2)}{\mathbb{K}(1/y^2)}-\left(\frac{\pi}{2\mathbb{K}(1/y^2)}\right)^2\right)\right] \tag{B.14}$$

This expression agrees with [Merle, 2012] and is close to [Zonca et al., 2007], up to the term $(\pi/2\mathbb{K}(1/y^2))^2$ replaced by $(\pi/2\mathbb{K}(1/y^2))\sqrt{1-y^{-2}}$

Appendix C

Analytical expressions for λ_K^{res}

C.1 General derivation

Using a normalized slowing-down distribution function

$$F_{eq}(\bar{r},\hat{v}) = \frac{3}{4\pi \ln[1+(v_b/v_c)^3]}\left(\frac{m}{2}\right)^{3/2} n(r)\frac{\sigma_H(v_\alpha - v)}{\hat{v}^3+\hat{v}_c^3} \tag{C.1}$$

with $\hat{v} = v/v_b$, $\hat{v}_c = v_c/v_b$, v_b the birth velocity of the slowing-down distribution function. The resonant contribution to the fishbone dispersion relation (equation (4.6)) can be decomposed as $\lambda_K^{res} = \lambda_K^{res,\omega_*} + \lambda_K^{res,\omega}$, where λ_K^{res,ω_*} corresponds to the term proportional to ω_*, and $\lambda_K^{res,\omega}$ the one proportional to ω.

$$\lambda_K^{res,\omega_*} = \frac{3\pi^2\epsilon_0 E_b}{2s_0 r_0 B_{p,0}^2 \ln[1+(v_b/v_c)^3]} \sum_{\sigma_\parallel=\pm 1}\int_0^{r_0}\frac{dn_\alpha}{d\bar{r}}\bar{r}d\bar{r}\int_0^{(1-\epsilon)^{-1}} d\lambda \frac{\sigma^2 I_b I_q^2}{\lambda I_d} I_{res,1} \tag{C.2}$$

with

$$I_{res,1} = \frac{4}{v_+ - v_-}\left[v_+\int_0^1 d\hat{v}\frac{\hat{v}^5}{(\hat{v}^3+\hat{v}_c^3)(\hat{v}-v_+)} - v_-\int_0^1 d\hat{v}\frac{\hat{v}^5}{(\hat{v}^3+\hat{v}_c^3)(\hat{v}-v_-)}\right] \tag{C.3}$$

$$\lambda_K^{res,\hat{\omega}} = \frac{3\pi^2\epsilon_0^2\hat{\omega}E_b}{2s_0 B_{p,0}^2 \ln[1+(v_\alpha/v_c)^3]} \sum_{\sigma_\parallel=\pm 1}\int_0^{r_0}\frac{x^2 n_\alpha}{q}d\bar{r}\int_0^{(1-\epsilon)^{-1}} d\lambda \frac{\sigma^2 I_b I_q^2}{\lambda I_d} I_{res,2} \tag{C.4}$$

$$I_{res,2} = \frac{1}{(1+\hat{v}_c^3)(1+v_1+v_2)} + \frac{3}{2(v_+-v_-)}\left[v_+\int_0^1 d\hat{v}\frac{\hat{v}^3}{(\hat{v}^3+\hat{v}_c^3)(\hat{v}-v_+)} - v_-\int_0^1 d\hat{v}\frac{\hat{v}^3}{(\hat{v}^3+\hat{v}_c^3)(\hat{v}-v_-)}\right] \tag{C.5}$$

The expressions for $I_{res,1}$ and $I_{res,2}$ are now explicitly derived in two limits, $v_c/v_b \ll \hat{v}$ and $v_c/v_b \gg \hat{v}$. The following expression enables to explicit $I_{res,1}$ and $I_{res,2}$

$$\int_0^1 \frac{v^n}{v-v_0} = \sum_{m=1}^{n-1} v_0^m \int_0^1 v^{n-m}dv + v_0^n \ln\left[1-\frac{1}{v_0}\right] \tag{C.6}$$

A numerical integration called the collocation method is also presented in the general case.

C.2 $v_c/v_b \ll \hat{v}$

When $v_c/v_b \ll \hat{v}$, $I_{res,1}$ and $I_{res,2}$ can be recast as

$$I_{res,1} = \frac{4}{v_+ - v_-}\left[v_+\int_0^1 d\hat{v}\frac{\hat{v}^2}{\hat{v}-v_+} - v_-\int_0^1 d\hat{v}\frac{\hat{v}^2}{\hat{v}-v_-}\right] \tag{C.7}$$

$$I_{res,2} = \frac{1}{1+v_1+v_2} + \frac{3}{2(v_+ - v_-)}\left[v_+ \int_0^1 d\hat{v} \frac{1}{\hat{v}-v_+} - v_- \int_0^1 d\hat{v} \frac{1}{\hat{v}-v_-}\right] \tag{C.8}$$

C.3 $v_c/v_b \gg \hat{v}$

When $v_c/v_b \ll \hat{v}$, $I_{res,1}$ and $I_{res,2}$ can be recast as

$$I_{res,1} = \frac{4}{\hat{v_c}^3(v_+ - v_-)}\left[v_+ \int_0^1 d\hat{v} \frac{\hat{v}^5}{\hat{v}-v_+} - v_- \int_0^1 d\hat{v} \frac{\hat{v}^5}{\hat{v}-v_-}\right] \tag{C.9}$$

$$I_{res,2} = \frac{1}{\hat{v}_c^3}\left(\frac{1}{1+v_1+v_2} + \frac{3}{2(v_+ - v_-)}\left[v_+ \int_0^1 d\hat{v} \frac{\hat{v}^3}{\hat{v}-v_+} - v_- \int_0^1 d\hat{v} \frac{\hat{v}^3}{\hat{v}-v_-}\right]\right) \tag{C.10}$$

C.4 The collocation method

When an ordering between $\hat{v}_c$ and $\hat{v}$ cannot be found for most $\hat{v} \in [0,1]$, the collocation method is used. The method aims at computing the following resonant integral

$$K = \int_{-\infty}^{+\infty} dv \frac{g(v)}{v - v_0} \tag{C.11}$$

In order to compute $I_{res,1}$ and $I_{res,2}$, $g(\hat{v}) = \hat{v}^n/(\hat{v}^3 + \hat{v}_c^3)$, with $n = 3$ or 5. The collocation method consists in computing K on uniformly spaced grid such as $v_0 = k\Delta v$, with Δv the length between two grid points and $k \in [0, N]$.

On that grid, g is approximated as

$$g(v) = \sum_j g_j h_j(v) \tag{C.12}$$

with $h_i(v) = 0$ when $|v - v_j| > \Delta v$, and

$$h_j(v) = 1 - \frac{|v - v_j|}{\Delta v} \tag{C.13}$$

otherwise. The resonant integral K can then be expressed as

$$K = \sum_{j=-N}^{N} g_j \kappa_{j,k} \tag{C.14}$$

with the kernel

$$\kappa_{j,k} = \int_{-1}^{1} dx \frac{1 - |x|}{x + j - k} \tag{C.15}$$

The kernel can be computed analytically. When $j - k \neq 0$ and $j - k \neq \pm 1$

$$\kappa_{j,k} = \ln\left[\frac{j-k+1}{j-k-1}\right] - (j-k)\ln\left[\frac{(j-k)^2}{(j-k)^2 - 1}\right] \tag{C.16}$$

and $\kappa_{j,k} = \pm 2\ln(2)$ when $j - k = \pm 1$, and $\kappa_{j,k} = i\pi$ when $j - k = 0$.

Bibliography

T. M. Antonsen. Electrostatic modification of variational principles for anisotropic plasmas. *Physics of Fluids*, 25(1):132, 1982. doi: 10.1063/1.863612.

G. Ara, B. Basy, and B. Coppi. Magnetic reconnection and m = 1 oscillations in current carrying plasmas. *Annals of Physics*, 111(2):504–505, apr 1978. doi: 10.1016/0003-4916(78)90073-8.

V.I. Arnold. *Mathematical Methods of Classical Mechanics.* Springer, 1978.

F. W. ASTON. The constitution of the elements. *Nature*, 105(2627):8–8, mar 1920. doi: 10.1038/105008a0.

A. Y. Aydemir. A unified monte carlo interpretation of particle simulations and applications to non-neutral plasmas. *Physics of Plasmas*, 1(4):822–831, apr 1994. doi: 10.1063/1.870740.

H. L. Berk, B. N. Breizman, J. Candy, M. Pekker, and N. V. Petviashvili. Spontaneous hole–clump pair creation. *Physics of Plasmas*, 6(8):3102–3113, aug 1999. doi: 10.1063/1.873550.

Duarte Borba and Wolfgang Kerner. Castor-k:stabilityanalysisofalfve n eigenmodes in the presence of energetic ions in tokamaks. *Journal of Computational Physics*, 1999.

B N Breizman and S E Sharapov. Major minority: energetic particles in fusion plasmas. *Plasma Physics and Controlled Fusion*, 53(5):054001, mar 2011. doi: 10.1088/0741-3335/53/5/054001.

S. Briguglio, G. Vlad, F. Zonca, and C. Kar. Hybrid magnetohydrodynamic-gyrokinetic simulation of toroidal alfvén modes. *Physics of Plasmas*, 2(10):3711–3723, oct 1995. doi: 10.1063/1.871071.

S. Briguglio, F. Zonca, and G. Vlad. Hybrid magnetohydrodynamic-particle simulation of linear and nonlinear evolution of alfvén modes in tokamaks. *Physics of Plasmas*, 5(9):3287–3301, sep 1998. doi: 10.1063/1.872997.

S. Briguglio, X. Wang, F. Zonca, G. Vlad, G. Fogaccia, C. Di Troia, and V. Fusco. Analysis of the nonlinear behavior of shear-alfvén modes in tokamaks based on hamiltonian mapping techniques. *Physics of Plasmas*, 21(11):112301, nov 2014. doi: 10.1063/1.4901028.

S. Briguglio, M. Schneller, X. Wang, C. Di Troia, T. Hayward-Schneider, V. Fusco, G. Vlad, and G. Fogaccia. Saturation of alfvén modes in tokamak plasmas investigated by hamiltonian mapping techniques. *Nuclear Fusion*, 57(7):072001, mar 2017. doi: 10.1088/1741-4326/aa515b.

A. J. Brizard and T. S. Hahm. Foundations of nonlinear gyrokinetic theory. *Reviews of Modern Physics*, 79(2):421–468, apr 2007. doi: 10.1103/revmodphys.79.421.

G. Brochard, R. Dumont, X. Garbet, H. Ltjens, T. Nicolas, and F. Orain. Comprehensive linear model for the n = m = 1 fishbone kinetic-MHD instability. *Journal of Physics: Conference Series*, 1125:012003, nov 2018. doi: 10.1088/1742-6596/1125/1/012003.

M. N. Bussac, R. Pellat, D. Edery, and J. L. Soule. Internal kink modes in toroidal plasmas with circular cross sections. *Physical Review Letters*, 35(24):1638–1641, dec 1975. doi: 10.1103/physrevlett.35.1638.

D. J. Campbell, D. F. H. Start, J. A. Wesson, D. V. Bartlett, V. P. Bhatnagar, M. Bures, J. G. Cordey, G. A. Cottrell, P. A. Dupperex, A. W. Edwards, C. D. Challis, C. Gormezano, C. W. Gowers, R. S. Granetz, J. H. Hammen, T. Hellsten, J. Jacquinot, E. Lazzaro, P. J. Lomas, N. Lopes Cardozo, P. Mantica, J. A. Snipes, D. Stork, P. E. Stott, P. R. Thomas, E. Thompson, K. Thomsen, and G. Tonetti. Stabilization of sawteeth with additional heating in the JET tokamak. *Physical Review Letters*, 60(21):2148–2151, may 1988. doi: 10.1103/physrevlett.60.2148.

J. Candy, H. L. Berk, B. N. Breizman, and F. Porcelli. Nonlinear modeling of kinetic plasma instabilities. *Physics of Plasmas*, 6(5):1822–1829, may 1999. doi: 10.1063/1.873440.

Liu Chen, R. B. White, and M. N. Rosenbluth. Excitation of internal kink modes by trapped energetic beam ions. *Physical Review Letters*, 52(13):1122–1125, mar 1984. doi: 10.1103/physrevlett.52.1122.

C. Z. Cheng. Energetic particle effects on global magnetohydrodynamic modes. *Physics of Fluids B: Plasma Physics*, 2(6):1427–1434, jun 1990. doi: 10.1063/1.859464.

C. Z. Cheng. Alpha particle destabilization of the toroidicity-induced alfvén eigenmodes. *Physics of Fluids B: Plasma Physics*, 3(9):2463–2471, sep 1991. doi: 10.1063/1.859618.

C.Z. Cheng. Kinetic extensions of magnetohydrodynamics for axisymmetric toroidal plasmas. *Physics Reports*, 211(1):1–51, feb 1992. doi: 10.1016/0370-1573(92)90166-w.

J.W. Connor and R. J. Hastie. The effect of shaped plasma cross sections on the ideal internal kink mode in a tokamak. *UKAEA memorandum*, 1985.

B. Coppi and F. Porcelli. Theoretical model of fishbone oscillations in magnetically confined plasmas. *Physical Review Letters*, 57(18):2272–2275, nov 1986. doi: 10.1103/physrevlett.57.2272.

B. Coppi, R.J. Hastie, S. Migliuolo, F. Pegoraro, and F. Porcelli. Suppression of internal plasma oscillations by trapped high energy nuclei. *Physics Letters A*, 132(5):267–272, oct 1988. doi: 10.1016/0375-9601(88)90563-4.

B. Coppi, S. Migliuolo, F. Pegoraro, and F. Porcelli. Global modes and high-energy particles in ignited plasmas. *Physics of Fluids B: Plasma Physics*, 2(5):927–943, may 1990. doi: 10.1063/1.859240.

Steven C. Cowley. The quest for fusion power. *Nature Physics*, 12(5):384–386, may 2016. doi: 10.1038/nphys3719.

B Davies. Locating the zeros of an analytic function. *Journal of Computational Physics*, 66 (1):36–49, sep 1986. doi: 10.1016/0021-9991(86)90052-5.

Joseph J. Devaney and Myron L. Stein. Plasma energy deposition from nuclear elastic scattering. *Nuclear Science and Engineering*, 46(3):323–333, dec 1971. doi: 10.13182/nse71-a22370.

E.J. Doyle, W.A. Houlberg (Chair Confinement Da Modelling), Y. Kamada (Chair Pedestal, Edge), V. Mukhovatov (co Chair Transport Physics), T.H. Osborne (co Chair Pedestal, Edge), A. Polevoi (co Chair Confinement Da Modelling), G Bateman, J.W Connor, J.G. Cordey (retired), T Fujita, X Garbet, T.S Hahm, L.D Horton, A.E Hubbard, F Imbeaux, F Jenko, J.E Kinsey, Y Kishimoto, J Li, T.C Luce, Y Martin, M Ossipenko, V Parail, A Peeters, T.L Rhodes, J.E Rice, C.M Roach, V Rozhansky, F Ryter, G Saibene, R Sartori, A.C.C Sips, J.A Snipes, M Sugihara, E.J Synakowski, H Takenaga, T Takizuka, K Thomsen, M.R Wade, H.R Wilson, ITPA Transport Physics Topical Group, ITPA Confinement Database, Model Group, ITPA Pedestal, and Edge Topical Group. Chapter 2: Plasma confinement and transport. *Nuclear Fusion*, 47(6):S18–S127, jun 2007. doi: 10.1088/0029-5515/47/6/s02.

A. S. Eddington. The internal constitution of the stars. *Nature*, 106(2653):14–20, sep 1920. doi: 10.1038/106014a0.

D Edery, X Garbet, J P Roubin, and A Samain. Variational formalism for kinetic-MHD instabilities in tokamaks. *Plasma Physics and Controlled Fusion*, 34(6):1089–1112, jun 1992. doi: 10.1088/0741-3335/34/6/013.

Jeffrey P. Freidberg. *Ideal MHD*. Cambridge University Press, 2014. doi: 10.1017/cbo9780511795046.

G. Y. Fu, W. Park, H. R. Strauss, J. Breslau, J. Chen, S. Jardin, and L. E. Sugiyama. Global hybrid simulations of energetic particle effects on the n=1 mode in tokamaks: Internal kink and fishbone instability. *Physics of Plasmas*, 13(5):052517, may 2006. doi: 10.1063/1.2203604.

J. P. Graves, I. Chapman, S. Coda, L.-G. Eriksson, and T. Johnson. Sawtooth-control mechanism using toroidally propagating ion-cyclotron-resonance waves in tokamaks. *Physical Review Letters*, 102(6), feb 2009. doi: 10.1103/physrevlett.102.065005.

Jonathan P. Graves. Influence of asymmetric energetic ion distributions on sawtooth stabilization. *Physical Review Letters*, 92(18), may 2004. doi: 10.1103/physrevlett.92.185003.

Jonathan P Graves. Toroidal drift precession and wave–particle interaction in shaped tokamaks with finite beta and neoclassical equilibrium effects. *Plasma Physics and Controlled Fusion*, 55(7):074009, jun 2013. doi: 10.1088/0741-3335/55/7/074009.

R. D. Hazeltine and J. D. Meiss. *Plasma confinement*. Dover Publications, 2003.

W.W. Heidbrink and G. Sager. The fishbone instability in the DIII-d tokamak. *Nuclear Fusion*, 30(6):1015–1025, jun 1990. doi: 10.1088/0029-5515/30/6/004.

Bo Hu, R. Betti, and J. Manickam. Kinetic stability of the internal kink mode in ITER. *Physics of Plasmas*, 13(11):112505, nov 2006. doi: 10.1063/1.2364147.

Malik Idouakass. *Linear and Nonlinear Study of the Precessional Fishbone Instability*. PhD thesis, Aix-Marseille Universit, 2016.

F. Imbeaux, S.D. Pinches, J.B. Lister, Y. Buravand, T. Casper, B. Duval, B. Guillerminet, M. Hosokawa, W. Houlberg, P. Huynh, S.H. Kim, G. Manduchi, M. Owsiak, B. Palak, M. Plociennik, G. Rouault, O. Sauter, and P. Strand. Design and first applications of the ITER integrated modelling & analysis suite. *Nuclear Fusion*, 55(12):123006, oct 2015. doi: 10.1088/0029-5515/55/12/123006.

iTER physics basics. ITER physics basis chapter 5: Physics of energetic ions. *Nuclear Fusion*, 40(3):429–429, mar 2000. doi: 10.1088/0029-5515/40/3/511.

M Keilhacker, A Gibson, C Gormezano, and P.H Rebut. The scientific success of jet. *Nuclear Fusion*, 41(12):1925–1966, dec 2001. doi: 10.1088/0029-5515/41/12/217.

Philipp Lauber. Super-thermal particles in hot plasmas—kinetic models, numerical solution strategies, and comparison to tokamak experiments. *Physics Reports*, 533(2):33–68, dec 2013. doi: 10.1016/j.physrep.2013.07.001.

David Leblond. *Simulation des plasmas de tokamak avec XTOR : r egimes des dents de scie et evolution vers une mod elisation cin etique des ions.* PhD thesis, Ecole Polytechnique X, 2011.

H. Lütjens, A. Bondeson, and O. Sauter. The CHEASE code for toroidal MHD equilibria. *Computer Physics Communications*, 97(3):219–260, sep 1996. doi: 10.1016/0010-4655(96)00046-x.

Hinrich Lütjens and Jean-François Luciani. XTOR-2f: A fully implicit newton–krylov solver applied to nonlinear 3d extended MHD in tokamaks. *Journal of Computational Physics*, 229(21):8130–8143, oct 2010. doi: 10.1016/j.jcp.2010.07.013.

M J Mantsinen, S Sharapov, B Alper, A Gondhalekar, and D C McDonald. A new type of MHD activity in JET ICRF-only discharges with high fast-ion energy contents. *Plasma Physics and Controlled Fusion*, 42(12):1291–1308, dec 2000. doi: 10.1088/0741-3335/42/12/305.

K. McGuire and al. Study of high-beta magnetohydrodynamic modes and fast-ion losses in PDX. *Physical Review Letters*, 51(20):1925–1925, nov 1983. doi: 10.1103/physrevlett.51.1925.2.

A. Merle. *Stability and properties of electron-driven fishbones in tokamaks.* PhD thesis, Ecole Polytechnique, 2012.

F. Nabais, D. Borba, M. Mantsinen, M. F. F. Nave, S. E. Sharapov, and Joint European Torus-European Fusio. Fishbones in joint european torus plasmas with high ion-cyclotron-resonance-heated fast ions energy content. *Physics of Plasmas*, 12(10):102509, oct 2005. doi: 10.1063/1.2096527.

F. Nabais, D. Borba, R. Coelho, A. Figueiredo, J. Ferreira, N. Loureiro, and P. Rodrigues. The CASTOR-k code, recent developments and applications. *Plasma Science and Technology*, 17(2):89–96, feb 2015. doi: 10.1088/1009-0630/17/2/01.

M.F.F. Nave, D.J. Campbell, E. Joffrin, F.B. Marcus, G. Sadler, P. Smeulders, and K. Thomsen. Fishbone activity in jet. *Nuclear Fusion*, 31(4):697–710, apr 1991. doi: 10.1088/0029-5515/31/4/007.

C. Nguyen. *Magneto-hydrodynamic activity and energetic particles : application to Beta Alfven Eigenmodes.* PhD thesis, Ecole Polytechnique, 2009.

A. Odblom, B. N. Breizman, S. E. Sharapov, T. C. Hender, and V. P. Pastukhov. Nonlinear magnetohydrodynamical effects in precessional fishbone oscillations. *Physics of Plasmas*, 9(1):155–166, jan 2002. doi: 10.1063/1.1421373.

Thomas O'Neil. Collisionless damping of nonlinear plasma oscillations. *Physics of Fluids*, 8 (12):2255, 1965. doi: 10.1063/1.1761193.

W. Park, S. Parker, H. Biglari, M. Chance, L. Chen, C. Z. Cheng, T. S. Hahm, W. W. Lee, R. Kulsrud, D. Monticello, L. Sugiyama, and R. White. Three-dimensional hybrid gyrokinetic-magnetohydrodynamics simulation. *Physics of Fluids B: Plasma Physics*, 4(7): 2033–2037, mar 1992. doi: 10.1063/1.860011.

W. Park, E. V. Belova, G. Y. Fu, X. Z. Tang, H. R. Strauss, and L. E. Sugiyama. Plasma simulation studies using multilevel physics models. *Physics of Plasmas*, 6(5):1796–1803, may 1999. doi: 10.1063/1.873437.

Thomas Sunn Pedersen, Ralf Knig, Maciej Krychowiak, Marcin Jakubowski, Jrgen Baldzuhn, Sergey Bozhenkov, Golo Fuchert, Andreas Langenberg, Holger Niemann, Daihong Zhang, Kian Rahbarnia, Hans-Stephan Bosch, Yevgen Kazakov, Sebastijan Brezinsek, Yu Gao, and Novimir Pablant and. First results from divertor operation in wendelstein 7-x. *Plasma Physics and Controlled Fusion*, 61(1):014035, nov 2018. doi: 10.1088/1361-6587/aaec25.

Youbin Pei, Nong Xiang, Youjun Hu, Y. Todo, Guoqiang Li, Wei Shen, and Liqing Xu. Kinetic-MHD hybrid simulation of fishbone modes excited by fast ions on the experimental advanced superconducting tokamak (EAST). *Physics of Plasmas*, 24(3):032507, mar 2017. doi: 10.1063/1.4978562.

F Porcelli. Fast particle stabilisation. *Plasma Physics and Controlled Fusion*, 33(13):1601–1620, nov 1991. doi: 10.1088/0741-3335/33/13/009.

F. Porcelli, R. Stankiewicz, W. Kerner, and H. L. Berk. Solution of the drift-kinetic equation for global plasma modes and finite particle orbit widths. *Physics of Plasmas*, 1(3):470–480, mar 1994. doi: 10.1063/1.870792.

Jean-Marcel Rax. *Physique des Tokamaks*. Ecole Polytechnique, 2011. ISBN 978-2-7302-1580-0. URL `https://www.amazon.com/Physique-Tokamaks-Jean-Marcel-Rax/dp/2730215808?SubscriptionId=AKIAIOBINVZYXZQZ2U3A&tag=chimbori05-20&linkCode=xm2&camp=2025&creative=165953&creativeASIN=2730215808`.

Zhen-Zhen Ren, G. Y. Fu, M. A. Van Zeeland, Feng Wang, Zheng-Xiong Wang, R. Nazikian, F. Turco, and C. C. Petty. Hybrid simulations of fishbone instabilities and alfvén eigenmodes in DIII-d tokamak. *Physics of Plasmas*, 25(12):122504, dec 2018. doi: 10.1063/1.5064647.

T H Stix. Heating of toroidal plasmas by neutral injection. *Plasma Physics*, 14(4):367–384, apr 1972. doi: 10.1088/0032-1028/14/4/002.

Y. Todo. Properties of energetic-particle continuum modes destabilized by energetic ions with beam-like velocity distributions. *Physics of Plasmas*, 13(8):082503, aug 2006. doi: 10.1063/1.2234296.

Y. Todo and T. Sato. Linear and nonlinear particle-magnetohydrodynamic simulations of the toroidal alfvén eigenmode. *Physics of Plasmas*, 5(5):1321–1327, may 1998. doi: 10.1063/1.872791.

Y. Todo, T. Sato, K. Watanabe, T. H. Watanabe, and R. Horiuchi. Magnetohydrodynamic vlasov simulation of the toroidal alfvén eigenmode. *Physics of Plasmas*, 2(7):2711–2716, aug 1995. doi: 10.1063/1.871235.

G. Vlad, S. Briguglio, G. Fogaccia, F. Zonca, V. Fusco, and X. Wang. Electron fishbone simulations in tokamak equilibria using XHMGC. *Nuclear Fusion*, 53(8):083008, jul 2013. doi: 10.1088/0029-5515/53/8/083008.

Feng Wang, G. Y. Fu, J. A. Breslau, and J. Y. Liu. Linear stability and nonlinear dynamics of the fishbone mode in spherical tokamaks. *Physics of Plasmas*, 20(10):102506, oct 2013. doi: 10.1063/1.4824739.

X. Wang, S. Briguglio, L. Chen, C. Di Troia, G. Fogaccia, G. Vlad, and F. Zonca. An extended hybrid magnetohydrodynamics gyrokinetic model for numerical simulation of shear alfvén waves in burning plasmas. *Physics of Plasmas*, 18(5):052504, may 2011. doi: 10.1063/1.3587080.

John Wesson and Amiya K. Sen. Tokamaks. *Physics Today*, 42(5):78–78, may 1989. doi: 10.1063/1.2811022.

R. B. White, F. Romanelli, and M. N. Bussac. Influence of an energetic ion population on tokamak plasma stability. *Physics of Fluids B: Plasma Physics*, 2(4):745–753, apr 1990. doi: 10.1063/1.859312.

Yanlin Wu, C. Z. Cheng, and R. B. White. Alpha particle effects on the internal kink and fishbone modes. *Physics of Plasmas*, 1(10):3369–3377, oct 1994. doi: 10.1063/1.870485.

F. Zonca, P. Buratti, A. Cardinali, L. Chen, J.-Q. Dong, Y.-X. Long, A.V. Milovanov, F. Romanelli, P. Smeulders, L. Wang, Z.-T. Wang, C. Castaldo, R. Cesario, E. Giovannozzi, M. Marinucci, and V. Pericoli Ridolfini. Electron fishbones: theory and experimental evidence. *Nuclear Fusion*, 47(11):1588–1597, oct 2007. doi: 10.1088/0029-5515/47/11/022.

F Zonca, L Chen, S Briguglio, G Fogaccia, G Vlad, and X Wang. Nonlinear dynamics of phase space zonal structures and energetic particle physics in fusion plasmas. *New Journal of Physics*, 17(1):013052, jan 2015. doi: 10.1088/1367-2630/17/1/013052.

Fulvio Zonca and Liu Chen. Theory on excitations of drift alfvén waves by energetic particles. II. the general fishbone-like dispersion relation. *Physics of Plasmas*, 21(7):072121, jul 2014. doi: 10.1063/1.4889077.

Titre : Dynamique du fishbone ionique dans les tokamaks : théorie et simulations non-linéaires multi-échelles

Mots clés : Fusion, plasma, magnétohydrodynamique, particules énergétiques, non-linéaire, fishbone

Résumé : Dans les plasmas de tokamak, les particules rapides générées par les réactions de fusion et par les méthodes de chauffage non-inductives peuvent interagir avec les instabilités Magnéto-Hydro-Dynamiques, conduisant potentiellement à leur transport en dehors du plasma de coeur. Cette problématique est importante dans le contexte des plasmas en combustion, où la relaxation collisionnelle des particules alpha est nécessaire pour compenser la perte d'énergie lors la décharge. Le temps de transport résonant des particules rapides étant bien plus petit que leur temps de thermalisation sur le plasma thermique, ces instabilités MHD-cinétiques peuvent engendrer une dégradation de l'efficacité énergétique de la réaction, qui est d'importance cruciale pour les futurs réacteurs commerciaux. Dans cette thèse, nous étudions l'interaction des ions énergétiques avec le mode de kink interne, qui conduit à l'émergence de l'instabilité fishbone. À cette fin, nous utilisons le code non-linéaire hybride XTOR-K, pour simuler les phases non-linéaires du fishbone ionique, durant lesquelles les particules rapides sont tranportées. Dans un premier temps, la théorie linéaire de l'instabilité fishbone est reproduite, retrouvant une relation de dispersion similaire à celle du modèle de Porcelli. Un écart est constaté pour les particules très passantes. Un code linéaire a été implémenté pour résoudre de façon non perturbative la relation de dispersion du fishbone obtenue. Les résultats obtenus avec ce code sont cohérents avec ceux d'XTOR-K dans la phase linéaire des simulations, avec des taux de croissance, des fréquences de rotation et des surfaces de résonance similaires. Ces résultats fournisent une vérification linéaire de XTOR-K, permettant son utilisation sur des équilibres plus complexes, et durant des phases non-linéaires. Dans un second temps, une étude paramétrique est fournise par XTOR-K sur la stabilité linéaire du fishbone alpha, avec des équilibres pertinents pour le cas ITER 15 MA. Nos simulations montrent que ce scénario sera probablement instable à l'égard du fishbone alpha, pour des densités de particules alpha réalistes dans ITER. Les résultats non-linéaires obtenus avec XTOR-K sur un équilibre circulaire peu énergétique et sur le cas ITER 15 MA sont ensuite présentés. Ces résultats documentent la dynamique auto-cohérente des particules rapides et des modes MHD lors de plusieurs oscillations fishbone. Le transport résonant de particules rapides est une caractéristique commune dans ces simulations, accompagnée d'une décroissance charactéristique de la fréquence du mode MHD-cinétique. Les différences dans ces simulations sont discutées, ainsi que le régime non-linéaire charactérisant le mode observé sur la base des théories existantes. Durant quelques oscillations fishbone, dans nos différentes simulations, le transport total de particules alpha au coeur du plasma est de l'ordre de 5 % de la population initiale, ce qui montre que la réduction des performances de fusion due à l'instabilité fishbone-alpha est limitée. À partir de ces simulations, un mécanisme expliquant le couplage non-linéaire entre le transport résonant de particules et la décroissance en fréquence du mode MHD-cinétique est présenté.

Title : Dynamics of ion-driven fishbones in tokamaks : theory and nonlinear hybrid fluid/kinetic simulations

Keywords : Fusion, plasma, magnetohydrodynamics, energetic particles, nonlinear, fishbone

Abstract : In tokamak plasmas, fast particles generated by fusion reactions and by non-inductive heating techniques can resonantly interact with Magneto-Hydro-Dynamic (MHD) instabilities, potentially leading to their transport out of the plasma core. This topic is important in the context of burning plasmas, where the collisional relaxation of alpha particles is expected to compensate the energy losses. The resonant transport time of fast particles being much lower than their typical relaxation, these Kinetic-MHD instabilities can adversely impact the plasma energy balance, and therefore the fusion performance of future commercial reactors. In this thesis, we study the interaction of energetic ions with the internal kink mode, resulting in the onset of the fishbone instability. To this end, we use the nonlinear hybrid Kinetic-MHD code XTOR-K to simulate the nonlinear phases of the fishbone instability, during which fast particles are being transported. Firstly, the linear theory of the fishbone instability is re-derived, recovering similar expressions with Porcelli's dispersion relation. Differences arise when considering deeply passing particles. A linear code has been implemented to solve non-perturbatively the fishbone dispersion relation obtained. Results with this code are consistent with those obtained from XTOR-K linear simulations, in terms of mode growth rates, rotations frequencies and resonant surfaces. This provides a linear verification of XTOR-K, that enables its use on complex equilibria and during nonlinear phases. Secondly, a parametric study is provided by XTOR-K regarding the alpha fishbone linear stability with equilibria relevant for the ITER 15 MA case. Our simulations show that this scenario is likely to be fishbone unstable for ITER relevant alpha particle densities. Finally, nonlinear results obtained with XTOR-K in low energy circular equilibria and in the ITER 15 MA case are presented. These results document the self-consistent dynamics of fast particles and MHD modes during several fishbone oscillations. Resonant fast particle transport is a common feature of these simulations, together with frequency chirping of the Kinetic-MHD mode. Differences between these simulations are discussed, as well as the nonlinear regime characterizing the observed mode based on existing theories. During a few fishbone oscillations, in our different simulations, the overall alpha particle transport in the core plasma impacts around 5% of the initial population, which shows that the reduction of fusion performances due to the alpha-fishbone instability is limited. From these simulations, a mechanism explaining the nonlinear coupling between resonant particle transport and mode chirping is presented.

Institut Polytechnique de Paris
91120 Palaiseau, France